Next-Generation Fluorophores for Single-Molecule and Super-Resolution Fluorescence Microscopy

Lisa-Maria Elizabeth Needham

Department of Chemistry

University of Cambridge

A dissertation submitted for the degree of

Doctor of Philosophy

Girton College May 2018

Declaration

This dissertation is the result of my own work except where specific reference is made to the work of others in the text. It is not substantially the same as any that I have submitted, or, is being concurrently submitted for a degree or diploma or other qualification at the University of Cambridge or any other University or similar institution except as declared in the Preface and specified in the text. I further state that no substantial part of my dissertation has already been submitted, or, is being concurrently submitted for any such degree, diploma or other qualification at the University of Cambridge or any other University or similar institution. This dissertation is fewer than 60,000 words including appendices, references, tables and equations and has fewer than 150 figures.

Lisa-Maria E Needham

30th May 2018

Acknowledgements

The work presented in this thesis would not have been possible without the guidance and support of many brilliant people.

First and foremost, I thank my supervisor, Dr Steven F. Lee. There are many things I could say that would probably extend over several pages but to keep it brief, thank you for being my mentor and for giving me the chance to be a part of the world-class research lab you have created here. It is a real privilege to be your first PhD student and I'm grateful every day to have had this opportunity. Finally thank you for making me into the scientist and person I am today. It has been a long and wonderful journey, but I would not have been able to do it if you hadn't supported and guided me every step of the way.

To my amazing friend Alexander Roy Carr, thank you for going through this with me and for being one of the best people I know. I can't imagine having started out with anyone better. I may have failed at turning you into a chemist, but you've created some of the most beautiful data I've ever seen. Whatever you do next, you're going to be epic. Dr. Aleks Ponjavic, you are one of the greatest scientists and friends I have ever had the privilege of knowing. You are going to change the world. Thank you for constantly being my rock, you teach me every day how to be a better scientist, I owe so much of this PhD to you. Anna Lippert, you are my best friend and a light in my life. You are the smartest person I know, and I just hope you remember me when you get your Nobel prize. Thank you for constantly supporting me in research and in life. Thank you to Judith Weber, Dr. Juan Varela, Dr. Margarida Rodrigues and Dr. Hannah Stern for all of your support and your collaboration in the lab and for reading and significantly improving this thesis. Much of this work could not have been completed without you and I am very grateful for that. Additionally, thank you for being wonderful friends. To all the members of both the Lee labs and Klenerman labs, thank you for your endless support in and outside of the labs. I could very easily name and write pages about you all individually but know that

I'm grateful to you. Specifically, thank you to Dr. Franziska Kundel, Dr Ji-Eun Lee, Dr Rohan T. Ranasinghe, Dr James McColl, Dr. Suman De, David Wirthensohn and Chieh Sang for being excellent colleagues and more importantly excellent friends.

This thesis represents work that is the result of extensive collaboration. In acknowledgement of that I thank Prof. David Klenerman, Prof. Ernest Laue and Dr. Srinjan Basu. I have been very lucky to have received your guidance and tutorage over these years. Specifically, Srinjan, you have taught me a lot about what it means to be a good scientist, you've also been a wonderful support and friend.

This thesis would not have been achieved without the love and support of my friends and family. Firstly, Mum and Dad, I am incredibly lucky to have such wonderful parents and I'm grateful for that every day. For my entire life you've supported my dreams and I owe so much of everything I've accomplished to you. Christina, the youngling, even though you're now in your 20's you're still my baby sister. Thank you for being the wonderful person that you are, for everything you do for me, the list of which is so long. I couldn't ask for a better sister. Thank you to Sue, Andy, Matt and Hannah, for being wonderful and supportive in-laws. Particularly to Andy for reading some of this thesis. I feel very lucky to be a part of your family.

I thank my wonderful friends, namely the 'squad', Hollie, Holly, Edward and Shaun. You all bring incredible happiness to my life. Thank you for letting me tell you about my work and for smiling and nodding when you're not sure what I'm waffling on about. Thank you for sticking with me when I'm at my worst and for still being there at the end of this journey. My life would be poorer without you all.

Finally, Ben. My amazing husband. There aren't enough words or ways to describe how grateful I am for you. Everything I am and everything I've achieved is because of you. You've supported me and my dreams for over a decade and have given everything, so I can follow them. I hope I can one day do the same for you. Therefore, I dedicate this thesis to you.

To Ben

Summary

The development of single-molecule and super-resolution fluorescence techniques has revolutionised biological imaging. Nano-scale cellular structures and heterogeneous dynamic processes are now able to be visualised with unprecedented resolution in both time and space.

The achievable localisation precision and therefore the resolution is fundamentally limited by the number of photons a single-fluorophore can emit. The ideal super-resolution dye would emit a large number of photons over a short period of time. On the contrary, an optimal single-molecule tracking probe would be highly photostable and undergo no transient dark-state transitions. Single-molecule instrument development is beginning to reach technological saturation and as the frontiers of bioimaging expand, exorbitant demands are placed on the gamut of available probes that often cannot be met. Thus, the next key challenge in the field is the development of the better fluorophores that underlie these techniques; this includes both the synthesis of new chemical derivatives and alternative novel strategies to augment existing technologies.

The results of this thesis are divided into two distinct parts; Project One details the development of new synthetic fluorescent probes for the study of amyloid protein aggregates implicated in neurodegenerative diseases. This includes a study of the photophysical and binding properties of a novel fluorophore library based on the amyloid dye Thioflavin-T. Following on from this, is the presentation of novel bifunctional dyes capable of simultaneously identifying hydrogen peroxide and amyloid aggregates by combining existing tools for the independent detection of these species. The sensing capabilities of these dyes are explored at the bulk and single-molecule levels.

Project Two describes a new photo-modulatable fluorescent-protein fusion construct that can undergo Förster resonance energy transfer (FRET) to an organic dye molecule. This FRET cassette is comprised of a photoconvertible

fluorescent protein donor, mEos3.2 and acceptor fluorophore, JF_{646}. This strategy imparts a strong photostabilising effect on the fluorescent protein and a resistance to photobleaching. The functionality of this approach is demonstrated with *in vitro* single-molecule fluorescence studies and its biological applicability shown by tracking single proteins in the nuclei of live embryonic stem cells. Furthermore, initial characterisations of the excited state dynamics in effect are presented through the systematic modification of parameters.

Abbreviations Glossary

αSyn	α-Synuclein
AD	Alzheimer's Disease
AF	Alexa Fluor
Aβ	Amyloid-beta
BODIPY	BOron-DIPYrromethene
CSF	Cerebral Spinal Fluid
DCDHF	2-DiCyanomethylene-3-cyano-2,5-DiHydroFuran
DCFH-DA	DiChlorodiHydroFluorescein DiAcetate
dSTORM	Direct STochastic Optical Reconstruction Microscopy
ECFP	Enhanced Cyan Fluorescent Protein
EMCCD	Electron Multiplying Charged Coupled Device
EYFP	Enhanced Yellow Fluorescent Protein
FCS	Fluorescence Correlation Spectroscopy
FP	Fluorescent Protein
FRAP	Fluorescence Recovery After Photobleaching
FRET	Förster Resonance Energy Transfer

FWHM	Full Width Half Maximum
GFP	Green Fluorescent Protein
HOMO	Highest Occupied Molecular Orbital
ICT	Intramolecular Charge Transfer
ISC	Inter-System Crossing
LCMS	Liquid Chromatography Mass Spectrometry
LE	Locally Excited
LoD	Limit of Detection
LUMO	Lowest Occupied Molecular Orbital
NA	Numerical Aperture
NHS	N-HydroxySuccinimide
NR	Non-Radiative
NuRD	Nucleosome Remodelling Deacetylase
OD	Optical Density
PA	PhotoActivatable
PAINT	Point Accumulation for Imaging in Nanoscale Topography
PALM	PhotoActivated Localisation Microscopy
PBS	Phosphate Buffered Saline

PC	PhotoConvertible
PD	Parkinson's Disease
PiB	Pittsburgh B
PLK	Poly-L-Lysine
PM	PhotoModulatable
PS	PhotoSwitchable
PSF	Point-Spread Function
QE	Quantum Efficiency
ROS	Reactive Oxygen Species
SAVE	Single Aggregate Visualisation by Enhancement
SM	Single-Molecule
smFRET	Single-Molecule Förster Resonance Energy Transfer
SML	Single-Molecule Localisation
SMT	Single-Molecule Tracking
SNR	Signal to Noise Ratio
SPR	Surface Plasmon Resonance
SPT	Single Particle Tracking
SR	Super-Resolution

STED	STimulated Emission Depletion
STORM	STochastic Optical Reconstruction Microscopy
ThT	Thioflavin-T
TICT	Twisted Intramolecular Charge Transfer
TIRF	Total-Internal Reflection Fluorescence
TMR	Tetra-Methyl Rhodamine
VR	Vibrational Relaxation

List of Figures

List of Tables

List of Schemes

Publications

Published and accepted peer-reviewed papers relevant to this thesis:

1. **L.-M. Needham***, J. Weber*, J.W.B. Fyfe, O.M. Kabia, D.T. Do, E. Klimont, Y. Zhang, M. Rodrigues, C.M. Dobson, S. Ghandi, S.E. Bohndiek#, T.N. Snaddon#, S.F. Lee#, Bifunctional fluorescent probes for detection of amyloid aggregates and reactive oxygen species, *Royal Society Open Science*, (2018). http://dx.doi.org/10.1098/rsos.171399

2. S. Basu*, **L.-M. Needham*,** D. Lando, E.J.R. Taylor, K. J. Wohlfahrt, D. Shah, W. Boucher, Y. L. Tan, L. E. Bates, O. Tkachenko, J. Cramard, B. C. Lagerholm, C. Eggeling, B. Hendrich, D. Klenerman#, S. F. Lee#, E. D. Laue#, FRET-enhanced photostability allows improved single-molecule tracking of proteins and protein complexes in live mammalian cells, *Nature Communications* (2018). DOI: 10.1038/s41467-018-04486-0

* These authors contributed equally to this work

Co-corresponding authors

Table of Contents

Chapter 1 Background and Theory: Fluorescence and Fluorophores

1.1 Overview of this chapter

This chapter addresses relevant background to the topics that form the fundament of the work in this thesis. The initial sections describe the energetic transitions a fluorescent molecule may undergo after photon absorption. The photophysical processes that are vital at the single-molecule level will be introduced followed by a discussion of the types of fluorophores typically used in fluorescence microscopy experiments.

1.2 Fundamental interactions of light with matter

1.2.1 A molecular orbital picture

A **fluorophore** is defined as a molecule or component of a molecule capable of absorbing and emitting photons of quantised energy in the UV/visible spectrum. Fluorescent molecules classically consist of a conjugated system of π electrons capable of delocalising across the molecule. The light induced motion of these electrons between discrete energy states can be studied with electronic spectroscopy, with which the absorption and emission of energy can be observed. Discussions of electronic transitions are often interchanged between descriptions of molecular electronic states and molecular orbitals. Both of these are relevant but not identical, molecular electronic states describe all electrons in the system whereas molecular orbitals are limited to single electrons in the molecule (Figure 1.1).

In a simple two electron system, prior to energy absorption, the electrons reside in the molecular ground state or the highest occupied molecular orbital (HOMO). The system then interacts with a photon of energy (E_{photon}) equal to

the energy between the HOMO and the lowest unoccupied molecular orbital (LUMO, $\Delta E_{HOMO\text{-}LUMO}$).

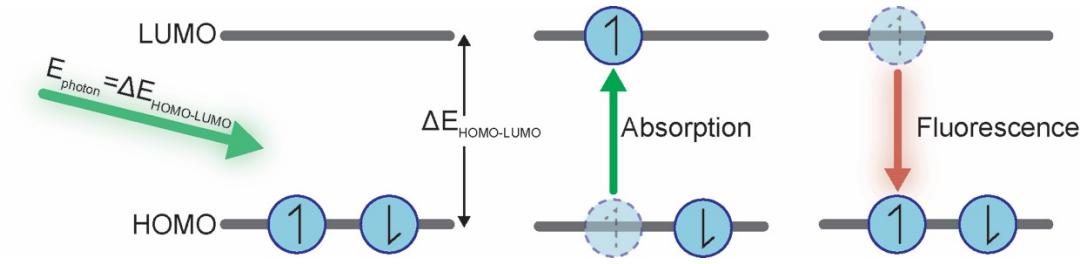

Figure 1.1. Molecular orbital illustration of electron dynamics that occur when a molecule absorbs and emits a photon.

This can be described by the relationship in Equation 1.1:

$$\lambda_{photon} = \frac{h\,c}{\Delta E_{HOMO\text{-}LUMO}} \qquad (1.1)$$

where λ_{photon} is the photon wavelength, h is Planck's constant (6.63×10^{-34} $m^2 kg s^{-1}$) and c is the speed of light (2.9979 ms^{-1}). One electron is then promoted to the LUMO and the molecule occupies an electronically excited state. The electron will then relax back to the HOMO to reform the electronic ground state with the emission of a lower energy fluorescence photon. Under the assumption that the two energy-level model is a complete description of absorption and fluorescence, experimental observations would manifest in sharp, discrete transitions between the two states. Furthermore, it would be expected that the absorbed and emitted photons are the same energy. However, both absorption and emission occur over a continuum of energies, which can be observed experimentally as spectra (Figure 1.2). This suggests that more complex electron dynamics are in affect that cannot be explained by the molecular orbital model alone. Discussion of electronic states provides a more complete picture of these processes and can be illustrated effectively with a Jablonski diagram.

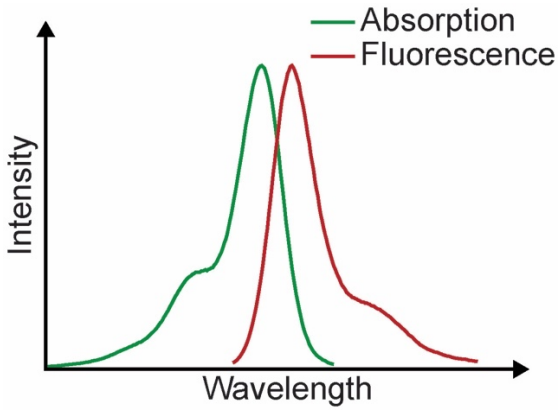

Figure 1.2. Illustration of typical absorption and fluorescence spectra of a fluorophore.

1.3 Electronic states of chromophores: The Jablonski diagram

Figure 1.3 is an example of a Jablonski diagram illustrating some of the electronic and vibrational states and transition pathways that exist when a fluorophore becomes excited by one or multiple photons. Most fluorescent molecules occupy either singlet (S) or triplet (T) electronic states. Electrons in S or T states are spin-paired or spin-parallel respectively. In accordance with the Pauli principle, the valence electrons in the lowest energy electronic state (ground-state) of a molecule with a closed-shell configuration will be spin-paired and therefore form a singlet-state (S_0). Within each electronic energy level there are sub-states corresponding to vibration, rotation and translation of the fluorophore. For the purposes of clarity and relevance only electronic and vibrational states will be discussed. These processes are dependent on a multitude of factors including the external environment, molecular structure and conformation and transition strengths.

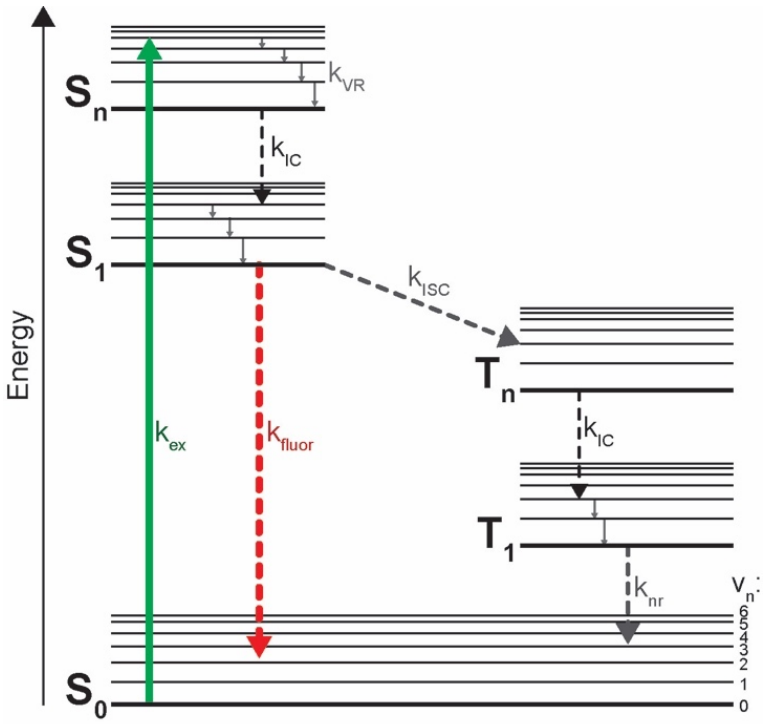

Figure 1.3. Jablonski diagram showing the electronic states of a fluorophore. The dye resides in the ground-state prior to photoexcitation from which it is promoted to an energetic excited state. There are multiple transitions that may occur between these states. Within each electronic level are sub-levels associated with molecular vibration. The vibrational levels have only been quantified on the S_0 for clearness.

The strength of a transition between electronic states can be described by the integrated products of quantum mechanical wave-functions of the respective states. This is known as the transition dipole moment μ_{GE} (1):

$$\mu_{GE} = \int \Psi_G \, \mu \, \Psi_E d\tau \qquad (1.2)$$

Ψ_G and Ψ_E are the quantum mechanical wavefunctions corresponding to energy levels G and E respectively. μ is the electric dipole moment operator which quantifies the distribution of electronic charge across the molecule. This fundamental equation forms the foundation of molecular spectroscopy and defines the probability of a transition occurring. μ_{GE} can be interpreted as the oscillation in the electric dipole moment of a molecule accompanying a transition between states G and E. For a fluorescence transition to be plausible

the transition moment must be non-zero, thus the molecule must undergo a redistribution of electron density during the transition.

1.3.1 An exciting transition: from S_0 to S_n

Once a molecule has absorbed a photon it will possess excess energy and transition from the ground-state to a **locally excited** (LE) state. Like all electronic state transitions, photon absorption is not instantaneous and has an associated rate constant, $\left(k_{abs} = \frac{1}{\tau_{abs}}\right)$ which is equal to approximately $10^{15}\ s^{-1}$. The probability of a molecule absorbing a photon of the correct wavelength is dependent on the strength of the interaction between the electromagnetic components of light and the molecule. Incident photons induce the motion of delocalised electrons within the fluorophore which produces an oscillating dipole if the oscillating frequency (v, Hz) of the incident radiation matches that of the electrons. This can be quantified in terms of the oscillator strength (f, Equation 1.3) (2) and describes the number of electrons in the absorbing molecule that have an induced oscillation in response to the light:

$$f = \frac{2303\ m\ c}{\pi\ N_A\ e^2\ n} \int \varepsilon\ (v)\ dv \qquad (1.3)$$

such that m is the mass of an electron (9.11×10^{-31} kg), N_A is Avogadro's constant ($6.02 \times 10^{23}\ mol^{-1}$), e is the electron charge (1.60×10^{-19} C), n is the refractive index of the medium and ε is the **molar extinction coefficient** ($M^{-1}cm^{-1}$). f can be determined experimentally due to the relationship with ε, a constant which describes the light attenuation capacity of a molecule. The Beer-Lambert law (Equation 1.4) quantifies the ensemble absorption of light through a substance, such as a solvated fluorophore.

$$\ln \frac{I_0}{I} = A = \varepsilon\ c\ L \qquad (1.4)$$

In the context of a liquid-phase experiment, light of an intensity (I_0) is transmitted through a solution with path length (L, cm) containing a concentration (c, M) of the absorbing molecule. The natural logarithm of I_0 over

the transmitted intensity (I) is equal to the absorbance (A). ε is typically on the order of 10^3-10^5 $M^{-1}cm^{-1}$ for organic fluorophores (3) and is an important quantity for determining the overall brightness of the fluorescence emission from a fluorophore (4, 5).

1.3.2 S_n to S_0 via non-radiative relaxation

An electronically excited fluorophore may occupy any of the vibrational states (v_n) within the LE state. The Jablonski diagram in Figure 1.3 shows a fluorophore excited to v_4 in S_n. From this state the molecule may rapidly undergo vibrational relaxation (VR) which involves the dissipation of thermal energy. These states have very short lifetimes and relaxation to the lowest vibrational state is complete in 10^{-12}-10^{-10} s (2). From the lowest vibrational state of S_n, the flurophore may relax to S_1 through internal conversion (IC) with $k_{IC} > 10^{11}$ s^{-1}. These processes lead to the formation of the **equilibrium excited-state** ($S_{1, v0}$), from which there are many competing routes that may depopulate the state. The molecule may undergo intersystem-crossing (ISC) to form a triplet excited state (T_1). In order for this transition to occur, the excited electron needs to undergo a spin conversion (Figure 1.4), hence ISC is inefficient and slow (k_{ISC}~ 10^5-10^8 s^{-1}). However, k_{ISC} can be increased by the presence of heavy metals and paramagnetic atoms and contrarily reduced by the addition of energy transfer pathways (6).

Decay from T_1 to S_0 can occur with the emission of a photon, a process known as phosphorescence. However, phosphorescence is not detected in typical fluorescence spectroscopy and therefore described as a non-radiative (NR) decay in this context (2). Re-forming S_0 from T_1 is spin-forbidden, resulting in T_1 lifetimes (τ_{T_1}) of ms (7).

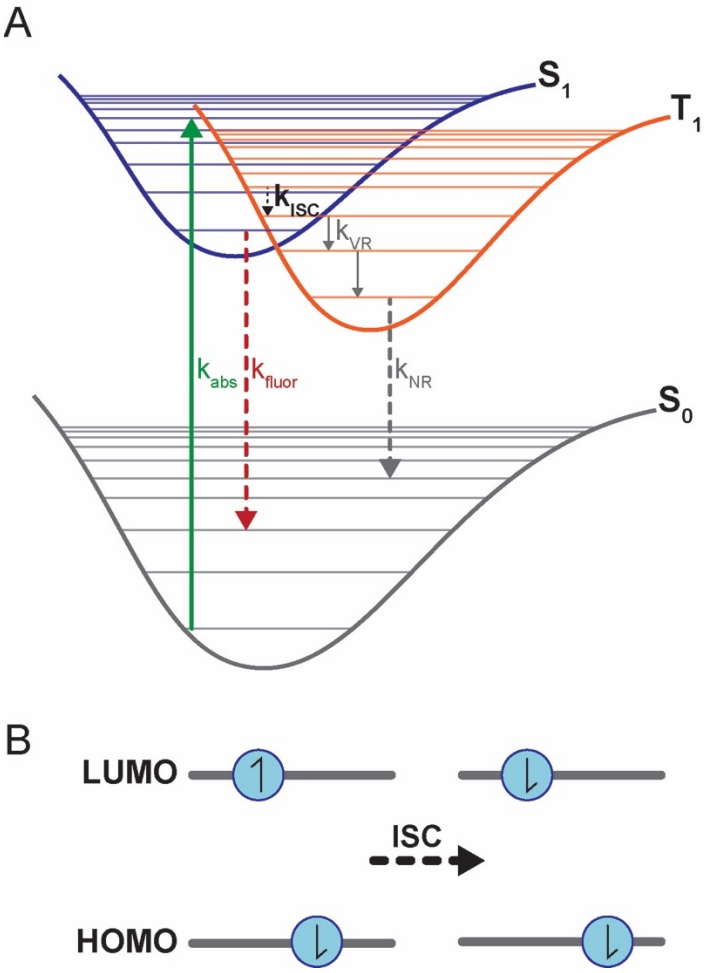

Figure 1.4. A) Electronic state diagram illustrating the overlap between S_1 and T_1 states that facilitates ISC. **B)** Molecular orbital picture of electron dynamics of ISC. A fluorophore will undergo an excited-state spin exchange from a singlet arrangement to form a triplet arrangement.

1.3.3 Relaxation: From S_1 to S_0:

Emission of a fluorescence photon occurs after the molecule has reached thermal equilibrium and is therefore a lower energy than the exciting photon. The separation between the maximum wavelengths of absorption (λ_{abs}) and emission (λ_{fl}) is known as **Stokes shift** ($\Delta\lambda$, Equation 1.5):

$$\Delta\lambda = \lambda_{fl} - \lambda_{abs} \quad (1.5)$$

This is a desirable property of fluorophores used in fluorescence spectroscopy and microscopy as it simplifies fluorescence signal collection by optimisation of excitation filtering (8).

The lifetime of the equilibrium state of S_1 (τ_{fl}) is equal to the reciprocal sum of the rate constants that depopulate the state (Equation 1.6):

$$\tau_{fl} = \frac{1}{k_{fl} + k_{NR}} \tag{1.6}$$

where k_{fl} is the rate constant of fluorescence. τ_{fl} is a measurable quantity, known as the fluorescence lifetime, and is typically on the order of 10^{-7}-10^{-9} s. In the circumstance that NR pathways are not the dominant route to ground-state return, a fluorophore will transition from the equilibrium state of S_1 to S_0 by emitting a fluorescence photon. A perfect fluorophore will emit photons with 100% efficiency, meaning that the number of fluorescence photons is equal to the number of absorbed photons. This is defined as the **fluorescence quantum yield** (Φ_{Fl}, Equation 1.7):

$$\Phi_{Fl} = \frac{\text{Number of emitted photons}}{\text{Number of absorbed photons}} = \frac{k_{fl}}{k_{fl} + k_{NR}} \tag{1.7}$$

There are multiple parameters that govern Φ_{Fl} which make it an impossible quantity to predict, but the chemical and physical structure of the fluorophore can indicate whether it will be an efficient emitter. The presence of labile or rotatable groups can increase k_{NR}. There are several dyes that exhibit this property, known as molecular rotors, which have been used effectively as sensors of viscosity (9). On the contrary, the development of push-pull chromophores have been shown to exhibit superior Φ_{Fl} (10). By positioning an electron donating group and an electron accepting group at opposite ends of a conjugated system of electrons, the hyperpolarisability and ground state dipole moment is increased. Although, some chromophores displaying this non-linear optical behaviour are less efficient emitters as a consequence. Photoinduced charge redistribution is often accompanied by a large conformational change, in which NR pathways dominate (11). Yet, this structural re-organisation leads to

large Stokes shifts as the flurophore reaches an energy minimum far-removed from the absorption energy.

Fluorescent probes with red to near-infrared emission are preferred in bioimaging due to the reduced background from the lack of naturally occurring red chromophores and reduced scattering ($1/\lambda^4$) in this spectral region (12, 13). In line with the *particle in the box model* (Equation 1.8), the simplest way to red-shift emission is to extend the length (L) of the delocalised system:

$$\lambda_{fl} = \frac{8\, m\, L^2\, c}{n^2\, h} \qquad (1.8)$$

in which *n* is the principle quantum number. Although theoretically straightforward, introducing more conjugated bonds often means more mobile groups which in turn increases the probability of NR relaxation and reduction of Φ_{Fl}.

Thus far, the discussion has been limited to general principles and electronic state processes of isolated fluorophores independent of external considerations. This picture is fundamental but unrealistic in the context of experimental practice. The environment of the fluorophore plays a very significant role in determining its fate and observable photophysics.

1.3.4 Environmental effects on fluorescence

When a solvated fluorophore is photoexcited, the surrounding solvent molecules will re-organise in order for the fluorophore to reach an energy minimum. This solvent relaxation occurs on the order of 10^{-10} s and is one of the contributors to significant Stokes shifts (**solvatochromism**) in polar fluorophores. Ordinarily, the magnitude of the excited state dipole moment (μ_E) is greater than the ground state (μ_G). Therefore, the greater the solvent polarity, the greater the excited state stabilisation and solvatochromism.

This is taken into account with the Lippert-Mataga relationship (Equation 1.9) (14, 15):

$$\bar{\nu}_{abs} - \bar{\nu}_{fl} = \frac{2(\mu_E \mu_G)^2}{h\, c\, a^3} \left(\frac{\varepsilon_d - 1}{2\varepsilon_d + 1} - \frac{n^2 - 1}{2n^2 + 1} \right) \quad (1.9)$$

where $\bar{\nu}_{abs}$ and $\bar{\nu}_{fl}$ are energies of absorption and fluorescence in cm^{-1} and ε_d and n are the solvent dielectric constant and refractive index respectively. a is the Onsager radius of the fluorophore when it is solvated. Stokes shift and solvent polarity are linearly correlated for many fluorophores and this relation has been used experimentally to report on the conditions of the fluorophore environment (16, 17). Despite this, the application of this equation is limited to a description of the electronic and molecular motion of solvent molecules and does not include interactions between fluorophore and solvent such as H-bonding and excited state reactions. The formation of non-covalent bonds between solvent and fluorophore can have a significant effect on Φ_{Fl}. This has been demonstrated by evaluating the effect of hydrogen (H) to deuterium (D) isotope exchange in water (H_2O). Fluorophores capable of undergoing excited-state proton transfer reactions with the aqueous solvent showed an increase of Φ_{Fl} in D_2O due to a reduction in the rate of the transfer reaction (18). H-D isotope exchange has also been shown to increase Φ_{Fl} of organic fluorophores and fluorescent proteins by reducing the H-bond donor capacity (19, 20). Fluorescence intensity can also depend on the capability of the solvent to accept vibrational and electronic energy. If ΔE between vibrational states is large, then the solvent may be an efficient acceptor of energy and consequently reduce the Φ_{Fl}.

1.3.5 Förster Resonance Energy Transfer

There are innumerate ways in which the energy of an excited fluorophore may be dissipated. Excited state energy transfer (ET), particularly **Förster resonance energy transfer** (FRET) between two fluorophores, has been widely employed as a tool throughout research (21–24). The implementation of this phenomenon has been successful due to the stringent set of rules that

govern the process. When fulfilled, FRET may provide extensive insight into the environment of the two molecules. The rate of non-radiative transfer (k_{FRET}) of excited state energy from a single donor (D) to a single acceptor (A) molecule separated by a distance, r, is governed by three physical factors:

- The over-lap between the emission spectrum of D and the absorption spectrum of the A.
- The inter-molecular distance between D and A.
- Alignment between relevant transition dipole vectors of D and A.

Discussion of ET will be in the context of fluorophores for the purposes of this work, however fluorescence emission is not a requirement for resonance energy transfer (25).

Overlap between D emission and A absorption spectra corresponds to a physical manifestation of energy degeneracy (Figure 1.5).

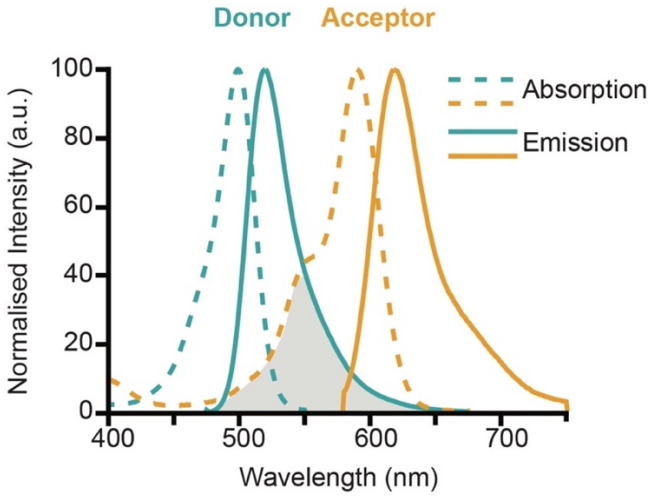

Figure 1.5. Absorption and emission spectra of FRET donor (turquoise) and FRET acceptor (orange) show the spectral overlap (grey).

The degree of wavefunction overlap (J) is one of the factors that dictate the efficiency of resonance between the D and A and can be described by Equation 1.10:

$$J = \int F_D(\lambda)\, \varepsilon_A(\lambda)\, \lambda^4\, d\lambda \qquad (1.10)$$

in which J is calculated from the integral of the normalised D fluorescence (F_D) and normalised acceptor absorption (ε_A) with respect to wavelength (λ). Intensities are normalised, as relative absorption and emission capabilities do not factor into determination of J. However, these are important physical quantities that effect the **FRET efficiency** (E_{FRET}), defined as the ratio between the number of photons absorbed and energy transferred to acceptor.

Ideally, D will have a high ε and Φ_{Fl}. E_{FRET} is very sensitive to inter-fluorophore distance changes and decreases with increasing distance (Figure 1.6). For this reason, k_{FRET} is often expressed in terms of the Förster radius (R_0).

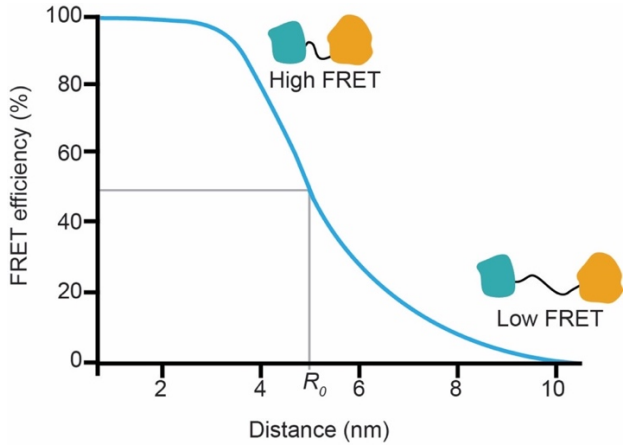

Figure 1.6. Illustration of relationship between FRET efficiency and D-A distance.

Physically, R_0 is the distance between D and A at which E_{FRET} is equal to 50%. In terms of excited state kinetics, R_0 is equal to the reciprocal fluorescence lifetime of D in the absence of A $\left(\frac{1}{\tau_D}\right)$ and can be expressed as:

$$R_0^6 = \left(\frac{9000\ (\ln 10)\ \Phi_D\ \kappa^2}{128\ \pi^5\ N_A\ n^4}\right) J(\lambda) \qquad (1.11)$$

where κ^2 is an orientation factor describing the relative arrangement of the transition dipole moment vectors of D and A in space. Φ_D is the fluorescence

quantum yield of D without A, N_A is Avogadro's constant and n is the refractive index of the medium.

This can be simplified to:

$$R_0 = 0.211\left(\kappa^2 n^{-4} \Phi_D J(\lambda)\right)^{\frac{1}{6}} \quad (1.12)$$

This r^6 dependence makes FRET a very effective reporter of D-A separation and can be measured experimentally by examining D-A and A fluorescence intensity (F) and fluorescence lifetime (τ):

$$E_{FRET} = 1 - \frac{\tau_{DA}}{\tau_D} = 1 - \frac{F_{DA}}{F_D} \quad (1.13)$$

This equates to:

$$E_{FRET} = \frac{R_0^6}{R_0^6 + r^6} \quad (1.14)$$

This photophysical ruler has been employed throughout bioimaging research (26–29) and is sensitive to D-A distances of ≤ 10 nm.

k_{FRET} is coupled to the relative orientation of the transition dipole moments of D and A. Specifically, the S_1-S_0 and S_0-S_1 transition dipole moments of D and A respectively. Figure 1.7 illustrates the directions of transition dipole moments of D and A and angles relative to the D-A join vector.

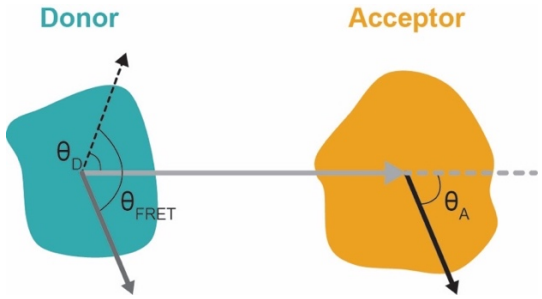

Figure 1.7. Directions and relative orientations of donor and acceptor transition dipole moments.

The angles θ_D and θ_A are the angles between this vector and the dipoles of D and A respectively and θ_{FRET} describes the angle between the D and A dipoles. Together these quantities form the dipole orientation factor, κ^2:

$$\kappa^2=(\cos\theta_{FRET}-3\cos\theta_D\cos\theta_A)^2 \quad (1.15)$$

κ^2 can equal between 0 and 4 which corresponds to completely out of phase and completely co-linear, parallel dipoles respectively (30). Typically, experimentalists take κ^2 as $\frac{2}{3}$, based on the assumption of the freely diffusing dipoles of D and A at a rate faster than $k_{FRET.}$ This assumption is reasonable as κ^2 cannot be measured in appropriate conditions.

Taken together k_{FRET} can be defined by:

$$k_{FRET}=\frac{\Phi_D\,\kappa^2}{\tau_D\,r^6}\left(\frac{9000\,(\ln 10)}{128\,\pi^5\,N_A\,n^4}\right)\int F_D(\lambda)\,\varepsilon_A(\lambda)\,\lambda^4\,d\lambda \quad (1.16)$$

E_{FRET} is directly proportional to k_{FRET} and the most commonly quoted experimental quantity.

1.4 Single-molecule photophysics of fluorophores

Understanding the photophysical properties of fluorophores is vital for any fluorescence experiment in order to ensure correct interpretation of the data and optimal experimental design. This becomes even more crucial when operating at the high sensitivities of **single-molecule** (SM) microscopy. In this regime, photophysical properties of fluorophores that are not detectable in bulk techniques become limiting. The two main photophysical inhibitors of using fluorescence for SM experiments are transient switching between emissive and non-emissive states (Figure 1.8), also termed **blinking**, and irreversible photodestruction, known as **photobleaching**.

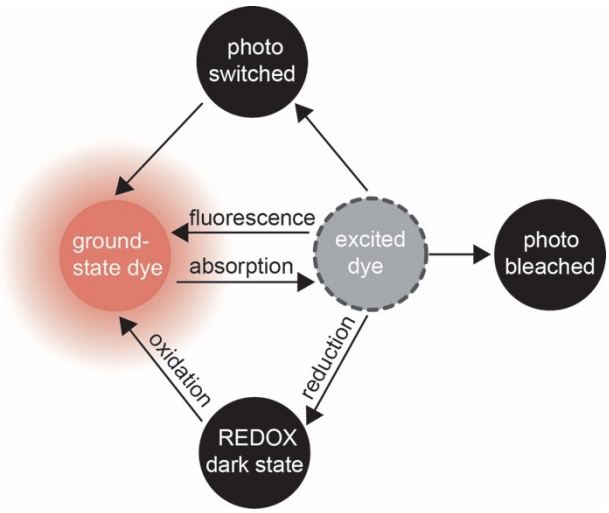

Figure 1.8. Schematic of electronic-state transitions in fluorescent dyes, highlighting a few of the many ways to transition between emissive and dark-states.

1.4.1 Blinking

Dark-state is a term used to describe a fluorophore in a non-emissive form, despite the unifying term these can be reached via a multitude of mechanisms. A blinking fluorophore is one that transitions to a reversible dark-state, meaning that the fluorescent form of the molecule can be recovered. These can arise from ISC, photoisomerism and redox chemistry.

Triplet blinking is a rare occurrence in the life-cycle of a fluorophore, approximately 0.1 % of excitation cycles result in an ISC transition. Despite this process being spin-forbidden, it is able to occur if a spin-orbit interaction exists (31) and becomes more prolific in SM detection modes due to the high irradiances used (32). Diatomic oxygen (O_2) acts as a triplet sensitiser and can facilitate this transition (30). The lifetime of the triplet state is variable and depends on the surrounding environment. In aerated aqueous solution the state lasts on the order of μs before ground-state return. The temporal resolution of most SM methods is ms, therefore these transitions are not detected and instead manifest as a reduction in total intensity. However, de-oxygenated environments increase the triplet life-time to the ms regime, which makes these blinking events visible in SM trajectories. There are many chemical additives

that can be introduced to reduce triplet blinking in organic dyes, such as triplet-state quenchers, these are discussed in detail in section 1.5.5. The first blinking observation made was of gel immobilised single green fluorescent protein (GFP) molecules with total-internal reflection fluorescence microscopy (33). Two dark states were identified in this work, a short-lived state which recovered spontaneously and a long-lived dark-state which was recovered with blue-shifted irradiation. SM blinking behaviour has since been observed in a large number of other fluorescent proteins (FP) (34).

Dark photo-products can form as a result of photoinduced electron transfer reactions in the excited states of fluorophores. These include non-fluorescent radical ions that form from a two-step process initiated by removal of the remaining electron in the LUMO. This facilitates ISC to the triplet state from which another oxidation or reduction can occur to form radical ion. The triplet state is rapidly depopulated in an environment with a high concentration of redox reagents and therefore the observed dark-state is attributed to the radical ion. The triplet state as a mediator for electron transfer and subsequent non-emissive states of SM fluorophores was first proposed following SM observations of rhodamine 6G (35). Blinking is normally an unfavourable process in SM experiments but has been exploited positively in super-resolution experiments (36–38). The radical anions of oxazine dyes have a high reduction potential which results in a dark-state with a lifetime of minutes in the presence of high reductant and low oxidant concentrations (39). It could have been presumed that the dye had undergone photobleaching, however an increase of oxidant concentration in the solution recovered the neutral fluorescent molecule. This demonstrated that the radical anion dark-state transition was reversible and could therefore be modulated by adjusting the relative amounts of oxidant and reductant.

1.4.2 Photobleaching

Photobleaching limits the longevity of SM experiments and differs from blinking in its permanence. However, the two processes are inherently linked by the function that oxygen plays in moderating SM photophysics. O_2 can act to both

populate and depopulate triplet dark-states. Organic fluorophores and FPs typically emit approximately 10^6 and 10^5 fluorescence photons prior to photobleaching respectively (40, 41). There are multiple mechanisms by which fluorophores in a solution may be reversibly or irreversibly quenched (3) but the excited state reactions between triplet fluorophores and singlet oxygen is understood to be the primary cause of photobleaching (42). There is a degree of overlap between S_1 and T_1 in most organic dyes hence photobleaching likely originates from the triplet state.

In its electronic ground-state O_2 is a triplet (Figure 1.9). The valence electron configuration of O_2 is $2s^2$, $2p^4$ and in accordance with Hund's rule of maximum multiplicity the degenerate HOMOs are each filled with one electron in a spin-parallel configuration.

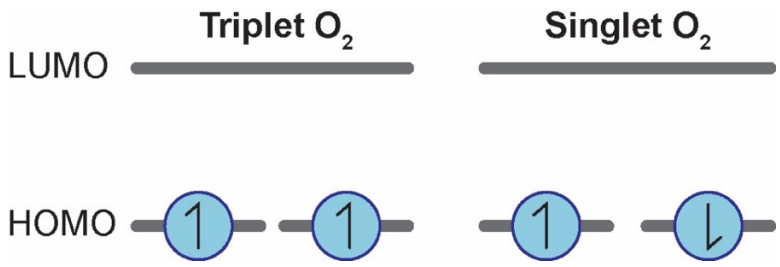

Figure 1.9. Molecular orbital illustration of the electron spin states of O_2.

The lowest excited state of O_2 is a singlet. Light-induced excitation to this state is spin-forbidden, however, an electron transfer reaction between a triplet fluorophore and triplet O_2 can effectively produce singlet O_2. Singlet O_2 is one of many in the class of reactive oxygen species (ROS) and has a short lifetime of μs in solution. These molecules can rapidly react with triplet fluorophores to yield a product that is no longer capable of emitting light. This process is a double-edged sword as triplet O_2 is an effective fluorophore triplet-state quencher which reduces the probability of photobleaching. However, as a result, reactive singlet O_2 is produced which increases the photobleaching likelihood.

The photobleaching quantum yield, Φ_{pb}, is equal to the number of photobleached molecules divided by the number of molecules in S_1. It has been

found that the Φ_{pb} of organic fluorophores increases exponentially with increasing excitation intensity (32). The conditions of SM include high irradiances and under these conditions there is a steady-state of triplet fluorophore production and high Φ_{pb}. Photobleaching may also occur from reactions between ground-state O_2 and the radical ion states of fluorophores, which in turn can produce other ROS (40).

Given the number of mechanisms by which oxygen contributes to fluorophore photobleaching, removal of oxygen would theoretically reduce the Φ_{pb}. This is true for some fluorophores but is not a universal solution (40) due to the efficiency of O_2 as a triplet state quencher. Currently employed solutions in SM microscopy involve buffers containing either oxygen-scavenging and triplet-state quenching agents or redox reagents. Oxygen has been shown to contribute to the photobleaching of FPs (43, 44) as ROS, including singlet O_2, is a product of the illumination of FPs (45). Although photostabilising reagents are effective with organic dyes they have no effect on FPs (46).

1.5 From theory to experiment: Fluorophores for fluorescence microscopy

The field of bioimaging has widely employed fluorescence microscopy due to the ease of filtering, relative non-invasiveness and simplicity to implement. As the majority of interesting biological objects are not intrinsically suitably fluorescent, they are typically tagged through a well-established mechanism with a fluorescent probe. There are four types of fluorophore used in fluorescence microscopy metal complexes (47), quantum dots, **organic dyes** and **FPs** (42). The discussion of fluorescent probes in this section will be limited to organic fluorophores and FPs as these relate specifically to this thesis.

1.5.1 Organic dyes

Organic fluorophores are small molecules consisting of a conjugated system of electrons. The development of advanced optical technologies has increased the

demand for novel organic fluorescent probes. Growing research has led to the development of fluorophores with a wide range of photophysical and chemical properties and absorptions spanning the visible spectrum. It is also possible to functionalise organic fluorophores without detriment to the fluorescence properties (48). This has greatly facilitated the ease of covalent attachment to biomolecules.

The most widely used organic dye classes can be divided into categories including; coumarins, **rhodamines, oxazines** and **cyanines** (Figure 1.10).

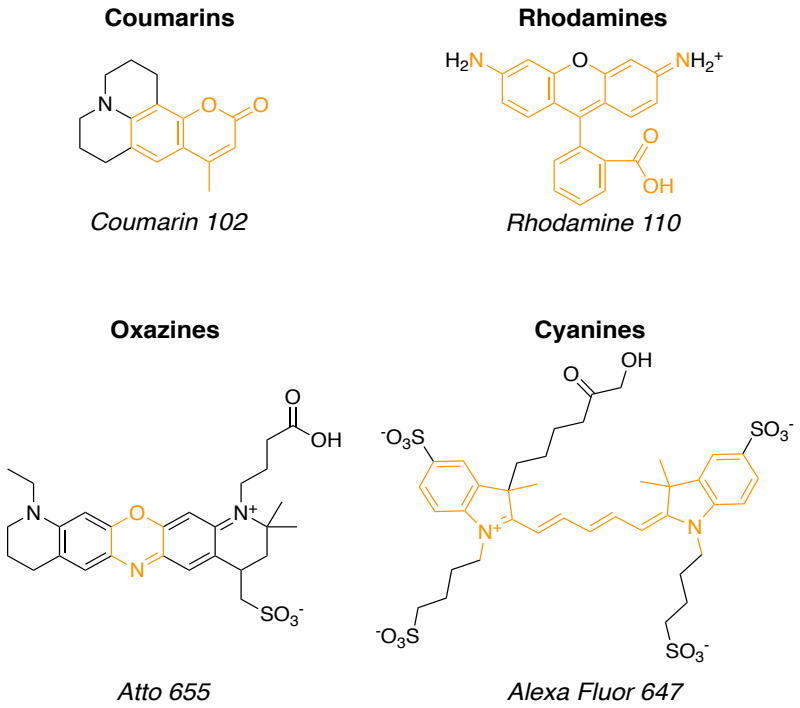

Figure 1.10. Chemical structures of example dyes in four dye classes. The orange component of the structures represents the chemical component that qualifies the dyes for each class.

The coumarins have been used for spectral tuning of dye lasers as they exhibit large Stokes shifts (49). The electron distribution between the ground and excited electronic states of coumarins are markedly different, with the excited state being more polar. The equilibrium excited state is highly stabilised by polar solvent molecules and fluorescence is significantly red-shifted relative to the absorption. Despite this, the use of these fluorophores in fluorescence

microscopies is limited by their poor photostability. On the contrary, rhodamine dyes exhibit high Φ_{Fl} due to their structural rigidity, with values between 0.45-0.95 (50, 51). They typically absorb between 500-570 nm but recent research has yielded a much broader colour palette of rhodamine derivatives with absorption maxima between 497-646 nm (51). These dyes can be fine-tuned for absorption/emission wavelengths by modifying heteroatoms in the chromophore and for photostability and photochromacy by modification of the amino substituents and the phenyl carboxyl group (4, 52).

Certain rhodamine dyes such as, tetramethyl rhodamine (TMR), display environmental sensitivity. TMR has a pH sensitive emission spectrum dependent on the position of an equilibrium between a protonated cation and deprotonated zwitterion (53). Other rhodamines including the recently developed silicon-rhodamines, display protein-enhanced fluorescence and absorption. These dyes have a high propensity to form a non-fluorescent lactone tautomer in low polarity solvents which is inhibited by protein binding to significantly increase ε and Φ_{Fl} (54).

The family of oxazine fluorophores are red-shifted in their absorption and emission maxima relative to their rhodamine ancestors. As previously mentioned, near-IR fluorescent probes are preferred for bioimaging applications. However, the caveat of emission at these wavelengths is the likelihood of a low Φ_{Fl}. This originates from the energetics of the conjugated proton vibrations. As ΔE between S_1 and S_0 reduces, these vibrations stimulate the chromophore to relax via IC. Several dyes have been derived from the oxazine parent scaffold and made commercially available (55) and are a popular choice in SM microscopy due to their photostability.

Cyanine fluorophores are essentially formed from two nitrogen atoms linked by a π-conjugated, polymethine bridge. The length of the bridge dictates the wavelength of absorption. Photoinduced cis-trans isomerism is an observed property of cyanines in solution and is heavily dependent on viscosity, temperature and steric hindrance (56). Two cyanine dyes known as Cy3 and Cy5 have been extensively used as a donor-acceptor pair for Förster

resonance energy transfer (FRET) experiments (56), however excited-state bond twisting and photoisomerism have led to artefacts in FRET data and also reduced Φ_{Fl} (57). Cy dyes with a shorter polymethine chain have lower Φ_{Fl} due to a relatively higher efficiency for bond rotation compared to longer chain cyanines. A structurally rigid analogue of Cy3, termed Cy3B was synthesised to combat this problem. Compared to Cy3, Cy3B had a 10-fold greater fluorescence lifetime and a 17-fold greater Φ_{Fl} (58).

1.5.2 Evolution of the fluorescent protein

The isolation of the GFP in 1962 (59) and its subsequent expression into non-native cells (60) considerably progressed cellular biophysics. Subsequent developments have resulted in a large palette of FPs many of which are very useful tags for cellular imaging. The main advantage of FPs lies in the capability to directly express a fluorescent tag to a protein of interest *in situ* effectively eradicating the need for chemical labelling with external fluorophores. Structurally, FPs are comprised internally of an unordered α-helix, surrounded by a well-organised β-barrel, this protects the internal chromophore from extrinsic reactive species (Figure 1.11) (61).

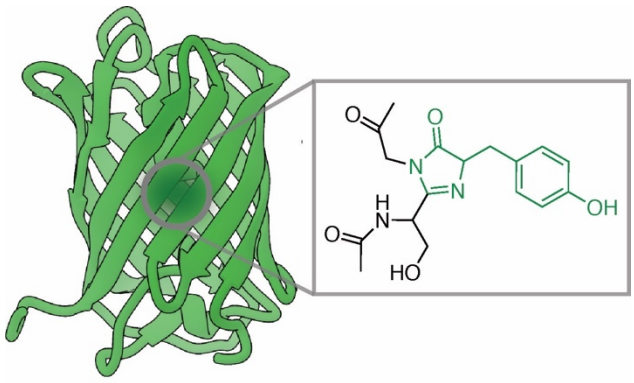

Figure 1.11. Illustration of 3D structure and chromophore of enhanced-GFP. The chromophore is enclosed within the tightly organised β-barrel structure.

The intrinsic fluorophore is comprised of only a few (typically 3) amino acid residues among >200, normally located at the amino acid positions 65-67 (62). Despite the small fraction of the FP responsible for forming the chromophore,

the entire structure is required for fluorescence. Residues surrounding the chromophore make up the complex nano-environment which plays a vital role in governing the fluorescence properties. Denaturing an FP destroys its fluorescence and modifications to non-chromophore residues can drastically alter the fluorescence properties. The reaction mechanism of green FP chromophore maturation has been studied thoroughly and it is understood that the only essential reagent is oxygen. The chromophore is formed via a nucleophilic substitution reaction between two amino acids which are then subsequently oxidised followed by the loss of water. The mechanism for the formation of red FP chromophores is less well-understood (46).

In order for an FP to be used as a probe for a fluorescence experiment it must obey certain requirements. It should be able to express at sufficiently high levels to the desired labelling density and fold efficiently in the conditions required for cell growth. For most applications it should be monomeric and finally it should have photophysical properties suited to the experiment. Most importantly the chromophore should be sufficiently bright ($\varepsilon \times \Phi_{Fl}$) and photostable to be detectable above background noise for the duration of the experiment. It is in these photophysical considerations where FPs compare less favourably to organic fluorophores.

Native GFP matured inefficiently at 37 °C, which is required for use in mammalian cells but a simple mutation of a phenylalanine to a leucine resolved this (63). Multiple single-point mutations have increased the utility of FPs and the available colour palette now spans the visible spectrum (λ_{fl}= 454-651 nm (64)). FPs are typically an order of magnitude less photostable than synthetic fluorophores (65) and despite the broad colour palette, only blue -green FPs are bright enough for most fluorescence microscopy applications (64, 66). The red emitting monomeric (m) FPs, mCherry and mPlum are members of the mFruit series, each of these have Φ_{fl} of 0.22 and 0.1 respectively (67, 68). This is significantly lower than blue FP mTurqoise2 (Φ_{fl}= 0.92) and green FP mClover (Φ_{fl}= 0.84) (69).

As with organic dyes, red to near-IR emission comes with the sacrifice of the superior brightness of blue-shifted fluorophores. The practicality of introducing mutations into FP structure is now relatively accessible, hence there is a drive towards developing red FPs with the spectroscopic properties of those in the blue and green (46, 64, 70, 71).

The gamut of available FPs is constantly evolving; several of them offer properties useful for SM and **super-resolution** (SR) fluorescence microscopies. It was identified that FPs exhibited blinking to transient dark-states (33). This can occur via multiple pathways such as conformational changes and proton transfer mechanisms. This discovery led to the development of **photomodulatable** (PM) FPs which change state in response to stimulating radiation. There are several different terms used to describe probes that can be switched between states in response to light. PM encompasses all of these terms and will be used throughout the remainder of this thesis. PMFPs can be easily placed into two distinct categories of either reversible or irreversible (Figure 1.12).

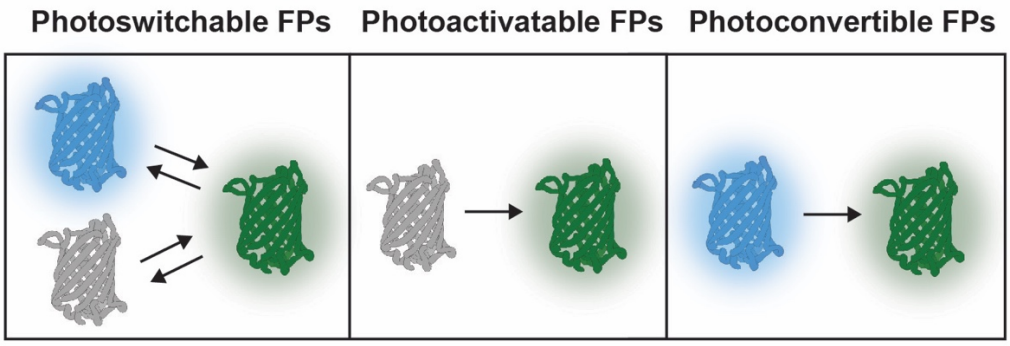

Figure 1.12. Scheme of detailing photomodulation of FPs, reversible photoswitchable FPs (left), irreversible photoactivable FPs (middle) and irreversible photoconvertible FPs (right).

Within these categories are several subclasses. **Photoswitchable** (PS) FPs can be reversibly switched from a dark to a fluorescent state or reversibly chromically switched between distinct emitting states (72). **Photoactivatable** (PA) FPs are irreversibly switched on from a dark state (73, 74) and **photoconvertible** (PC) FPs are irreversibly switched from one emitting state to another (75).

The first PMFP to be isolated and purified was Kaede, a PCFP with intrinsic fluorescence (75). Following illumination with UV radiation, typically 350-400 nm, the PCFP will undergo irreversible photochemical conversion to another emitting state. Kaede and another naturally isolated PCFP, **Eos**, are green emitters in their native state; photoconversion with near-UV light yields a spectrally distinct, red-shifted FP.

Both Kaede and Eos exist as tetrameric complexes in solution which hinders their ability to be used as a fluorescent labels in SR imaging (76). Many variants of the protein Eos have been engineered, dimeric and monomeric forms have been prepared (77) however problems with localisation and maturation conditions have prevented their use in mammalian cell imaging. Further alteration yielded **mEos2** which demonstrated superior photostability compared to GFP and dimeric Eos, as well as greater extinction coefficients of both green and red forms of the protein. mEos2 was also able to mature at 37 °C, making it suitable for *in vivo* tagging (76). It was later observed that mEos2 was prone to aggregation at high concentrations thus mEos3, mEos3.1 and **mEos3.2** were engineered (78).

1.5.2.1 Properties of mEos3.2

mEos3.2 is a monomeric protein that was generated by careful examination of the crystal structure of mEos2. It demonstrated superior Φ_{Fl}, chemical stability and maturation kinetics compared to other forms of Eos as well as the greatest photostability among all green to red PCFPs (78). Spectrally, mEos3.2 was almost identical to its ancestor mEos2. In the green form mEo3.2 has maximum λ_{abs} and λ_{em} at 507 and 516 nm respectively. It has a ε of 64200 $M^{-1}cm^{-1}$ and a Φ_{Fl} of 0.84. The conversion is achieved by a photo-induced (405 nm) decarboxylation via cleavage of a C-N bond in the chromophore (Figure 1.13).

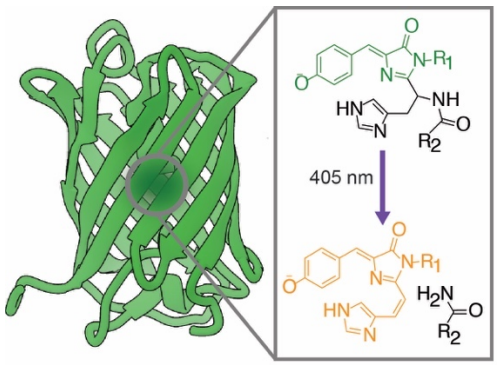

Figure 1.13. Photoinduced chemical switching of the mEos3.2 chromophore.

This reaction forms a fluorophore with an extended network of conjugating electrons (79) that has maximum λ_{abs} and λ_{em} of 572 and 580 nm respectively. Red mEos3.2 has an ε of 32200 and a Φ_{Fl} of 0.55 making it among the brightest of monomeric PCFPs (80). mEos3.2 has a fast maturation half-time of approximately 20 minutes, this is a particularly important metric when considering live cell experiments, in this circumstance a rapidly maturing FP is preferred (78). The pKa of mEos3.2 is 5.8, this is very suitable considering the intra-cellular pH is around 7.

In order for a PMFP to be used in a **SM tracking** or SR mode there are several properties that need to be understood. These include but are not limited to, the achievable labelling density, blinking kinetics, photostability and photon budgets. mEos3.2 demonstrated favourable optical properties at the bulk level and these were also observed at the SM regime. Higher labelling densities were achieved with mEos3.2 compared to other FPs and Eos variants, due to better maturation and folding properties (78). Like many FPs, mEos3.2 undergoes blinking, approximately 50 % of photoconverted molecules undergo >2 switching events prior to photobleaching which is fewer than other monomeric PCFPs (81). For SM tracking, high fluorophore photostability is preferred, on the contrary for SR imaging low photostability and high photon budgets are favoured. mEos3.2 has a photobleaching half-life of 48 seconds (at a laser power of 64 μW), higher than its predecessor mEos3.1 measured under the same conditions. The photon number of mEos3.2 has been measured as the highest among PC and PA FPs including PAmCherry, mMaple3, PA-GFP

and Dendra2 (82). mEos3.2 has been employed in the field of SM and SR bioimaging to study protein-protein interactions (83), protein quantification (84), structure elucidation (85), smFRET (86) and SM tracking (87). The superior efficacy of mEos3.2 as a genetically encodable probe is clearly evidenced by this extensive use.

1.5.3 Fluorophores for FRET microscopy

There are three primary ways to measure FRET in biological samples, these involve the measurement of either; D and A intensities, fluorescence lifetimes or anisotropy (88). For the purposes of clarity, intensity-based methods will be the focus of this discussion. Advantages of applying FRET-based detection methods in fluorescence microscopy include higher signal to noise ratios (SNR) and compatibility with advanced imaging techniques such as SM and SR fluorescence microscopies (89).

In almost all cases the species of interest must be physically tagged with a fluorophore, whether that is through expression of a genetically encodable emitter or chemical attachment of a synthetic fluorophore. Suitable fluorophores must be chosen to optimally adhere to FRET requirements. In addition to selecting fluorescent probes with sufficient energy degeneracy, large acceptor Stokes shifts are also desirable to enable optimal filtering, hence maximum, selective collection of respective D and A signals. The D-A spectral overlap integral is linearly proportional to E_{FRET} however, the greater this overlap, the greater the effect of direct acceptor excitation. This is a particularly significant problem when operating in the high sensitivity regimes of SM and SR fluorescence and requires complex analysis methods to deconvolute direct excitation from FRET induced fluorescence.

An archetypal FRET pair would consist of two highly absorbing ($\varepsilon > 100{,}000\ M^{-1}cm^{-1}$), efficiently emitting ($\Phi_{Fl} > 0.5$), photostable fluorophores. These properties are of even greater importance in **single-molecule FRET** (smFRET) in which the achievable localisation precision is controlled fundamentally by the photon

output of the dye. For bioimaging, spectrally red emitting probes are preferred, and the greatest offering is provided by organic dyes (Table 1.1).

Table 1.1. Select optical properties of example organic fluorophore FRET pairs. The properties include wavelengths of maximum absorption (λ_{abs}) and emission (λ_{em}), molar extinction coefficients (ε) and fluorescence quantum yields (Φ_{Fl}).

Donor				Acceptor				
Dye	**$\lambda_{abs}/\lambda_{em}$ (nm)**	**ε ($M^{-1}cm^{-1}$)**	**Φ_{Fl}**	**Dye**	**$\lambda_{abs}/\lambda_{em}$ (nm)**	**ε ($M^{-1}cm^{-1}$)**	**Φ_{Fl}**	**Ref**
Cy3	550/565	150000	0.2	Cy5	655/667	250000	0.3	(90)
AF488	495/519	73000	0.9	AF594	590/617	92000	0.7	(48)
Atto550	554/577	120000	0.8	Atto647N	650/667	150000	0.7	(91)

There are several advantages in opting for organic fluorophores for FRET studies. Selective tuning of optical properties such as λ_{abs}, λ_{em} and photostability can be readily achieved with established synthetic methods by minor structural modifications (4, 51, 92). Several chemical buffer additives have been developed to modify excited states and have proved very effective with organic fluorophores, these will be discussed in detail in section 1.5.5. However, the solvent exposed nature of organic probes can be both a help and hindrance in FRET studies.

Cyanine dyes, Cy3 and Cy5 form one of the most popular organic dye FRET pairs owing primarily to ease of use and comparable photophysics relative to each other (93). Cy3-Cy5 has been used in smFRET studies of DNA conformation (94) and protein-protein interactions (95). Despite this, both dyes are poor emitters compared to other organic fluorophores and prone to isomerism (96) and solvatochromism (56). Alternative FRET fluorophores are available including the cyanine derived Alexa Fluor (AF) and their oxazine counterparts, the Atto dyes. These probes, with their greater Φ_{Fl}, have been adopted in smFRET studies of dynamic protein conformations and aggregation

(97–99). Choosing organic fluorophores to form FRET pairs is not as simple as evaluating the individual fluorophore photophysics, the application must also be considered. Covalent attachment of fluorophores have been shown to mitigate protein aggregation kinetics (100) hence inherently biasing results of smFRET studies of these processes. Certain fluorophores are also known to undergo proximity induced quenching when bound to DNA (100). Hence, the most efficiently absorbing and emitting dyes may not be the best probes for every experiment.

Until recently SR FRET had many associated challenges. SR imaging technique stochastic optical reconstruction microscopy (STORM) operates via induced random photoswitching (blinking) of organic fluorophores between non-emissive (dark) and emissive (bright) states. Transiently switching fluorophores significantly complicate already convoluted FRET data. The development of photophysically high-performing photoactivatable fluorophores (52) have significantly simplified the possibility of SR-FRET studies through controllable photomodulation.

Despite these advantages, many prefer to employ FPs for their high specificity, intracellular stability and inertness of the chromophores from their surrounding environment (101). The ability to endogenously tag cellular species is incredibly advantageous when studying cells into which organic dyes are unable to permeate. The most commonly used FP FRET pair is enhanced cyan fluorescent protein (ECFP) and enhanced yellow fluorescent protein (EYFP) (Table 1.2). The most notable advantage of this pair is the high Φ_{Fl} compared to the organic fluorophore pair Cy3-Cy5. However, they exhibit poor photostability and spectral separation which significantly increases the probability of cross-talk between emission channels (101). The near-UV light required to excite ECFP has adverse toxicity effects on EYFP.

Table 1.2. Select optical properties of example fluorescent protein FRET pairs. The properties include wavelengths of maximum absorption (λ_{abs}) and emission (λ_{em}), molar extinction coefficients (ε) and fluorescence quantum yields (Φ_{Fl}).

Donor				Acceptor				
Dye	**$\lambda_{abs}/\lambda_{em}$ (nm)**	**ε ($M^{-1}cm^{-1}$)**	**Φ_{Fl}**	**Dye**	**$\lambda_{abs}/\lambda_{em}$ (nm)**	**ε ($M^{-1}cm^{-1}$)**	**Φ_{Fl}**	**Ref**
ECFP	433/475	33000	0.4	EYFP	513/527	83000	0.6	(70)
EGFP	488/507	56000	0.6	mCherry	587/610	72000	0.2	(70)
mClover3	506/518	109000	0.8	mRuby3	558/592	128000	0.5	(102)

The development of bathochromically shifted FPs such as EGFP, mCherry and others (Table 1.2) have overcome some of these problems. Higher Φ_{Fl} and ε quantities of FPs monomeric (m) Clover3 and mRuby3 have improved their performance as FRET sensors in intensity-based methods. FPs are inherently prone to blinking and are significantly less photostable than organic fluorophores (46). Both of these factors decrease the potential utility of FPs in smFRET microscopy. The poor photostability reduces the achievable temporal resolution when considering studying dynamic interactions. Deconvolution of blinking from calculated FRET efficiencies is an arduous process (103).

Photophysical modifications to FPs are achieved via mass mutagenesis and properties determined by these bulk spectroscopic methods often do not translate to other experiments. The insensitivity of FPs to their surrounding environment is advantageous in many ways however this also renders the photostabilising reagents employed with organic fluorophores ineffectual (46).

The severe lack of understanding surrounding FP photophysics in relation to internal environment highlights the need for simple methods to modulate these properties systematically.

1.5.4 *In vivo* labelling technologies

The adoption of FPs as labels for cellular species is ubiquitous throughout bioimaging applications. Despite this, as fluorophores they are limited. They are approximately an order of magnitude less photostable than organic dyes, they are prone to blinking and cannot be simply modified by buffer additives due to their chemical inertness and external environment insensitivity. There are multiple methods available to label proteins with organic fluorophores, such as the use of amine coupling chemistry and reactive fluorophore linkers. However, this methodology results in heterogeneously labelled proteins at multiple levels of stoichiometry due to the vast availability of exposed amines. A preferred alternative is provided in **enzymatic fusion tags**. These non-fluorescent proteins have provided a compromise between FPs and organic fluorophores. They can be directly genetically expressed onto the protein of interest and used to facilitate the covalent labelling of suitably functionalised ligands, such as organic dyes, to other proteins. These reactions are highly specific, fast and irreversible. The two most commonly used fusion tags are O^6-methylguanine-DNA alkyl-transferase (SNAP-tag) (104) and haloalkane dehalogenase (**HaloTag**) (105).

SNAP-tag catalyses the 2-step nucleophilic substitution reaction between benzyl-guanine functionalised ligands and a cysteine residue in the tag to form a stable thioether bond (106). SNAP-tag is easily employed as an endogenous tagging mechanism in bacteria and yeast cells, but unspecific binding occurs in mammalian cells unless methylguanine-DNA alkyl-transferase deficient cell-lines are used (104). The SNAP-tag methodology has been employed generally in diffraction limited SR bioimaging to study protein localisations and dynamics (107, 108). An alternative to the SNAP-tag is HaloTag, another genetically specific fusion tag. Attachment of a ligand is achieved through a chloroalkane moiety separated from the desired entity for attachment by a linker of 2 or 4 ethylene glycol repeats. The terminal chlorine on the reactive ligand is displaced following nucleophilic attack by a deprotonated carbonyl of aspartate

at the enzyme active site (Figure 1.14) (109), this irreversible reaction is stoichiometric.

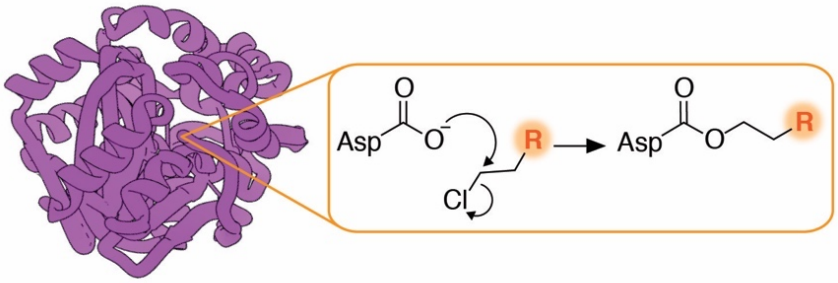

Figure 1.14. Nucleophilic substitution reaction between HaloTag ligand and enzyme.

The HaloTag enzyme is monomeric and has a molecular weight of 33 kDa, comparable with FPs (110). The absence of haloalkane dehalogenase inside mammalian cells ensures specificity, unlike SNAP tag, and no altered cell-lines are required. There is a vast array of HaloTag fluorophore ligands available including multiple dyes suitable for SM and SR imaging. Synthesis of bespoke ligands is trivial and can be achieved via reactive amine coupling chemistry.

Unlike FPs, with all forms of *in vivo* dye labelling, there will be an unwanted background component from residual free dye after labelling and washing. The development of PA dyes has minimised this to an extent, but there will likely be free dye present. The main advantage of fusion tags over FPs is the ability to incorporate photophysically desirable fluorophores stoichiometrically and specifically. However, the choice of labelling method will likely depend on the priorities of the experiment.

1.5.5 Chemical photoprotection of organic fluorophores

Fluorophore photobleaching is the primary limiter of achievable longevity SM experiments. Resistance to photobleaching, or photostability, is particularly desirable in SM tracking, where *in vivo* dynamics can occur on long time-scales. The origin of fluorophore photodestruction under the conditions of SM detection is attributed to chemical reactions between excited triplet fluorophores and reactive oxygen species, primarily singlet oxygen. In the ground electronic

state molecular oxygen (O_2) exists as a triplet, with 2 unpaired electrons in the π anti-bonding, highest occupied molecular orbitals (HOMO). Reaction with other triplet state molecules in the surrounding environment can result in the formation of excited, singlet state O_2, a highly reactive unstable species with heterogeneously occupied HOMOs with spin paired electrons. Singlet oxygen is then capable of oxidising triplet state fluorophores to yield non-fluorescent products. Considering this process, it may be thought that methods of oxygen removal be employed to mitigate photobleaching, however, triplet oxygen is also a good **triplet state quencher** and can facilitate the relaxation of triplet fluorophores to the singlet ground state where they may be re-excited. Therefore, oxygen removal should be utilised with the addition of alternative triplet state quenchers.

Many chemical additives have been suggested and used to achieve this, a glucose oxidase catalase system has been widely used in which glucose reacts with oxygen to produce gluconic acid and hydrogen peroxide which is then decomposed by the catalase (111). Problems associated with long-lived triplet dark states led to investigation of reducing agents for singlet ground state recovery, it was in this that 6-hydroxy-2,5,7,8-tetramethylchroman-2-carboxylic acid (**Trolox**), a derivative of vitamin E (Figure 1.15A) was discovered to alleviate blinking and improve **photostability** (112).

Trolox behaves as a redox system; in itself Trolox is a reducing agent. When it is oxidised, a quinone product is formed (Figure 1.15A) which acts as an oxidising agent. The two species work coherently to produce singlet ground state fluorophores from their excited triplet states (Figure 1.15B).

Trolox reduces the triplet state fluorophore to form a radical anion, which is non-emissive. The Trolox quinone partner can then oxidise the radical anion to re-form the ground state dye. Trolox quinone can be formed photochemically by near-UV radiation and the concentration may be measured using the Beer-Lambert relationship. However, under some modes of SM detection the relative concentrations of Trolox and Trolox quinone cannot be ascertained exactly.

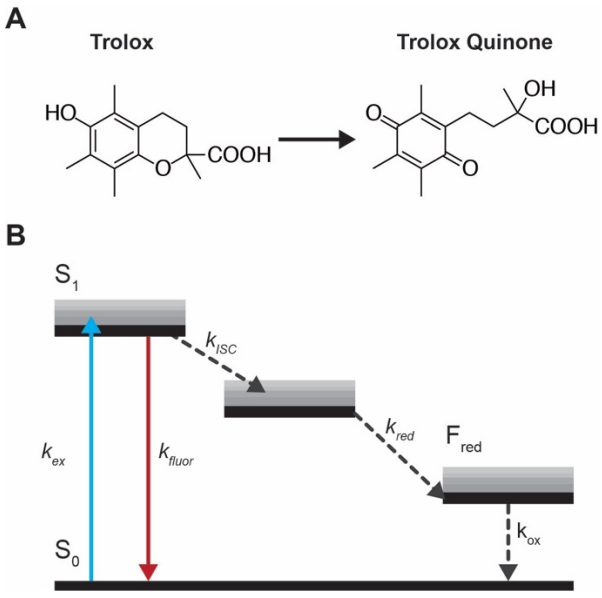

Figure 1.15. **A)** Structures of Trolox and photochemical product Trolox quinone. **B)** Excited state schematic showing the redox interaction of Trolox/Trolox quinone with a triplet fluorophore.

Molecular photostabilising additives such as Trolox have been shown to reduce photobleaching quantum yields throughout dye classes (113). However, the redox scheme was ineffective at mitigating blinking in oxazines due to their high reduction potential resulting in the formation of long-lived dark states (114). Furthermore, these chemical additives are ineffectual with FPs, due to the protection of the chromophore by the β-barrel of the protein (46, 93).

Trolox has been used very successfully to extend fluorescence activity in SM experiments, it is non-cytotoxic and membrane permeable, therefore a useful additive for *in vitro* (115) and cellular imaging (112), smFRET (116, 117) and SM tracking (118–120). The photostabilising effect is dependent on the collisional frequency of Trolox with the fluorophore; therefore, high concentrations are required (mM). This is close to the limit of solubility for Trolox in aqueous buffers therefore; solutions must be well prepared before use in SM experiments.

Chapter 2 Single-Molecule and Super-Resolution Fluorescence Microscopy

2.1 Overview of this chapter

This chapter describes the theory behind **single-molecule localisation** (SML) based **super-resolution** (SR) microscopies and **single-molecule tracking** (SMT), focussing on 2D acquisition with **total-internal reflection fluorescence** (TIRF) approaches. Following this, the practical implementation will be discussed through a detailed description of a typical, bespoke instrument optimised for 2D SM TIRF experiments.

2.1.1 Contributions

I constructed the microscope described in this chapter and collected data to evaluate localisation precision. The code to analyse this data was written by Alexander Carr.

2.2 Defying the diffraction limit: Single-molecule imaging

2.2.1 Super-resolution with single-molecule localisation

Physicist Richard Feynman stated in his 1959 lecture entitled 'There's Plenty of Room at the Bottom', '*it's very easy to answer many of these fundamental biological questions; you just look at the thing!*'. The ascent of SM and SR techniques into the forefront of biological research epitomises the continual endeavour to find innovative ways to '*just look at the thing!*'. In 2014 the Nobel Prize for Chemistry was awarded to three scientists, W.E Moerner, Stefan Hell and Eric Betzig, for pioneering the development of super-resolved fluorescence microscopy. Two main SR techniques formed the basis of the prize, wide-field,

SML and confocal, stimulated emission depletion (STED) methods. Briefly, STED employs a spatially patterned excitation approach to achieve SR and SML utilises fluorophore photophysics to spatially isolate single-molecules. For the purposes of this thesis STED will not be discussed and the focus will remain on SML techniques.

All optical techniques to study biomolecules require tagging a species of interest with an optically active label, such as a nano-particle, quantum dot or small fluorescent molecule. All labels are susceptible to the same fundamental inhibitor to observing nano-scale objects with optical methods; diffraction of light. This was first proposed by Ernst Abbe in 1873 (121) that when light of a certain wavelength (λ), is focussed by an imaging system with a numerical aperture (NA) to produce an image, objects closer together than a distance (d) will not be individually resolvable, it is described by Equation 2.1:

$$d = \frac{\lambda}{2NA} \tag{2.1}$$

Practically, the resolution of an image of two fluorophores emitting mid-visible (~500 nm) light with a NA of 1.0 would be mean this distance, often referred to as the optical diffraction-limit of light, is restricted ~250 nm. The diffraction limit is an inherent property of light that prevents the waves converging to a well-defined point and instead forms blurred puncta in the image plane. The intensity distribution of the spot is known as a **point-spread function** (PSF, Figure 2.1). Light microscopy is a useful and widely employed method to study biological samples, it is minimally perturbative and can be performed in physiological environments (122). However, the spatial scale of many biological processes, particularly those in the cell nucleus, are much smaller than the diffraction limit. Under the confines of the diffraction limit, conventional fluorescence microscopy is restricted to observe mean behaviour of populations of nano-scale species. The development of advanced optical systems and mathematical understanding of PSFs brought the advent of SML-based SR fluorescence methods that allowed for the observation of biological heterogeneity in cells.

SML fluorescence microscopy, also termed pointillism-based SR microscopy, represents a multitude of different approaches to achieve SR.

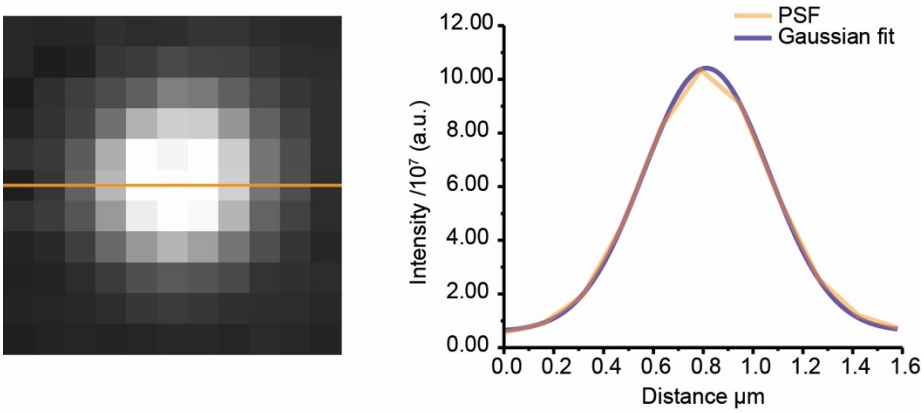

Figure 2.1. Illustration of an example PSF (left). The intensity of the point emitter can be plotted against distance and fit to a mathematical function to obtain the likely centre position (right).

One of most important factors in an SR imaging experiment lies in the prior knowledge that the observed PSF is the result of a single emitter. From this, the central position of each PSF, hence the likely location of the fluorophore, can be determined with a precision below the diffraction limit. The achievable localisation precision (Δ_{loc}) is inherently determined by the number of **photons emitted** by the fluorophore (N, Equation 2.2) (123):

$$\Delta_{loc} = \frac{\Delta}{\sqrt{N}} \tag{2.2}$$

in which Δ is the size of the PSF. The size of the smallest observable object is determined by all the factors that govern the resolution of the instrument. However, with sufficiently high emission intensities, single-fluorophores can be localised with a precision of approximately 2-orders of magnitude greater than the diffraction limit (124). Towards lower emission intensities it becomes increasingly important to minimise the contributions of background noise as this effects the precision at a scale of N^{-1} (125), this is considered in Equation 2.3:

$$\Delta_{loc} = \frac{2\sqrt[4]{\pi}\,\Delta^{\frac{3}{2}}\,b}{N\sqrt{a}} \qquad (2.3)$$

where b is the background contribution and a is the pixel size. A further complication arises due to pixilation noise, a consequence of the finite pixel size and uncertainty of photon localisation within the pixel. This is assumed to be diminutive and is not considered in Equation 2.3. These relationships emphasise the need for dyes with high photon budgets.

Typically, the super-localisation of single-emitters with high localisation precision requires them to be spatially isolated at a given time. Spatial isolation can be achieved with conventional fluorophores in biological samples by reducing the labelling density. However, this results in under-sampling which can drastically reduce the resolution (Figure 2.2).

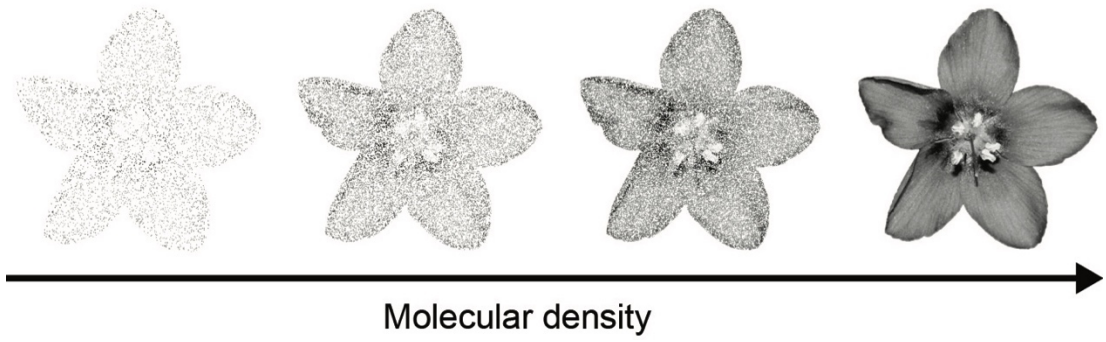

Figure 2.2. Illustration of the Nyquist sampling criterion. As the density of localisations increases the resolution of the flower image is improved. This highlights the importance of collecting a high number of points when performing a SR experiment.

The resolution of the final image is related to the density of emitters localised during the acquisition. This is described by the Nyquist sampling criterion (Equation 2.4) which dictates the need for at least two emitters per resolution unit (126). For example, to attain a resolution of 10 nm there must be fluorophores distributed at 5 nm intervals in the sample volume.

The 2D Nyquist resolution ($r_{Nyquist}$) can be calculated from:

$$r_{Nyquist} = \frac{1}{a^{\frac{1}{d}}} \tag{2.4}$$

where a is the labelling density and d is the imaging dimension, in this case 2. The final resolution of the subsequent image (r_{image}) can be extracted from the sum of the squares of the Nyquist resolution and the localisation precision (Equation 2.5):

$$r_{image} = r_{Nyquist}^2 + \Delta_{loc}^2 \tag{2.5}$$

It is difficult to achieve the high labelling densities required to produce a super-resolution image. The practical implementation requires that thousands of localisations are collected with each one being spatially isolated. As an example, in order to resolve a 500 nm slice of a cell membrane with a circumference 50 μm to 10 nm resolution, approximately 10,000 spatially isolated localisations would need to be collected. One way this has been achieved is through fluorophore development and control over the active state of single-emitters. Possible modes to achieve spatial isolation include utilising **photomodulatable** (PM) fluorophores, which allow for the control of fluorophore density by switching them between bright and dark states with light. Alternatively, freely diffusing fluorophores capable of transitioning to a bright state in response to transiently binding to a biomolecule can be exploited to collect SR data.

Under the term SR microscopy are several methods each of which employs these tools for spatial isolation. However, the process involves switching point emitters between bright and dark states such that they are well separated in space and repeating this process for multiple cycles until sufficient data has been collected to generate a super-resolved image of the sample (Figure 2.3). SML techniques sacrifice temporal resolution to gain superior spatial resolution in biological samples. The super-resolved image represents a virtual

reconstruction *in silico* obtained from fitting the raw PSFs in each frame with an appropriate mathematical approximation, typically a 2D Gaussian function (Equation 2.6):

$$PSF_{Gaussian} = Ae^{\left(-\frac{x^2 + y^2}{2\sigma_{xy}^2}\right)} \quad (2.6)$$

with the PSF having an amplitude A and Gaussian standard deviation σ_{xy}. The centre of the distribution indicates the likely position of the molecule and the FWHM indicates the positional uncertainty. The PSF centre has been determined to Ångström accuracy (127). However more typical photon values for organic dyes which lead to localisation precision values of 10-20 nm are now achieved routinely by researchers in the field.

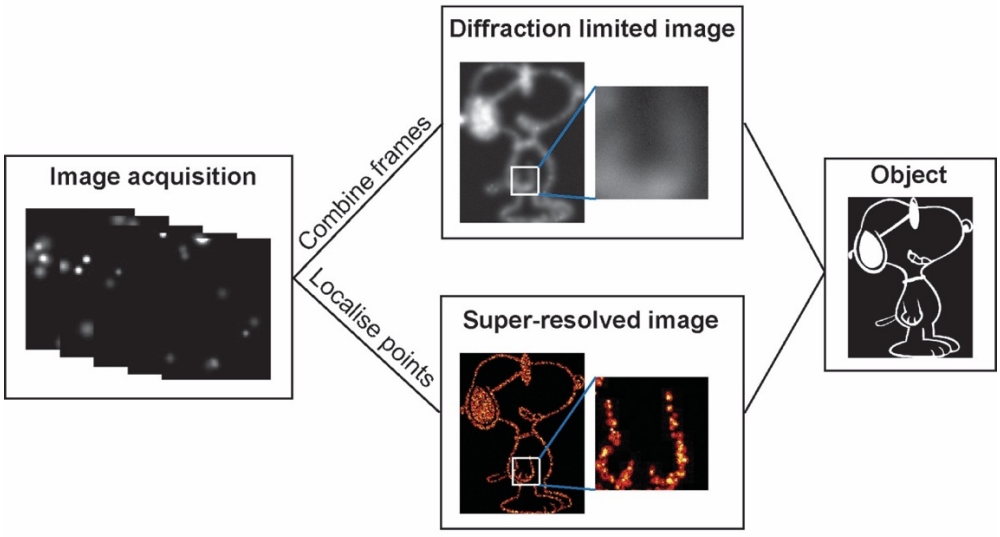

Figure 2.3. A schematic showing a simplified process to obtain a SR image of an object. Spatially isolated localisations are collected in the form of a movie over time. The images can then be combined to create a diffraction limited image of the object. The inset shows a zoomed area of the image, in this mode fine, structural detail cannot be discerned. Alternatively, the points in each frame of the movie can be fitted and their positions localised to build up a high-resolution picture with which it is possible to observe fine details down to the nm level. The super-resolved image provides a much closer representation of the actual object.

The different approaches to achieve SR through SML are typically discerned by the manner in which they achieve spatial isolation. The use of PM fluorophores was first demonstrated in SML microscopy with a photoactivatable (PA) fluorescent protein (FP) in a technique termed **photoactivated localisation microscopy** (PALM) (128). PA-FPs can be switched on photochemically and irreversibly from a dark state. This implementation showed it was possible to switch on thousands of PA-FPs successively over time, such that they were spatially isolated. The first application of PALM was to visualise the membranes of cellular lysosomes in physiological conditions to a resolution competitive with cryo-electron microscopy. Typically, low densities of PAFPs are switched to an on-state following a chemical change of the chromophore in response to near-UV radiation. The emissive FPs are then excited until they are irreversibly photobleached and therefore no-longer fluorescent. Following this, another subset of PA-FPs can be activated. This process is continued until enough or all molecules have been imaged. Further developments yielded FPs that are able to switch chromatically or reversibly between emissive and non-emissive states in response to radiation which have also shown to be useful PALM probes, these have been discussed in Chapter one.

Where PALM employs the intrinsic photomodulation properties of some FPs, **stochastic optical reconstruction microscopy** (STORM) demonstrated the switching capabilities of organic fluorophores to achieve sub-diffraction limited resolution (129). This was first shown with cyanine dyes, Cy3 and Cy5, which undergo reversible photoswitching when placed in close proximity (~2 nm) and in the presence of primary thiols. This photoswitching is inherently complex and multifaceted, the primary thiol is thought to bind reversibly to the polymethine chain of Cy5 and disrupt the conjugated electron system (130). Redox chemistry and the subsequent formation of radical anionic dark-states has also been proposed to play a role in the photoswitching mechanism of cyanines in STORM (39). However, the thiol is not required for redox-based switching of cyanines and a prolonged radical anion can be formed in de-oxygenated buffers containing ascorbic acid (131).

The first demonstration of STORM was *in vitro* with Cy3 and Cy5 conjugated to double stranded DNA. It has since been used successfully *in vivo* (132–134). The STORM principle can be extended to include the exploitation of the long-lived dark-states exhibited by many synthetic fluorophores, known as direct STORM (dSTORM) (135). dSTORM has been applied throughout the commonly used dye classes including cyanines, rhodamines and oxazines (136). The stochastic photoswitching of fluorophores can be controlled with light of a different wavelength to excitation and suitable buffer conditions. During each imaging cycle a subset of fluorophores are emissive and spatially isolated from each other. Each fluorophore may undergo several reversible switching cycles before being irreversibly photobleached, resulting in a large number of localisations. The on/off duty-cycle and photon number per switching cycle are two key quantities in a STORM experiment. The duty cycle is defined as the amount of time the fluorophore spends in the on-state $\left(\frac{\text{on-state time}}{\text{total on-state time}}\right)$. An optimal STORM fluorophore would have a low duty-cycle and high photon number per switching event as the number of fluorophores that can be localised in a diffraction-limited region is proportional to the reciprocal duty-cycle. If these criteria are satisfied both the Nyquist criterion and localisation precision may be optimised.

Point accumulation for imaging in nanoscale topography (PAINT) operates via a constant flux of fluorophores diffusing in and out of the excitation volume and binding electrostatically to cellular species (137). The rate at which probes interact with a biomolecule is dependent on the concentration of the probe in solution and can be optimised such that probes are spatiotemporally isolated. This is repeated until thousands of molecules can be localised. The photophysics of the probe are not limiting in this method, the photon emission per localisation is controlled by the affinity of the fluorophore for the biomolecule. However, the high concentration of free dye in solution may contribute to an increased background signal at detriment to the localisation precision and resolution.

2.2.2 Diffusion analysis with single-molecule tracking

2.2.2.1 Principles of single-molecule tracking

The organisation of cellular components is most often dynamic, and observation of these processes is crucial for understanding these complex systems. Many optical techniques have been employed to study the motion of cellular species including fluorescence recovery after photobleaching (FRAP) (138) and fluorescence correlation spectroscopy (FCS) (139). However, these are typically ensemble methods and the heterogeneity of molecular motions cannot be studied. Single-molecule tracking (SMT), also described as single particle tracking (SPT), brought the study of cellular dynamics to the nano-scale and greater understanding of cellular complexity. Many of the requirements of SML are relevant for SMT. Individual fluorophores must be spatially isolated during the acquisition. In the common case of high fluorophore density, this can be achieved by under-labelling, or temporally with a combination of SMT and PALM, termed sptPALM (140–142). Up to now, most SMT studies have employed organic dyes (143, 144), due to favourable photon budgets and photostability compared to FPs. Under-labelling approaches are typically utilised, but they only allow imaging of the dynamics of few molecules in each cell. In contrast, temporal control to image single molecules in dense environments, such as the cell nucleus, is greatly facilitated by PM fluorophores. As with SML microscopies, the achievable resolution is linked, in part, to the photophysics of the label. Unlike SML, where an optimal probe emits a large number of photons over a short time, an SMT probe would emit photons over a longer period and be resistant to photobleaching (photostable) and transient dark-state transitions. Moreover, it is equally important to ensure that the label does not perturb the motion of the biomolecule. Unfortunately, these properties are not mutually exclusive. Small fluorescent molecules can be used without perturbing the system but are much less photostable than nano-particle emitters, however these are large (~40 nm) and perturbative (145). The optical properties of small molecule fluorophores can be modified with the

addition of buffer additives such as oxygen scavengers and triplet state quenchers (136).

2.2.2.2 Implementation of single-molecule tracking

The practical application of SMT can be divided simply into three parts; to paraphrase Michael J. Saxton one must 'label and image the dots' (Figure 2.4i), 'connect the dots' and 'interpret the connected dots' (146).

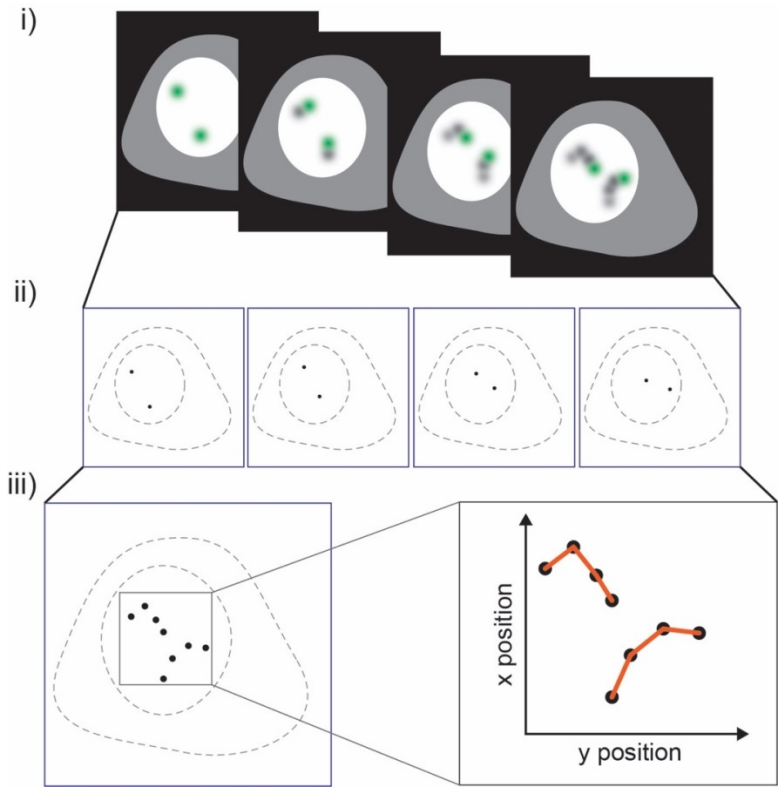

Figure 2.4. Schematic illustrating the fundamentals of an SMT experiment. **i)** Firstly, the dynamics of isolated emitters are imaged, following this the points are **ii)** localised and then **iii)** joined to form displacement trajectories with the desired algorithm. These trajectories can then be fitted to models to extract diffusion coefficients and make conclusions on diffusion modes.

The illumination intensity is reduced compared to SML to achieve the minimum useful **signal to noise ratio** (SNR) and greatest fluorophore photostability. This allows for increased fluorophore trajectories and therefore longer observation times. The temporal resolution is limited by both the acquisition rate of the

detector and the photon emission of the fluorophore, these properties must be tuned according to the desired experiment. The positions of spatially isolated PSFs can be approximated mathematically with a 2D Gaussian function (Equation 2.6, Figure 2.4ii) and linked between frames to build a complete trajectory map (Figure 2.4iii). Connecting single-fluorophores between frames is simple at low density and involves joining molecules with positions closest to each other. At higher densities, linking molecules becomes more complex and prone to error. Several algorithms have been developed and tested for complex SMT analysis (147) and the ideal analysis method depends on the conditions of the experiment (148). Quantitation of diffusion modes can be extracted from trajectories by fitting to a probability distribution function, the mean of which can be used to calculate a mean diffusion coefficient. With this information it is possible to gain a complete statistical picture of the dynamics of a cellular system.

2.3 Single-molecule total-internal reflection fluorescence

The quest for the maximum achievable SNR is fundamental within SML microscopies. One of the factors dictating resolution is in the capability to identify a single emitter in the image, which is determined, in part, by the signal above background. One manner of improving the SNR by minimising background is by employing TIRF illumination to excite fluorescent molecules in the sample. This method uses an induced **evanescent wave** capable of penetrating up to 200 nm into the sample volume (149). This reduction in excitation volume compared to epi-fluorescence illumination can increase the SNR by at least an order of magnitude (150).

There are a specific set of physical constraints that are required to achieve TIRF illumination. There must be a barrier at which there is a change in the refractive index (n) of the medium. In the context of TIRF microscopy this is typically the interface of a glass cover-slide (n=1.5) and aqueous sample medium (n=1.3) (151). There must be a decrease in n with the direction of

propagating light. Additionally, the collimated incident beam must reach the interface of mediums at a sufficient angle (θ), termed the critical angle (θ_c). At or above θ_c the propagating beam is refracted back into the higher n medium and an evanescent wave of exponentially decaying intensity, but same frequency, propagates into the lower n medium. Objective-based TIRF is represented graphically in Figure 2.5 and can be described mathematically by:

$$\theta_c = \frac{\sin^{-1} n_1}{n_2} \qquad (2.7)$$

where, in the context of TIRF microscopy, n_1 is the refractive index of the aqueous medium and n_2 is the refractive index of the glass sample surface and θ_c is equal to ~61.5 ° (152).

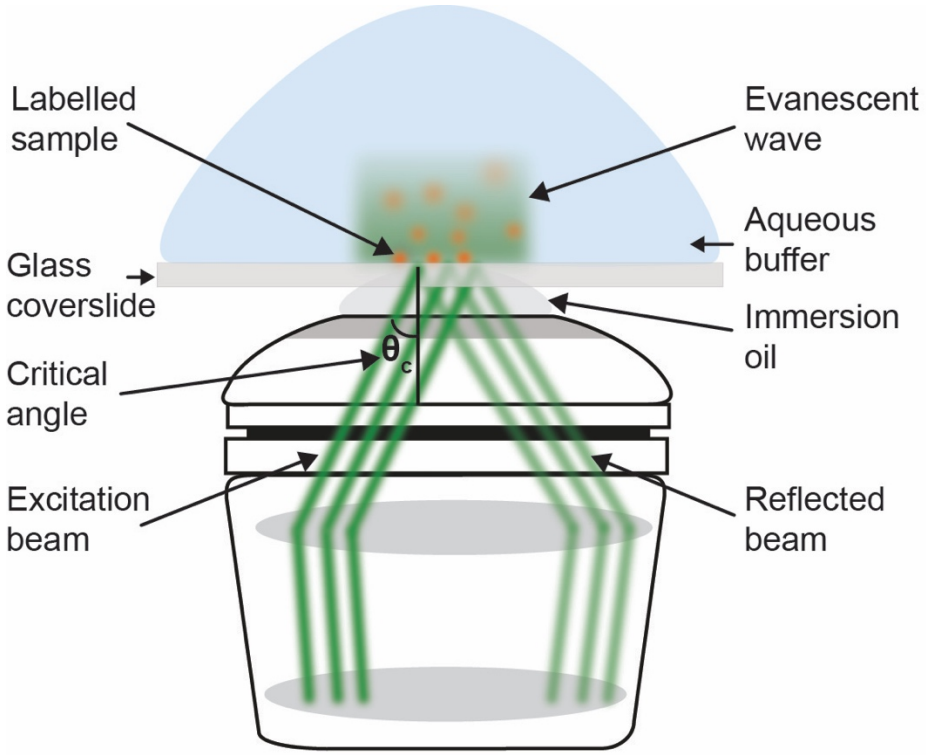

Figure 2.5. Illustration of objective-based TIRF microscopy. Propagating exciting light arrives at the glass-aqueous interface at θ_c and is totally-internally reflected to produce an evanescent wave which excites fluorophores within the wave penetration depth. The reflected light passes back through the objective.

The intensity of the evanescent wave decays along the axis at which it propagates. This is perpendicular to the interface normal (parallel to the surface). The wave intensity (I) at a distance (z) from the boundary can be described as a function of the energy at the interface (I_{int}) and the penetration depth (d). d is dependent on multiple variables including the incident wavelength (λ), n_1, n_2 and θ:

$$d = \frac{\lambda}{4\pi \left(\left(n_2^2 \sin^2 \theta \right) - n_1^2 \right)^{\frac{1}{2}}} \tag{2.8}$$

Hence, I_Z is equal to:

$$I_z = I_{int}\, e^{-\frac{z}{d}} \tag{2.9}$$

For visible wavelengths, d ranges between 80 and 200 nm.

TIRF is very useful for SM measurements of surface bound species due to the high intensity of the evanescent wave close to the interface and low background from sub-wavelength depth penetration. The optical set-up is relatively simple to implement with few essential components, a high NA objective being the most important for objective-based TIRF. The excitation beam must pass through an objective with an NA greater than n_1 as:

$$NA = n_1 \sin(\theta) \tag{2.10}$$

where θ is the angle of incidence of the illumination beam. For *in vitro* and cellular imaging n_1 is 1.33 and approximately 1.38 respectively, therefore an objective of NA ≥ 1.4 is able to be used. In order to employ TIRF imaging to study the basal surface of a cell, the alignment must be optimum to prevent lensing by the cell which increases background signal.

As well as the NA it is important to consider the capabilities of objectives to correct for chromatic aberrations and coverslip thickness. The collection efficiency and immersion medium should also be considered. The incorporation

of suitable filters and dichroics into the setup are important to ensure narrow bandwidth excitation beams and good separation of excitation and emission. As with other SM fluorescence microscopy techniques a camera with a high efficiency and fast read-out speed, such as an advanced electron multiplying charged coupled device (EMCCD), is essential. With these simple considerations it is possible to collect SM data with high SNR.

2.4 A typical single-molecule TIRF microscope

Understanding the theory of TIRF and SM TIRF microscopy enabled me to construct a bespoke TIRF microscope optimised for SM detection. This section provides a detailed explanation of the mechanical and optical components of the custom-built SM TIRF instrument (Figure 2.6), followed by a discussion of achievable localisation precision when using the instrument.

Figure 2.6. Photograph of the excitation path of the bespoke SM TIRF microscope described in this chapter.

Figure 2.7 is a labelled diagram of the instrument and can be divided into two light paths; the excitation path and emission path. The excitation path consists of four laser lines (405, 488, 561 and 641 nm) with individual optical

components which are then combined to form one unifying route through the objective to the sample. The emission is then collected by the same objective which is focussed onto the detector. For the purposes of clarity, the optical components will be described in the order they are used from the excitation laser to the detector. I constructed and optimised this instrument specifically for the experimental investigations detailed in this thesis. Designing and assembling a bespoke instrument enabled me to understand the requirements for collecting high-quality data.

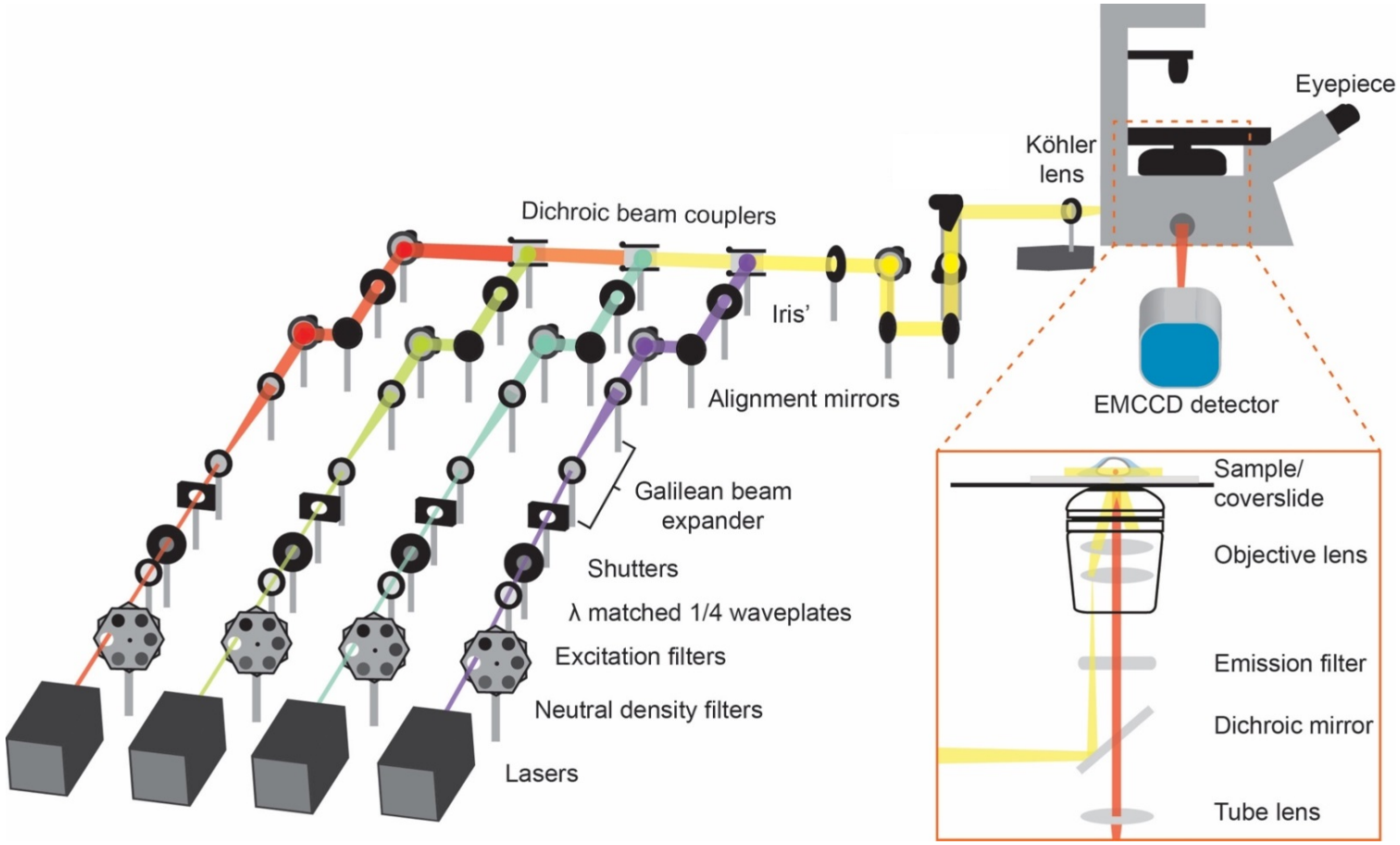

Figure 2.7. Schematic diagram detailing the light paths and optical and mechanical components of the instrument described in this chapter.

2.4.1 Optical components

Lasers

In this set-up, fluorophore excitation is achieved with single-mode, continuous wave, TEM_{00}, diode lasers. Four wavelengths covering the visible spectrum are employed, 405 nm, 488 nm, 561 nm and 641 nm. The maximum intensities of the beams at the aperture ranges between 100-200 mW. In order to achieve a focussed spot from a collimated beam, it is important to have Gaussian beams, therefore all lasers had M^2 <1.2.

Beam attenuation

The lasers operate at maximum internal power in order to minimise fluctuations from inherent electronic instability. Therefore, the laser power is controlled via neutral density filters in the optical path. The filters with a particular optical density (OD) operate by attenuating an incident beam (I_0) to yield a lower intensity beam (I), this can be described by:

$$\frac{I}{I_0} = 10^{-OD} \tag{2.11}$$

The filters are separated into two filter wheels, one wheel with integer ODs (1.0-4.0) and a second with decimal ODs (0.2-0.6) to allow for a large range of laser intensities.

Beam polarisation

In SM and SR experiments it is vital to achieve many spatially isolated, high precision localisations in a short period of time. The molecules and by extension the fluorophores will be oriented in multiple directions. Hence, the polarisation of the incident excitation must satisfy all fluorophore dipole orientations. This is achieved with a wavelength specific, quarter wave-plate, which converts linearly polarised light to circularly polarised light. All lasers have polarisation ratios of 100:1, therefore only 1 % of the output beam is unaligned relative to the global polarisation of the beam. The beam power is

measured at the sample-plane to ensure 50 % of the total laser intensity is in each polarisation axis.

Excitation filter

Bandpass ‘clean-up’ excitation filters are used in each laser line to discard unwanted stray wavelengths that may be emitted from the laser and transmit only the desired wavelength (Figure 2.8). Typically, optical filters transmit 95 % of the light in the desired range.

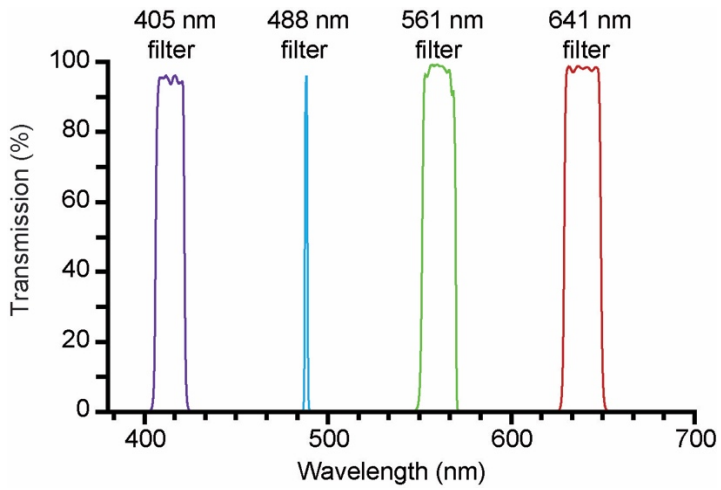

Figure 2.8. Transmission versus wavelength plots of the four band-pass excitation filters used for the laser-lines in this instrument.

Galilean beam expansion

The lasers typically have beam diameters of approximately 1 mm. In order to image a full field of view with uniform power density the beam should be expanded such that the back aperture of the objective is over-filled. This is achieved with a Galilean beam expander setup (Figure 2.9). This comprises of two lenses; the first lens has a negative focal length to diverge the beam and the second lens has a positive focal length to re-collimate.

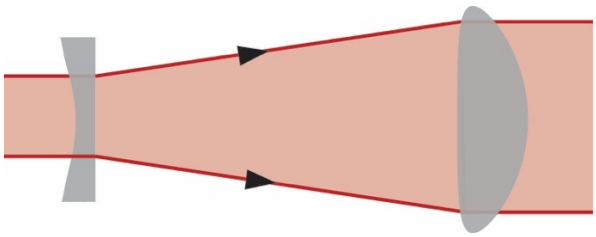

Figure 2.9. Schematic illustrating the magnification and collimation of the excitation beams using a Galilean beam expansion.

The lenses are positioned relative to each other at a distance equal to the sum of their focal lengths. This distance is then optimised to ensure the expanded beam is collimated. The magnification (M) is equal to:

$$M = -\left(\frac{f_2}{f_1}\right) \tag{2.12}$$

where f_1 is the focal length of the negative (diverging) lens and f_2 is the focal length of the positive (collimating) lens. The beam expander in this work magnifies the beam 10×, using a negative lens with a focal length of -25.0 mm and a positive lens with a focal length of +250 mm. The distance between the lenses is equal to approximately 225.0 mm.

Alignment mirrors

Control of the vertical and lateral beam position is managed by pairs of alignment mirrors on kinematic mounts. In the individual beam paths these are used to align beams such that they overlap in the combined path and travel in parallel, co-linear trajectories. This is achieved by arranging alignment mirrors at 45 ° angles relative to the propagating beam and ensuring the beam is centred on the mirrors. With this set-up fine axial and lateral control of the beam position is achieved.

Beam combining dichroics

Dichroic mirrors are arranged in the combined beam path to couple the lasers into a single line (Figure 2.10). The dichroics reflect certain wavelengths whilst

being transparent to others and can therefore be used for additional alignment of the laser beams.

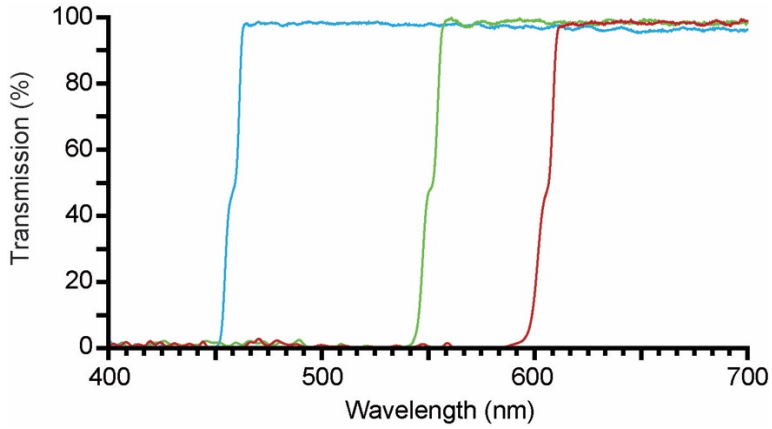

Figure 2.10. Transmission versus wavelength plots of the three beam-combining dichroics used in this instrument.

Combined beam alignment and wide-field illumination

In the combined beam path, mirrors are positioned to ensure co-linear entry through the centre of the objective lens. Wide-field illumination is achieved by positioning a lens (Köhler lens) the focal distance away from the back focal plane of the objective lens. This optical geometry is described by wide-field illumination and ensures that the propagating beam is collimated at the sample plane. In this TIRF configuration, one mirror in the combined path is designated to adjust the position of the beam on the Köhler lens. In doing so, the position of the focussed beam on the back focal plane of the objective lens is changed such that the critical angle of incidence is achieved at the interface. It is important to position the TIRF-mirror the focal length distance away from the Köhler lens to ensure the propagating beam continues parallel after focussing. With this mirror, the imaging geometry can be changed between epi-fluorescence, oblique-angle illumination and TIRF.

Internal dichroics

After passing through the Köhler lens the propagating excitation beam enters the microscope body and is reflected 90 ° upwards towards the objective by a

dichroic beam-splitter. These dichroics separate emission from the excitation by being transparent to the red-shifted wavelengths. In this set-up, a quad-band dichroic mirror is used to satisfy the four excitation lasers and typical fluorophore emission.

Objective lens

In this wide-field illumination geometry the infinity corrected objective lens is able to collimate the focussed excitation. This is important to achieve a uniformly propagating evanescent wave when operating in TIRF mode. In this instrument the objective used is an oil immersion, plan apochromatic lens and is therefore corrected for chromatic aberrations and field uniformity. Furthermore, the objective is infinity corrected to allow for the incorporation of additional optical components between the objective and the image plane without negatively effecting the focus and aberration corrections. The NA is high at 1.49 which makes it suitable for TIRF and the magnification is 100×. The emission light is also collected through the same objective and the high NA facilitates greater collection efficiency of fluorescence photons. The collection efficiency is related to the cone angle of collection (θ), the NA of the objective and the refractive index of the oil (n_{oil}):

$$\theta = \sin^{-1}\left(\frac{NA}{n_{oil}}\right) \tag{2.13}$$

θ is calculated to equal 78.5 °. The efficiency with which the objective can collect isotropic light emitted from a point source (E_{coll}) was calculated to be 49.0 % with Equation 2.14:

$$E_{coll} = -\frac{1}{2}\left(\cos\left(\frac{\theta}{2}\right) - 1\right) \tag{2.14}$$

Emission filters

Long-pass and band-pass filters use thin-film interference to isolate the desired fluorescence wavelengths and are placed in the emission path of the

instrument. The filters are combined and optimised for chosen experiments to ensure good contrast and SNR. They allow for peak transmission of desired signal and exclusion of unwanted background such as Raman scattering, cross-talk and auto-fluorescence.

Tube lens

A tube lens is present in the infinity space between the objective and the detector and has a focal length of 180 mm. The collimated fluorescence emission is focussed to form the image plane. The detector is then placed at the focal point of the tube lens.

Camera

The method of fluorescence detection used in this set-up is an EMCCD. The EMCCD technology enhances the sensitivity down to single-photon levels by introducing an electron multiplication structure onto the chip, which amplifies the signal produced by the incident photons. One of the main advantages of this type of detector is the high quantum efficiency (QE) at visible wavelengths. The QE is normally distributed between 300-1100 nm reaching peak values of 98 % efficiency between 500-700 nm. The collection ability is also maximised by the large pixel area (16 x 16 μm). Coupled with the objective magnification of 100×, the image pixel size is theoretically equal to 160 μm, however this was measured directly to be equal to 158 nm. Each field of view is 512 x 512 pixels which equates to an area of 6400 μm^2.

2.4.2 Mechanical components

Shutters

Electronic shutters are integrated with the system to allow for automatic control of the beam propagation. These shutters are able to switch at high speeds, with maximum frequencies of 40 Hz.

Irises

Small aperture irises are used to assist with alignment. They are positioned in both the individual and combined beam paths to ensure propagating beams are parallel to the table and co-linear with the beam paths of different wavelength.

Stage

An electronic, linear-encoded, x-y axis stage is used to control the lateral position of the sample relative to the objective lens. The stage controller is capable of inducing fine and coarse movement with reproducibility of a maximum of 15 μm. A custom anodised steel insert was made for mounting of the sample.

Piezo

A piezoelectric z-stage is used to obtain sub-nm control of the objective axial position over 100 μm range. This is most often used for axial scanning through a cell to obtain a pseudo-3D image. The piezo offers good reproducibility of the axial position to 5 nm.

Active vibration damping

The instrument is constructed on an actively vibration-damped optical table. It is designed to improve the mechanical stability of the instrument by isolating it from surrounding vibrations. This is particularly important for SM techniques which operate at high-levels of sensitivity; any significant vibrations would result in a reduction in localisation precision and spatial resolution.

2.4.3 Characterisation of localisation precision

Despite the active damping of the microscope from external vibrations there will always be mechanical instability during the acquisition process, resulting in a detriment to the achievable localisation precision. The localisation precision can be determined by SML fitting algorithms; however, this convolutes errors introduced from photon emission and mechanical instability (153), often

underestimating the ultimate achievable precision. The mechanical stability of this instrument was determined with previously established methods (153, 154).

Static diffraction-limited fluorescent beads were imaged on poly-L-lysine-coated coverslips for 2000 frames; with the resulting positional distribution of each bead fit to a Gaussian function. The standard deviation of each fitted Gaussian measures the localisation precision of each fluorescent bead. These values were plotted against the number of detected photons to determine the relationship between localisation precision and detected photons for SM fitting (Figure 2.11).

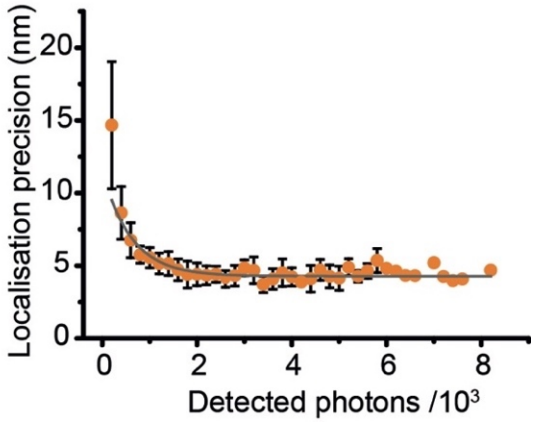

Figure 2.11. Graph showing the localisation precision of single fluorescent beads relative to their intensities. This method of measuring the precision takes into account the mechanical stability of the instrument. The error bars represent the standard deviation of replicates. Both curves have been fitted to an exponential decay function.

The maximum achievable 2D localisation precisions determined by SM fitting and both SM fitting and mechanical stability were 4.0 ± 0.6 nm and 4.3 ± 0.4 nm respectively and was reached at ~4000 detected photons. However, typically used fluorophores do not emit photons in the regimes required to achieve this level of precision. At 1000 photon counts the localisation precision would be 14.7 ± 4.4 nm and 8.6 ± 1.8 nm at 2000 photons. These values are in line with the highest-performing instruments within the lab.

Two sources of noise affect the localisation precision; shot noise and background noise. These contribute to reducing the localisation precision by different scales ($N^{-1/2}$ and N^{-1} respectively). At low photon emission the contribution from background is a dominant factor in determining the localisation precision, therefore the prevailing source of error is in the localisation fitting. At high photon numbers the background contribution is less impactful, and the highest achievable localisation precision is a result of a convolution of fit error and mechanical stability (154).

2.5 Conclusion

SML based SR microscopy has become a widely adopted technique in the field of bioimaging and has provided previously unprecedented resolution at relevant length scales in physiologically relevant conditions. It has provided mechanisms to study not only biological structures but also the motions of biomolecules in cells. Well established physical principles such as TIRF have been implemented into SML microscopy to improve the achievable resolution further.

This chapter has detailed some of the key theory that underpins these techniques and described the practical implementation through the description of a custom built 2D SM microscope. Furthermore, the mechanical stability of the set-up was discussed by way of analysis of the localisation precision of single-emitters.

The primary aim of this chapter was to highlight the importance of understanding the key physical and practical principles of single-molecule and super-resolution fluorescence microscopies. A firm comprehension of these will enable researchers to carry out successful SM and SR experiments and interpret the results.

Chapter 3 Materials and Methods

3.1 Materials and methods- Project One

3.1.1 Synthesis of ThT derivatives

Briefly, the aryl-bromide precursor 2-(4-bromophenyl)-6-methoxybenzo[d]thiazole, $Pd_2(dba)_3$, BINAP, NaO^tBu and the desired amine was added to an oven-dried microwave vial. Toluene was added to the vial and the mixture was heated to 80 °C for 18 hours. The mixture was cooled to room temperature, diluted with ethyl acetate and filtered. The filtrate was concentrated, and the residue was triturated with diethyl ether. The solid was filtered and rinsed with cold diethyl ether to give the coupling product (155) (E derivatives, Scheme 3.1). The specified amine and methyl iodide were added to an oven- dried vial. Chlorobenzene was added, and the reaction was stirred at 110 ºC for 18 hours. The reaction was then cooled to room temperature and triturated with diethyl ether. The solid was collected by filtration to give the mono N-methylated product (mE derivatives, Scheme 3.1). The compounds were confirmed with IR and NMR spectroscopy and mass spectroscopy.

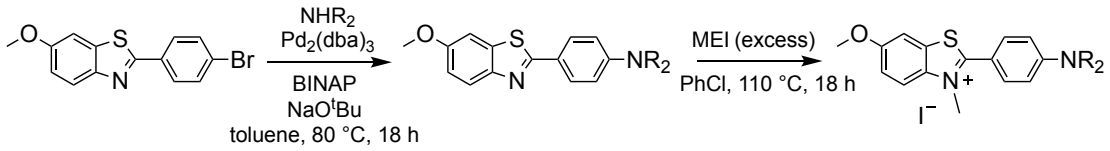

Scheme 3.1. Synthesis of the E and mE dyes from an aryl-bromide precursor.

3.1.2 Synthesis of bifunctional probes

Scheme 3.2 shows the reaction path used to synthesise both the BE and mBE compounds. Briefly, BE01 and BE02 were synthesised from the precursor bromide X (156) via a palladium catalysed borylation. Treatment with trimethyloxonium tetrafluoroborate provided the *N*-methylbenzothiazolium dyes

mBE01 and mBE02. Each compound was prepared in useful quantities (>100 mg) and were confirmed with NMR spectroscopy (Appendix Figure A.2.1).

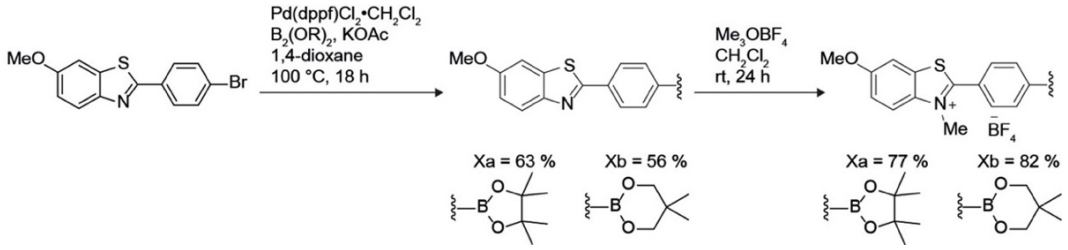

Scheme 3.2. Synthesis of BE and mBE probes.

3.1.3 Preparation of amyloid probe stock solutions

Stock solutions of novel amyloid dyes discussed in Chapters 5 and 6 and ThT (Sigma-Aldrich, T3516) were prepared by dissolving solid into dimethyl sulfoxide (DMSO, Sigma Aldrich, 276855) to a concentration of 1 mM, these were stored in the dark at -80 °C. The stock solutions were diluted into filtered (0.02 µm syringe filter, Whatman, 6809-1102) phosphate buffered saline (PBS, pH 7.4) to a concentration of 25 µM. The diluted dye solutions were then filtered (0.02 µm syringe filter, Whatman, 6809-1102). The diluted solutions were stored in the dark at 4 °C for a maximum of a week after preparation.

3.1.4 Preparation of αSyn Aggregates

Monomeric wild-type αSyn was purified from *Escherichia coli* as previously described by Hoyer *et. al.* (157). To generate amyloid fibrils, a solution of αSyn (70 µM) in PBS buffer (pH 7.4) with 0.01% NaN_3 to prevent bacterial growth was incubated in the dark at 37°C with constant agitation (200 rpm) for several months before use.

3.1.5 Bulk fluorescence measurements of ThT derivatives

Samples were placed into a quartz fluorescence cuvette (Hellma Analytics, 3 × 3 mm) and bulk fluorescence spectra were recorded using a fluorescence spectrophotometer (Cary Eclipse, Varian) in which emission was collected

perpendicular to direction of propagating excitation. Initial fluorescence spectra of E, mE dyes and ThT (10 μM) were recorded free in PBS (pH 7.4) and in the presence of late stage αSyn aggregates (~2 μM). Replicates were made with n=3 separately prepared dye samples. UV-Vis absorption spectra were collected by placing samples in a quartz transmission cuvette (Hellma Analytics, 1 cm path length) and measured with an absorption spectrometer (Cary 400, Varian). Buffer blanks were collected for both fluorescence and absorption spectra and used for background correction.

Solvent dependence UV-Vis and fluorescence spectra were measured in the same cells and spectrophotometers described above. The E, mE dyes and ThT (1 mM) were diluted to a final concentration of 10 μM into either ethanol (99.8 %, VWR, 20821.296), 2-propanol (99.5 %, Sigma-Aldrich 278475), dimethylsulfoxide (99.9 %, Sigma-Aldrich, 276855), deuterium oxide (99.9 %, Sigma-Aldrich, 151882) or water (ultra-pure, 18.2 MΩcm, Merck, SIMSV00WW) separately.

3.1.6 Bulk fluorescence measurements of bifunctional probes

H_2O_2 was prepared by diluting a stock solution (9.7 M, VWR) into filtered ultra-pure, 18.2 MΩcm water (Merck, SIMSV00WW) (0.2 μm syringe filter, Whatman, 6780-1302) to 10 mM. Samples were placed into a quartz fluorescence cuvette (Hellma Analytics, 3 × 3 mm) and bulk fluorescence spectra were recorded using a fluorescence spectrophotometer (Cary Eclipse, Varian). Fluorescence spectra of BE, mBE dyes and ThT (5 μM) were recorded free in PBS (pH 7.4), in the presence of H_2O_2 (100 μM) (158), in the presence of αSyn aggregates (~10 μM) and in the in the presence of both H_2O_2 and αSyn aggregates simultaneously at excitation maxima. The error bars represent standard deviations from triplicate experiments.

To assess the bulk fluorescence response of the dyes to H_2O_2 the dyes were incubated with H_2O_2 and the fluorescence intensity recorded over 5 hours at 20-minute intervals. Fluorescence emission was recorded instantly following incubation of the dyes with αSyn aggregates. The dyes (25 μM) were then

incubated with H_2O_2 (100 μM) for 60 minutes. Following this incubation period, the dyes were diluted to 5 μM and the emission spectra were recorded with αSyn aggregates. Spectra of the free dyes in PBS were also recorded at appropriate excitation wavelengths for calculation of Φ_{FI} relative to a standard (30).

3.1.7 Preparation for fluorescence imaging

Glass cover-slides for fluorescence imaging were cleaned for 1 hour using an argon plasma (PDC-002, Harrick Plasma) and the slide surface incubated with poly-l-lysine (PLK) for 30 minutes as previously described (159). Working solutions of dye (10 μM-1 pM) and αSyn (0.5 μM) in filtered (0.2 μm syringe filter, Whatman, 6780-1302) PBS (pH 7.4) were prepared 5 minutes prior to imaging. The working solution (50 μL) was added to the clean, PLK coated cover-slide and incubated for 2 minutes. The slide was then washed twice with PBS and imaged. H_2O_2 (100 μM) was then added directly to the cover-slide and the sample imaged again.

3.1.8 Single-aggregate fluorescence imaging

Fluorescence imaging experiments were carried out in TIRF mode with the bespoke inverted microscope (Olympus, IX73) set-up described in Chapter 2, section 2.4. Excitation of BE, mBE compounds and ThT in the presence of αSyn aggregates were performed with a collimated 405 nm laser (Stradus, Toptica, 405-100, 100 mW) which was aligned parallel to the optical axis and directed into an oil immersion objective lens (1.49 NA, 60×, Plan Apo, TIRF, Olympus) above the critical angle to ensure TIR at the coverslip-sample (glass/water) interface. Fluorescence emission was also collected by the same objective and selected by the presence of a dichroic (Di01-R405/488/561/635, Semrock) and subsequently passed through appropriate emission filters (BLP01-488R-25, Semrock). Images were then recorded by an EMCCD camera (Evolve delta 512, Photometrics) with an electron multiplication gain of 250 running in frame transfer, clear pre-sequence mode. Each pixel on the

image was 266 nm. Images were recorded at either 50 ms (Chapter 5) or 100 ms (Chapter 6) exposure for 200 frames using a custom beanshell script through Micro-manager software (v. 1.4) (160).

3.1.9 Fluorescence image analysis of ThT derivatives

Single aggregate visualisation by enhancement (SAVE) images were analysed with a bespoke ImageJ (161) macro (Appendix A.1.1). Figure 3.1 shows a schematic of the process. Image stacks of 200 frames taken at 50 ms per frame of the E, mE dyes and ThT with late-stage αSyn aggregates were compressed in time to create single frame images representing the summed pixel intensities. Pixels of intensity above background were determined with a fixed intensity threshold and the image scanned to find aggregate edges. Filled masks are then formed of identified aggregates and those above a diameter threshold of 700 nm (~3 pixels) were analysed for the mean intensity of the aggregate.

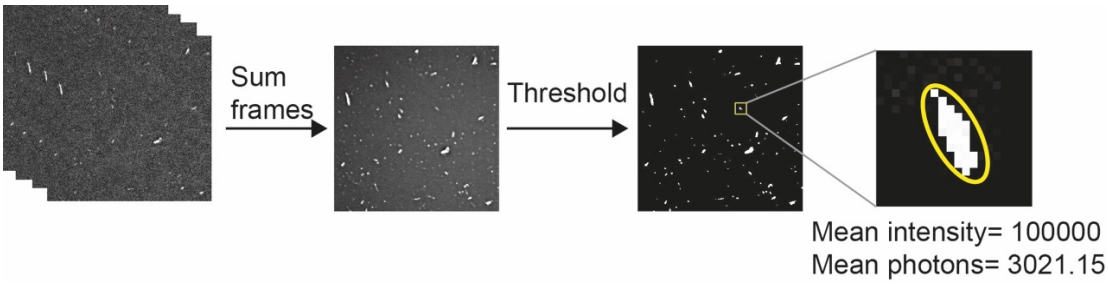

Figure 3.1. Simplified illustration of the single-aggregate image analysis process used in this work.

3.1.10 Fluorescence image analysis of bifunctional probes

Single Aggregate Visualisation by Enhancement (SAVE) images were analysed with a bespoke ImageJ (161) macro. Image stacks of 200 frames taken as 100 ms per frame of the BE, mBE dyes and ThT with αSyn aggregates and either in the presence or absence of H_2O_2 were compressed in time to create single frame images representing the average pixel intensities. Pixels of intensity above background were determined with a fixed threshold and αSyn aggregate species in each field of view identified and counted. The density of species was

determined from the division of the number of species by the area of the field of view (4495 μm^2). Five fields of view in the presence of H_2O_2 and five in the absence of H_2O_2 were analysed for each dye. Error bars represent the standard deviations of the species density between the five fields of view.

3.1.11 Determination of ensemble photophysical properties

Several photophysical quantities were determined from ensemble absorption and emission data (162) using a custom Matlab script. These included absorption maxima (λ_{abs}), emission maxima (λ_{em}) Stokes shift, molar extinction coefficient (ε), fluorescence quantum yield (Φ_{Fl}) and brightness (B). Stokes shifts were calculated from the difference of λ_{em} and λ_{abs} ($\lambda_{em} - \lambda_{abs}$). ε was determined from the dye UV-vis absorbance (A) and sample path length (l) using the Beer–Lambert law with solutions of known concentrations. Φ_{Fl} of the dyes were determined by referencing against either quinine sulfate (Sigma-Aldrich, Q0132) in 0.1 M H_2SO_4 (Φ_{Fl}=0.5) (30) or rhodamine 101 (Sigma-Aldrich, 83694) in ethanol (Φ_{Fl}= 1) (163) and discrepancies in absorbance and solvent refractive index were corrected for with Equation 3.1:

$$\Phi_{Fl} = \Phi_{ref} \times \left(\frac{\int I}{\int I_{ref}} \; \frac{1\text{-}10^{-A_{ref}}}{1\text{-}10^{-A}} \; \frac{n^2}{n_{ref}^2} \right) \qquad (3.1)$$

where Φ_{ref} is the fluorescence quantum yield of the reference dye, I is the fluorescence intensity and n is the refractive index of the medium. Fluorescence emission spectra of Φ_{Fl} standards, quinine sulfate and rhodamine 101 were collected at several concentrations in either sulfuric acid (0.5 M, 99.99 %, Sigma-Aldrich, 339741) or ethanol (99.8 %, VWR, 20821.296) respectively (see Appendix A.1, Figure A.1.2 for calibration curves).

3.1.12 Determination of binding affinities

In short, binding affinities were measured using Biacore T200 SPR instrument. Measurements were made in HBS-EP$^+$ buffer (10 mM HEPES, 150 mM NaCl, 3 mM EDTA and 0.05 % v/v surfactant P20 in ultra-pure 18.2 MΩcm water). αSyn

aggregates were covalently coupled to a sensor chip (BIAcore) via primary amine functionalities.

Dye stock solutions (10 mM) were diluted to the desired concentrations (30, 20, 15, 10, 5, 2.5, 1, 0.75, 0.5, 0.25, 0.1 μM) in HBS-EP$^+$ buffer. The SPR measurement set for each dye was repeated at least 3 times on different sensor chips and αSyn aggregates. K_D values were obtained by nonlinear curve fitting the response values to Equation 3.2:

$$y = \frac{B_{max} - X}{(K_D + X)} \tag{3.2}$$

3.1.13 Cell Viability Assay- Trypan Blue staining

In short, HEK293 cells were seeded at 80 % confluence in 6-well plates and treated with 10 μM BE01, BE02, mBE01, mBE02, BE-Ox and mBE-Ox separately. Cell viabilities were sequentially tested at 3 hours, 12 hours and 24 hours after the treatment. The total cell population and trypan blue stained cells were counted under a microscope. Healthy cell cultures were considered to be more than 85 % viable cells as determined by Equation 3.3

$$\text{viable cells} = \left(1 - \left(\frac{\text{number of blue cells}}{\text{total number of cells}}\right)\right) \times 100 \tag{3.3}$$

3.2 Materials and methods- Project Two

3.2.1 Purification and dye labelling of mEos3.2-HaloTag and HaloTag-SNAP-tag fusion proteins

An mEos3.2-HaloTag construct was cloned from plasmids containing mEos3.2 and HaloTag (Promega), fused via a short linker (Leu-Glu-Gly-Ser) and inserted

into an EcoRI/HindIII digested pET30a expression vector. A HaloTag-SNAP-tag construct was cloned in the same way.

His-tagged mEos3.2-HaloTag and HaloTag-SNAPtag constructs were expressed in *E. coli* BL21(DE3)pLysS cells by growing cells (1 L) from a starter culture (50 mL) to an $OD_{600\ nm}$ of 0.7 to 1.0 in LB media containing kanamycin (35 $\mu g ml^{-1}$) and chloramphenicol (34 $\mu g ml^{-1}$) before inducing expression using IPTG (1 mM) for 4 hours at 25 °C. Cells were pelleted and stored at -20 °C. For protein purification, cells were thawed rapidly at 37 °C and re-suspended in three volumes of lysis buffer (50 mM HEPES pH 7.5, 300 mM NaCl, 5 % glycerol and protease inhibitor cocktail (Roche)) per volume of pellet. The cell resuspension was then sonicated for 13 minutes at 33 % amplitude (5 seconds on and 10 seconds off) using a Sonic Dismembrator (Model 505, Fisher Scientific), the cell debris was pelleted, and the protein lysate collected and filtered through a 0.45 µm filter.

The fusion proteins were first purified by nickel affinity chromatography. The protein lysate was re-suspended in a Ni-nitrilotriacetic acid (Ni-NTA, 50 % 5 mL) bead slurry (Qiagen), which had been pre-equilibrated in buffer (50 mM NaH_2PO_4, 300 mM NaCl, pH 8.0), and was rotated overnight at 4 °C. The fusion protein was purified using a 20 ml gravity column (Bio-Rad), washed in 3 column volumes of wash buffer (50 mM NaH_2PO_4, 300 mM NaCl, 5 mM imidazole, pH 8.0) and finally eluted into 10 ml of elution buffer (50 mM NaH_2PO_4, 1 M NaCl, 250 mM imidazole, pH 8.0). The protein was then dialysed (into 50 mM NaH_2PO_4, 1 M NaCl, pH 8.0) to remove imidazole using a Vivaspin 500 with a molecular weight cut-off (MWCO) of 5 kDa (Sartorius Stedim Biotech). The fusion protein was then further purified by gel filtration (50 mM NaH_2PO_4 and 1 M NaCl, 75 mL Sephadex200 column, GE Healthcare). Mass spectrometry was carried out to verify the mass of the protein (65096.8 Da), amino acid analysis was used to determine its concentration and gel electrophoresis was used to further determine purity (Appendix A.3, Figure A.3.1).

The protein was stored in 500 µl aliquots of 15 µM at -80 °C and re-purified using size exclusion chromatography prior to dye labelling. The fusion proteins (5-10 µM) were labelled with the HaloTag-dye or SNAP tag-dye ligands by reacting them at an equi-molar ratio at room temperature for 1 hour before purification by gravity with an Illustra Nap-5 gravity column (GE Healthcare). Labelling was confirmed to be close to 100 % by mass spectrometry (Appendix A.3, Figure A.3.2).

The HaloTag and SNAP-tag PA-JF_{549} and JF_{646} dyes were a kind gift from Luke D. Lavis (HHMI).

3.2.2 HaloTag ligand synthesis

The O-2 HaloTag amine ligand (0.2 mM, Promega) was reacted with a N-hydroxysuccinimidyl ester of the Alexa Fluor 647 dye (Life Technologies) (0.2 mM) in $NaHCO_3$/Na_2CO_3 (0.1 M, pH 8.5) for 4 hours. The resulting HaloTag-dye ligand was then purified using a C18 reversed phase Brownlee column (Spheri-5 RP-18, PerkinElmer) on a high-performance liquid chromatography (HPLC) system (Agilent 1100 series) using a gradient of 0-50 % acetonitrile for 30 min, 50-100% for 10 min, and finally 100-0 % for 5 min. The relevant peak was then isolated and verified by mass spectrometry (Appendix A.3, Figure A.3.3)

3.2.3 Bulk fluorescence characterisation

Bulk fluorescence spectra were obtained with mEos3.2 or PA-JF_{549} with or without the JF_{646} dye (15-25 µM) using a fluorescence spectrophotometer (Cary Eclipse). The sample was placed in a quartz cuvette (Hellma Analytics, 3×3 mm). To determine the actual FRET efficiency of the mEos3.2-HaloTag proteins with the different dyes, emission spectra were collected after exciting at 532 nm and detecting fluorescence over a range of wavelengths (550-800 nm). FRET efficiency (E_{FRET}) was calculated using the standard Equation 3.4:

$$E_{FRET} = 1 - \frac{F_{DA}}{F_D} \tag{3.4}$$

where F_D is the fluorescence intensity of the donor fluorophore alone (mEos3.2) and F_{DA} is the fluorescence intensity of the donor in the presence of the acceptor (mEos3.2-JF_{646}).

The distance r between the donor mEos3.2 or PA-JF_{549} and acceptor JF_{646} fluorophores was calculated using the equation for FRET efficiency (E_{FRET}) (Equation 3.5):

$$E_{FRET} = \frac{1}{1 + \left(\frac{r}{R_0}\right)^6} \tag{3.5}$$

R_0 was calculated to be 6.01 nm for mEos3.2-JF_{646} and 5.81 nm for PA-JF_{549}-JF_{646} from Equation 3.6:

$$R_0^6 = \left(\frac{9000\ (\ln 10)\ \Phi_D\ \kappa^2}{128\ \pi^5\ N_A\ n^4}\right) J(\lambda) \tag{3.6}$$

where N_A is Avogadro's number, κ^2 is the dipole orientation factor ($\frac{2}{3}$ for freely rotating donor and acceptor fluorophores), Φ_D is the quantum yield of the donor mEos3.2 or PA-JF_{549} fluorophores (0.55 and 0.88 respectively), n is the refractive index of the medium (1.33), and J is the spectral overlap integral between the donors mEos3.2 or PA-JF_{549} and acceptor JF_{646} spectra calculated over different wavelengths λ using the extinction coefficient ε_A of the acceptor JF_{646} dye (max value of 152 000 $M^{-1}cm^{-1}$) (Equation 3.7):

$$J = \int F_D(\lambda)\ \varepsilon_A(\lambda)\ \lambda^4\ d\lambda \tag{3.7}$$

3.2.4 Fluorescence lifetime characterisation

Time-Correlated Single Photon Counting (TCSPC) measurements were performed on a Leica SP8 STED 3X system additionally equipped with Single Molecule Detection (SMD) software (SymPhoTime version 5.3.2.2) and hardware (PicoHarp 300; PHR 800) from PicoQuant. Fluorescence excitation in

this system was achieved with a pulsed (80 MHz) tuneable white light laser (WLL; Super-K; NKT Photonics) while fluorescence was detected with an internal hybrid single molecule detector (Leica HyD SMD). Donor excitation was performed at 561 nm with a detection band of 570-620 nm and using a water-immersion objective (20×, 0.75NA, HC PL APO CS2) with a zoom factor of 1× and a mono-directional scan speed of 400 Hz. Photo-activation/conversion was achieved using the 405 nm laser for 1 minute at activation powers of 1.75 $kWcm^{-2}$ at the focal plane of the objective prior to the lifetime measurement. FLIM measurements were performed in triplicate pre- and post-activation/conversion on purified protein in PBS (pH 7.4) in 8 well glass bottom µ-Slides (iBidi). Protein was adhered to the coverslip by incubating with poly-L-lysine (PLK, Sigma Aldrich) for 30 minutes and then with 5-10 µM protein for 10 minutes.

Post-activation/conversion TCSPC decay data were analysed using SymPhoTime software (version 2.1) from Picoquant. The tail of the cumulative TCSPC decay data from all pixels in the image with a minimum number of 50 photons and with a raw time range of 1.5 ns ≤ τ ≤ 7.0 ns was analysed. The decay curve was fit to a sum of exponential tail decay curves defined by:

$$I(t) = I_{Bkgd} + \sum_i \alpha_i e^{-t/\tau_i} \qquad (3.8)$$

where I_{Bkgd} is an intensity offset for the background counts, and α, i and τ_i are the amplitude and lifetime values for the ith exponential.

3.2.5 Single-molecule TIRF microscope

The microscope described in detail in Chapter 2, section 2.4 was used to carry out the work detailed in Chapter 7.

Single-molecule experiments were carried out on a bespoke inverted fluorescence microscope (Olympus, IX73). Circularly polarised laser beams aligned and focussed at the back aperture of an oil-immersion objective (Olympus, Universal Plan Super Apochromat, 100×, NA 1.49). Continuous

wavelength diode laser light sources used include a 641 nm (Coherent, CUBE 640-100C, 100 mW), a 561 nm (Cobolt, Jive 200, 200 mW) and a 405 nm laser (Stradus, Toptica, 405-100, 100 mW). Total internal reflection was achieved by aligning the laser off axis such that the emergent beam at the sample interface was collimated and incident at an angle greater than the critical angle (θ_c ~ 67°) and slightly less than θ_c for oblique-angle illumination imaging. This generated a ~50 µm diameter excitation footprint. For TIRF, the power density at the coverslip for the 561 nm laser was calculated to be approximately 0.4 $kWcm^{-2}$ measured with the laser beam in epi-illumination. For oblique-angle illumination, the power of the collimated beams at the back aperture of the microscope was 10 $kWcm^{-2}$ and 10-100 Wcm^{-2} for the 561 nm and 405 nm laser beams respectively. The lasers were reflected by dichroic mirrors, which also separated collected fluorescence emission from the TIR beam (Semrock, Di01-R405/488/561/635). The fluorescence emission was collected through the same objective and then further filtered using a combination of long-pass and band-pass filters (BLP01-561R and FF01-587/35 for 561 nm excitation). The emission signal was projected onto an EMCCD (Photometrics, Evolve 512 Delta) with an electron multiplication gain of 250 ADU/photon operating in a frame transfer mode. The instrument was automated using the open-source software micro-manager (v. 1.4) and the data displayed using the ImageJ software (v. 1.52d) (161)

3.2.6 Preparation for single-molecule TIRF imaging

Borosilicate glass coverslips (VWR Int, 22 × 22 mm) were cleaned to remove any fluorescent residues in an argon plasma cleaner (Harrick plasma) for 1 hour. Frame-seal incubation chambers (Bio-rad) were attached to the coverslip and 50 µl of 0.1 % poly-L-lysine (Sigma Aldrich) added to the center of the chamber for 30 minutes. 50 µl of 10 nM protein was then added to the poly-L-lysine-coated coverslip for 10-15 minutes. The sample was washed 3 times with 50 µl of filtered (0.2 µm syringe filter, Whatman, 6780-1302) MilliQ water and fluorescence images collected as movies of 500 images at 500 ms exposures.

Photo-conversion was achieved as a single pulse in the first frame of each movie.

3.2.7 Analysis of *in-vitro* single-molecule photophysics

A brief description of the software used for data analysis is presented here. A maximum-intensity projection of the first two images after photo-conversion was used as the basis for detecting single molecules. A Laplacian-of-Gaussian filter was applied to the projection, and local maxima found. A region centered on each peak with a threshold value of >600 analogue to digital units (ADU) was extracted from each image. This region consisted of a 7-by-7-pixel signal area, and a surrounding 2-pixel wide background area. A hidden Markov model was set up with four states: two on-states, one off-state, and one bleached state. Single emitters were only analysed if they exhibited single-step photobleaching prior to the end of the movie.

The total on-state time of each molecule was calculated by counting the number of images in an on-state. A switching event was defined as a run of consecutive fluorescent images; the mean run length multiplied by the exposure time to extract the on-state time, and the number of runs detected for a particular molecule is the number of switching events. Finally, the total photon emission was calculated for each fluorescent image by subtracting the mean of the background region from the signal region.

In order to calculate the number of emitted photons per molecule the total camera gain in units of analog-to-digital units (ADU)/photon was determined by (Equation 3.9):

$$G_{total} = \frac{1}{G_{camera}} \times G_{EM} \times QE \qquad (3.9)$$

where G_{camera} is the signal amplification inherent in the EMCCD in units of ADU/electron, G_{EM} is the ratio of the charge on the camera with and without gain, and QE is the quantum efficiency – the ability of the camera to produce a

charge as a result of an incident photon with units of electrons/photon. G_{total} is equal to 35.7 ADU/photon.

The measured signal (I) in units of electrons was converted to emitted photons (n) as follows (Equation 3.10):

$$n = \frac{I}{G_{total} \times TE} \tag{3.10}$$

TE is defined as the transmission efficiency of all optical components in the emission path of the instrument and can be described by (Equation 3.11):

$$TE = \eta_{coll} \times T \times \eta_{EMCCD} \tag{3.11}$$

Where η_{coll} is the collection efficiency of the objective, T is the transmission of the internal optical components of the microscope and η_{EMCCD} is the quantum efficiency of the EMCCD (164).

All histograms were generated using the Origin package (OriginPro, 2017, OriginLab, Northampton, MA).

3.2.8 Stem cell culture

Embryonic stem (ES) cells were cultured in standard serum and mouse leukaemia inhibitory factor (mLIF) conditions. They were passaged every two days by washing in PBS, adding Trypsin-EDTA 0.25 % (Life tech) to detach the cells, and then washing in media before re-plating in fresh media. To help the cells attach to the surface, plates were incubated for 15 minutes at room temperature in PBS containing 0.1 % gelatine (Sigma Aldrich, G1890). The background ES cell lines were characterized by qPCR, RNA-seq, ChIP-seq and potency assays.

ES cells expressing mouse CHD4 tagged with the mEos3.2-HaloTag were generated as previously described by CRISPR/Cas9 based knock-in of a cassette containing mEos3.2-HaloTag and a puromycin selection gene into one

CHD4 allele of the ES cells. After 2 weeks of geneticin selection, cells were sorted using a MoFlo flow sorter (Beckman Coulter) to ensure that they were labelled with the mEos3.2 fluorophore.

3.2.9 Live cell single-molecule tracking

ES cells expressing mEos3.2-HaloTag-tagged CHD4 were passaged two days before imaging onto 35 mm glass bottom dishes (MatTek Corporation P35G-1.0-14-C Case) in phenol red-free serum and mLIF conditions. Just before imaging, if necessary, cells were labelled with 5 μM HaloTag-JF_{646} ligand for at least 15 minutes, followed by two washes in PBS and a 30-minute incubation at 37 °C in media, before imaging the cells in fresh phenol red-free serum and mLIF conditions containing 5 mM Trolox. *In vivo* fluorescence images were collected as movies of 10,000 frames at 500 ms exposure. Continuous photo-conversion was achieved using the 405 nm laser at low activation powers of ~ 10 Wcm^{-2}.

3.2.10 Cell image processing and analysis

Live-cell single-molecule movies were analysed using Rapidstorm software (165). Only fluorescent puncta less than 5 pixels wide and with a fixed global threshold were analysed. Single CHD4 molecules, were tracked with a custom code to connect single-molecule localizations and extract the length of their trajectories. Fluorescent puncta were considered to be the same molecule if they were within 100 nm between frames. Trajectories smaller than 3 localizations were discarded.

Project One

Novel Fluorophores for the Study of Neurodegenerative Disease

Chapter 4 Fluorescence for Studying Neurodegenerative Disease: An Introduction

4.1 Overview of this chapter

This chapter provides important context relevant to the work presented in Chapter 5 and Chapter 6. The background discussed here outlines the key biological aspects of neurodegenerative disease and currently used methods of study through fluorescence techniques, principally with the dye **Thioflavin-T** (ThT).

4.2 Protein misfolding and neurodegeneration

Finding the fundamental cause of cellular toxicity and neuronal loss in neurodegenerative diseases such as Alzheimer's disease (AD) (166) and Parkinson's disease (PD) (167) has been the focus of extensive research. The phenomenon of protein mis-folding, aggregation and subsequent accumulation of previously disordered neuronal proteins has been implicated in cell death (168). Following synthesis, proteins may fold via various pathways and intermediates (169). There are multiple forms of **protein aggregate**, amyloid aggregates are highly organised, insoluble and functionless, their intra and extra-cellular presence is a distinguishing feature of many neurodegenerative diseases (170). The mechanism of amyloid fibril formation (Figure 4.1) is widely accepted as adhering to the nucleated growth model (171–173).

The process begins with a lag phase, during which no bulk alterations in structure and property are detected. It is hypothesised that misfolded monomeric species begin to assemble to form oligomeric precursors to fibrillar aggregates. The successive phase invokes the rapid formation of extended

structures during which fibrillation occurs (174). The oligomeric species formed are thought to be the primary cyto-toxic component of neurodegenerative diseases and possess some β-sheet structure (175, 176). Amyloid fibrils form the final stage of the aggregation process and are dominated by cross-β sheet architecture which runs perpendicular to the fibrillary axis (177), whereas oligomers are highly heterogeneous due to the multitude of aggregation pathways (178).

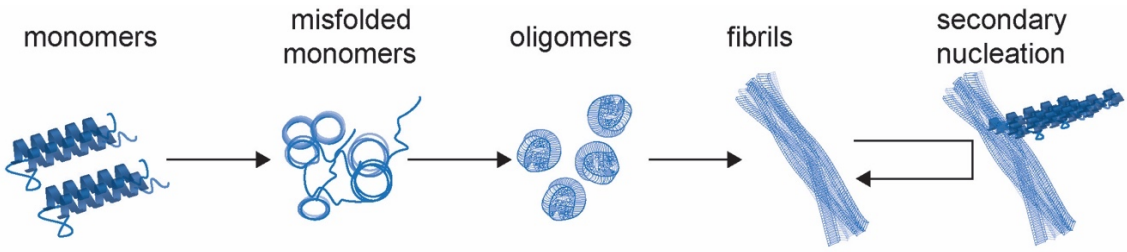

Figure 4.1. One of many potential pathways towards amyloid fibril formation from monomeric protein. Monomeric protein units mis-fold and lose function. These species begin to aggregate into disordered oligomeric species with some β-sheet tertiary structure. This primary nucleation process terminates with the formation of highly ordered, insoluble fibrils with β-sheet tertiary structure. Fibrils are able to catalyse the formation of new aggregates by providing a nucleation site on their surface on which monomers may aggregate, a process known as secondary nucleation.

α-Synuclein (αSyn) is an intrinsically disordered protein that has been associated with Parkinson's disease since it was detected as the main component of Lewy bodies (179). The primary structure consists of a high concentration of hydrophobic residues. This region is thought to be responsible for the aggregation and formation of **β-sheet** containing species of αSyn (180). The mechanism behind the triggering of αSyn aggregation is unknown but there are several factors promoting αSyn aggregation such as genetic mutations. Although its function is currently unknown, αSyn is expressed highly in the brain. PD is characterised by neuronal loss and the presence of Lewy Bodies; solid, insoluble deposits within nerve cells (181), of which aggregates of αSyn are a dominant component (167).

In addition to proteinaceous aggregate species, direct observations of oxidative damage have been made in post-mortem brains showing neurodegenerative pathology (182–184). The production of **reactive oxygen species** (ROS) such as hydrogen peroxide (H_2O_2) has been associated with multiple diseases and widely reported in models of neurodegenerative disease such as PD. The term ROS includes a vast number of highly reactive compounds, one of the most common being H_2O_2. These species are capable of detrimentally disrupting a cellular environment by reacting with biomolecules and causing alterations or loss of function which is in most cases proceeded by cell mortality (185).

4.3 Fluorescence detection of protein aggregates

There are many methods available to study amyloid, to gain detailed structural information as well as methods to study mechanisms of aggregation. The kinetics of amyloid formation is most commonly studied by employing extrinsic fluorophores.

Throughout the history of studying amyloid proteins the most commonly used extrinsic amyloid dye has been Congo Red (Figure 4.2). Congo Red is structured and oriented in one plane when bound to amyloid fibrils, under these conditions it demonstrates birefringence and dichroism. These optical properties are not apparent in solution where dye molecules are randomly oriented (186) and therefore can be used diagnostically. However Congo red staining cannot be used to detect aggregates *in situ* (187). More recently, several fluorophores for this purpose have been developed. Conjugated oligothiophenes such as p-FTAA (Figure 4.2) have been shown to be spectrally sensitive to small changes in the orientation of the fluorophore backbone, which is directly affected by the mode and site of protein binding (188, 189). In addition, it has been successfully applied to specifically stain amyloid in tissue. Aryl-benzothiazole compounds are β-sheet sensitive probes of which there are different types used for either *in vivo* or *in vitro* study. These typically operate via a turn-on response, in this case an increase in fluorescence quantum yield

upon amyloid binding. Pittsburgh compound B (PiB, Figure 4.2) is a neutral dye with high affinity (nM) for amyloid deposits present in the brain of Alzheimer's disease patients known to harbour high concentrations of amyloid deposits. As this dye is able to cross the blood-brain barrier, and can be readily radiolabelled, it has been utilised in positron emission tomography (PET) to distinguish between healthy and neurodegenerative disease brain (190). However, PiB and other neutral benzothiazole dyes have poor fluorescence quantum yields and fluorescence turn-on responses to amyloid binding (191).

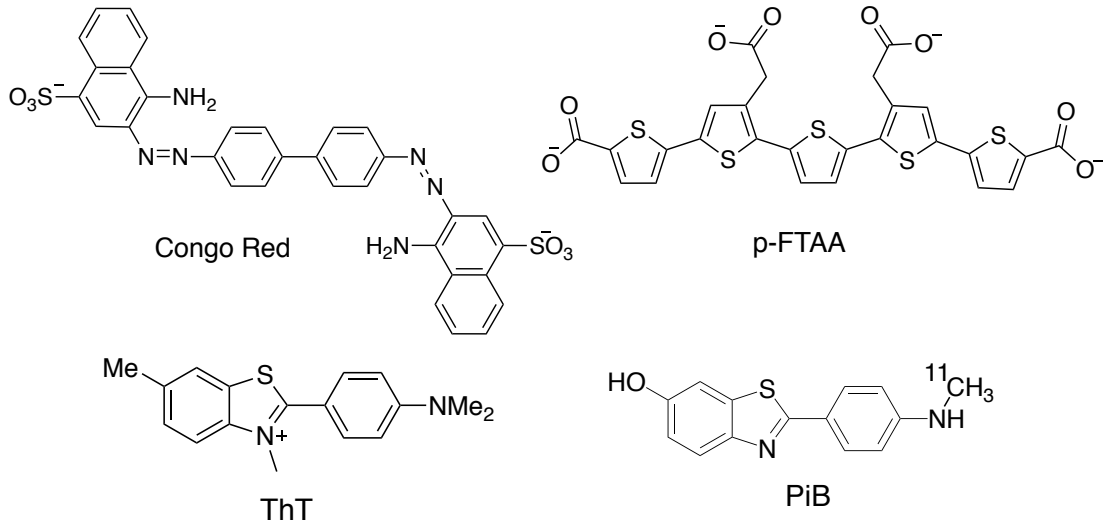

Figure 4.2. Chemical structures of four dyes, Congo red, p-FTAA, PiB and ThT, used to study protein aggregation and aggregates.

The N-methyl benzothiazolium cation, ThT (Figure 4.2) has become the gold-standard fluorophore of choice for the study of amyloid formation kinetics *in vitro* (192).ThT fluorescence has been traditionally used to observe the formation of large, insoluble amyloid fibril species with bulk fluorescence (192), however there is now significant evidence to suggest that the smaller, soluble, **oligomeric** species are cytotoxic and of more critical interest (175, 193–197). Single-molecule fluorescence imaging has been employed to study the aggregation process optically and observe these oligomeric species (198). However, the required covalent dye-labelling of the monomeric proteins causes

artefacts generated by high background as well as active interference in aggregation kinetics (199). ThT binds non-covalently but specifically to extended β-sheet structures with moderate μM affinity. ThT has many favourable photophysical properties, discussed later in this chapter, which have been utilised to observe the formation of single amyloid fibrils in a total-internal reflection fluorescence (TIRF) imaging modality (200, 201). This technique, termed single-aggregate visualisation by enhancement (SAVE) (159), exploits the large Stokes shift, low fluorescence quantum yield in solution, subsequent fluorescence turn-on upon aggregate binding and moderate affinity of ThT to image αSyn aggregates at singe-molecule level. Total-internal reflection fluorescence (TIRF) microscopy is employed to maximise signal-to-background ratios. Unlike typical single-molecule techniques, the low background produced by the free dye allows for imaging at high concentrations (μM). Furthermore, the rapid exchange of dye molecules relative to the temporal regime of the technique exempts it from the constraints of photobleaching. This was shown to be advantageous not only with *in vitro* studies but also to identify the presence of β-sheet containing species in human bio-fluid samples, specifically **cerebral spinal fluid** (CSF). The increased resolution of SAVE imaging compared to bulk fluorescence allowed for the potentially cyto-toxic and low abundance oligomers to be detected.

4.4 Fluorescence detection of hydrogen peroxide

The temporal and spatial regime in which fluorescence imaging operates makes it a suitable technique for the study of ROS. There are several probes capable of measuring **H_2O_2** production such as hydroethidine, dihydrorhodamine and dichlorodihydrofluorescein diacetate (DCFH-DA), being among the most common (202). Generally, in this context, a non-fluorescent probe forms a fluorescent product via an oxidation reaction with an oxygen radical. However, complicated intracellular redox mechanisms often limit the capabilities of these probes to definitively report the presence of H_2O_2.In the

case of DCFH-DA, oxidation via other ROS, fluorescent side-products and self-production of ROS can yield data that is complicated to interpret (203).

The boronate functionality provides an alternative moiety for specific and irreversible H_2O_2 detection and quantitation (158) (Scheme 4.1). Miller *et. al.* demonstrated the synthesis and application of two novel boronate-based fluorescein conjugated fluorophores, termed PX1 and PR1, which adopt closed, non-fluorescent conformations prior to oxidation with H_2O_2. Together with a change in conformation the resultant phenol moiety is an electron donating substituent. Combined, these properties yield a dye with an integrated emission intensity of several orders of magnitude greater than the precursor.

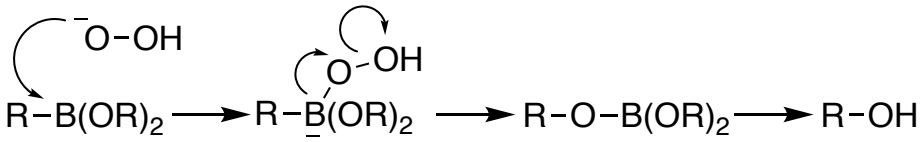

Scheme 4.1. Reaction mechanism of oxidative cleavage of boronate ester into hydroxyl group by H_2O_2.

4.5 Properties of Thioflavin-T

4.5.1 Photophysical Properties

ThT has several photophysical properties that make it a desirable probe to follow the formation of protein aggregates. Most of these properties and the excited state behaviour can be effectively explained by the molecular rotor model (9, 204). Multiple spectroscopic studies of ThT has elucidated the presence of two electronic excited states, the locally excited (LE) and **intramolecular charge transfer** (ICT) states (204–207). ThT undergoes a subtype of ICT known as **twisted ICT** (TICT). In low viscosity solvents the TICT state is formed as a result of photo-induced charge redistribution coupled with a dihedral twist about the C-C σ- bond between the benzothiazole and dimethylaniline moieties (208, 209) (Figure 4.3).

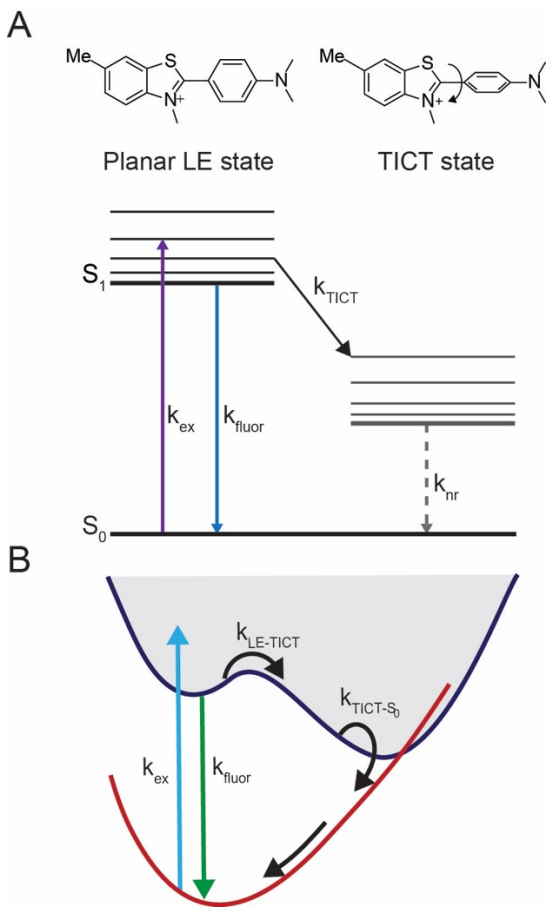

Figure 4.3. **A)** Simplified Jablonski diagram illustrating the photoinduced formation of the TICT state in low-viscosity environments. **B)** Schematic of the potential energy surfaces of the adiabatically coupled ground state and TICT excited state (210).

In this TICT state the molecular geometry is such that the π orbitals on the benzylamine and benzothiazole rings are oriented perpendicular to each other, prohibiting delocalisation across the whole chromophore. The energy gap between the TICT and ground state is low therefore relaxation is non-radiative. The extent of this twisting, hence the population of the TICT state is sensitive to the absolute viscosity of the surrounding environment (206). In low viscosities, the fluorescence quantum yield (Φ_{Fl}) has been measured to be as low as 0.0001 (211). In high viscosities the rotation is, to some extent, inhibited and fluorescence emission from the LE state dominates and manifests as an increase in Φ_{Fl} of several orders of magnitude (206).

The Glasbeek model was proposed to explain excited state dynamics of another molecular rotor dye Auramine O (212) and has since been applied to describe ThT (210). The model describes decreasing S_1-S_0 transition dipole moment as a function of twist angle (C-C bond between dimethylaniline and benzothiazole components). Following photon absorption, the distribution of electrons shifts from the fluorescent locally excited state to the non-emissive TICT state as a result of geometric relaxation. The torsion is induced to minimise the coulombic interaction between the unpaired electrons corresponding to the ICT. The twist induced non-radiative decay from S_1-S_0 is a result of two processes: 1) the mixing of the LE and CT states to form a conical intersection reduces the oscillator strength of the excited state fluorophore and 2) the geometric relaxation lowers the energy of the TICT state to such an extent that emission is no longer as photons. This has been observed spectroscopically with time-resolved emission studies and manifests as a time-dependent Stokes shift with a rate dependent on solvent viscosity (213).

This molecular rotor phenomenon is understood to be the origin of the significant increase in fluorescence Φ_{Fl} upon binding to protein aggregates (206, 213, 214). It is thought that the intramolecular rotation of ThT is hindered when it occupies a protein binding site. The relative change in Φ_{Fl} between the unbound states of ThT may be up to 3 orders of magnitude (211). It is here that the origin of the success of ThT as a protein aggregate fluorescence marker lies.

Therefore, there is a need to understand the excited state behaviour of ThT, especially when considering experimental results in a life-science application and even more so in the rational design of analogous molecules.

4.5.2 Protein binding properties

Amyloid fibrils possess a series of cross-β sheets which run parallel to the long axis of the fibril (Figure 4.4A). Within each of these sheets is contained multiple ordered array of side-chains. ThT is generally understood to bind transiently to channels formed by the solvent exposed side chains (215, 216) (Figure 4.4B).

The relative distance between these side chains has been measured with x-ray diffraction to be 0.48 nm. The long axis of ThT is approximately 1.4 nm in length therefore may bind in a planar conformation along a channel formed by multiple chains. Regular tyrosine residues in the side-chains have been proposed as an optimal binding site, facilitating adsorption of the dye with aromatic π-π stacking interactions (215).

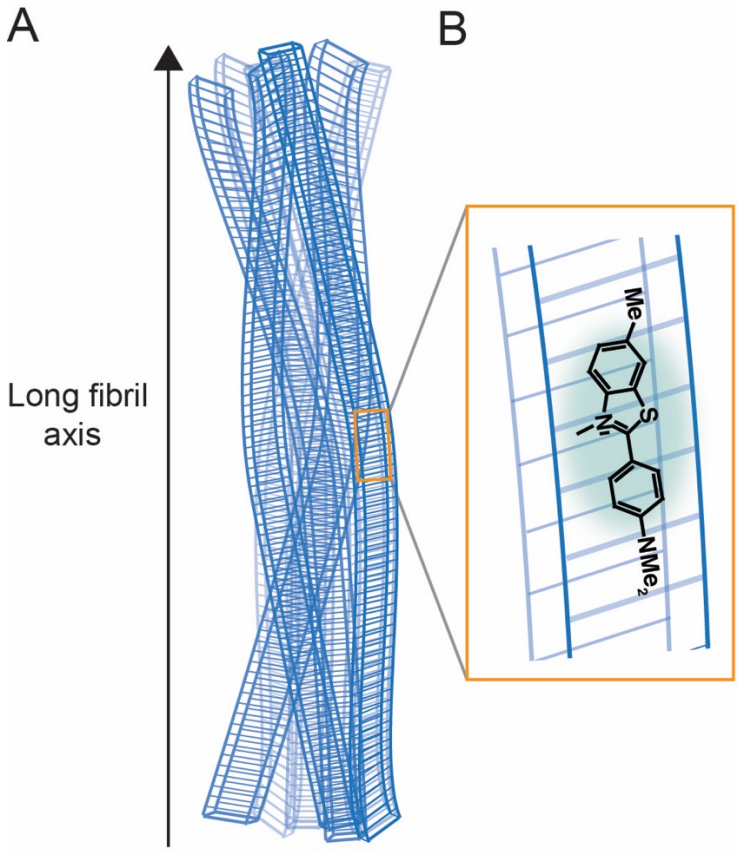

Figure 4.4. **A)** Model of amyloid fibril comprised of organised β-sheets. **B)** Schematic of ThT binding to side chains of the β-sheets that run perpendicular to the fibrillary axis (not to scale).

ThT has been found to bind to fibrils and some oligomers in a regular orientation (193, 216), consistent with β-sheets. In addition, the αSyn aggregate species with ordered β-sheet content may be more cyto-toxic than the disordered species (210). This insight further reinforces the need for a well-

characterised, photophysically optimal amyloid binding dye that could be used to detect toxic species in high-background bio-fluids

Chapter 5 Next-Generation Derivatives of Thioflavin-T

5.1 Overview of this chapter

This chapter will describe the characterisation of a library of dyes derived from ThT to provide a greater number of examples toward understanding the relationship between dye structure and photophysical function in the context of amyloid aggregate detection. This work presents a detailed photophysical characterisation of two categories of ThT analogues; the **neutral 'E'** and the **methylated** and *Z*=+1 **charged 'mE' derivatives** (Figure 5.1) and compare these to ThT. Several bulk photophysical and binding properties have been quantified. Furthermore, a subset of probes was measured at the single-aggregate level in a total internal reflection fluorescence (TIRF) imaging mode relative to ThT and in the presence of recombinant, late-stage **α-Synuclein** (αSyn) aggregates. This chapter explores whether modifications to chemical moieties give rise to large-scale changes in photophysical properties (≥10-fold).

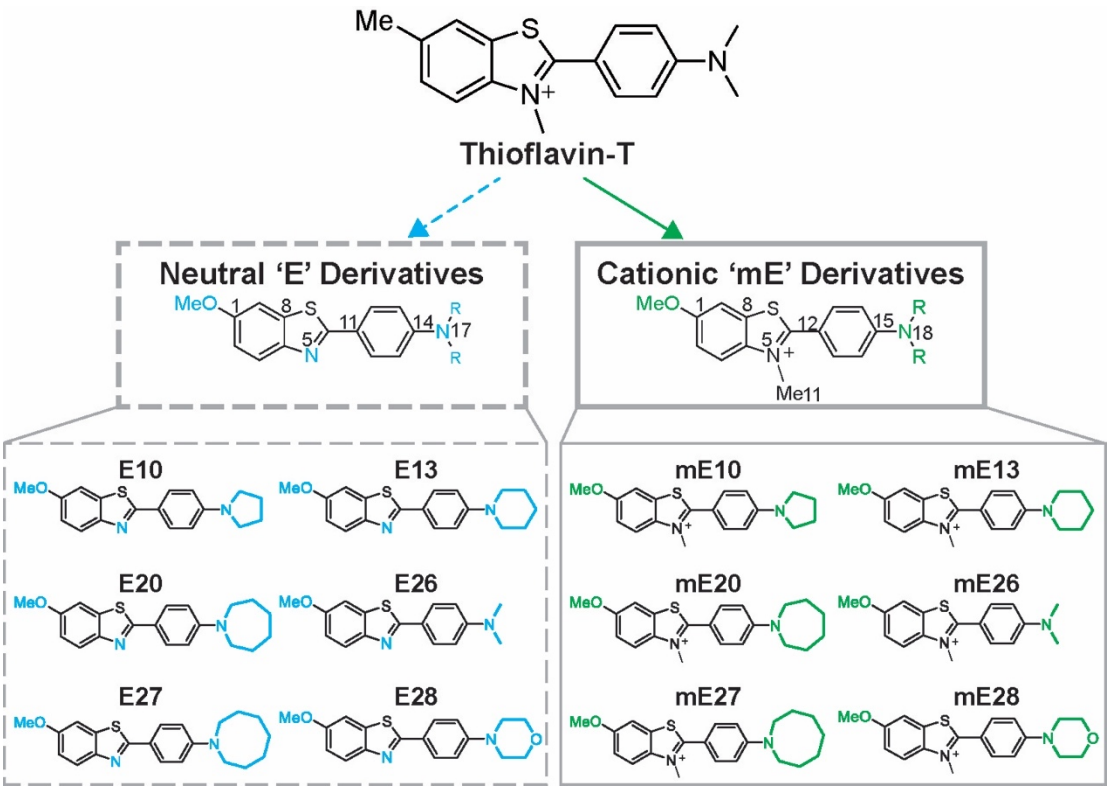

Figure 5.1. Graphic showing the two libraries of ThT derived fluorophores, the neutral E derivatives (left) and cationic mE derivatives (right). The numbered carbons may be referenced in the main text. The coloured substituents (blue for E and green for mE) indicate the main structural modifications relative to ThT.

5.1.1 Contributions

Synthesis was performed by James Fyfe, Omaru Kabia and Dr. Dung Do. αSyn was purified by Ewa Klimont. αSyn fibrils were prepared by Dr. Margarida Rodrigues. Judith Weber and I performed bulk fluorescence and absorption measurements and analyses. SPR experiments were performed by Judith Weber. I performed fluorescence imaging experiments, wrote all code and performed analyses.

5.2 Results and Discussion

5.2.1 Bulk properties

In the context of fluorescent detection of amyloid aggregates, it is important to have an understanding of both the solution-phase and protein bound behaviour of the dyes. In the context of molecular rotors, this can be thought of as a characterisation of both the desired 'signal' and 'background'. Furthermore, detailed understandings of the photophysical behaviours of the probes in multiple environments can greatly aid the interpretation of often complex results of biological experiments.

Blank corrected bulk fluorescence and absorption spectra of ThT (Figure 5.2), E (Figure 5.3) and mE dyes (Figure 5.3) were measured in PBS and in the presence of recombinant αSyn aggregates. From these data we extracted several photophysical quantities including wavelengths of maximum absorption (λ_{abs}) and fluorescence emission (λ_{em}), Stokes shift (λ_{em}-λ_{abs}), molar extinction coefficient (ε), fluorescence quantum yield (Φ_{Fl}) and total integrated fluorescence or brightness (B). Tables 5.1 and 5.2 (section 5.3.1.1) detail the properties of the E and mE derivatives respectively, in PBS. Tables 5.3 and 5.4 (section 5.3.1.3) show the properties of the E and mE derivatives respectively, in the presence of αSyn aggregates. Symbols of the aforementioned photophysical properties are denoted by subscript '1' for the dyes in PBS and '2' for the dyes with αSyn.

5.2.1.1 Intrinsic photophysics

The maximum λ_{abs1} of ThT was measured here to be 413 nm, this concurs well with previously measured values of 412 nm (217) in water. The corresponding λ_{em1} maxima occurred at 488 nm, resulting in a large Stokes shift of 75 nm (Table 5.1).

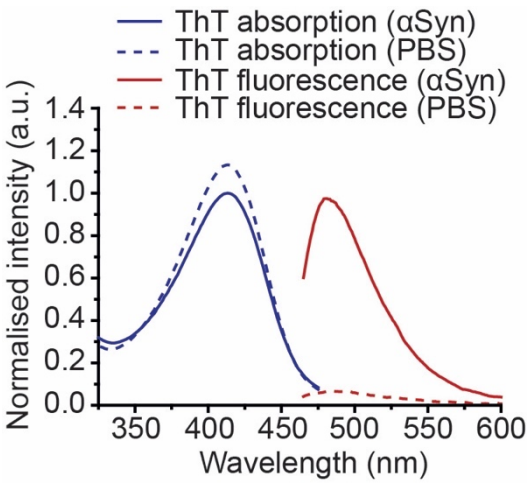

Figure 5.2. Bulk UV-vis absorption and emission spectra of 10 μM ThT in PBS and with ~2 μM recombinant αSyn aggregates. The absorption and emission spectra have been independently normalised relative to the maximum intensity of fluorescence produced by ThT in the presence of αSyn. Each spectrum represents the mean of results from 3 independent preparations of dye.

Fluorophores capable of forming twisted intramolecular charge transfer (TICT) states, like ThT, often have high Stokes shifts. In order for this to occur a fluorophore must comprise of an electron donor and an electron acceptor unit. Following excitation electron density is mobilised from the donor component of the molecule to the acceptor. This physically equates to the promotion of an electron from the highest occupied (HOMO) to the lowest unoccupied molecular orbital (LUMO) (218). In the case of ThT, this high energy state is rapidly stabilised by geometric relaxation manifesting as rotation about the central C-C bond

Significant energy is lost during the conformational rearrangement and subsequent reorganisation of polar solvent molecules.

ThT had a moderate ε_1 of 36000 $M^{-1}cm^{-1}$ at 413 nm calculated here which is in good agreement with previously calculated values (192, 219). The total integrated intensity or B can be calculated from the product of ε and Φ_{Fl}, in this work B was extracted by directly integrating the fluorescence spectra. Emission from the TICT state is non-radiative due to orthogonal orientation and therefore π orbital decoupling of the benzothiazole and benzylamine moieties. In

aqueous solution, return to the ground state is dominated by ThT molecules occupying the TICT excited state, hence is non-radiative. This is made clear by the low B_1 of 39.43 and Φ_{Fl1} of < 0.01. It is desirable for B_1 to be at a level below the detection capabilities of the detector in the amyloid aggregate sensing context as any signal produced from unbound ThT is considered background.

The E derivatives exhibit some of the same behaviour as ThT in PBS however there are some clear differences that likely originate from the lack of the methyl group on N-5. The E derivatives all have maximum λ_{abs1} in the ultraviolet region between 300-371 nm, hypsochromically shifted relative to the λ_{abs} of ThT. This was expected, as the +1 charge on N-5 of ThT provided a partly filled π molecular orbital that extended electron delocalisation and decreased the energy gap between the HOMO and LUMO (220). The absorption spectra were broad, spanning 250 nm in some cases (Figure 5.3), which suggests either the presence of multiple states or species. Other work has attributed complicated spectral features in the absorption spectra of neutral ThT analogues to the formation of micelles or aggregates in solution (191). However, later pH dependent studies of these analogues have attributed the origins of these features to be a result of reversible protonation of N-5 to form a Z=+1 species (221). This possibility concurs with our findings; however, the E derivatives are poorly soluble in aqueous solution and despite rigorous preparation of dye solutions to maximise dissolution, the possibility of aggregate or micelle formation cannot be completely discounted.

Although the unsubstituted N-5 of the E derivatives reduces electron conjugation (lowering of λ_{abs1} and λ_{em1}) they exhibited large Stokes shifts like ThT. This is consistent with molecular rotor behaviour and has been observed with other TICT fluorophores (222). Adiabatic re-organization of the molecular geometry from the electronic excited state to the ground state during the TICT process results in an energy minimum.

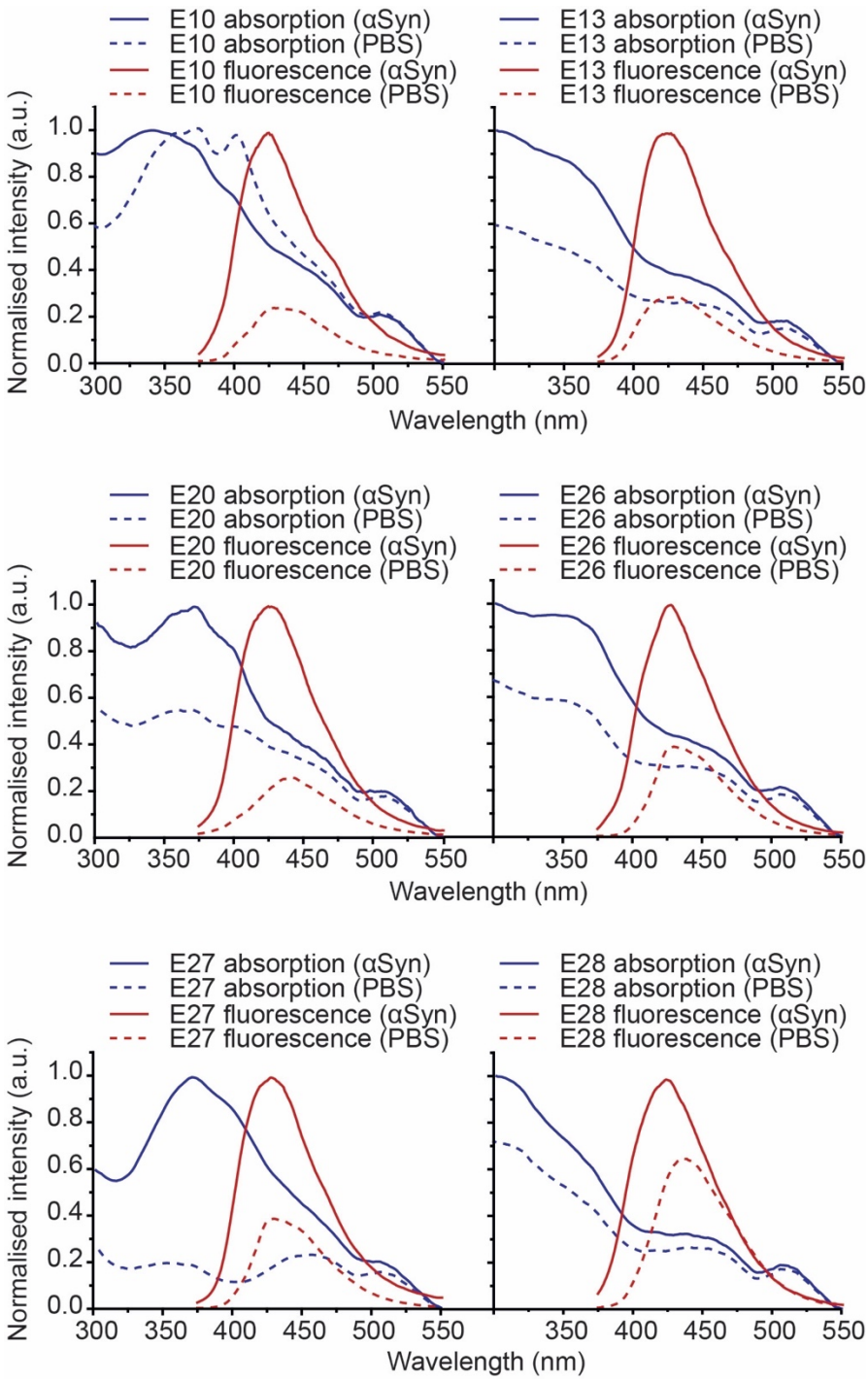

Figure 5.3. Bulk UV-vis absorption (blue lines) and emission (red lines) spectra of 10 μM E dye in PBS (dashed lines) and with ~2 μM recombinant αSyn aggregates (solid lines). The absorption and emission spectra have been independently normalised relative to the maximum intensity of the dye in the presence of αSyn.

The E derivatives were weak photon absorbers. At maximum λ_{abs1} all ε_1 values were <6000 $M^{-1}cm^{-1}$. The elite among the array of fluorophores available for fluorescence spectroscopy and microscopy have ε of >100,000 $M^{-1}cm^{-1}$ (42). Molecular rotor probes such as boron-dipyrromethene (BODIPY) (223) and dicyanomethylenedifuran (DCDHF) (162) have lower ε values between 30,000-50,000 $M^{-1}cm^{-1}$, similar to ThT. This implies that the absence of the N-5 methyl group and therefore the net single positive charge significantly reduces the oscillator strength of the molecule. Electronic resonance and inductive effects of fluorophore substituents often impact the ε as it is related directly to the transition dipole moment. Strategic optimisation of ε has been demonstrated effectively by modification of the fluorophore head group (224). It is important to mention that in order for ε_1 to be determined accurately, atomic absorption spectra should be obtained particularly when characterising probes with poor water solubilities.

Despite the E derivatives having ε_1 values approximately ten-fold lower than ThT, Φ_{Fl1} and B_1 were two orders of magnitude greater. This may be explained by the different rotational behaviour of ThT and the E derivatives affecting degree of relative planarity between the benzothiazole and substituted aryl components. As mentioned in Chapter 4, electrons occupying π orbitals are unable to delocalise across the entire chromophore when these two components are oriented orthogonally resulting in the formation of a non-emissive TICT excited state. Maskevich *et al.* (217) demonstrated with *ab initio* methods that the methylated N-5 in ThT lowers the energy between planar and non-planar conformations (8.4 $kJmol^{-1}$), which increases the likelihood of populating the TICT state (<10 %). Upon substitution of the methyl group for a proton they reported an increase in the energy barrier to such an extent (33.5 $kJmol^{-1}$) that only 0.001 % of ThT-like molecules had orthogonal internal torsion angles. Extending this premise, it is probable that this structural modification was responsible for the higher Φ_{Fl1} of the E derivatives compared to ThT.

Table 5.1. Table of photophysical properties of the E dyes and ThT. These were obtained from bulk UV-vis absorption and fluorescence measurements of the dyes free in PBS buffer (denoted by subscript 1).

Dye	Structure	λ_{abs1} (nm)	λ_{em1} (nm)	λ_{em1}- λ_{abs1} (nm)	ε_1 ($M^{-1}cm^{-1}$)	Φ_{Fl1}	B_1 (a.u.)	$\frac{B_1^E}{B_1^{ThT}}$
ThT	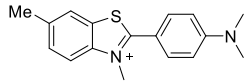	413.0	488.0	75.0	36000	0.00	39.4	1.00
E10	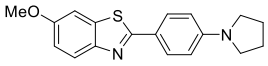	370.0	428.9	58.9	5394	0.01	53.9	1.37
E13	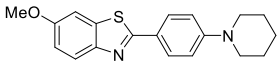	327.9	432.9	104.9	1305	0.02	26.1	0.66
E20	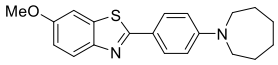	371.0	444.8	73.8	1963	0.01	19.6	0.50
E26	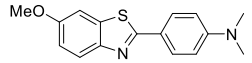	301.0	432.0	131.0	2542	0.04	101.7	2.58
E27	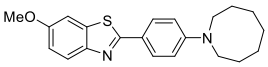	300.0	440.9	140.9	1346	0.02	26.9	0.68
E28	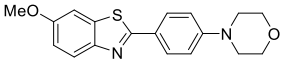	325.0	438.9	113.9	4822	0.02	96.4	2.45

The mE derivatives were comprised of N-5 methylated, Z=+1, congeners of the E derivatives discussed above. Expectedly they exhibit broadly similar photophysical behaviour to ThT. Discrepancies in these may originate from the methoxy substituent at C-1 on the mE compounds which differs from the methyl of ThT. Most mE dyes had λ_{abs1} greater than 410 nm, bathochromically shifted from their E partners (Figure 5.4).

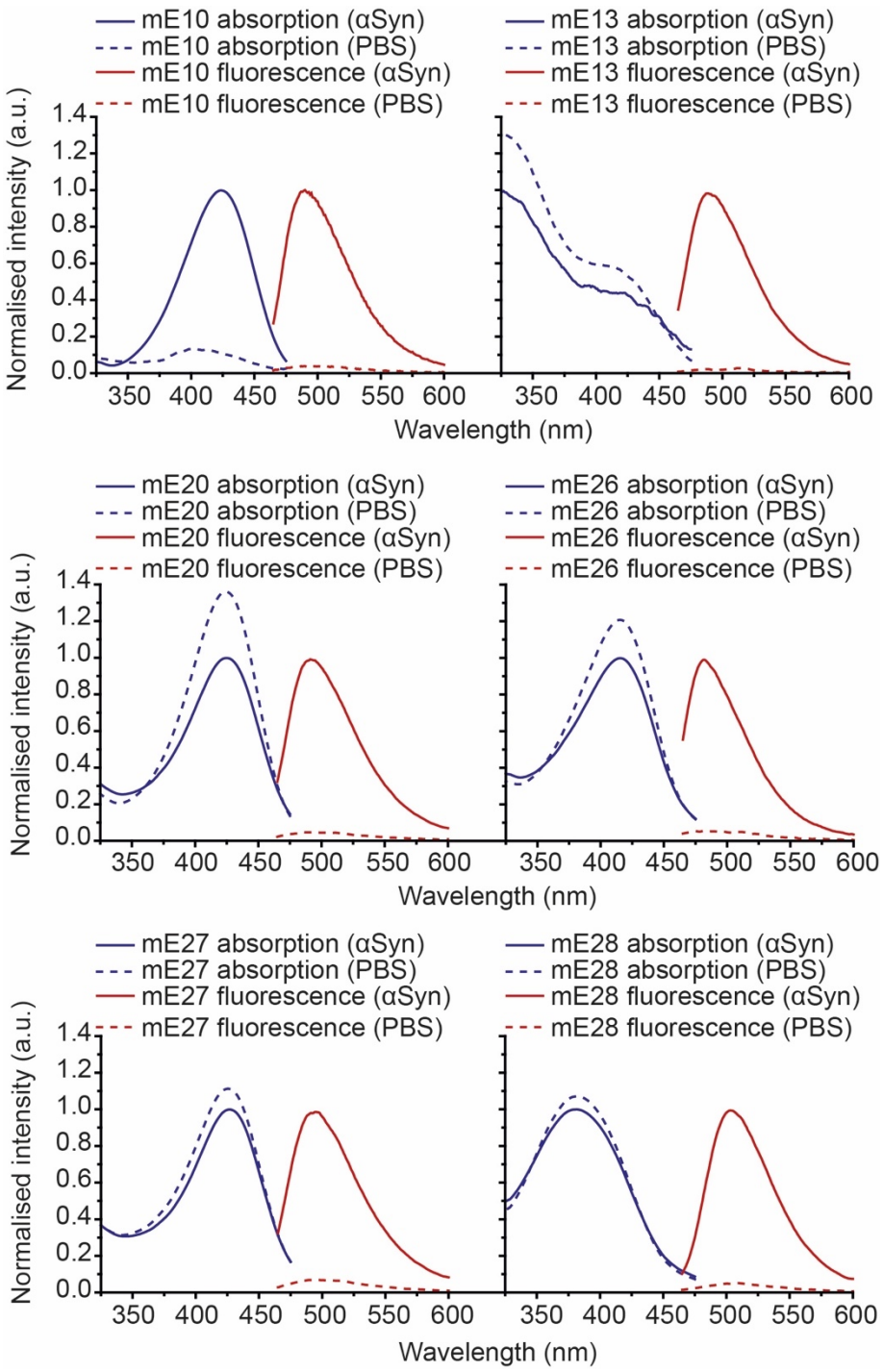

Figure 5.4. Bulk UV-vis absorption (blue lines) and emission spectra (red lines) of 10 μM mE dye in PBS (dashed lines) and with ~2 μM recombinant αSyn aggregates (solid lines). The absorption and emission spectra have been independently normalised relative to the maximum intensity of fluorescence of the dye in the presence of αSyn.

mE26 is almost structurally identical to ThT with the exception of the C-1 substituent and the measured λ_{abs1} was 423 nm, 10 nm lower in energy than ThT. mE13 and mE28 both absorbed at wavelengths lower than 400 nm.

Table 5.2. Table of photophysical properties of the mE dyes and ThT. These were obtained from bulk UV-vis absorption and fluorescence measurements of the dyes free in PBS buffer (denoted by subscript 1).

Dye	Structure	λ_{abs1} (nm)	λ_{em1} (nm)	λ_{em1}-λ_{abs1} (nm)	ε_1 ($M^{-1}cm^{-1}$)	Φ_{Fl1}	B_1 (a.u.)	$\frac{B_1^{mE}}{B_1^{ThT}}$
ThT	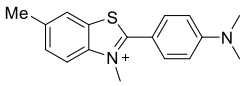	413.0	488.0	75.0	36000	0.00	39.4	1.00
mE10	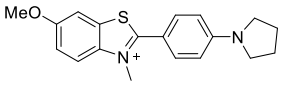	420.0	494.0	74.0	31130	0.04	1245.2	31.60
mE13	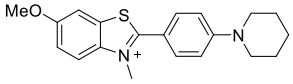	326.0/416.0	511.9	95.9	4394	0.01	43.9	1.11
mE20	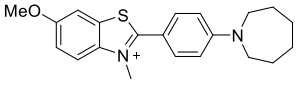	423.0	500.0	76.9	26318	0.03	789.5	20.04
mE26	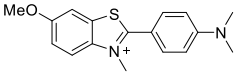	414.0	483.9	69.9	14088	0.02	281.8	7.15
mE27	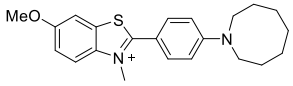	423.0	498.0	68.9	19471	0.05	973.6	24.71
mE28	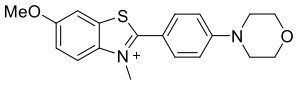	380.0	513.0	133.0	20638	0.03	619.1	15.71

Emission maxima and subsequent Stokes shifts of the mE dyes were similar to ThT as expected. The red-shifted λ_{em1} of the mE's compared to the E dyes was consistent with the anticipated extension of delocalisation following methylation.

The emission peak of mE13 at 512 nm was obtained by excitation at 425 nm, which likely corresponded to the desired species hence λ_{em1}-λ_{abs1} was calculated from that value.

Interestingly, the mE derivatives had poorer absorption capabilities than ThT illustrated by lower ε_1. A comparison of mE26 and ThT is the most informative as they are structurally indistinguishable but for one oxygen atom. ε_1 of mE26 was 2.6 times lower than ThT but was 5.6 times greater than E26. Coupled together these data suggest two things; 1) the methoxy substituent at C-1 negatively influences the oscillator strength, 2) extended degree of conjugation improves oscillator strength as previously discussed. The methoxy substituent is considered a strong electron donator by resonance and has been shown to improve ε in styryl-based TICT molecules with electron withdrawing substituents (225), however these molecules utilise the push-pull approach to modify photophysics. In this model a fluorophore is comprised of an electron donor and acceptor unit at opposing ends of the molecule linked via a π conjugated system (226). The transition dipole moment is subsequently increased, and the fluorophore may occupy a photoinduced CT state. Here the photophysics of the probes are modulated by tuning of these donor and acceptor moieties.

The mE derivatives exhibited at least 10-fold higher Φ_{Fl} than ThT but comparable B_1. Additionally, B_1 of the mEs was at least an order of magnitude less than the corresponding E dye. This further supports the possibility of N-5 methylation impacting relative LE and TICT state energies. The TICT nature of these derivatives makes it complex to definitively isolate the origins of relative differences in photophysical properties. Fluorophores of this kind are known to be highly sensitive to their surrounding environment. Radiative and non-radiative processes are greatly affected by inter- and intramolecular interactions through a multitude of modes. Therefore, interpretation of this data must be considered hypothetical.

5.2.1.2 Solvent dependent optical properties

Substantial work describes ICT and TICT molecules as highly effective reporters of their environment (5, 30, 227, 228). ThT fluorescence emission has, on multiple occasions, been shown to be labile to changes in solvent viscosity and polarity (204, 205, 217). Therefore, the fluorescence response of ThT and a subset of E and mE derivatives ((m)E10, (m)E13, (m)E26) were characterised in different solvents (Figure 5.5, Figure 5.6).

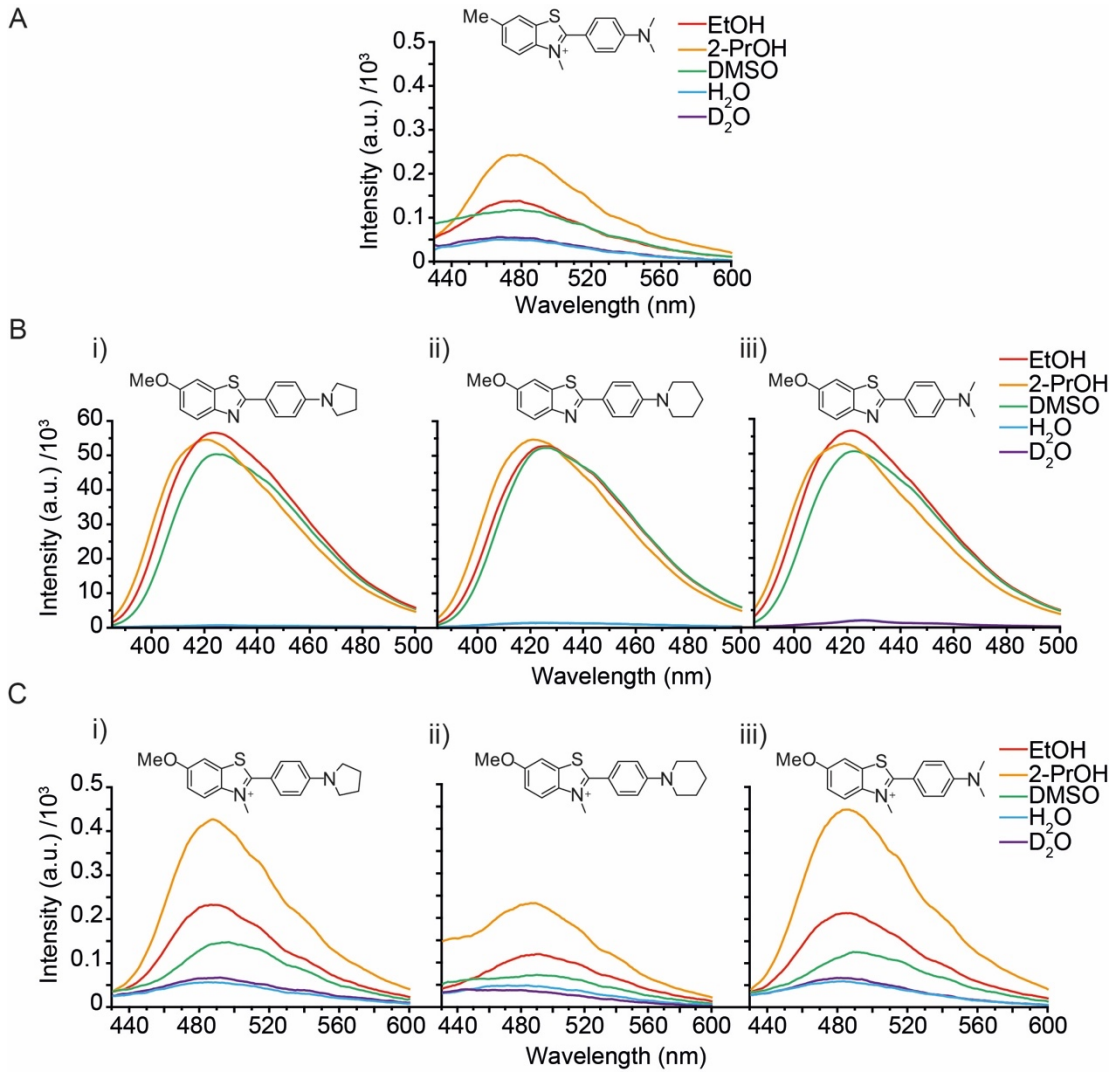

Figure 5.5. Fluorescence emission spectra of 10 µM **A)** ThT, **B) i)** E10, **ii)** E13, **iii)** E26 and **C) i)** mE10, **ii)** mE13, **iii)** mE26 measured in different solvents.

The Lippert-Mataga relationship can be used to describe some features of solvent-dependent emission, primarily spectral shifts, however many complex solvent-solute interactions are not explained by this theory and physical observations often disagree with theory.

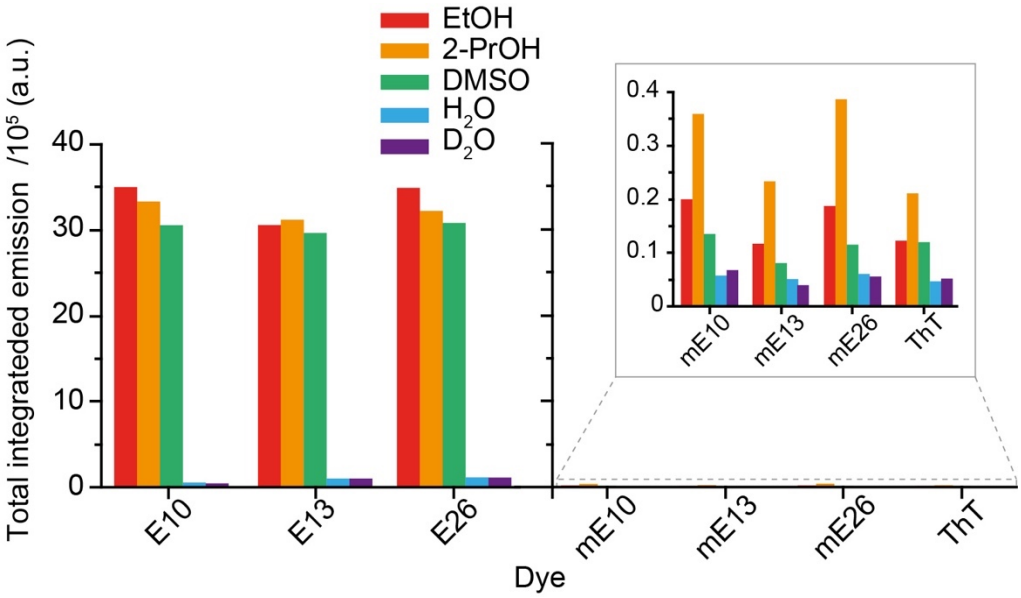

Figure 5.6. Bar graphs illustrating the total integrated fluorescence intensity of the E (left), mE dyes and ThT (right) measured in different solvents.

UV-Vis absorption and fluorescence spectra of the dyes were measured in ethanol (EtOH), propan-2-ol (2-PrOH), dimethylsulfoxide (DMSO), water (H_2O) and deuterated water (D_2O). UV-Vis absorption spectra of the E and mE dyes were unaffected by different solvent properties. This was anticipated as the timescale on which photon absorption occurs is approximately 10^{-15} s, 5 orders of magnitude faster than solvent relaxation (10^{-10} s). The LE state energies and Stokes shifts of E and mE derivatives were largely unaltered by changes in solvent polarity, however there were significant changes in emission intensities (Figure 5.5, Figure 5.6) most notably by the E derivatives. Large increases in the total integrated emission from the neutral E derivatives occurred in an alcohol solvent relative to water (Figure 5.6). In ethanol, increases in emission of 70-fold for E10 and 31-fold for E13 and E26 were measured. The mE derivatives also emitted more photons in alcohol relative to water, however the integrated emission was <100 times lower than the E derivatives in the same

conditions. As ε was unchanged here we can state that the change in total integrated intensity or brightness was a manifestation of an increased Φ_{Fl}, hence a decrease in the non-radiative rate constant.

This observation might be explained by the presence of the TICT excited state. Theoretically, in the event of the formation of two photo-excited states, a LE state without charge separation and an ICT state, polar solvent molecules would stabilise the ICT state to a greater degree than the LE state (227, 229). In this circumstance the ICT state would be lower in energy. On the contrary, less polar solvent molecules would stabilise a homogeneously charged LE state to a greater extent than an ICT state and that would become the lowest energy state. Therefore, the environment may indicate from which excited state ground-state return will occur and in the case of superior TICT state stabilisation, this return would be non-radiative and would manifest in lower fluorescence intensity.

Electrostatic interactions with solvent molecules are likely not the only factor governing the transition from LE to non-radiative states. In accordance with the molecular rotor behaviour, solvent viscosity may also be a contributor. On the contrary if torsional oscillations within ThT were the only physical factor governing Φ_{Fl} it would be expected that in solvents of near 100 % viscosity Φ_{Fl} would be close to 1, however this is not the case (211). To discern the primary cause of the large increase in Φ_{Fl} of the E derivatives in different solvents, we measured the fluorescence of E10 as a function of ethanol and glycerol concentration (Figure 5.7). E10 emission showed a sigmoidal dependence on both variables.

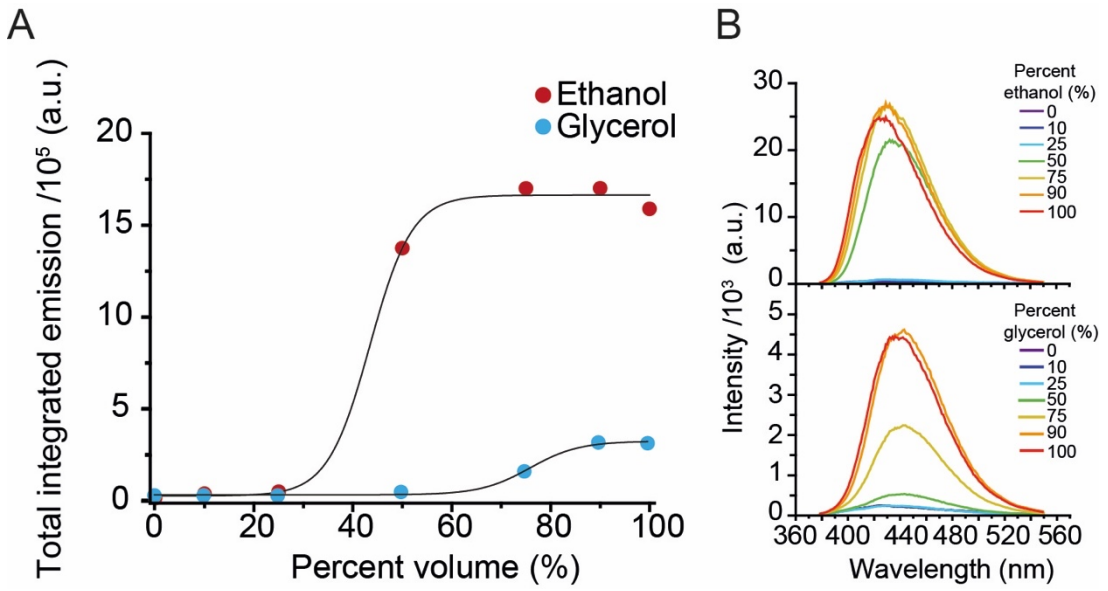

Figure 5.7. **A)** A plot of the total integrated emission intensities of E10 in varying concentrations of either ethanol or glycerol. The data has been fit to a sigmoidal curve with the following equation: $y = \frac{A_1 - A_2}{1 + e^{\frac{(x - x_0)}{dx}}} + A_2$, where A1 and A2 were the maximum and minimum points on the curve respectively. **B)** Fluorescence spectra of E10 in varying concentrations of either ethanol (top) or glycerol (bottom).

The fluorescence of E10 grows rapidly between 25 and 50 % ethanol and reaches saturation at 74 % at which point the integrated intensity was 100-fold greater than 0 % and Φ_{Fl} equal to ~1. Therefore, non-radiative pathways were almost completely deactivated. In glycerol intramolecular torsion was minimised and an accompanying increase in radiative decay observed. However, the E10 fluorescence intensity at 100 % glycerol was 14-fold greater than 0 %, with Φ_{Fl} equal to 0.14, consistent with values measured for ThT in glycerol (211). This implies that inhibition of rotation is not the dominating control of Φ_{Fl} of neutral derivatives of ThT. The measured polarity of glycerol is similar to that of DMSO (230), despite this emission of E10 in glycerol was significantly lower than in DMSO.

These data show that it is not only physical inhibition of the intramolecular twist but also solvent relaxation dynamics that effect the radiative rate. This is significantly more pronounced with the E derivatives which appear to be effective reporters of their environment by Φ_{Fl} changes. Extrapolating this into

amyloid aggregate detection, it could be considered that the fluorescence intensity may not only be indicative of degree of fibrilisation but also properties of the microenvironment in which it is bound. This has been shown with spectrally resolved super-resolution fluorescence microscopy in which the hydrophobicity of aggregates changes during the aggregation process (16).

5.2.1.3 Incorporation into αSyn aggregates

Photophysical characterisation of ThT and derivatives within the context of amyloid binding involves deconvolution of several more complicated effects than those in solvent. Aggregate mixtures are inherently heterogeneous with numerous species capable of binding these probes in multiple manners which are poorly understood (192). We have characterised the bulk binding photophysical properties of ThT, E and mE dyes in the presence of late stage recombinant αSyn aggregates.

Binding affinities

Models describing ThT photophysics detail its sensitivity to changes environment, viscosity in particular. By extension, amyloid aggregates present suitable binding sites in which ThT docks in a more planar conformation leading to an increase in Φ_{Fl}. ThT has been proposed to bind to tyrosine residues in the side chains via a π-stacking interaction in a cavity of similar size to the molecule (231). The affinity of this interaction directly impacts the perceived fluorescence properties; therefore, it is necessary to quantify the binding capabilities of amyloid probes as well as the photophysics.

The binding capabilities of the E and mE dyes to αSyn aggregates was measured with surface plasmon resonance (SPR) spectroscopy (Figure 5.8). In this mode in αSyn aggregates were covalently attached to a surface via an amide bond coupling.

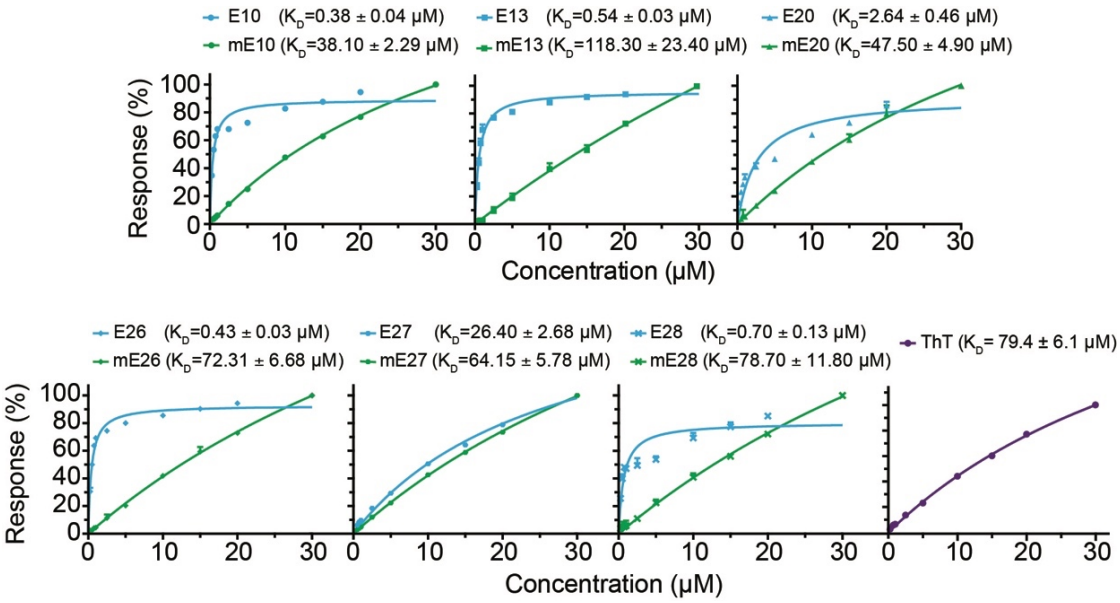

Figure 5.8. Binding affinity data obtained from SPR experiments of the E and mE dyes and ThT binding to αSyn aggregates immobilised onto a surface. The error bars represent the standard deviations from at least replicates of surface conjugation.

The E derivatives were significantly stronger binders to αSyn aggregates than their corresponding mE partners as well as ThT. This was a consequence of N-5 methylation and subsequent +1 charge and is in agreement with current literature comparing methylated and non-methylated benzothiazole compounds (232). Relative solvation energies are thought to determine the superior binding of neutral compared to charged derivatives of ThT (233). The micro-environment in the binding channel imposes a greater stabilising effect on an uncharged, hydrophobic ligand. On the contrary, ionic ligands are more stabilised in their unbound, exterior solvent exposed state. The K_D of ThT has been reported to range from 0.033 to 64 µM (192), the K_D measured in this work was above the upper bound of this range (79.40 ± 6.61 µM). This was likely due to differences in the physical interactions in surface and solution phase methods. During SPR, covalently fixed, heterogeneous protein aggregates (159) are constantly exposed to a solvent flow, whereas more frequently used fluorescence-based measurements (192), are carried out in solution.

At 38.10 ± 2.29 μM, mE10 had the greatest affinity for αSyn of all the mE derivatives as well as ThT. To isolate whether the origin of this superior binding was the result of the methoxy modification compared to the methyl of ThT at C-1, the affinities of ThT and mE26 can be compared. mE26 has a K_D of 72.31 ± 6.68 μM, similar to ThT. This implies that any possible additional electrostatic interactions introduced by the oxygen did not affect the affinity towards αSyn. It is therefore likely that the origin of the superior binding capabilities of mE10 were steric.

Literature evidence supports the possibility that E and mE derivatives may occupy idiosyncratic sites on the aggregates; hence comparative interpretation of absolute values of affinity should be cautious. However, these data taken together with spectral characterisation provides a more complete framework to understand the structure-function relationship of these probes.

Bulk optical properties

ThT and, in all cases, the E and mE derivatives showed a reduction in Stokes shift upon αSyn incorporation. This observation may be indicative of inhibition of molecular rotation and TICT or changes in the surrounding micro-environment of the dye. However, solvent dependent emission data presented in section 5.3.1.2 indicated that excited and ground state energies were independent of solvent environment. A conformationally locked fluorophore would no longer undergo excited state geometric relaxation; therefore, emission would occur from a higher energy vibrionic state. This data is in agreement with current models that describe the origins of Φ_{Fl} increase of ThT upon amyloid incorporation (216). In fluorescence spectroscopy and microscopy high Stokes shifts are desirable as filtering of interfering excitation light can be optimised to maximise signal collection. In fluorescence bioimaging, fluorophore emission at the near infra-red region of the visible spectrum are generally preferred due to the lower quantity of naturally occurring red emitting chromophores resulting in significantly less endogenous auto-fluorescence at these wavelengths (159).

Table 5.3. Table of photophysical properties of the E dyes and ThT. These were obtained from bulk UV-vis absorption and fluorescence measurements of the dyes in the presence of 2 μM αSyn aggregates (denoted by subscript 2).

Dye	Structure	λ_{abs2} (nm)	λ_{em2} (nm)	λ_{em2}-λ_{abs2} (nm)	ε_2 ($M^{-1}cm^{-1}$)	Φ_{Fl2}	B_2 (a.u.)	$\frac{B_2^E}{B_2^{ThT}}$
ThT	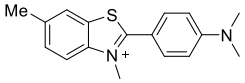	414.0	483.0	69.0	25283	0.24	6067.0	1.00
E10	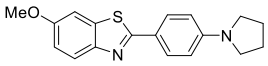	367.0	424.9	57.9	1800	0.04	72.0	0.01
E13	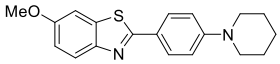	330.0	424.9	94.9	3300	0.08	264.0	0.04
E20	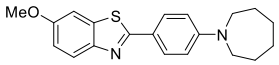	373.0	426.9	53.9	3100	0.05	155.0	0.03
E26	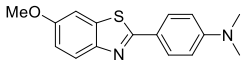	305.0	428.9	123.9	2000	0.11	220.0	0.04
E27	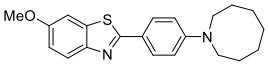	374.0	430.9	56.9	1100	0.09	99.0	0.02
E28	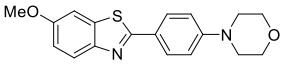	320.0	426.9	106.9	4300	0.04	172.0	0.03

The differences in ε at λ_{abs} of the mE derivatives upon αSyn binding are difficult to interpret. There was a decrease in ε relative to that in PBS of all mE dyes with the exception of mE10. On the contrary, all E derivatives improve as photon absorbers except E10 which remained unchanged. The conformation the dyes adopt when they dock onto an aggregate may account for this. However, this scenario is complex and there is insufficient information known to attribute a cause.

Table 5.4 Table of photophysical properties of the mE dyes and ThT. These were obtained from bulk UV-vis absorption and fluorescence measurements of the dyes in the presence of 2 μM αSyn aggregates (denoted by subscript 2).

Dye	Structure	λ_{abs2} (nm)	λ_{em2} (nm)	λ_{em2}-λ_{abs2} (nm)	ε_2 ($M^{-1}cm^{-1}$)	Φ_{Fl2}	B_2 (a.u.)	$\frac{B_2^{mE}}{B_2^{ThT}}$
ThT	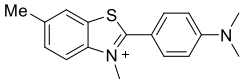	414.0	483.0	69.0	25283	0.24	6067.0	1.00
mE10	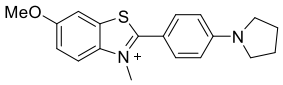	421.0	490.0	69.0	33107	0.81	31590.0	5.21
mE13	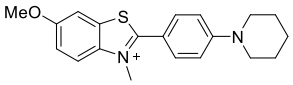	326.0/422.0	491.0	69.0	7700	0.30	2310.0	0.38
mE20	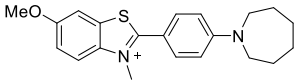	424.0	495.1	71.1	26400	0.61	16104.0	2.65
mE26	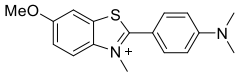	420.0	483.0	63.0	14000	0.26	7070.0	1.17
mE27	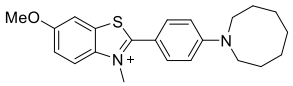	432.0	491.9	66.1	20300	0.69	14007.0	2.31
mE28	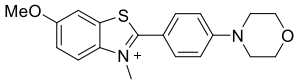	382.0	506.0	124.0	17000	0.58	9860.0	1.63

The primary large-scale photophysical response of aryl-benzothiazole probes to amyloid aggregates is an increase in Φ_{Fl}. ThT had a measured Φ_{Fl2} of 0.24 in this work, a 1000-fold increase from Φ_{Fl1}. The E and mE derivatives also displayed this property. The N-5 methylation elicits not only a lower Φ_{Fl1} but also a higher Φ_{Fl2} evidenced by comparison between E and mE derivatives.

The changes in Φ_{Fl} (Figure 5.9) of the E and mE dyes were not as substantial as ThT. mE13 showed the greatest increase of 30-fold to a Φ_{Fl2} of 0.30 ± 0.04. After mE13, mE10 showed the next highest change in Φ_{Fl} of 21-fold, however mE10 also displayed the highest Φ_{Fl2} of 0.81 ± 0.13. This was interesting as mE10 also showed the greatest binding potential of the mE dyes (Figure 5.8). Moreover, mE10 has exhibited superior binding and photophysical properties when compared to ThT, the current gold-standard in amyloid dyes, in the same conditions.

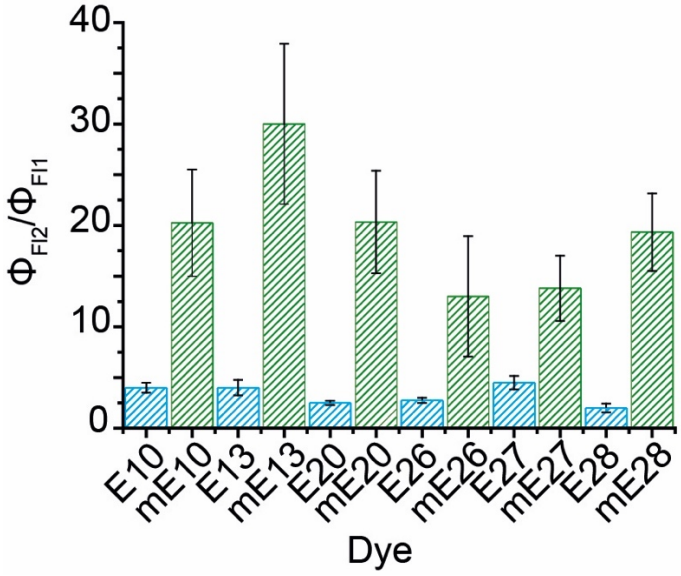

Figure 5.9. Bar graph illustrating the fold change in Φ_{Fl} of the E and mE dyes upon binding to αSyn aggregates. The error bars represent the propagated standard deviations of results obtained from three separately prepared dye samples.

This finding incited enquiry into a correlation between binding affinity and Φ_{Fl2}, which was uninformative. However, a comparison of the binding constants and Φ_{Fl2} of mE derivatives with C-15 substituted N-heterocyclic rings showed a linear dependence (weaker binding resulted in lower Φ_{Fl2}). The opposite was true for the E derivatives (stronger binding resulted in lower Φ_{Fl2}). With only four dyes in each category to make this comparison, more data would be required to make informative conclusions. Albeit this may be further evidence to support

the occupation of different binding sites by neutral and charged aryl-benzothiazole amyloid stains.

Furthermore, there was no correlation between N-heterocyclic ring size and Φ_{Fl2} of both E and mE dyes (Figure 5.10). The relationship between Φ_{Fl1} and ring size was preserved following aggregate incorporation, suggesting minimal steric hindrance affecting the fluorescence. There are several factors which may affect the Φ_{Fl} of these photophysically complex molecules. It has been long understood that solvent-solute H-bonding with dimethyl aniline substituted molecules induces conformational torsion in the ground state (234, 235), specifically to ThT, in aqueous solution the H-bonding of the dimethylaniline with water molecules induces a rotation about the Me_2N-Ph bond. In turn, this physical effect coupled with TICT significantly reduces the achievable Φ_{Fl}. Peripheral factors such as formation of non-covalent bonds with residues may have significant effect on the photophysical properties of these dyes.

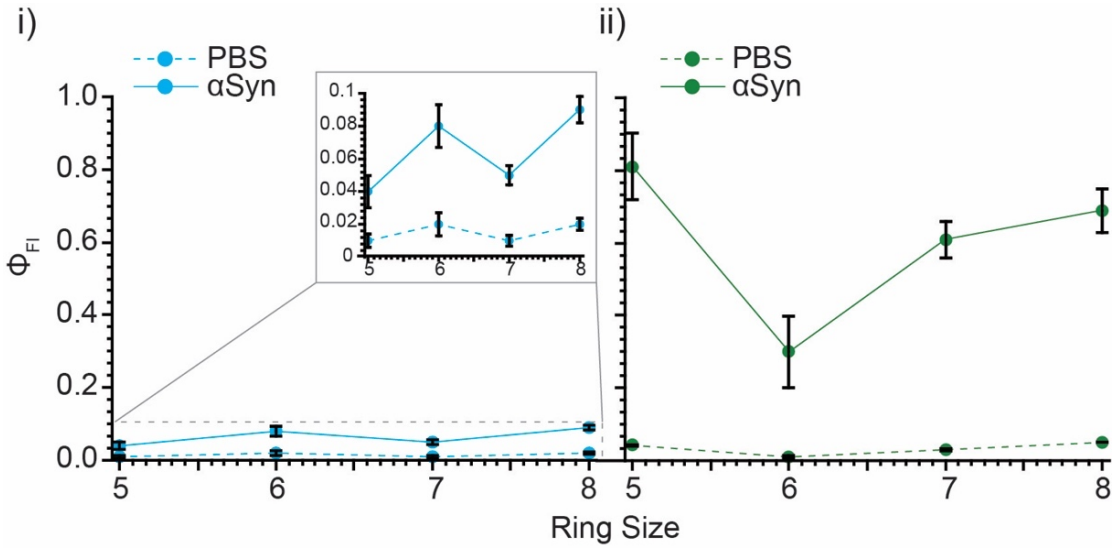

Figure 5.10. Plot of Φ_{Fl} against the N-heterocyclic ring size of the C-14/15 substituent on **i)** E and **ii)** mE dyes. The rings are composed of 5,6,7 and 8 atoms corresponding to (m)E10, (m)E13, (m)E20 and (m)E27 respectively. The error bars represent the propagated standard deviations of results obtained from three separately prepared dye samples.

Intensive study of probe responses to different environments will allow researchers to establish more complete insights about biomolecules. There is

much that is still unknown about amyloid proteins (236). The heterogeneity of aggregate mixtures, synthetic and pathological, enforces the need for them to be studied at high resolution.

5.2.2 Single aggregate fluorescence imaging

Certain photophysical properties of ThT coupled with suitable instrumentation make it an incredibly useful tool to observe amyloid with single-aggregate resolution. The characteristics of ThT described in sections 5.3.1.1 and 5.3.1.3 enabled researchers to design the SAVE method to detect individual β-sheet containing species both *in vitro* and in the cerebral spinal fluid of healthy and Parkinson's disease patients (159). Despite this advance, ThT remains a poor single-molecule fluorophore. For SAVE to fulfil its potential as an early diagnostic technique for neurodegenerative disease superior fluorophores are required. The development of such dyes would reduce the confidence interval at which patients are determined pathological, as well as allowing imaging in high-background samples such as blood plasma.

The bulk spectral characterisation of the complete library of ThT analogues (E and mE) in this chapter led to the selection of a subset with the potential to replace ThT as the gold-standard amyloid dye. Fluorescence emission of three E (E10, E13 and E26) and three mE (mE10, mE13 and mE26) derivatives along-side ThT were characterised with SAVE imaging (159). Figure 5.11 shows the SAVE images of ThT, E and mE dyes as well as intensity versus time plots of the dyes on single αSyn aggregates. The images show the emission of the dyes bound to late-stage recombinant aggregates of αSyn. The aggregation sample used in these experiments were from the same preparation of those used in the bulk characterisations. All measurements were taken together, and sample preparation was the same, therefore consistent surface coverage between imaging samples may be presumed.

Despite low Φ_{Fl2} values (<0.1), single late-stage αSyn aggregates were visualised with E dyes. Additionally, the dyes were excited with 405 nm light, red-shifted relative to their absorption maxima. A constant level of ThT

fluorescence intensity over time was observed, consistent with previously shown data (159). The mE derivatives showed the same fluorescence intensity profiles, however, the E derivatives showed decreasing fluorescence intensity with time. These observations may be ascribed to higher association constants of the E dyes towards αSyn aggregates and therefore increased binding times.

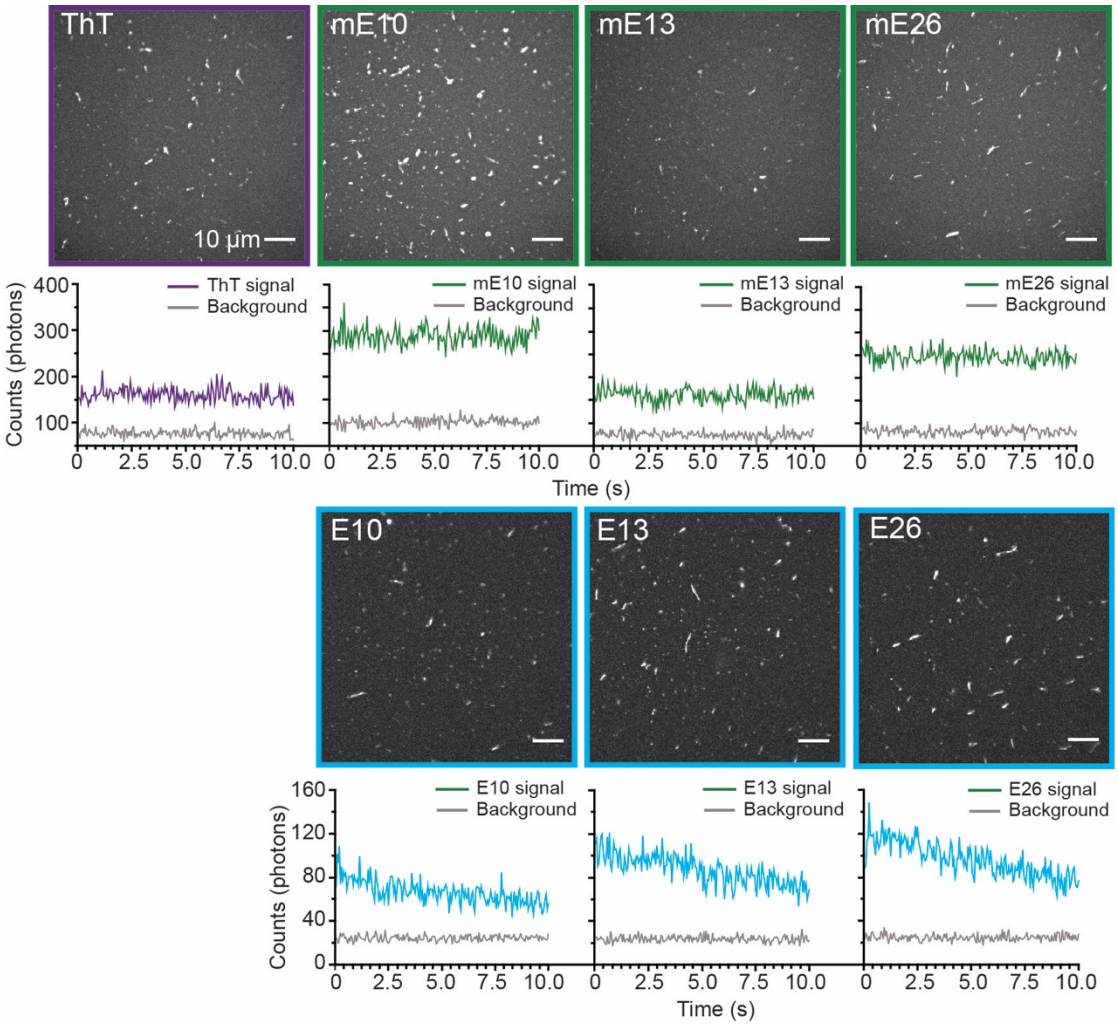

Figure 5.11. Single-aggregate TIRF images of 5 µM ThT (purple), mE dyes (green) and E dyes (blue). Underneath each image is a representative plot of the signal and background photons detected over time from a single aggregate. Scale bar= 10 µm.

Figure 5.12 shows histograms of the mean number of photons detected across a single aggregate for each dye during the 10 s acquisition time. The number of photons detected from ThT was 94000, which corresponds well with the

number of ThT photons detected in *in vitro* SAVE experiments performed by Horrocks and Lee *et al.* During a 5 s acquisition they detected a mean of 40000 photons from ThT at the same concentration (5 μM). mE26 and mE13 emitted a similar number of photons to ThT, 97000 and 92000 photons were detected for mE26 and mE13 respectively. The photon counts produced by E derivatives were approximately a third of those from the methylated counter-parts. The number of photons detected from E10, E13 and E26 were 38000, 34000 and 33000 respectively.

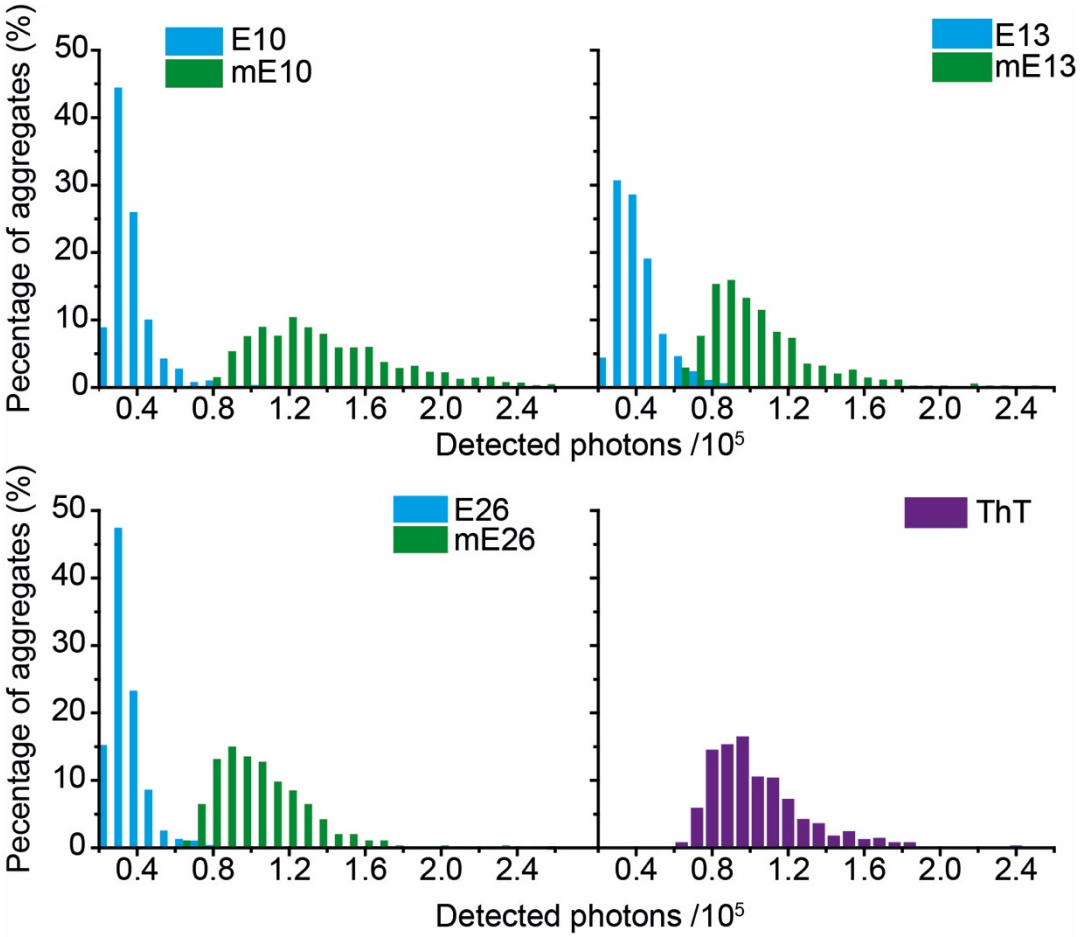

Figure 5.12. Histograms illustrating the number of photons detected from the E and mE dyes and ThT bound to surface immobilized αSyn aggregates during a TIRF microscopy experiment. The number of aggregates analysed was ≥ 500.

As well as having the highest Φ_{Fl2} of all the dyes at the bulk level, mE10 also emitted more photons in the single-aggregate regime (123000). The photon distribution of mE10 was much broader than ThT and other mE dyes with a

FWHM of 82000 photons, this may suggest that mE10 is capable of detecting a greater distribution in species than ThT and other mE dyes. Qualitatively, the raw images also allude to this possibility (Figure 5.11), however further characterisation would need to be performed to confirm this.

5.3 Conclusions and Future work

ThT is, at present, the gold-standard for the fluorescence detection β-sheet containing amyloid species. Despite this, the photophysical properties are far-from desirable for use in single-molecule fluorescence imaging and furthermore cellular and bio-fluid samples. The utility of single-molecule methods is paramount in this context as the diversity of aggregate species cannot be determined by bulk methods alone. In addition to this the potentially cytotoxic oligomeric species are rare and unobservable in the ensemble. The work in this chapter described the bulk photophysical characterisation of a completely new library of aryl-benzothiazole based fluorophores. The primary goal of this work was to understand the relationship between chemical structure and photophysical function in the setting of neurodegenerative research.

The catalogue of dyes consisted of two categories, the neutral E and nitrogen methylated, cationic mE derivatives. These molecules were structurally identical, with the exception of the methyl, also present on ThT, and were therefore comparable. There were several key differences in properties between the E and mE derivatives in solution, including energies of maximum absorption and emission, molar absorptivity constants and affinity for αSyn aggregates.

Both the E and mE compounds behaved as molecular rotors, as ThT, evidenced by large Stokes shifts, low Φ_{Fl} in solution (<0.1) and a positive change in Φ_{Fl} following amyloid incorporation. The E dyes had low ε (<10,000 $M^{-1}cm^{-1}$) but binding affinities of approximately 2-orders of magnitude higher than their mE counterparts. They were also highly sensitive to changes in the polarity of their environment; E10 had a Φ_{Fl} of 0.01 in aqueous solution which

increased 100-fold to near unity in 100 % ethanol. There were small increases in Φ_{Fl} of the E dyes in the presence of aggregates of αSyn. They were able to be used in a fluorescence imaging mode to detect single αSyn aggregates with a mean photon output of around 30000. The mE derivatives also had low Φ_{Fl} in aqueous buffer, similar to the E dyes, but underwent a large-scale increase of Φ_{Fl} upon incorporation into αSyn aggregates.

Most interestingly, taken together, all data indicate mE10 performs better as an αSyn stain than ThT. At the bulk level mE10 had a Φ_{Fl} of 0.81, 3.4 times higher than ThT. mE10 bound to αSyn aggregates twice as well as ThT, with K_D values of 38.1 and 79.4 μM respectively. Finally, at the single-aggregate level 123000 photons were detected from mE10 as opposed to 94000 from ThT.

This work may continue down two potential avenues. The first would involve further characterisation of mE10 against ThT as a possible superior amyloid dye. This would include observing the bulk kinetics of a recombinant protein aggregation to elucidate whether the better photophysics of mE10 allow for earlier aggregate detection on the bulk level. Following on from this the same experiment may be carried out at the single-aggregate level simultaneously with another dye known to bind early aggregates such as the oxazone Nile Red (16). Should this work yield positive results additional characterisation with other proteins known to form amyloid and associated with neurodegeneration such as Tau, and amyloid-β should be carried out. Alternatively, continual modification of chemical functionalities of this dye catalogue to gain more understanding of the structure-function relationship. Specifically beginning with modification of the electron acceptor and electron donor capacities of substituents at C-1 and C-14/15. Alteration of non-linear optical properties may improve properties such as Stokes shift and environmental sensitivity. Additionally, the modification of functional groups to improve binding affinities, aiming to be able to detect early aggregates. Work by Klingstedt, *et al.* has suggested the requirement for this class of probe to be conformationally flexible

to satisfy heterogeneous binding requirements; this premise would be investigated in relation to derivatives of ThT. The result of the successful conclusion of this second avenue of research would involve the development of a molecular rotor fluorophore with moderate-high affinity for aggregates, single-molecule capabilities and the ability to report information on not only the presence of β-sheets but the conditions of the nano-environment in which it is bound.

Chapter 6 Bifunctional Fluorescent Probes: Detection of Amyloid and Hydrogen Peroxide

The results presented in this chapter represent work in publication 1 listed in the Publications section.

6.1 Overview of this chapter

As reviewed in Chapter 5, aryl-benzothiazole based fluorescence reporters such as **Thioflavin T** (ThT) are frequently used to identify the **β-sheet** containing mis-folded protein species that are pathological hallmarks of neurodegenerative diseases (Figure 6.1A). In this mode, detection of amyloid aggregates is achieved through a significant fluorescence turn-on. The functionality of aryl-benzothiazole probes occurs as a result of an alteration of the excited state conformation of the dye when immobilised within β-sheets. Fluorescence methods have been shown capable of detecting the intermediate oligomeric species of the Parkinson's disease associated protein α-Synuclein (αSyn) (159) and Alzheimer's linked 42 amino acid peptide Amyloid-β ($A\beta_{42}$) (197). There is mounting evidence that these rare species are associated with cellular toxicity in these diseases (195, 196, 237, 238)

Oxidative damage is a result of an imbalanced equilibrium between antioxidants (239, 240) and the interaction between protein aggregates and oxidative stress in neurodegenerative disease is bidirectional. Oxidative stress stimulates aggregation of proteins such as αSyn whilst the misfolding of αSyn generates oligomeric species associated with high levels of ROS such as H_2O_2 (239). There are copious amounts of intracellular H_2O_2 and it plays a significant role in cell signalling processes. Its chemical stability, compared to other ROS,

results in high concentrations *in vivo*. This relationship incentivises the need for a bifunctional sensor capable of localising and characterising the presence of these potentially disease-causing species simultaneously.

This work describes the design and characterisation of four new fluorescent probes that represent the successful combination of established methods to create a novel strategy for the concomitant fluorescence detection of αSyn aggregates and H_2O_2 (Figure 6.1B).

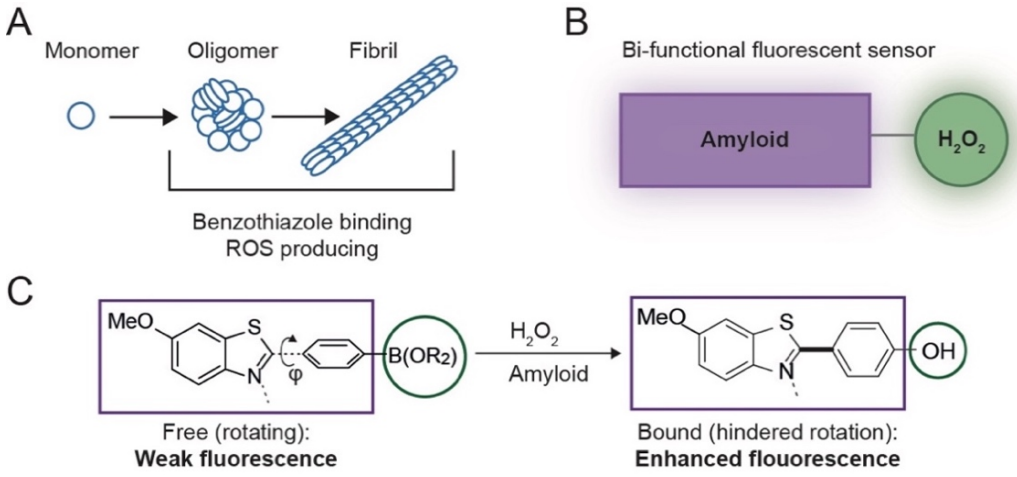

Figure 6.1. **A)** Protein misfolding pathway of amyloid fibril formation. **B)** Concept of the bifunctional fluorescence sensor design. **C)** Molecular structure of the bifunctional fluorescence sensors. The aryl-benzothiazole core for amyloid binding and the boronate ester for reaction with H_2O_2.

A general **bifunctional fluorophore** capable of responding to both amyloid aggregates and H_2O_2 via a change in intrinsic photophysics has been devised. This was achieved by functionalising an aryl-benzothiazole chromophore with a boronate ester unit for amyloid and H_2O_2 detection respectively (Figure 6.1C).

All four probes, **BE01, BE02, mBE01 and mBE02** (Figure 6.2A), have an aryl-benzothiazole core based on either PiB, which has a net charge of 0 and no methylated nitrogen, or ThT, which is singly positively charged due to the

methylated nitrogen. The dyes were substituted with either a tetramethyl-dioxaborolane (BE01, mBE01) or dimethyl-dioxaborinane (BE02, mBE02) group. BE-Ox and mBE-Ox (Figure 6.2B) result from the oxidation of the aryl boronate ester groups of the neutral BE and mBE dyes respectively.

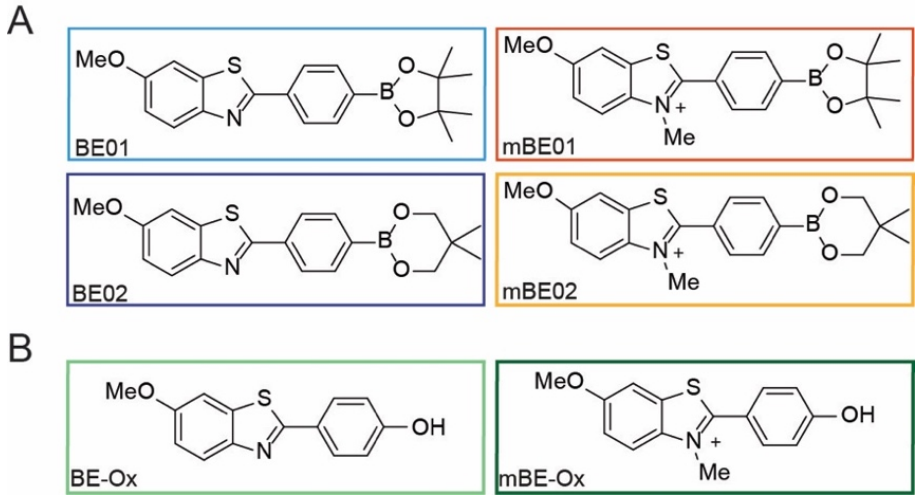

Figure 6.2. **A)** Molecular structures of the four bifunctional fluorescence sensors evaluated in this chapter. Neutral dyes BE01 and BE02 and methylated, charged dyes mBE01 and mBE02. **B)** Molecular structures of the dyes after oxidation of the boronate ester to the hydroxyl group by H_2O_2. The neutral oxidised dye is BE-Ox and the charged, methylated oxidised dye is mBE-Ox.

The remainder of this chapter will describe the characterisation and application of the novel probes using both bulk and single-molecule methods. The complete characterisation of the dyes toward their suitability for *in vitro* sensing of late-state αSyn aggregates and H_2O_2 independently as well as simultaneously will be discussed.

6.1.1 Contributions

Synthesis was performed by James Fyfe, Omaru Kabia and Dr. Dung Do. αSyn was purified by Ewa Klimont. αSyn fibrils were prepared by Dr. Margarida Rodrigues. Cell viability experiments were performed by Dr. Yu Zhang. Surface

plasmon resonance (SPR) binding affinity, liquid chromatography mass spectrometry (LCMS) measurements and analyses were performed by Judith Weber. I performed the bulk fluorescence, absorption and fluorescence imaging experiments and analyses.

6.2 Results and Discussion

6.2.1 Bulk Properties of the Dyes

6.2.1.1 Optical properties

In order to understand the fundamental photophysical behaviour of these fluorophores the bulk fluorescence (Figure 6.3) and absorption spectra of the BE and mBE dyes were measured in PBS buffer and compared to ThT as the photophysics have been well studied (206, 207, 217).

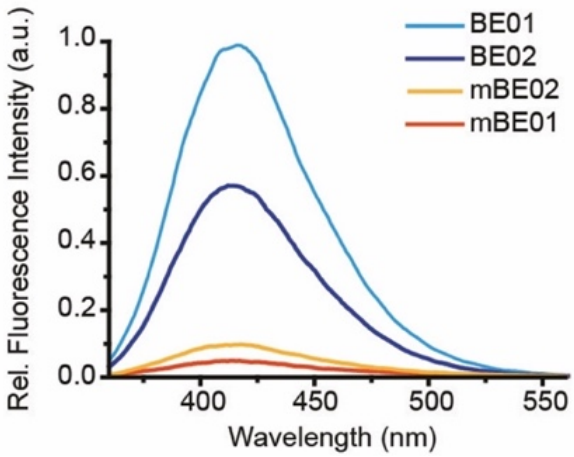

Figure 6.3. Fluorescence spectra of 5 µM BE and mBE dyes in PBS. Spectra are shown at intensities relative to the maximum intensity of BE01 λ_{ex}= 330 nm.

The optical properties extracted from these measurements are shown in table 6.1 and include wavelengths of maximum absorption (λ_{abs}) and emission (λ_{em}), Stokes shift, molar extinction coefficient (ε), fluorescence quantum yield (Φ_{Fl}) and total integrated emission or brightness (B), which were extracted and calculated using the same methods described in Chapter 3.

The Φ_{Fl} of the BE and mBE dyes in PBS were minimal (<0.05). However, the BE dyes were more effective emitters than the mBE dyes in this mode, which correlated with the studies of ThT derivatives presented in Chapter 5. Likewise, in this case it may be that the methyl-group reduces the energy discrepancy between the locally excited (LE) singlet state and the non-emissive twisted intramolecular charge transfer (TICT) state.

Table 6.1. Photophysical properties of BE, mBE dyes and ThT in PBS.

Dye	λ_{abs1} (nm)	λ_{em1} (nm)	Stokes Shift (nm)	Φ_{Fl1}	ε_1 ($M^{-1}cm^{-1}$)	B_1 ($M^{-1}cm^{-1}$)
BE01	330	416	86	0.06	6400	390
BE02	330	412	82	0.04	4200	172
mBE01	330	417	87	0.01	16800	174
mBE02	330	417	87	0.01	14800	152
BE-Ox	325	406	81	0.08	12700	1059
mBE-Ox	328	416	88	0.04	20500	782
ThT	412	486	74	0.00	37500	15

All probes had λ_{abs} in the ultraviolet region at 330 nm and there was no red-shift from neutral to cationic dye suggesting that the extent of electron delocalisation has not been altered by the methylation. This was likely due to the Lewis acid character of the boron substituent. Interestingly, there was negligible change in absorption or emission energies from the boronate ester to the hydroxyl functionalities.

Both λ_{abs} and λ_{em} of BE-Ox was hypsochromically shifted relative to the BEs by 5 and 6-10 nm correspondingly. The λ_{abs} and λ_{em} of ThT is red-shifted relative to the mBEs and mBE-Ox. This data coupled with the similarity of λ_{abs} and λ_{em} values between mBEs and mBE-Ox suggests that modification of the phenyl functional group has very little influence on ground and excited state energies. Alteration of the substituent at carbon-1 on the benzothiazole ring may have more bearing on this.

The calculated ε of 6400 and 4200 $M^{-1}cm^{-1}$ for BE01 and BE02 compared well with those of other novel boronate ester based fluorophores (158). Similar to the ThT derivatives presented in Chapter 5, the methylated congeners were more effective absorbers; hence it is likely that addition of the positive charge increases the oscillator strength hence the efficiency of transition from the singlet ground to excited state. Phenol functionalised BE-Ox and mBE-Ox had greater ε values (BE-Ox=12700 and mBE-Ox=20500 $M^{-1}cm^{-1}$) compared to BE and mBE. In this context one of the most significant quantifiable properties considered is the total integrated emission intensity of a fluorophore and conventionally this is optimal when maximised. However, in this particular approach the BEs and mBEs are optimal if the B_1 is minimised as this will improve contrast when the dyes sense changes in their environment. The contrasting magnitudes of ε and Φ_{Fl} for the BEs and mBEs resulted in comparable B1 values. BE02, mBE01 and mBE02 were within 20 $M^{-1}cm^{-1}$ of each other; BE01 was ~2-fold brighter. Compared to ThT all four BE and mBE dyes were significantly brighter in solution. ThT had a much larger ε and correspondingly low Φ_{Fl}. This is noteworthy as the dimethylaniline substituent has previously been shown to double ε when compared with a furan (224). BE-Ox and mBE-Ox were at least 5-times brighter than the BEs and mBEs, this quantification infers the potential for these probes in a H_2O_2-sensing life-science application.

6.2.1.2 Cellular Toxicity

In order for the boronate ester dyes to be considered for *in vivo* applications they must be non-toxic to cells over the time course of a typical fluorescence experiment as a minimum requirement. Therefore, the cellular bio-toxicity of the probes were assessed using a standard trypan blue cell-death assay (Figure 6.4) The cells were treated with the dyes and incubated for 24-hours and cell viability was >90 % in all cases as determined by Equation 6.1.

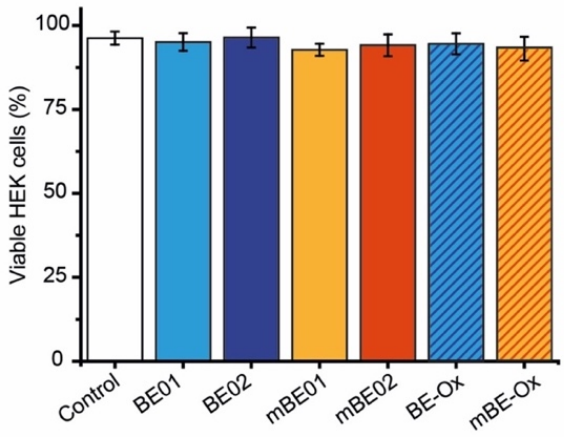

Figure 6.4. Bar graph illustrating percentage of viable HEK293 cells after a 24-hour treatment with BE and mBE probes

6.2.1.3 ROS Sensing

Characterisation of the optical properties of the BE and mBe probes highlighted their modest fluorescence (low Φ_{Fl} and ε), these traits are desirable in this approach of species detection via fluorescence turn-on. The abilities of the BEs and mBEs to respond to H_2O_2 with a change in emission properties was evaluated with bulk fluorescence spectroscopy. Initially, the probes responses were characterised following addition of 100 μM H_2O_2, a physiologically realistic concentration in a cellular environment undergoing oxidative stress (241). An immediate increase in the fluorescence intensity of all the BE and mBE probes was observed following the addition of H_2O_2 (Figure 6.5A, Figure 6.6) to

differing extents. BE01, BE02. mBE01 and mBE02 showed 1.5, 1.1, 15.4 and 3.3-fold increases respectively approximately 0.1 minutes after the addition of H_2O_2.

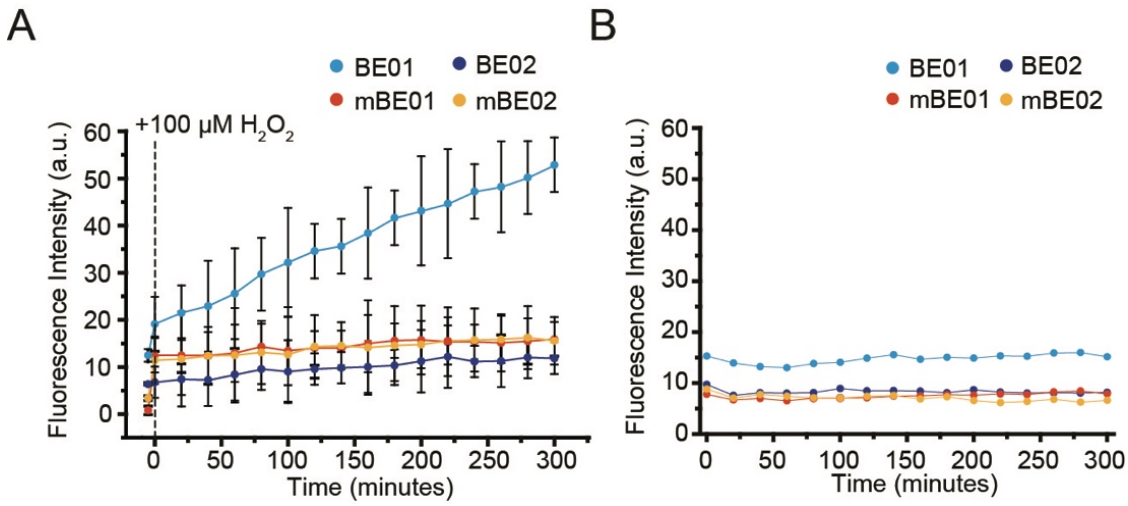

Figure 6.5. Fluorescence *vs.* time kinetics of the BE and mBE dyes **A)** upon the addition of H_2O_2 and **B)** in PBS buffer. The vertical dashed line denotes the time-point at which H_2O_2 was added. λ_{ex}= 330 nm.

The kinetics of this reaction were followed for a 5-hour period in which the probes emission intensities continued to increase in a linear regime at differing rates with positive gradients (BE01= 0.112 ± 0.002 minutes^{-1}, BE02= 0.017 minutes^{-1}, mBE01= 0.011 minutes^{-1}, mBE02= 0.015 minutes^{-1}). At the final time point the relative change in fluorescence intensities were 4.2, 1.9, 19.6 and 4.6-fold for BE01, BE02. mBE01 and mBE02 respectively. The oxidation reaction was irreversible therefore the sensors recorded the total exposure to the system rather than an equilibrium value making boronate-ester based probes suitable for H_2O_2 quantification. To confirm that the change in fluorescence occurred as a result of oxidative cleavage of the boronate ester, the dyes were analysed by LCMS before and after 60-minute incubation with 100 μM H_2O_2 (Appendix A.2.2, Table A.2.1). These data showed conversion of BEs and mBEs to BE-Ox and mBE-Ox to different extents (BE01=100 %, BE02= 90 %,

mBE01= 73 % and mBE02= 88%). This conflicts with the fluorescence data as the emission intensity of BE01 with H_2O_2 continued to increase over 300 minutes without reaching saturation. In addition, the emission intensities of BE01 with H_2O_2 at 60 and 300 minutes are 300 and 440 % greater than BE02 with H_2O_2. However, several repeat measurements show significant variability in the kinetics of this reaction which suggests inherent sensitivity to competing processes.

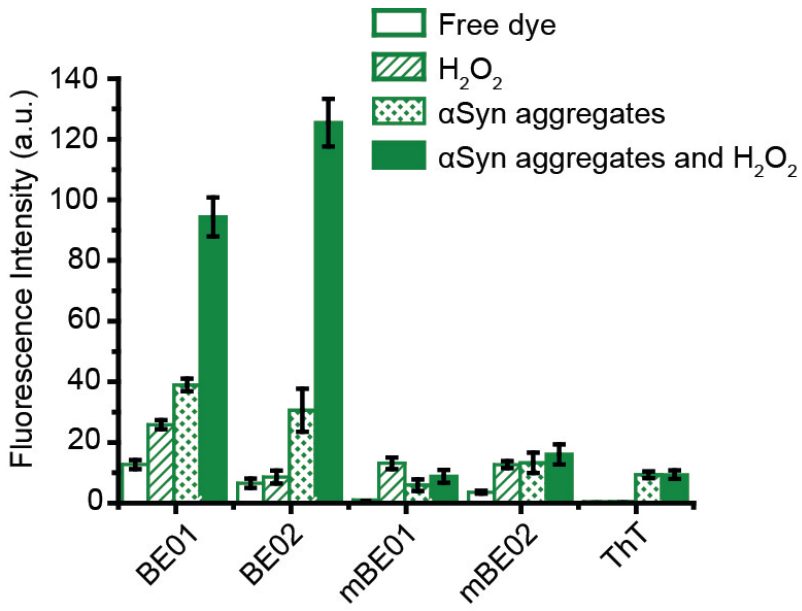

Figure 6.6. Bar graph showing the fluorescence intensities of the BE, mBE and ThT dyes, in PBS buffer, with H_2O_2, with αSyn aggregates and with concomitant H_2O_2 and αSyn aggregates.

It was important to consider the potential for factors competing with H_2O_2 mediated oxidation affecting the fluorescence. It is well understood that photosensitised ROS are produced as a result of the quenching of triplet oxygen by the fluorophore triplet state (242) that may have contributed towards increasing the oxidation potential. Furthermore, LCMS analysis of the dyes with H_2O_2 showed partial *in situ* hydrolysis in aqueous solution (Appendix A.2.2, Table A.2.1). As a control, the fluorescence emission of the BEs and mBEs in

PBS was also measured over the course of 5 hours (Figure 6.5B) and no change in emission intensity of the BE and mBE dyes was observed. Therefore, these extraneous factors could be neglected. The fluorescence of ThT was also measured before and after the addition of H_2O_2 as a further control and as anticipated, due to the lack of ester, the emission was unaffected.

All dyes responded to the presence of <1 μM H_2O_2 with a fluorescence turn-on (Figure 6.7). The fluorescence intensities of BE01 and BE02 increased asymptotically up to 100 μM H_2O_2 at rates of 0.89 s^{-1} and 0.93 s^{-1} (Appendix A.2, Figure A.2.2).

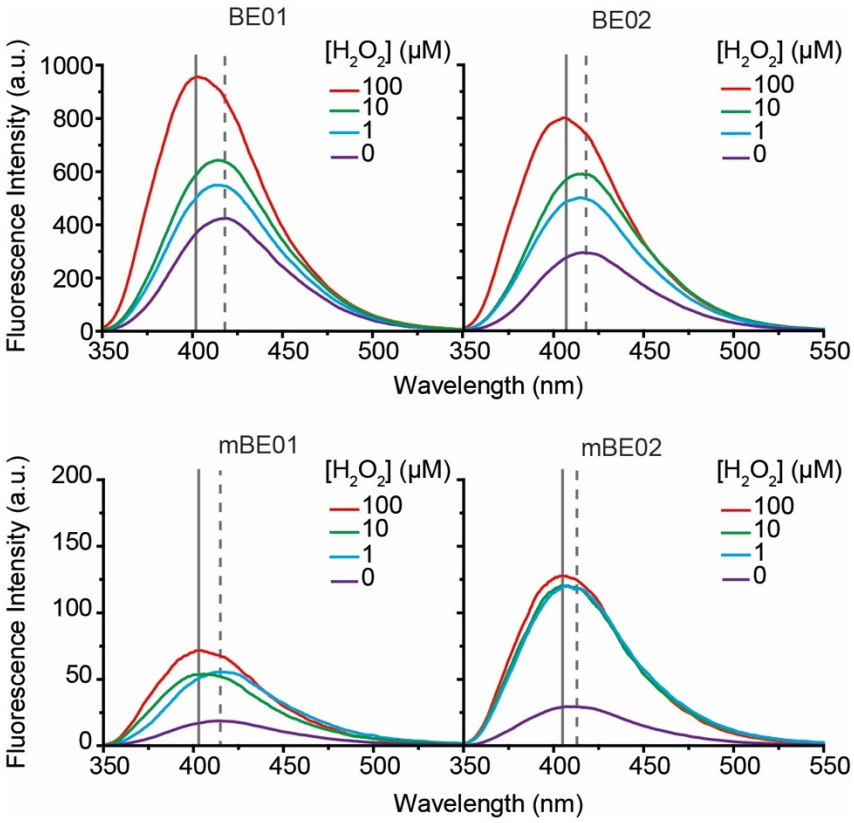

Figure 6.7. Fluorescence spectra of 5 μM BE01, BE02, mBE01 and mBE02 following 5 h incubation with H_2O_2 at concentrations from 0-100 μM. The dashed grey lines represent the maximum emission wavelength at 0 μM H_2O_2 and the solid grey lines denote the maximum emission wavelength at 100 μM H_2O_2. λ_{ex}= 330 nm.

LCMS analysis of the mBEs with 100 μM H_2O_2 showed evidence of the demethylation of 9 and 18 % of mBE01 and mBE02 molecules respectively, which may have contributed to the non-asymptotic fluorescence activation.

The changes in total integrated emission were coupled with a blue spectral shift of 16, 11, 12 and 8 nm for BE01, BE02, mBE01 and mBE02 respectively, suggesting greater ground state stabilisation of the hydroxyl substituted fluorophore by the polar aqueous buffer. These chromatic shifts of λ_{em} were not significant enough to be used as a metric for H_2O_2 identification and as the fluorescence intensities of the mBEs are not clearly quantitative with differing amounts of H_2O_2 these dyes would be poor sensors for H_2O_2 quantification. On the contrary the fluorescence of the BEs increased exponentially with H_2O_2 concentration hence would be capable of determining amounts. The primary disadvantage of the BEs in comparison to the mBEs is the higher intrinsic B_1 which negatively affects the turn-on ratio and therefore the achievable contrast between activated and non-activated fluorophores.

The boronate ester functionality on the BE and mBE dyes provided a mechanism to achieve fluorescence activation via a chemical reaction. Through physical modification of the excited state molecular conformation, the aryl-benzothiazole scaffold of the BE and mBE dyes facilitated another potential pathway to fluorescence activation by non-covalent binding to protein aggregates containing β-sheet tertiary structure. As well as demonstrating H_2O_2 sensing capabilities the BE and mBE dyes responded to the presence of αSyn aggregates with an increase in the fluorescence quantum yield (Φ_{Fl2}, Table 6.2). The mechanism of β-sheet binding was presumed to be analogous to ThT as the responsible aryl-benzothiazole core was preserved. The turn-on ratio is defined as the ratio of the maximum fluorescence intensity of the dye incorporated into aggregates (I_2) relative to the intensity of the dye free in an aqueous buffer (I_1).

Table 6.2. Photophysical properties of BE, mBE dyes and ThT with αSyn aggregates.

Dye	λ_{abs2} (nm)	λ_{em2} (nm)	Φ_{Fl1}	Φ_{Fl2}	B_2 ($M^{-1}cm^{-1}$)	ΔI	$\frac{\Phi_{Fl1}}{\Phi_{Fl2}}$
BE01	330	391	0.06	0.110	704	3.1	1.8
BE02	330	393	0.04	0.140	588	4.8	3.4
mBE01	330	386	0.01	0.013	218	7.1	1.3
mBE02	330	392	0.01	0.022	325	3.8	2.1
ThT	412	479	0.00	0.360	13500	30.8	600.0

Consistent with other analogues of ThT and PiB discussed in this thesis, the turn-on ratio was larger when the probe was methylated and positively charged due to superior quenching of the fluorescence excited state which manifested as very low values of Φ_{Fl1} and I_1. This distinction was not evidenced as clearly with the BE and mBE probes, with turn-on ratios 4-10 times less than ThT (Table 6.2). This was due to the higher Φ_{Fl1} of the BEs and mBEs as B_2 of all four dyes with αSyn was greater than ThT (Table 6.2, Figure 6.8).

The Φ_{Fl} increase as a result of αSyn incorporation was comparable across the four dyes. For BE01 the increase was 2-fold and even greater with BE02 with a 3.5-fold improvement. Φ_{Fl} of mBE01 and mBE02 increased 1.3 and 2.2-fold respectively. However, these were poor relative to ThT which underwent a 610-fold increase in Φ_{Fl} upon addition of αSyn. Positive changes in Φ_{Fl} of up to 3 orders of magnitude have been reported for ThT bound to lysozyme and amyloid-β (Aβ) fibrils (243).

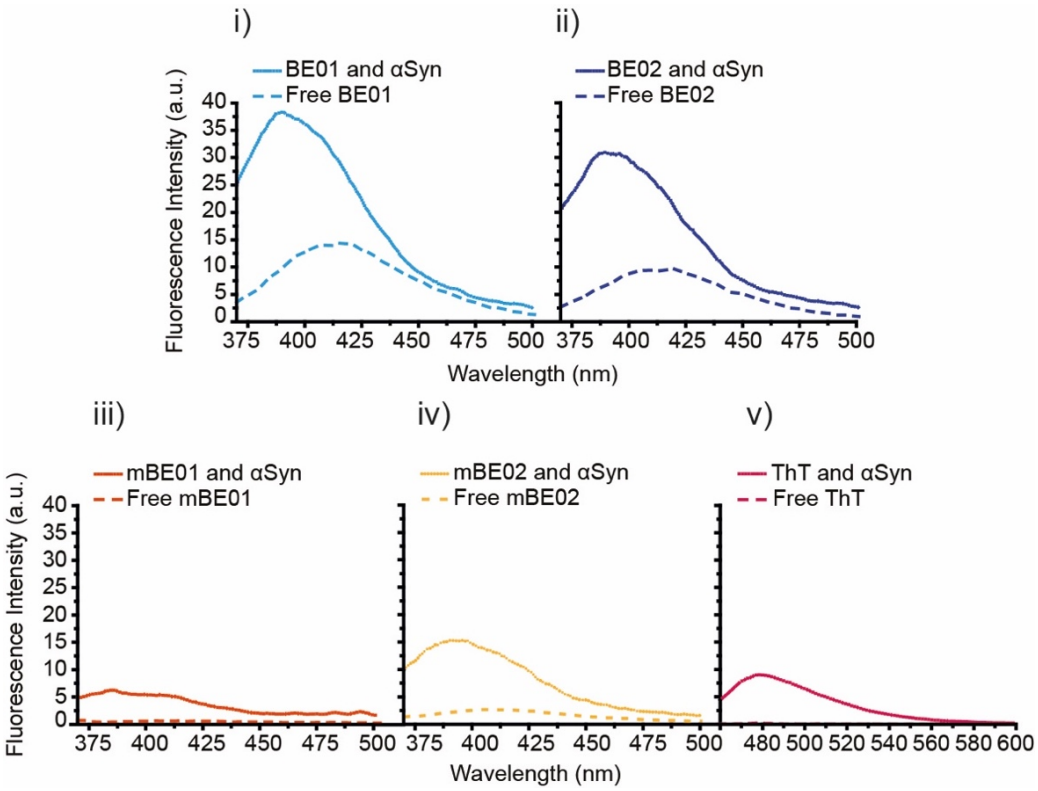

Figure 6.8. Bulk fluorescence spectra of 5 μM **i)** BE01, **ii)** BE02, **iii)** mBE01, **iv)** mBE02 and **v)** ThT free in PBS buffer, with 10 μM αSyn aggregates and with concomitant 10 μM αSyn aggregates and 100 μM H_2O_2. λ_{ex}= 330 nm.

If binding to aggregates effected only the properties of the fluorescence excited state it would be expected that I_2/I_1 would be approximately equal to Φ_{Fl2}/Φ_{Fl1}. However, in this circumstance this is not the case (Table 6.2). The two quantities are not correlated with each other which implies that there is also a change in the ground state properties of the dyes upon binding. The ratios of brightness in the free and bound cases (B_2/B_1) are equal to $\Phi_{Fl2}\varepsilon_2/\Phi_{Fl1}\varepsilon_1$. Theoretically, if B_2/B_1 and Φ_{Fl2}/Φ_{Fl1} are not equivalent but are greater than 1, there must also be a corresponding increase in ε_2 relative to ε_1. It was not possible to determine an accurate value of ε_2 for the BEs and mBEs as there was significant overlap in λ_{abs} of the dyes and the aggregates. At the concentrations of αSyn aggregates required, the interfering signal they produced made deconvolution of the two signals uninformative.

The affinity with which an aryl-benzothiazole probe docks onto a particular binding site on the protein is an additional factor affecting the extent of fluorescence. Binding of the BEs and mBEs to αSyn fibrils was confirmed with SPR spectroscopy (Figure 6.9) in which αSyn aggregates were covalently attached onto a surface via an amide bond coupling.

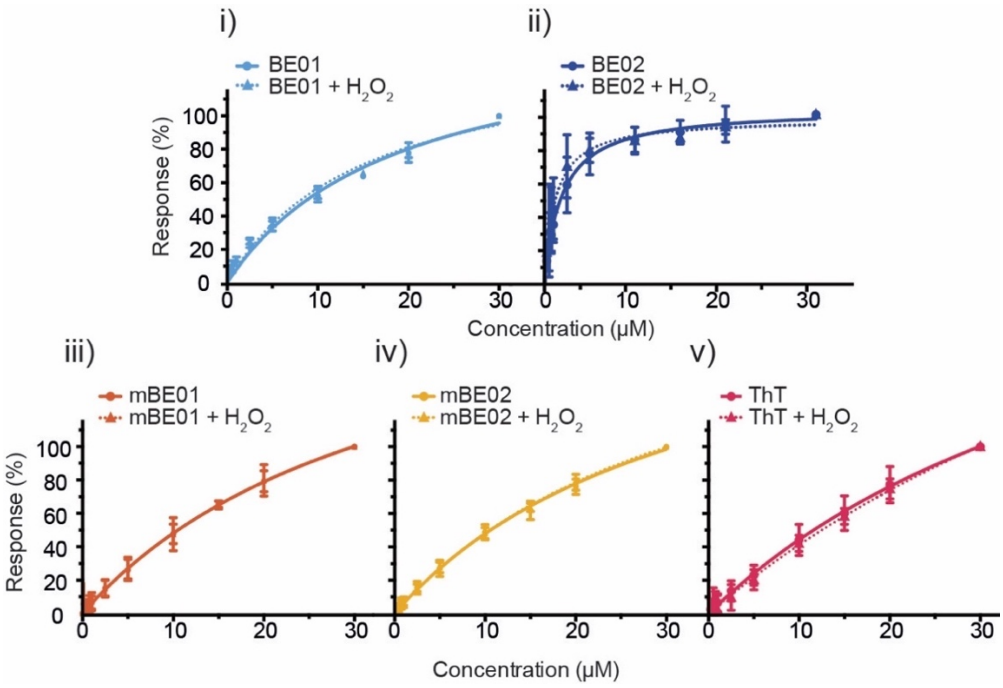

Figure 6.9. Equilibrium affinity analysis of αSyn interactions with **i)** BE01, **ii)** BE02, **iii)** mBE01, **iv)** mBE02 and **v)** ThT before (circular symbols, solid lines) and after (triangular symbols, dotted lines) incubation with 100 μM H_2O_2. The mean ($n \geq 3$), normalised SPR response upon injection of different concentrations of dye solution (0.1 μM -30 μM), from independent measurements are shown. Dissociation constants (K_D) were obtained from non-linear fits.

The main purpose of this was not to establish accurate K_D values but to ascertain a comparison of the dye binding capabilities before and after oxidation with H_2O_2. Compared to ThT (K_D = 51.2 ± 5.9 μM), all four boronate dyes showed enhanced binding to αSyn aggregates. BE01 and BE02 (K_D^{BE01} = 18.7 μM, K_D^{BE02} = 2.0 μM) outperformed their methylated counterparts (mBE01 and mBE02; K_D^{mBE01} = 35.2 μM; K_D^{BE02} = 33.5 μM). This is comparable with

other methylated and non-methylated benzothiazole compounds (232) as discussed in Chapter 5. Furthermore, the K_D of ThT measured in this work was high and can likely be attributed to the differences in physical conditions between SPR and commonly used fluorescence-based measurements (192).

6.2.1.4 Bifunctional Sensing

All four dyes have demonstrated capabilities of independent fluorescence sensing of either H_2O_2 or αSyn aggregates as the response to a chemical or physical modification. However, these effects combined do not seem to be additive. A large, compounded increase in fluorescence intensities of BE01 and BE02 resulted from the presence of both αSyn aggregates and H_2O_2 (Figure 6.6, Figure 6.10). BE01 responded to the addition of αSyn aggregates and H_2O_2 with 3.3 and 2.0-fold increases in fluorescence intensity respectively. The presence of both components resulted in a 7.5-fold increase in fluorescence. Likewise, incorporation into αSyn aggregates resulted in a 4.8-fold increase in the fluorescence of BE02 whilst the addition of H_2O_2 left the dye emission approximately unchanged. Addition of αSyn aggregates and H_2O_2 increased the fluorescence intensity 19.6-fold. Despite the abilities of mBE01 and mBE02 to sense αSyn aggregates and H_2O_2 independently, the probes underwent no positive change in fluorescence in response to both factors relative to the emission with αSyn aggregates or H_2O_2 alone. As expected, ThT emission remained unchanged by the presence of both αSyn aggregates and H_2O_2.

The likely origin of the non-linear changes in the emission properties of BE01 and BE02 arose from differences in the binding affinities (K_D) when going from the boronate ester to hydroxyl functionality following the oxidation step. To explore this, SPR measurements were also performed on the BE-Ox and mBE-Ox compounds (Figure 6.9). No change in the affinities of the probes for the αSyn aggregates occurred as a result of oxidation, therefore the changes in

emission resulted from modification of the photophysical properties of the dyes themselves.

The total integrated fluorescence intensity of BE-Ox in the presence of αSyn aggregates was approximately 2-fold greater than ThT (Figure 6.10).

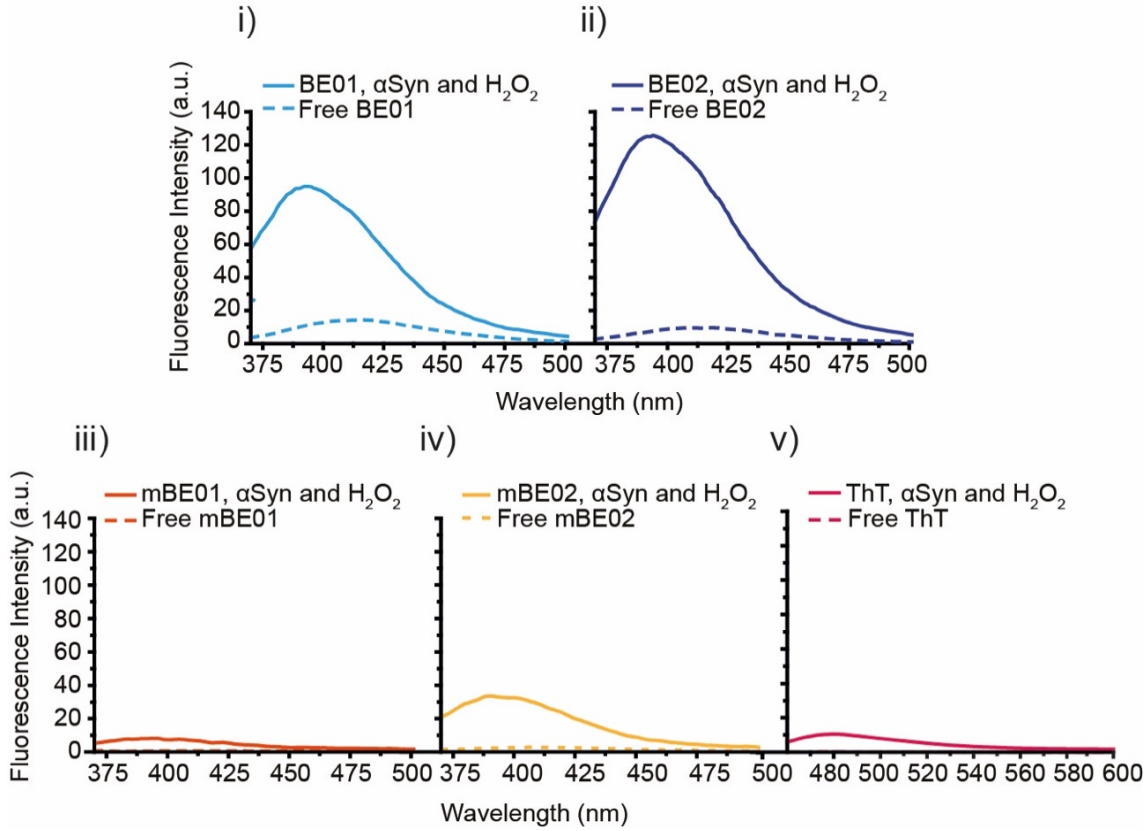

Figure 6.10. Bulk fluorescence spectra of 5 μM **i)** BE01, **ii)** BE02, **iii)** mBE01, **iv)** mBE02 and **v)** ThT free in PBS buffer, with αSyn aggregates and with concomitant 10 μM αSyn aggregates and 100 μM H_2O_2. λ_{ex}= 330 nm.

However, the fluorescence produced from these amyloid dyes varies between protein aggregation samples (Appendix A.2, Table A.2.3) and optimal conditions may need to be adjusted for each experiment. Even when these factors were considered, the measured B_2 of BE-Ox was always greater than ThT. Therefore the BE probes could be considered suitable for the fluorescence detection of single αSyn aggregates and H_2O_2 (159).

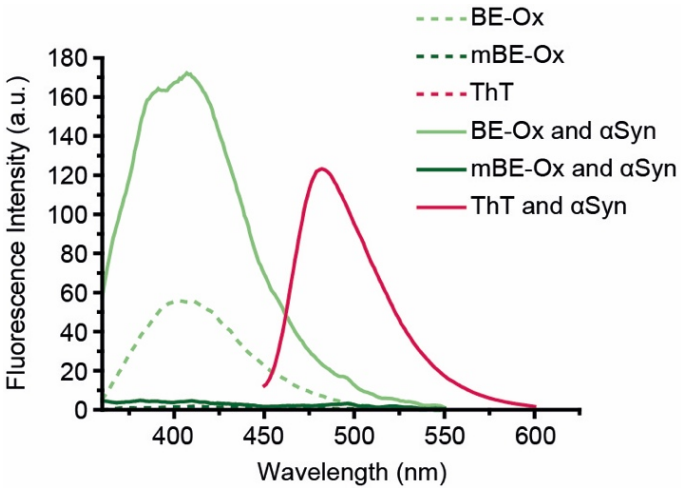

Figure 6.11. Fluorescence spectra of 5 μM BE-Ox, mBE-Ox and ThT in PBS buffer and with 10 μM αSyn aggregates. λ_{ex}= 325 nm for BE-Ox, λ_{ex}= 328 nm for mBE-Ox and λ_{ex}= 412 nm for ThT.

6.2.2 Single Aggregate and H_2O_2 Fluorescence Imaging

Aryl-benzothiazole based fluorescent probes have been used extensively to study *in vitro* protein aggregation kinetics at the ensemble level. The single-aggregate visualisation by enhancement (SAVE) imaging method demonstrated that ThT could be used to visualise not only the heterogeneity in an aggregated protein mixture but also to identify the presence of rare, potentially toxic oligomeric species. In order to determine if the probes were suitable for detecting late-stage αSyn aggregates and H_2O_2 at the single-aggregate level, the protein was incubated with the probes and imaged before and after the addition of 100 μM H_2O_2. The principles of SAVE imaging were successfully applied and coupled with H_2O_2 sensing in this experiment. However, λ_{abs} and λ_{em} of the BE and mBE probes were 70-80 nm blue-shifted compared with ThT therefore the 405 nm excitation was off-resonant in these cases. Nonetheless it was possible to use the probes visualise αSyn aggregates on the surface. Despite having affinities for αSyn aggregates greater than ThT, both the BE and mBE probes underwent the same transient binding at a rate which resulted in a

constant, low-level of fluorescence over time with no apparent photobleaching, therefore imaging for long periods of time would not be inhibited by the optical stability of these probes. Figure 6.12 shows SAVE images of BE01, BE02, mBE01, mBE02 and ThT taken on a TIRF microscope (Chapter 2, section 2.4) optimised for single-molecule detection.

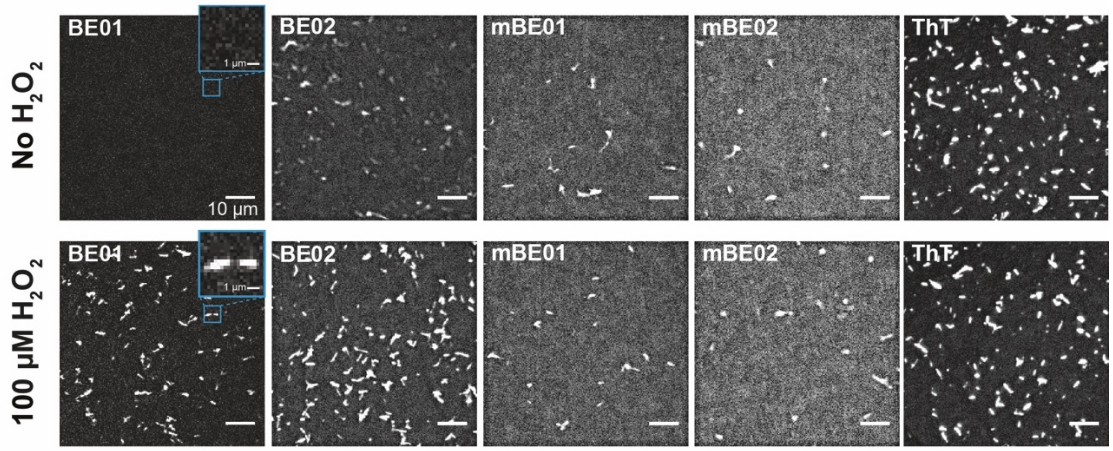

Figure 6.12. Representative average intensity SAVE images of BE01, BE02, mBE01, mBE02 and ThT in the absence (top) and presence of H_2O_2. Scale bar on full images= 10 µm, scale bar on inset =1 µm.

Qualitatively, the success of the bifunctionality of BE01 is exemplified in Figure 6.12 as fluorescence from the protein bound dye was not detectable prior to the addition of H_2O_2. However, following the addition of H_2O_2 the probe underwent significant fluorescence activation. This was quantified by analysing the density of aggregates in several fields of view before and after oxidation by H_2O_2. A reasonable assumption of consistent surface coverage between different coverslide preparations was made. Figure 6.13 shows no αSyn aggregate species were detected by BE01 prior to the addition of H_2O_2, following the oxidation and the formation of BE-Ox the density of species detected increased to 0.020 ± 0.004 aggregates/ µm^2. The density of detected species increased 5-fold upon oxidation of BE02 to BE-Ox, from 0.005 ± 0.001 aggregates/ µm^2 to

0.025 ± 0.006 aggregates/ μm^2. ThT was used as a control and there was no change in the fluorescence properties, hence the density of detected species as a result of H_2O_2 (0.025 ± 0.004 and 0.026 ± 0.002 aggregates/ μm^2). Interestingly the densities of αSyn aggregates detected by oxidised BE01 and BE02 were similar to ThT despite the significantly higher fluorescence intensity of oxidised BE01 and BE02 with αSyn aggregates at the ensemble level. This suggests that both BE01 and BE02 are sensitive to similar species to ThT. The densities of species detected by mBE01 and mBE02 were low, 0.0040 ± 0.0004 and 0.006 ± 0.001 aggregates/ μm^2 respectively. There was negligible change in this for oxidised mBE01 (0.0051 ± 0.004 aggregates/ μm^2) and mBE02 (0.0060 ± 0.0005 aggregates/ μm^2).

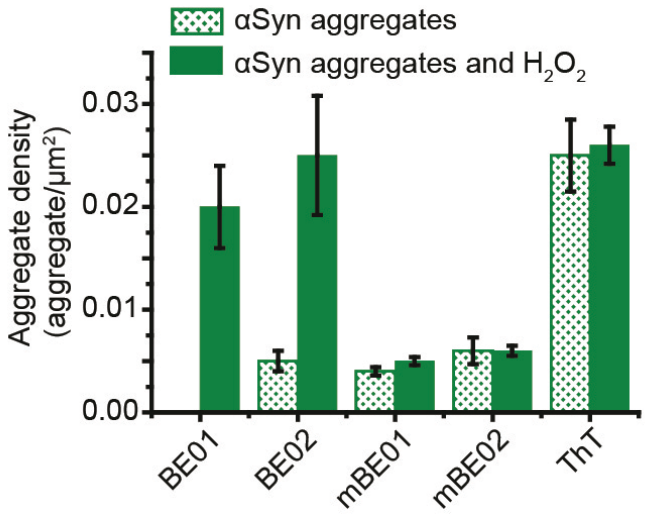

Figure 6.13. Bar graph showing the Density of single αSyn aggregate species detected by BE, mBE and ThT dyes before and after addition of 100 μM H_2O_2.

In order for these probes to be of potential use in a cellular system or in bio-fluid samples it is important to consider the limits at which they can detect protein species at the single-aggregate level. The limits of detection (LoD) of the probes to αSyn was characterised with pure samples of synthetic BE-Ox and mBE-Ox using SAVE imaging (Figure 6.14) and calculated by evaluating the first concentration at which the number of detected aggregates deviated

significantly from the mean background (3 S.D.). Again, constant αSyn surface coverage was assumed and the concentration of dye was varied between 10 μM- 1 pM. Contrary to SAVE data in Figures 6.12 and 6.13, mBE-Ox was able to detect aggregate species more successfully with a low concentration of 0.044 ± 0.005 nM whilst the LoD for BE-Ox and ThT were 4.58 ± 1.94 and 2.4 ± 0.64 μM respectively. This discrepancy is likely due to variations of aggregates between aggregation mixtures.

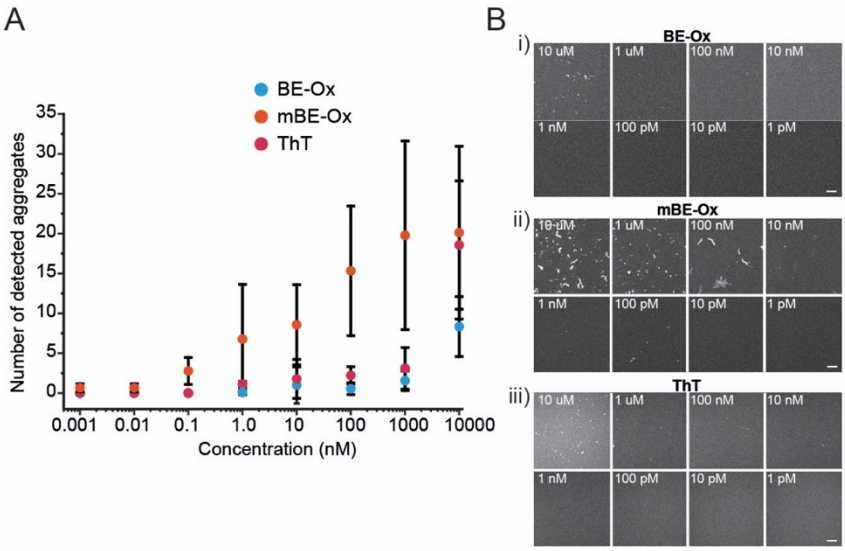

Figure 6.14. Determination of the LoD of oxidised BE and mBE bifunctional probes and ThT. **A)** Plot of the number of single αSyn aggregate species detected per field of view against dye concentration. Error bars represent the standard deviation from n=10 fields of view. **B)** Representative SAVE images of immobilised αSyn aggregates with 10 μM- 1 pM **i)** BE-Ox, **ii)** mBE-Ox, **iii)** ThT. Scale bar= 10 μm.

6.3 Conclusions and Future Work

New methods for the detection of H_2O_2 and protein aggregates will be critical to advance our clinical understanding of diseases. Accordingly, this chapter described the design and successful application of a new class of bifunctional-

fluorescent probes for the independent or simultaneous detection of both αSyn aggregates and H_2O_2. Existing approaches for independently detecting either β-sheet containing aggregates of amyloid or H_2O_2 were united to create four dyes BE01, BE02, mBE01 and mBE02. The BE and mBE dyes were distinguished only by *N*-methylation of the benzothiazole core, which provided the corresponding mBE fluorophores. The net positive charge significantly affected the intrinsic optical properties and furthermore the bifunctional capabilities of the mBE probes relative to the neutral BE analogues. Ensemble measurements showed the mBE probes were competent independent H_2O_2 or αSyn aggregate sensors as they responded with a fluorescence turn-on but poor sensors of the two species simultaneously. Despite this, the brightness of the mBE and mBE-Ox dyes at both the ensemble and single-aggregate level was poorer than probes currently used for H_2O_2 and aggregate detection. Therefore, there is no clear benefit of the utility of *N*-methylated boronate and hydroxyl functionalised dyes in this field of study. On the contrary, both BE01 and BE02 very successfully detected the simultaneous presence of both H_2O_2 and αSyn aggregates, providing large increases in ensemble fluorescence intensity and detected single aggregates. These tools may prove useful in cellular studies of neurodegeneration where it is desirable to study both processes simultaneously.

The work discussed in here and in Chapter 5 has laid a promising foundation for the development of strategies to systematically design fluorescent probes with optimal optical properties for the study of neurodegenerative diseases. Potential avenues of future research would include modification of the carbon-1 substituent on the benzothiazole ring of the BE probes to improve I_2/I_1 and yield a more effective aggregate sensor. It would be of equal importance to characterise these probes *in vivo* for their efficacy in a relevant life-science application.

Project Two

FRET-enhanced photomodulatable fluorophores

Chapter 7 Development of FRET-enhanced Photomodulatable Fluorophores

The results presented in this chapter represent work in publication 2 listed in the Publications section.

7.1 Overview of this chapter

Single-molecule fluorescence (SM) **tracking** allows for study of the dynamics of individual proteins in live cells with nano-scale precision (244). **Photo-modulatable fluorescent proteins** (PMFPs) facilitate the study of single-proteins in high density environments but are approximately an order of magnitude less photostable than typically used organic dyes. The PMFP chromophore is also enclosed from the surrounding environment, hence the use of photostabilising reagents, often used for organic dyes, are ineffective (20, 93) .

The work presented in this chapter introduces a novel concept for the external modification of the photophysical properties of PMFPs. This simple strategy employs the existing physical principle of **Förster resonance energy transfer** (FRET). By covalently linking a suitable acceptor fluorophore in close spatial proximity to the donor PMFP (Figure 7.1), in such a manner that the two can FRET, the excited state properties of the donor are altered. This interaction improves the **photophysics** of the donor fluorophore in the context of SM fluorescence.

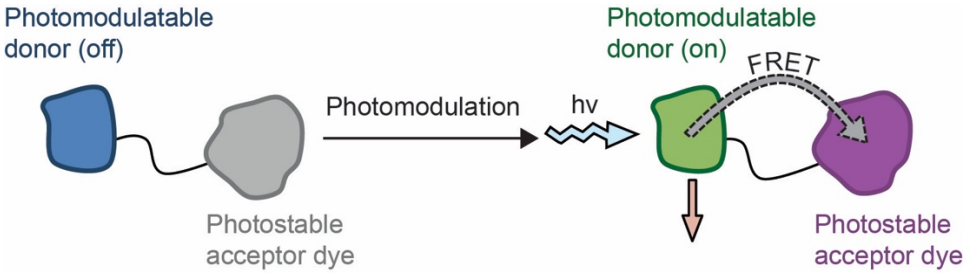

Figure 7.1. Schematic illustrating the concept of covalently linking a photomodulatable donor fluorophore to a photostable acceptor fluorophore such that they may undergo FRET.

In order for fluorophores to be suitable FRET partners they must be closely positioned in space (<10 nm) and there must be sufficient overlap between the emission spectrum of the donor fluorophore and the absorption spectrum acceptor fluorophore. A high donor fluorescence quantum yield and acceptor extinction coefficient is also favourable. Considering these requirements, PMFP **mEos3.2** (78) and silicon-rhodamine derived organic flurophore **JF_{646}** (51) were adopted to form a novel FRET pair (Figure 7.2). JF_{646} was conjugated in proximity to purified mEos3.2 via the modified halogenase enzyme, HaloTag (110). In this mode, FRET is unconventionally exploited to improve the photophysical properties of the PMFP donor to yield FRET-enhanced mEos3.2 (Figure 7.2A).

The contents of this chapter will describe the characterisation of FRET-enhanced mEos3.2 at the bulk and SM levels. Moreover, the utility of FRET-enhanced mEos3.2 as a way to achieve superior trajectories of single proteins diffusing in live mammalian cells will be discussed. Finally, preliminary experiments to characterise this phenomenon quantitatively will be discussed.

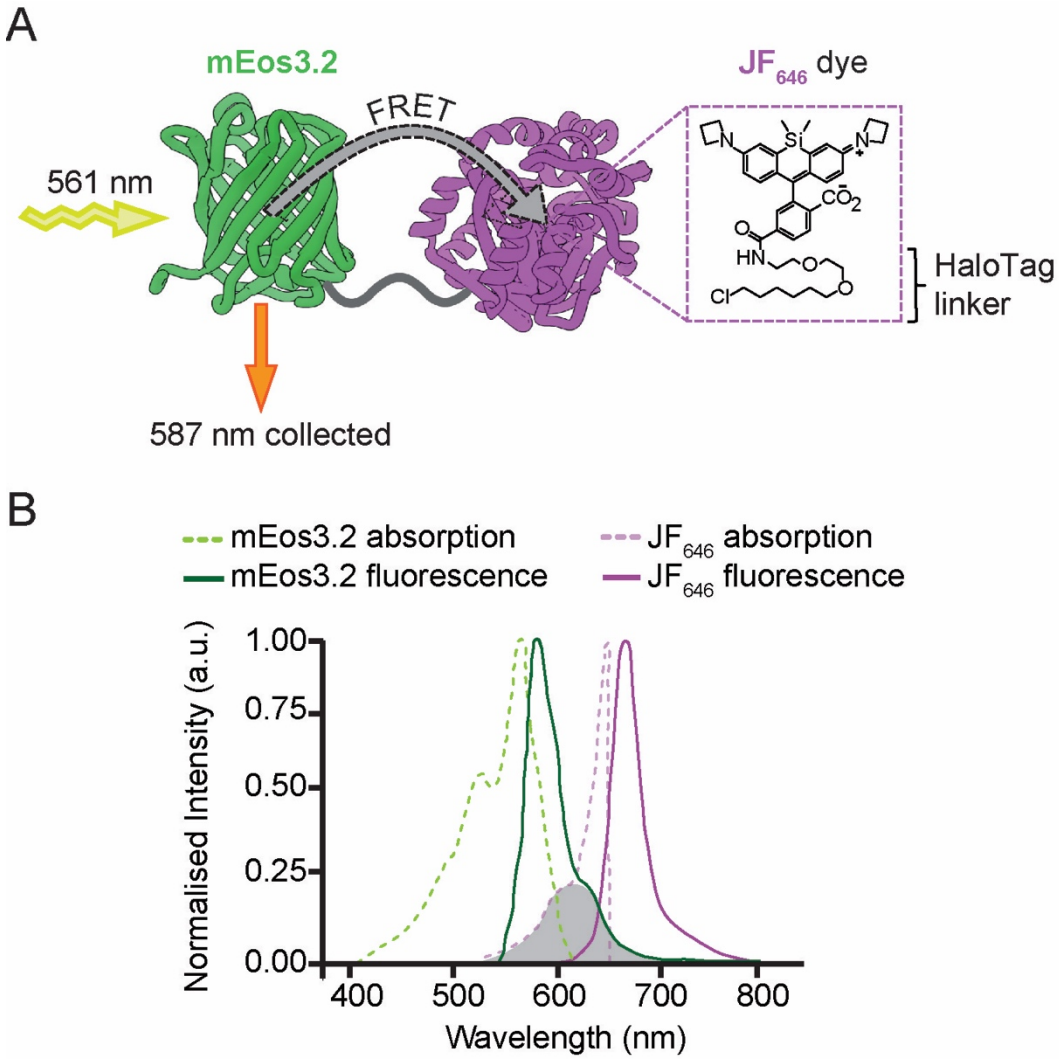

Figure 7.2. **A)** A protein fusion construct consisting of a donor fluorophore, photoconvertible FP mEos3.2, and modified halogenase enzyme HaloTag. In this construct the JF_{646} fluorophore ligand forms the photostable FRET acceptor. **B)** Bulk normalised UV-vis absorption and fluorescence spectra of photoconverted mEos3.2 and JF_{646}. The spectral overlap between mEos3.2 emission spectrum and JF_{646} absorption spectrum is highlighted in grey.

7.1.1 Contributions

Dr. Srinjan Basu performed all cell culture and *in vivo* labelling. Dr. Srinjan Basu and I expressed mEos3.2-HaloTag. Dr. Srinjan Basu and I performed live-cell

SM tracking experiments. Devina Shah and I expressed, purified and labelled the SNAP-tag-HaloTag protein. Kai Wohlfhart and Dr. Steven Lee designed and wrote the code for the SM TIRF data analysis. Dr. Laura Weimann wrote the SM tracking code. I performed mEos3.2 protein purification, dye labelling, HaloTag ligand synthesis and purification, bulk fluorescence, fluorescence lifetime and *in vitro* SM TIRF measurements.

7.1.2 Results and Discussion

7.1.3 Confirming FRET between mEos3.2 and JF_{646}

mEos3.2 is categorised as a photoconvertible (PC) FP, its chromophore can undergo a large bathochromic shift in both absorption and emission in response to near-UV radiation. Following photoconversion it has absorption and emission maxima at 572 nm and 580 nm respectively (78). It is monomeric and has a high fluorescence quantum yield (Φ=0.55) (78) when compared to other PMFPs such as photoswitchable (PS) mOrange (Φ=0.28) (245), photoactivatable (PA) mCherry (Φ=0.46) (74) and PA-cyan FP (Φ=0.23) (246). The absorption profile of JF_{646} overlaps well with the emission spectrum of mEos3.2 (Figure 7.2B). Furthermore, JF_{646} is a photostable fluorophore with a high molar extinction coefficient (ε=152000 $M^{-1}cm^{-1}$) and Φ of 0.54 (51), comparable to mEos3.2. JF_{646} is fluorogenic, in solution the dye preferentially forms a closed, lactone tautomer and when conjugated to a biological molecule such as the HaloTag the local environment is changed such that an open conformation is adopted and a large increase in fluorescence occurs. The distance between the mEos3.2 and JF_{646} chromophores was estimated to be significantly less than 10 nm as the respective radii of mEos3.2 and HaloTag proteins are 1.5 nm and 2 nm. These properties suggested that mEos3.2-JF_{646} would form a suitable test system for this concept.

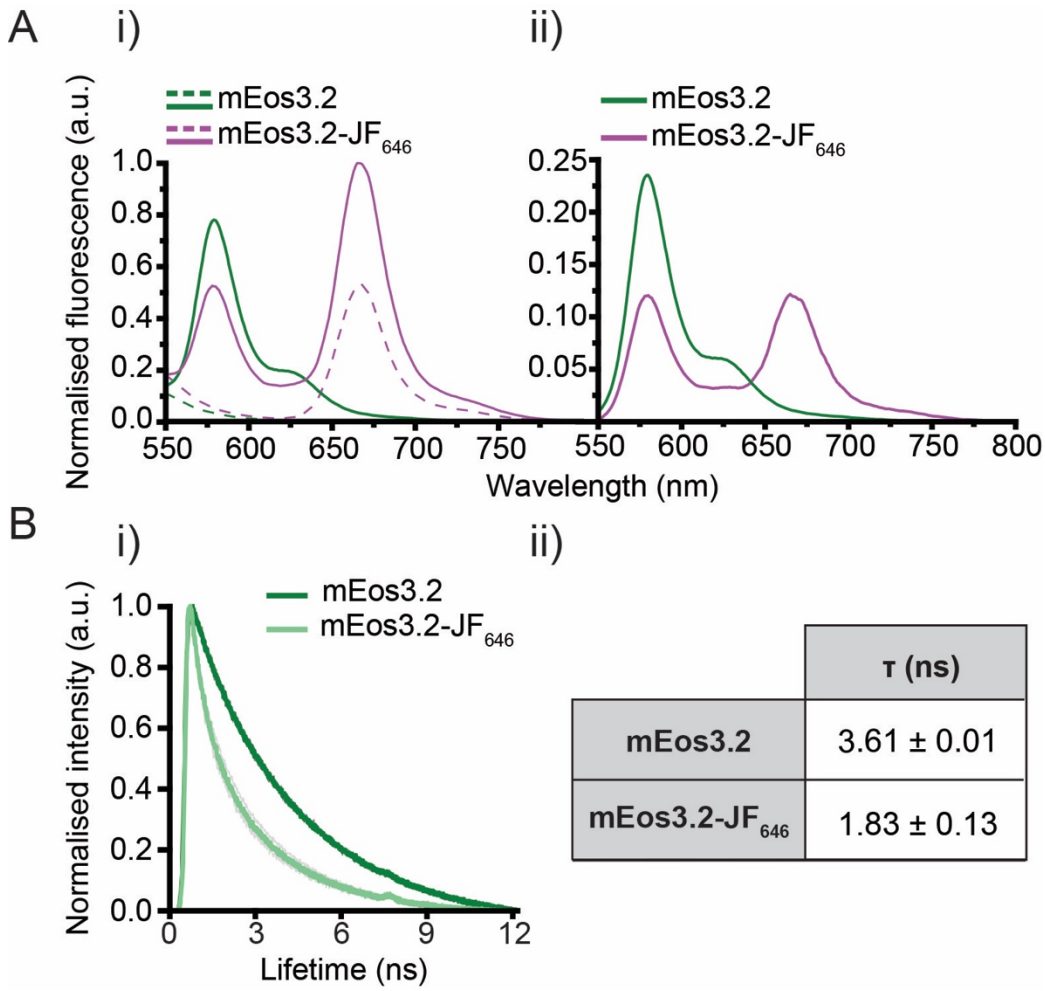

	τ (ns)
mEos3.2	3.61 ± 0.01
mEos3.2-JF$_{646}$	1.83 ± 0.13

Figure 7.3. **A) i)** Bulk fluorescence spectra of non-photoconverted (dashed lines) and photoconverted mEos3.2 (solid lines) with and without JF_{646} illustrating the change in intensity as a result of FRET. Spectra were normalised to the maximum intensity value. **ii)** Bulk spectra of photoconverted mEos3.2 with and without JF_{646} and normalised to remove the JF_{646} direct excitation component. **B) i)** Fluorescence lifetime exponential decay curves of photoconverted mEos3.2 and mEos3.2-JF_{646}. Each background corrected and independently normalised relative to the maximum intensity. **ii)** Fluorescence lifetime values extracted from fits of the decay curves, errors correspond to the standard deviation of replicate measurements. All experiments contained a minimum of n=3 replicates.

FRET was first confirmed with bulk fluorescence spectroscopy (Figure 7.3A). The fluorescence spectra of purified mEos3.2 were measured before and after photoconversion both in the presence and absence of JF_{646}. Figure 7.3Aii

shows the fluorescence of mEos3.2 and mEos3.2-JF_{646} following subtraction of JF_{646} fluorescence resulting from direct excitation at the mEos3.2 excitation wavelength. The remaining spectra represent the FRET between mEos3.2 and JF_{646} and manifested as an anti-correlated change in donor and acceptor emission intensities. The fluorescence lifetime (τ) of photoconverted mEos3.2 was also measured with and without JF_{646} (Figure 7.3Bi). The mean τ of mEos3.2 was found to be 3.6 ns (Figure 7.3Bii) which was consistent with previously measured values of red FPs (247). Expectedly in the presence of covalently conjugated JF_{646} the mean τ of mEos3.2 decreased to 1.8 ns. E_{FRET} for mEos3.2-JF_{646} was calculated to be 0.49 ± 0.04 from Equation 3.4 (Chapter 3-Project Two Materials and methods). A mean inter-fluorophore distance of 6 ± 1 nm was calculated from Equation 3.3 (Chapter 3- Project Two Materials and methods). These data combined provided strong evidence for FRET between photoconverted mEos3.2 and JF_{646} in this construct.

7.1.4 Single-molecule properties of FRET-enhanced mEos3.2

In order to explore the single-molecule photophysical behaviour of FRET-enhanced mEos3.2, TIRF movies of spatially isolated, surface immobilised mEos3.2 with and without JF_{646} were collected (Figure 7.4). In this mode mEos3.2 was photoconverted with a single pulse of 405 nm light and excited with 561 nm. The subsequent fluorescence was collected until the majority of molecules visible in the first frame had photobleached. The initial photoconversion pulse needed to be sufficiently intense to convert enough molecules, but also at a suitable power to ensure all molecules were individually resolvable. The SM fluorescence from JF_{646} could not be measured simultaneously; as mEos3.2 is a PCFP the surface concentration required to achieve a significant number of fluorescently active molecules per field of view are 1-2 orders of magnitude higher than concentrations typically used for non-PM fluorophores such as JF_{646}. FRET and direct excitation meant that emissive JF_{646} molecules were not spatially isolated.

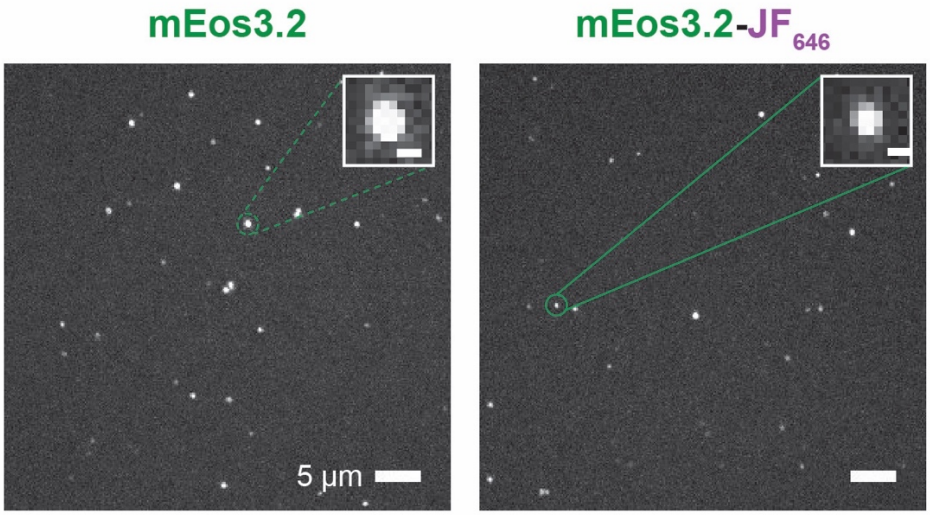

Figure 7.4. Maximum intensity time projections of SM TIRF images of single mEos3.2 (left) and FRET-enhanced mEos3.2 (right) molecules adhered to a surface and imaged in PBS. The inset in each projection signifies a representative molecule (scale bar= 500 nm).

To characterise FRET-enhanced mEos3.2 several photophysical parameters were evaluated (Figure 7.5). This included quantifying the total number of photons emitted by each single mEos3.2 molecule prior to irreversible photobleaching, and the number of photons emitted in each frame. The reversible dark-state switching events (blinking) were quantified by way of the on-state time, off-state time and the number of occurrences. The total on-state time corresponds to the sum of on-state events and is equal to the total amount of time single mEos3.2 molecules were fluorescent before being photobleached. mEos3.2 molecules were selected for analysis from the first frame immediately following the photoconversion pulse, as mEos3.2 is prone to spontaneous thermal conversion of the chromophore. Moreover, only molecules that were photoconverted were analysed to negate the low probability event of any cross talk from the JF_{646} channel being considered.

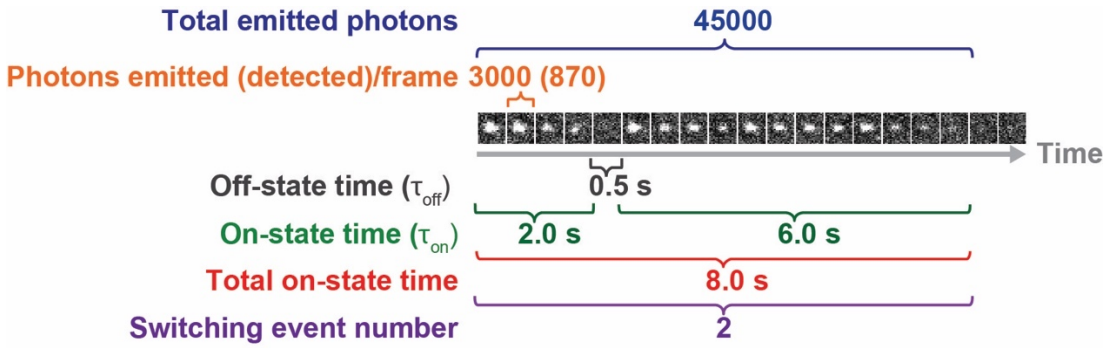

Figure 7.5. A schematic illustrating the photophysical quantities extracted from SM TIRF data of mEos3.2 and FRET-enhanced mEos3.2.

This quantification allowed the comparison of the heterogeneity in the photophysical properties of mEos3.2 and FRET-enhanced mEos3.2 (Figure 7.6). This analysis showed that there was a mean increase of 1.9-fold in the total on-state time of FRET-enhanced mEos3.2 (6.9 ± 1.1 s) compared to mEos3.2 (3.6 ± 0.6 s) alone. A theoretical increase of 2-fold was expected given the reduction in fluorescence lifetime and this agreed well with that. However, there was an unexpected concomitant increase in the total number of emitted photons of 1.8-fold, from 28000 ± 9000 to 51000 ± 8000 photons, which suggested there were potentially other excited state dynamics in affect. The number of emitted photons for mEos3.2 matched well with a previously measured value of 21,000 photons for EosFP (77).

The on-state time is an important property when considering the suitability of a fluorophore for single-molecule tracking. It designates the time the fluorophore spends in a fluorescently active state before transitioning to a transient or permanent dark state, during which the motion or position of the molecule cannot be determined. The mean on-state time of FRET-enhanced mEos3.2 (5.1 ± 0.8 s) was 2-times higher than mEos3.2 alone (2.5 ± 0.4 s). Despite these increases, the number of switching events remained the same, therefore there was a decrease in the off-state time of 2-fold.

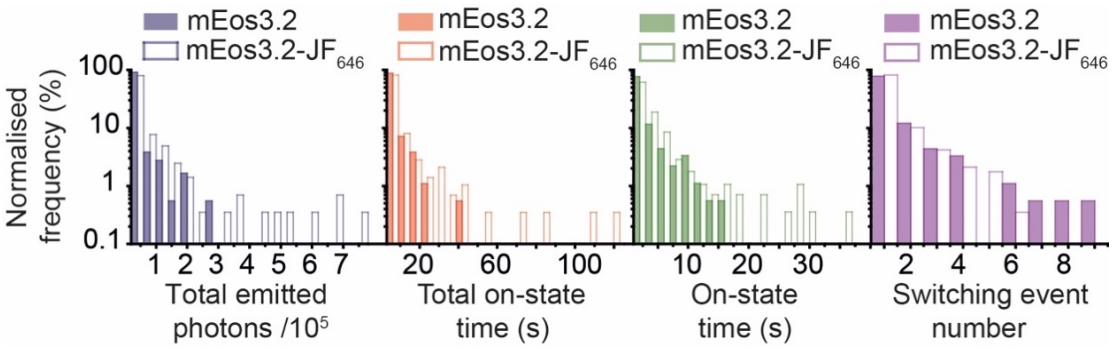

Figure 7.6. Histograms comparing the SM photophysical properties of mEos3.2 and FRET-enhanced mEos3.2 in PBS. The data was normalised to 100 % for mEos3.2 and FRET-enhanced mEos3.2 independently. There were n ≥ 500 molecules for each experiment.

The cumulative histogram in Figure 7.7A shows the percentage of single mEos3.2 and FRET-enhanced mEos3.2 molecules that were fluorescently active at a given time. At the point at which 99 % of mEos3.2 molecules had photobleached, 10 % of FRET-enhanced mEos3.2 molecules were still fluorescently active.

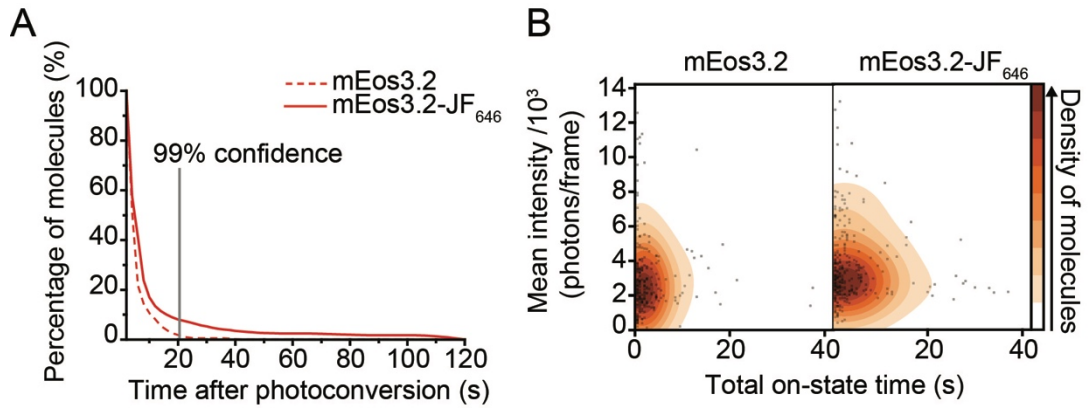

Figure 7.7. **A)** Cumulative histogram of the total on-time of single mEos3.2 and FRET-enhanced mEos3.2 molecules in PBS. The grey vertical line shows the point at which 99 % of mEos3.2 molecules have photobleached. **B)** Density plots of the mean number of photons emitted per frame versus total on-state time for mEos3.2 and FRET-enhanced mEos3.2 in PBS.

Furthermore, there was a correlation between the mean number of photons emitted in a single frame and the total on-state time (Figure 7.7B). The

molecules with the lowest intensities or highest FRET efficiencies had the longest on-state times, suggesting that this process is governed by the presence of the non-radiative FRET pathway.

7.1.5 Improving FRET-enhanced mEos3.2 with Trolox

It has been long understood that FRET is capable of reducing the photobleaching rate of the donor fluorophore in the pair (248). Therefore, it was hypothesised that the photobleaching rate of the acceptor fluorophore directly influenced that of the donor. As mentioned previously, commonly used chemical methods to photostabilise organic fluorophores have been shown to be ineffective with FPs (20, 93). However, it could be postulated that improving the photostability of the solvent exposed JF_{646} with a photostabilising additive, such as Trolox, may photostabilise mEos3.2 as a secondary consequence. Should this be true it would suggest that the existence of the FRET pathway and, by extension, the JF_{646} chromophore, governed the photophysical properties of the mEos3.2.

To explore this hypothesis, SM TIRF experiments were performed with the addition of a triplet state quencher, Trolox to the buffer (Figure 7.8). As photobleaching likely occurs from the triplet state of the dye (249), Trolox has been used widely used to improve the photostability of organic fluorophores in SM and super-resolution (SR) experiments (112, 250). Trolox was chosen as it is membrane permeable and non-cytotoxic therefore would not negatively affect cell-viability (251).

Qualitatively, from the images there were clear differences in fluorescence properties between mEos3.2 and FRET-enhanced mEos3.2. Several FRET-enhanced mEos3.2 molecules appeared to be fluorescently active for significantly longer times compared to mEos3.2 alone (Figure 7.8Aii), as well as different on-off state behaviour (Figure 7.8B). Furthermore, several FRET-enhanced mEos3.2 molecules appeared to have intensities close to

background values, for this reason data was collected with long integration times (500 ms).

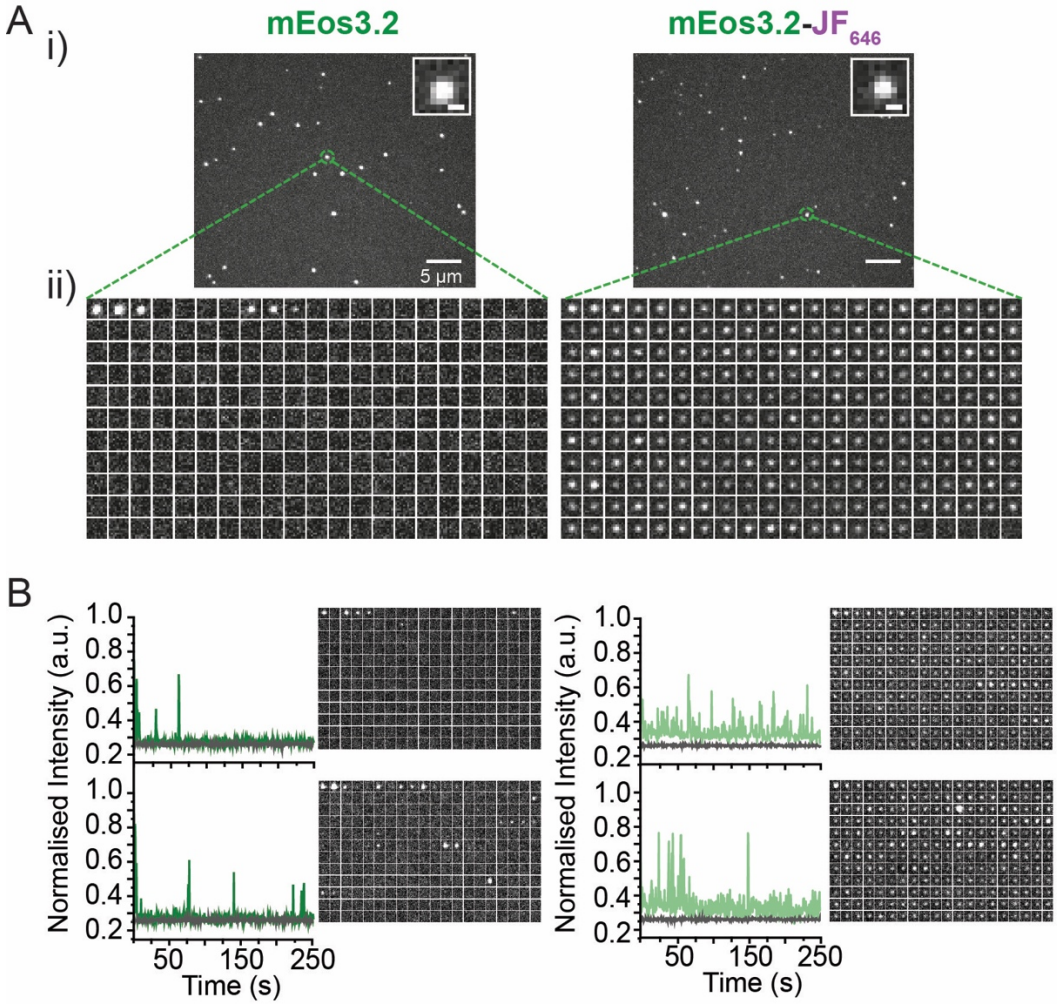

Figure 7.8. A) i) Maximum intensity time projections of SM TIRF images of single mEos3.2 (left) and FRET-enhanced mEos3.2 (right) molecules adsorbed to a surface and imaged in PBS with 2 mM Trolox. The inset in each projection signifies a representative molecule (scale bar= 500 nm). **ii)** Representative montages showing the fluorescence of single molecules. Each square represents the molecule in every second frame. **B)** Normalised intensity traces and montages of single mEos3.2 (left) and FRET-enhanced mEos3.2 molecules (right).

These observations were reflected in the quantification of photophysical properties (Figure 7.9). In the presence of Trolox the mean total on-state time improved by a factor of 8, from 2.9 ± 0.35 s for mEos3.2 to 22.7 ± 3.0 s for

FRET-enhanced mEos3.2. This led to an increase in the mean photon budget from 20,000 ± 3000 from mEos3.2 to 94,000 ± 11000 photons from FRET-enhanced mEos3.2, a 4.7-fold positive change. The number of photons emitted from single green FP molecules was measured to be 100,000 (41), which agreed well with the value measured for FRET-enhanced mEos3.2 in this work. This increase in photon budget was observed despite the of 39 ± 2 % reduction in the rate of photon emission. The mean number of reversible switching events, again, remained unchanged (1.8 ± 0.2 for mEos3.2 and 1.74 ± 0.4 for FRET-enhanced mEos3.2) and was similar to those reported in previous studies (81). As the number of switching events was unaltered, there was both a 7-fold decrease and increase in off-state and on-state times respectively. The mean on-state time for FRET-enhanced mEos3.2 was 13 ± 1.6 s which is highly suitable for single-molecule tracking studies (252).

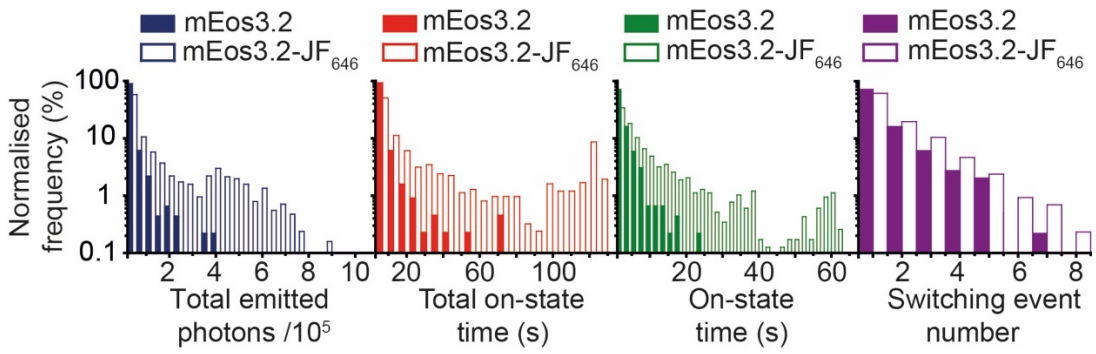

Figure 7.9. Histograms comparing the SM photophysical properties of mEos3.2 and FRET-enhanced mEos3.2 in PBS and 2 mM Trolox. The data was normalised to 100 % for mEos3.2 and FRET-enhanced mEos3.2 independently. There were n ≥ 1000 molecules for each experiment.

It was clear that a population of FRET-enhanced mEos3.2 molecules were emissive for significantly longer than mEos3.2. After 99% of mEos3.2 molecules were photobleached, more than 20 % of FRET-enhanced mEos3.2 molecules were still fluorescently active (Figure 7.10A). There were twice as many emissive molecules compared to Trolox-free conditions. Furthermore, 5 % of FRET-enhanced molecules were in the on-state for >100 s, a greater than

35-fold increase. There was considerable variation in the mean number of photons detected in each frame and the correlation between FRET-enhanced mEos3.2 intensity and total on-state time was clearer in the presence of Trolox (Figure 7.10B). The molecules that showed the lowest donor emission intensities had higher total on-state times. This further suggested that if E_{FRET} was the same high value for all molecules, it could have resulted in consistently superior enhancements of the mEos3.2 photophysics.

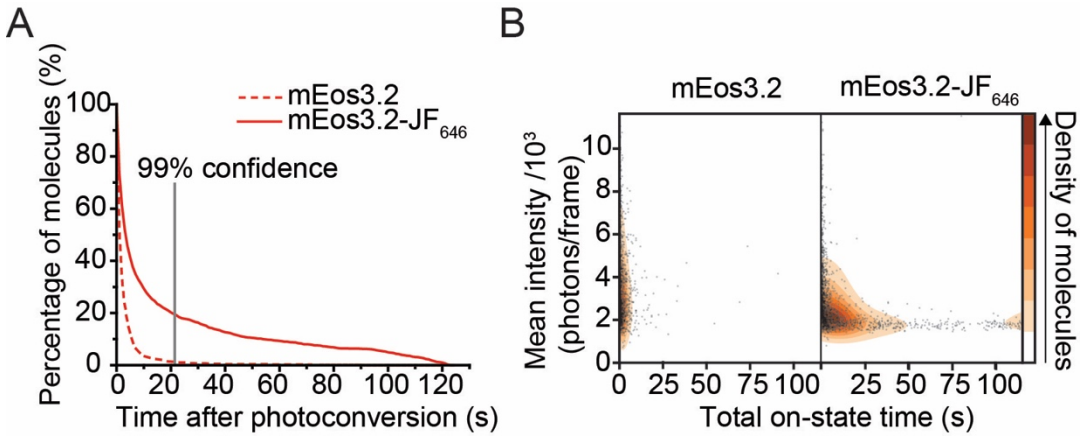

Figure 7.10. **A)** Cumulative histogram of the total on-time of single mEos3.2 and FRET-enhanced mEos3.2 molecules in PBS and 2 mM Trolox. The grey vertical line shows the point at which 99 % of mEos3.2 molecules have photobleached. **B)** Density plots of the mean intensity versus total on-state time for mEos3.2 and FRET-enhanced mEos3.2 molecules in PBS with 2 mM Trolox.

As expected, Trolox had no impact on mEos3.2 alone and the mean photophysics remained unchanged (Figure 7.11), therefore it was likely that Trolox photostabilised JF_{646} alone. Additionally, it can be presumed that the number of photons and on-state times of FRET-enhanced mEos3.2 were directly connected to the photostability of JF_{646}.

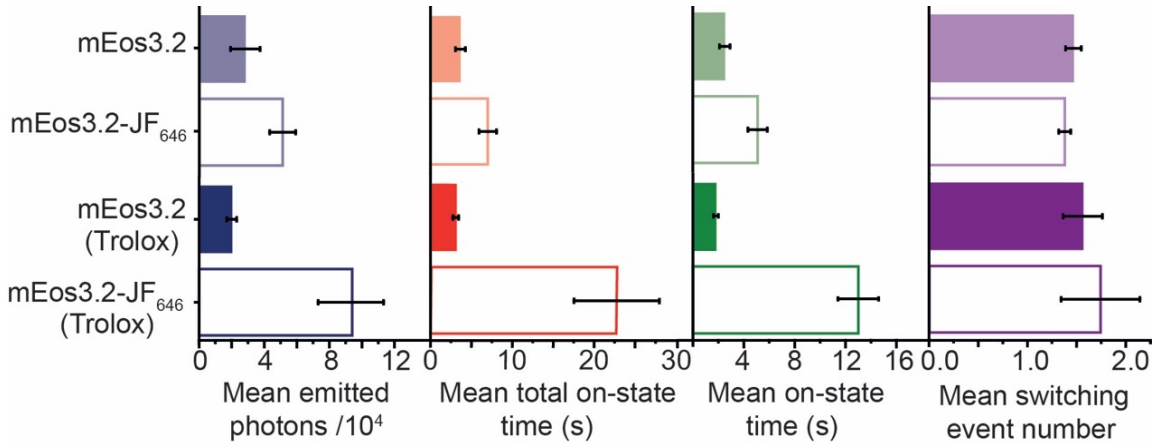

Figure 7.11. Bar graphs detailing the mean SM photophysical properties of mEos3.2 and FRET-enhanced mEos3.2 with and without 2 mM Trolox. The error bars represent the standard deviations of means from separate fields of view (n=9).

7.1.6 A hypothetical model to describe FRET-enhancement

The phenomenon of FRET-enhanced mEos3.2 may be attributed to differences in excited state kinetics (Figure 7.12). This preliminary, hypothetical model is based on previous work (250, 253). Studies have shown that photobleaching of mEos3.2 mainly occurs through a mechanism that is likely to involve the triplet state (T_1) (254). It can be assumed that FRET-enhanced mEos3.2 photobleaching was reduced due to the presence of an additional excited state, such as the singlet excited state of JF_{646} (S_1). The rate of this FRET pathway (k_{FRET}) would compete with the rate of intersystem crossing (k_{ISC}) and reduce the probability of the formation of T_1.

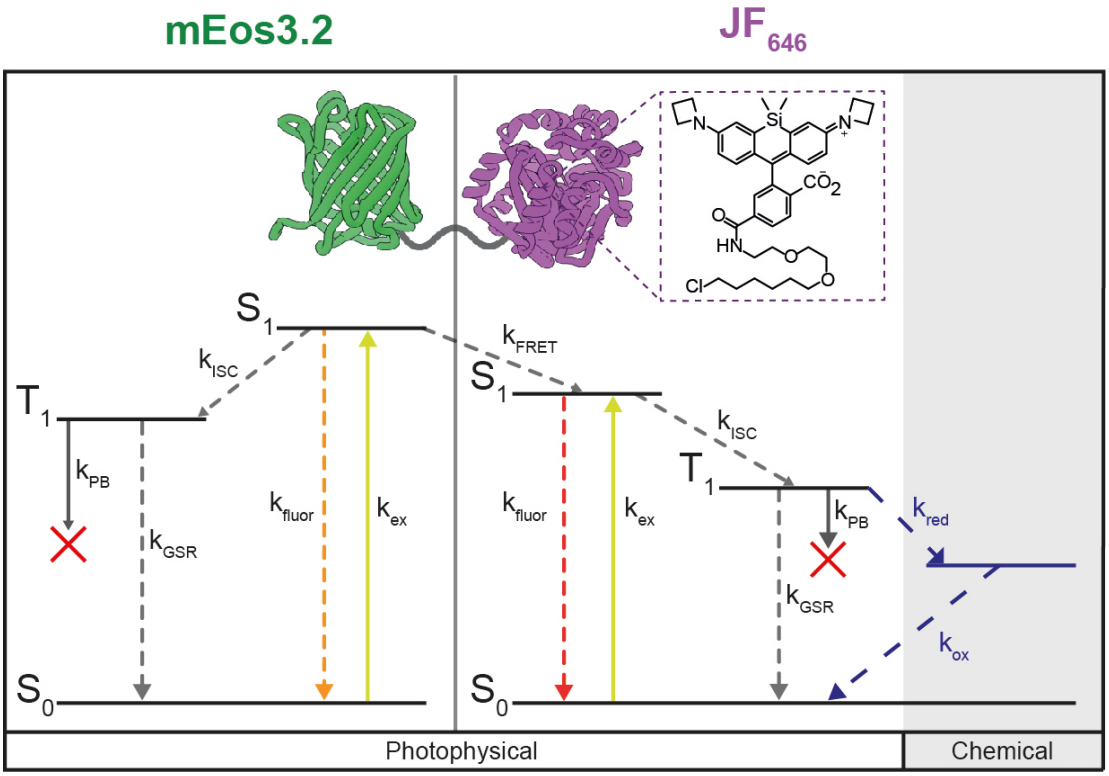

Figure 7.12. A hypothetical Jablonski diagram of potential excited state pathways occurring between mEos3.2 and JF_{646} in the FRET construct.

In this circumstance there are three possibilities that may be considered:

1. $k_{FRET} = k_{ISC}$: There would be a small increase in the number of photons emitted by FRET-enhanced mEos3.2 compared to mEos3.2 alone. As the probability of transfer to T_1 would be reduced by 33 %.

2. $k_{FRET} << k_{ISC}$: The number of photons emitted by FRET-enhanced mEos3.2 would equal the number emitted by mEos3.2 alone as ISC would dominate and significantly reduce the probability of FRET.

3. $k_{FRET} >> k_{ISC}$: The number of photons emitted by FRET-enhanced mEos3.2 would be significantly greater than the number emitted by mEos3.2 alone as FRET would dominate and significantly reduce the probability of ISC and formation of T_1.

Should this be true, the measurements made in this work concurred with the third possibility. The preservation of the FRET state due to the stabilisation of JF_{646} by Trolox may account for the greater enhancement in photon budget and on-state times relative to FRET-enhanced mEos3.2 in the absence of Trolox.

This explanation remains theoretical and further study would be required to confirm the hypothesis.

7.1.7 FRET-enhanced mEos3.2 for single-molecule tracking

FRET-enhanced mEos3.2 demonstrated superior SM photophysics compared to mEos3.2 alone. Following this, the effectiveness of FRET-enhanced mEos3.2 was evaluated in a live-cell SM tracking mode. Inside the nucleus of embryonic stem (ES) cells, the protein CHD4 was genetically encoded with the mEos3.2-HaloTag fusion construct at the C-terminus. CHD4 is a chromatin re-modeller protein and is a component of the nucleosome remodelling and deacetylase (NuRD) complex. CHD4 regulates ES cell pluripotency and also has roles in the DNA damage response (255). It is distributed throughout the nucleus of ES cells at high density. The dynamics of single CHD4-mEos3.2-HaloTag molecules were observed with oblique-angle illumination (141), with and without conjugated JF_{646} in the presence of Trolox (Figure 7.13).

As the primary focus of this experiment was to characterise the on-state times of FRET-enhanced mEos3.2 *in vivo,* high exposures were used to blur the motion of fast-moving CHD4 molecules (84, 256). This rapidly diffusing population left the imaging plane during the acquisition due to the narrow depth of focus of this 2D technique. At 500 ms exposure, the immobile chromatin bound population were localised.

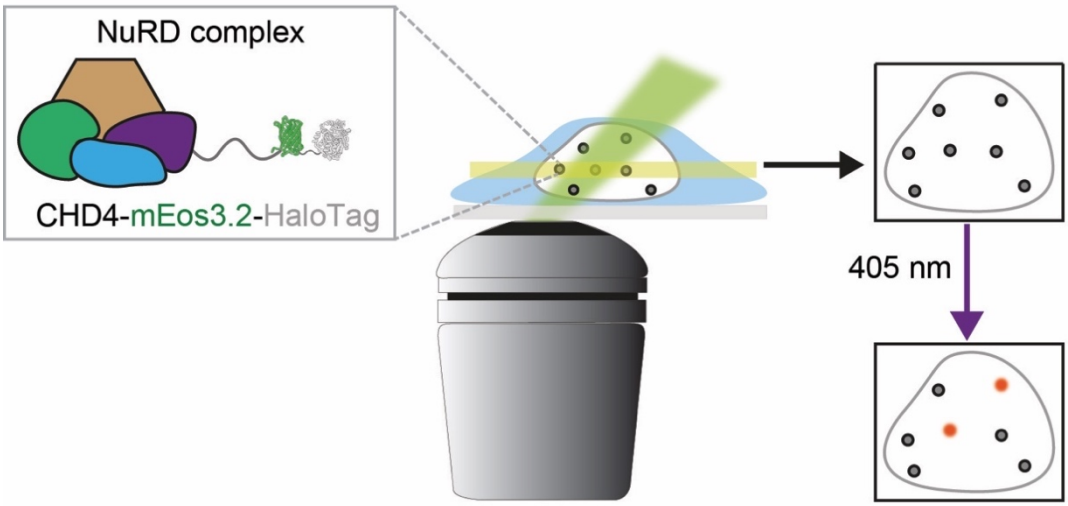

Figure 7.13. A schematic showing the SM tracking experiment. CHD4, a protein associated with the NuRD complex was tagged with mEos3.2-HaloTag and its motion tracked in 2D with oblique-angle illumination. This was done both in the absence and presence of JF_{646}.

Despite the reduction in intensity due to FRET, single FRET-enhanced mEos3.2 molecules were detected (Figure 7.14A). Furthermore, several FRET-enhanced mEos3.2-tagged CHD4 molecules showed increased on-state times compared to mEos3.2-CHD4 (Figure 7.14B). A 10 % population of FRET-enhanced mEos3.2-CHD4 molecules exhibited on-state times or trajectories greater than 99 % of mEos3.2-CHD4 molecules. The majority of CHD4 molecules were static, however a portion of FRET-enhanced mEos3.2-CHD4 molecules showed previously unseen dynamics. The population of FRET-enhanced mEos3.2-CHD4 molecules with trajectories greater than mEos3.2 underwent periods of confined diffusion interrupted by rapid linear motion (Figure 7.14C), the origins of which are unclear. However, previous work has reported the possibility of ATP-dependent chromatin remodelling (255) which may account for this diffusion.

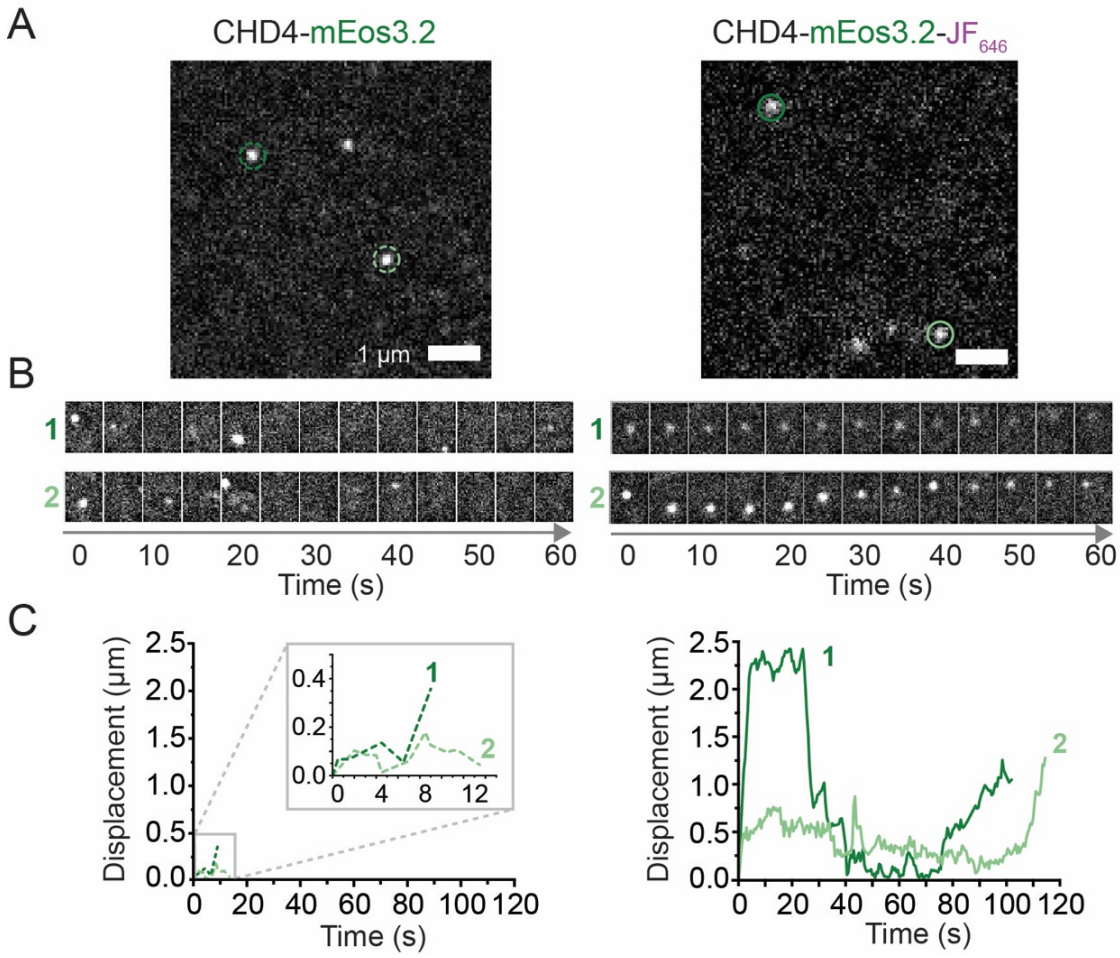

Figure 7.14. **A)** Single-frame image of the ES cell nucleus showing single CHD4 tagged with mEos3.2 (left) and FRET-enhanced mEos3.2 (right). **B)** Montages illustrating the trajectories of single CHD4 molecules. Many FRET-enhanced mEos3.2-CHD4 molecules showed longer trajectory lengths. **C)** FRET-enhanced CHD4 molecules with longer trajectory lengths (right) compared to mEos3.2-CHD4 (left) allowed for observation of dynamics unable to be seen, illustrated by displacement versus time curves.

Figure 7.15 shows the distribution of on-state times for mEos3.2 and FRET-enhanced mEos3.2 tagged CHD4. mEos3.2-CHD4 showed a mean on-state time of 1.6 ± 0.3 s, comparable to the *in vitro* result, the relative improvement to FRET-enhanced mEos3.2-CHD4 was 3.8-fold to a value of 6.0 ± 0.8 s. This was approximately 50 % of the on-state time observed from FRET-enhanced mEos3.2 *in vitro*. This was somewhat expected as the environment in the nucleus differed significantly from the ideal conditions adopted for the TIRF

experiments and it was unclear how this environment affected the solvent exposed JF_{646}.

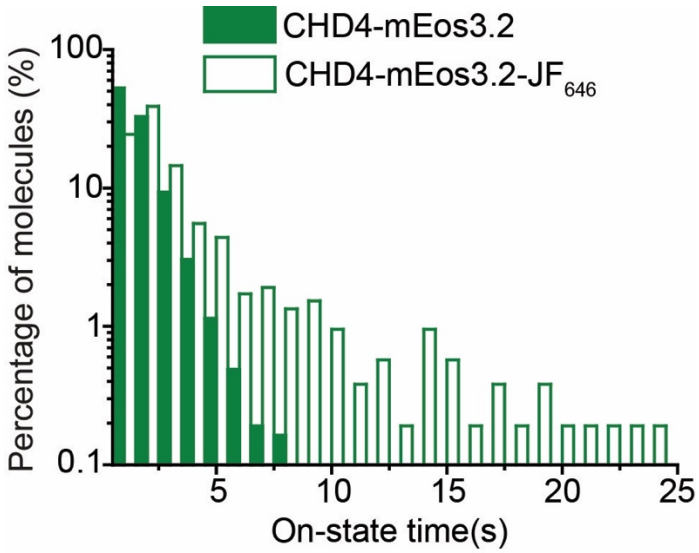

Figure 7.15. Histogram showing the distribution of on-state times (trajectories) of CHD4 tagged with mEos3.2 and FRET-enhanced mEos3.2 extracted from live ES cell tracking data. n ≥ 2500 molecules.

These experiments have demonstrated the utility of FRET-enhanced mEos3.2 in a cellular environment. Furthermore, the trajectory lengths were extended such that the likelihood of detecting low-probability changes in dynamics was increased.

7.1.8 Preliminary characterisation of FRET-enhanced mEos3.2

FRET-enhanced mEos3.2 has shown superior photophysics compared to mEos3.2 in optimal *in vitro* conditions. The utility of the construct was demonstrated in a SM tracking mode inside mammalian cells. The next objectives involve detailed characterisation of the mEos3.2 FRET in the SM regime and the dynamics and relative populations of excited states at the bulk level. Preliminary work detailing the beginnings of the characterisation of FRET-enhanced mEos3.2 is discussed below.

7.1.8.1 Trolox concentration dependence

It has been shown that there is a relationship between the off-state time of a fluorophore and Trolox concentration, with mM concentrations being optimal (257). Considering this, the impact of Trolox concentration on the properties of FRET-enhanced mEos3.2 was explored (Figure 7.16).

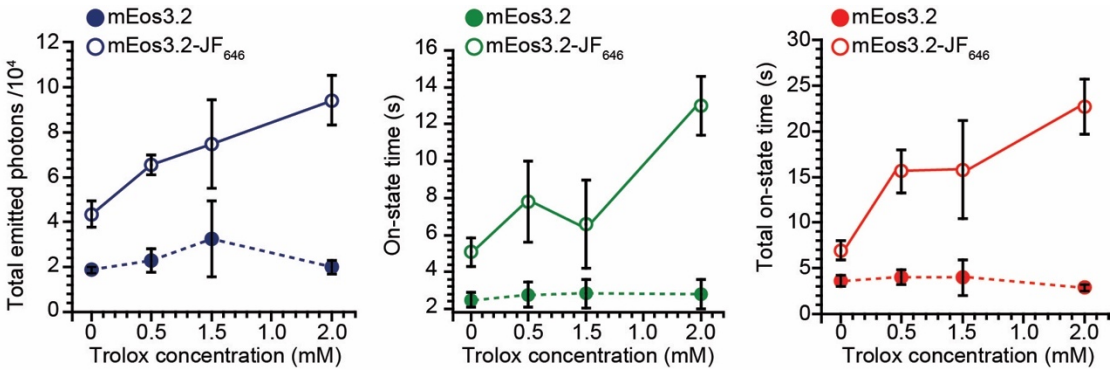

Figure 7.16. Plots showing the means of photophysical properties, total photon emission (blue), on-state time (green) and total on-state time (red) as a function of Trolox concentration. The error bars represent the standard deviations between means extracted between datasets. n ≥ 300 molecules

Surface immobilised mEos3.2 and FRET-enhanced mEos3.2 were imaged with SM TIRF in PBS with Trolox at concentrations between 0.5 and 2.0 mM. Initially Trolox was titrated up to 10 mM, however above 5 mM evidence of mEos3.2 aggregation was apparent on the surface.

There was a general positive increase in the number of emitted photons, on-state time and total on-state time with increasing Trolox concentration, however there was significant variation in the distribution of values hence the change in photophysical quantities between 0.5 and 1.0 mM cannot be considered statistically significant. These results were consistent with other observations of effect of Trolox concentration on organic fluorophore photostabilisation (258) and further confirms that the improved photophysics of FRET-enhanced mEos3.2 evolved from the existence of a stable FRET pathway. As expected

there was no change in any of the properties of mEos3.2 alone with varying Trolox concentrations.

These properties were likely dependent on the relative amount of reductant and oxidant in the imaging buffer. In this case the reductant was Trolox and the oxidant being the photochemical product, Trolox quinone. Trolox quinone is produced from the photo-oxidation of Trolox by near-UV radiation. As mEos3.2/FRET-enhanced mEos3.2 is a PCFP, converted by 405 nm light, this process likely simultaneously induced the production of Trolox quinone in unknown quantities, which may have contributed to the variation in results.

7.1.8.2 Effect of linker length

In addition to investigating changes in JF_{646} photostability on the photophysics of the FRET-enhanced mEos3.2, the effect of modifying the FRET efficiency was examined. The inter-fluorophore distance was reduced by removing the amino acid linker between the two proteins (Appendix A.3, Figure A.3.1). Theoretically, in this circumstance, k_{FRET} should increase which may improve the photostability of FRET-enhanced mEos3.2 further. Immediately after purification, bulk fluorescence spectra were collected to confirm FRET (Figure 7.17). As expected, the relative decrease and increase in mEos3.2 and JF_{646} emission intensities respectively was greater in the absence of the linker. Unfortunately, SM TIRF data was not collected due to gel and observational evidence of significant protein aggregation <24 hours after purification. However, this data may be taken as further confirmation of FRET between mEos3.2 and JF_{646}.

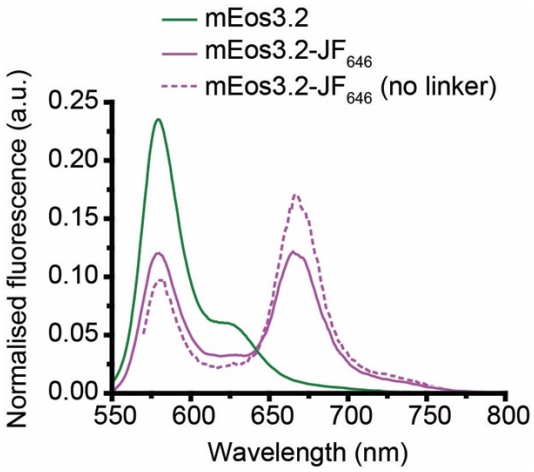

Figure 7.17. Comparison of bulk fluorescence spectra for photoconverted mEos3.2 (green line) and FRET-enhanced mEos3.2 with (solid magenta line) and without (dashed magenta line) the amino acid linker (λ_{ex}= 561 nm).

7.1.8.3 mEos3.2-AF647

It is now clear that mEos3.2-JF_{646} is an effective FRET pair and the photophysical properties of mEos3.2 in this FRET pair are improved relative to mEos3.2 alone. In order for FRET to be confirmed as the origin of this enhancement, alternative FRET pairs must be considered. Hence, the same SM characterisation was performed on another construct, mEos3.2-HaloTag-Alexa Fluor (AF) 647 (Figure 7.18A). AF647 is in the cyanine family of dyes and is a close derivative of Cy5. It has a λ_{abs} at 650 nm and a λ_{em} at 668 nm and is a very efficient absorber of photons (ε=270,000 $M^{-1}cm^{-1}$) and a moderate emitter (Φ=0.33) (48). Moreover, photostabilisation of cyanine fluorophores has been well-demonstrated with redox additives (257). These optical properties imply AF647 would be a very suitable FRET acceptor for mEos3.2. On the contrary, AF647 is prone to photo-induced conformational isomerism giving rise to cis and trans excited states. In the cis state, AF647 is a poor FRET acceptor and the efficiency is diminished (57). AF647 is also membrane impermeable (259), which presents difficulties for its use as an *in vivo* probe. mEos3.2-AF647 was designed as a second test system to further understand the origin of the

enhancement. The AF647 HaloTag ligand was not commercially available and was therefore synthesised using NHS ester coupling chemistry (see Chapter 3-Project Two materials and methods). FRET between mEos3.2 and AF647 was confirmed with bulk fluorescence spectroscopy (Figure 7.18B).

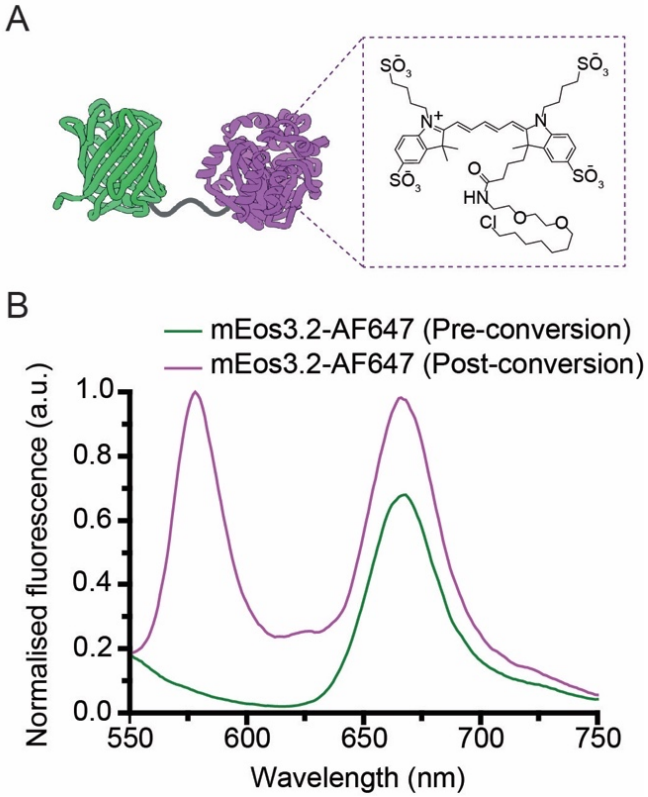

Figure 7.18. **A)** mEos3.2-HaloTag-AF647 FRET construct. **B)** Bulk fluorescence spectra of pre-photoconverted (green line) and photoconverted (magenta line) mEos3.2-AF647 illustrating the change in intensity as a result of FRET (λ_{ex}= 561 nm). Spectra were normalised to the maximum intensity value.

mEos3.2-AF647 was imaged in PBS buffer with 2 mM Trolox, and the photophysical properties were quantified in the same way as mEos3.2-JF_{646} (Figure 7.19).

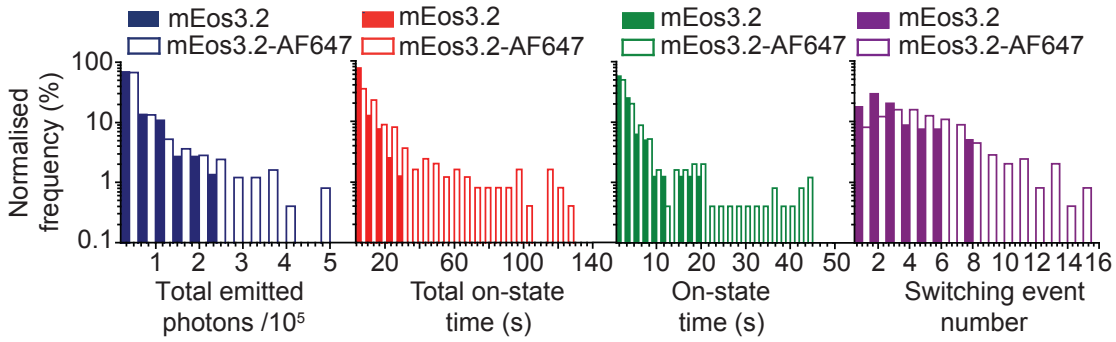

Figure 7.19. Histograms comparing the SM photophysical properties of mEos3.2 and mEos3.2-AF647 in PBS and 2 mM Trolox. The data was normalised to 100 % for mEos3.2 and FRET-enhanced mEos3.2 independently. There were n ≥ 250 molecules for each experiment.

The mean number of emitted photons increased 1.7-fold from 32693 ± 23760 to 56405 ± 14226 for mEos3.2 and mEos3.2-AF647 respectively. This increase was not as significant as that observed from mEos3.2-JF_{646}. The decrease in the number of photons emitted in each frame was 27 %, suggesting that the FRET between mEos3.2 and AF647 was less efficient than FRET between mEos3.2 and JF_{646}. Interestingly, the mean total on-state time was the most enhanced property increasing from 3.4 ± 1.1 s to 29.1 ± 10.8 s, a 9.4-fold positive change. A 3-fold change in on-state time was also observed. Unlike mEos3.2-JF_{646} these enhancements suggest a change in the blinking dynamics in this FRET construct. The number of switching events increased a factor of 2 from 2.9 ± 0.4 to 6.0 ± 0.8 blinks, this may be attributed to the excited state switching behaviour of AF647, but a more detailed characterisation would be required to confirm this. The large standard deviations were likely due to insufficient data points (≥ 250 molecules), yet, this preliminary work implies the FRET-enhanced donor phenomenon may be translated across acceptor dye classes.

7.1.9 FRET-enhanced PA-JF$_{549}$

In order to discern whether FRET-enhancement can be employed generally across PM donors, a photoactivatable (PA) organic dye, PA-JF$_{549}$ (52) was employed as a donor. The new FRET pair, PA-JF$_{549}$-JF$_{646}$ was created, termed FRET-enhanced PA-JF$_{549}$ (Figure 7.20).

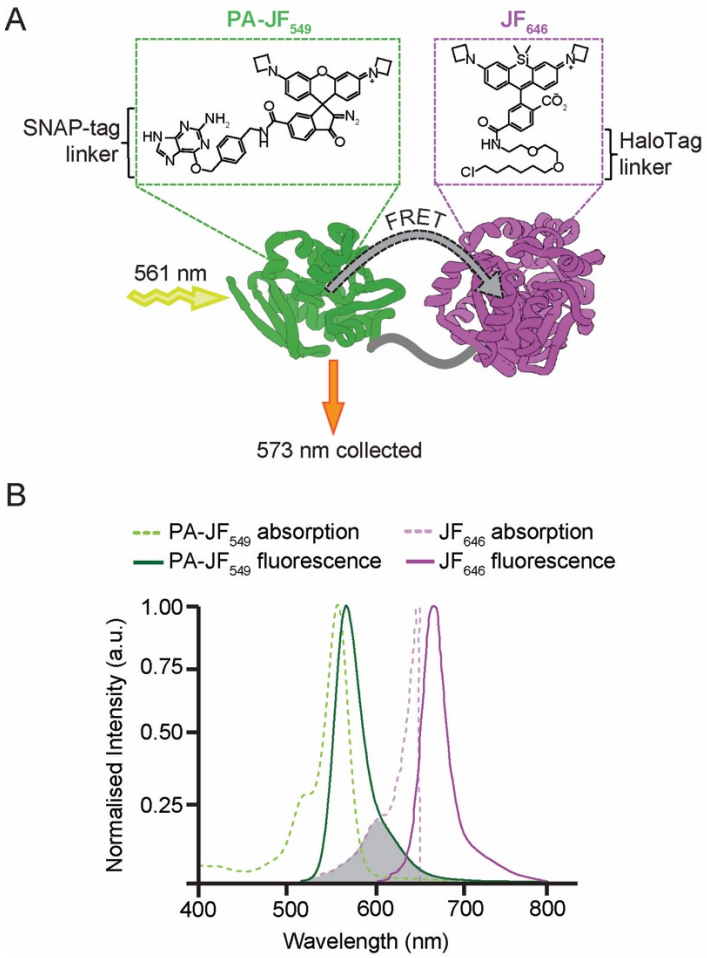

Figure 7.20. **A)** A protein fusion construct consisting of a SNAP-tag (green) and HaloTag (magenta). The SNAP tag protein was labelled with PA-JF$_{549}$ and the HaloTag protein was labelled with JF$_{646}$. In this construct PA-JF$_{549}$ was the PM donor and JF$_{646}$ formed the photostable FRET acceptor. **B)** Bulk normalised UV-vis absorption and fluorescence spectra of photoactivated PA-JF$_{549}$ and JF$_{646}$. The spectral overlap between PA-JF$_{549}$ emission spectrum and JF$_{646}$ absorption spectrum is highlighted in grey.

In order to conjugate the two fluorophores a new protein fusion construct comprised of the SNAP-tag and HaloTag proteins was expressed and purified. Each protein was able to be stoichiometrically labelled with the corresponding donor and acceptor fluorophores. Prior to photoactivation, PA-JF_{549} is a caged dye via a structurally strained spirocyclic diazoketone, which renders the dye non-fluorescent (260). Irradiation with 405 nm uncages the fluorophore to yield the fluorescent phenylacetate, rhodamine dye. In this form, PA-JF_{549} exhibited λ_{abs} 549 nm, λ_{em} of 571 nm, ε at 549 nm of 101000 $M^{-1}cm^{-1}$ and Φ of 0.88. Like JF_{646}, PA-JF_{549} is fluorogenic, and sufficient fluorescence is only achieved when conjugated to a protein such as SNAP-tag or HaloTag.

7.1.9.1 Confirming FRET between PA-JF_{549} and JF_{646}

FRET between PA-JF_{549} and JF_{646} was confirmed in the same way as previously described for mEos3.2-JF_{646}, with bulk fluorescence spectroscopy (Figure 7.21A) and fluorescence lifetime spectroscopy (Figure 7.21B).

The mean excited state lifetime measured for PA-JF_{549} was 2.9 ns which decreased in the presence of JF_{646} to 2.1 ns, which corresponded to a FRET efficiency of 0.28 ± 0.05 and a mean inter-fluorophore distance of 7 ± 3 nm. These results confirmed that PA-JF_{549}-JF_{646} underwent FRET after photo-activation.

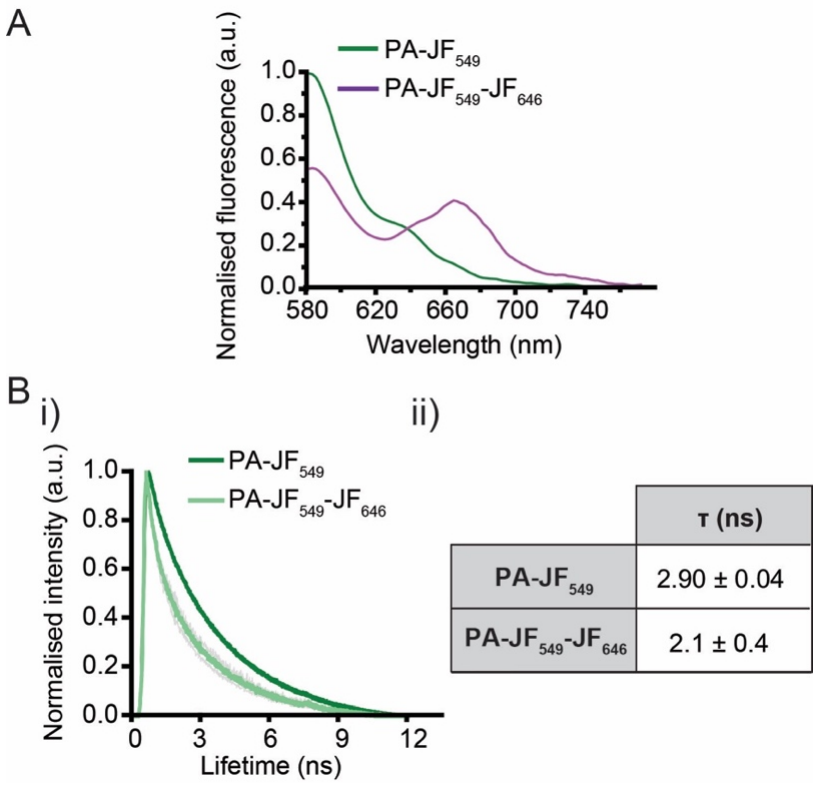

Figure 7.21. **A)** Bulk fluorescence spectra of photoactivated PA-JF_{549} with (magenta line) and without (green line) JF_{646} illustrating the change in intensity as a result of FRET (λ_{ex}= 561 nm). Spectra were normalised to the maximum intensity value and the direct excitation component subtracted. **B) i)** Fluorescence lifetime exponential decay curves of photoactivated PA-JF_{549} and PA-JF_{549}-JF_{646}. Each background corrected and independently normalised relative to the maximum intensity. **ii)** Fluorescence lifetime values extracted from fits of the decay curves, errors correspond to the standard deviation of replicate measurements. All experiments contained a minimum of n=3 replicates.

7.1.10 Single-molecule properties of FRET-enhanced PA-JF_{549}

SM TIRF measurements of PA-JF_{549} and FRET-enhanced PA-JF_{549} were performed in PBS with 2 mM Trolox as with mEos3.2 (Figure 7.22).

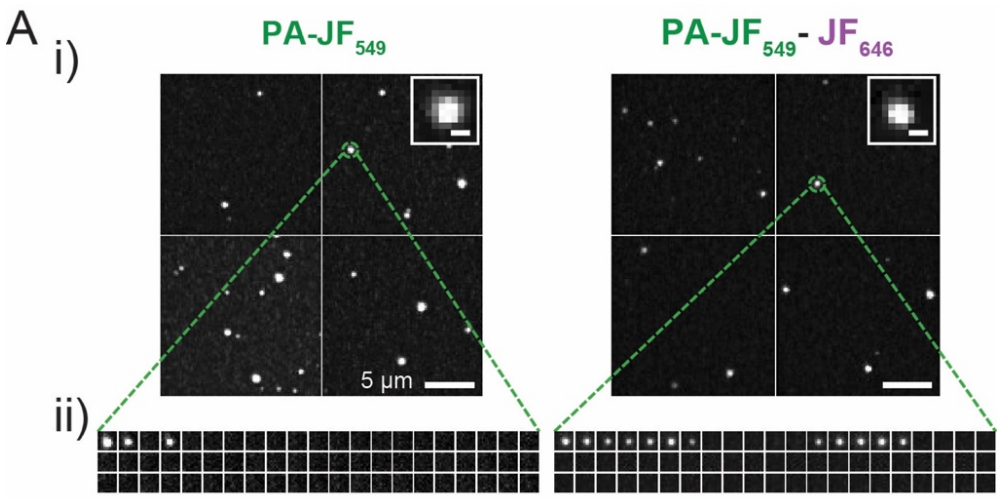

Figure 7.22. **A) i)** Maximum intensity-based time projections of SM TIRF images of PA-JF_{549} (left) and FRET-enhanced PA-JF_{549} (right) molecules adsorbed to a surface, with 2 mM Trolox in the buffer. The inset in each projection signifies a representative molecule (scale bar= 500 nm). **ii)** Representative montages showing the fluorescence of representative molecules. Each square represents the molecule in every second frame.

These *in vitro* characterisation experiments of PA-JF_{549} and FRET-enhanced PA-JF_{549} were limited by the tendency of the purified SNAP-tag-HaloTag construct to form multimers, at least in part due to the presence of an exposed cysteine residue in the SNAP-tag protein. To combat this, dithiothreitol (1 mM) was added and only dilute samples could be imaged. In addition, problems with surface adherence of the protein construct were experienced. The construct had a very weak affinity for positively charged poly-L-lysine and was prone to detach from this coated surface. The protein had a greater affinity for argon plasma cleaned glass, which was negatively charged, but still had a propensity to detach from the surface. Despite this improvement, washing procedures employed to reduce background by removing unbound molecules resulted in very few single-molecules present in the first frame per acquisition. To ensure that the results of this experiment were statistically relevant, approximately >20 acquisitions were collected for each condition. As a result, error values for the extracted photophysical parameters could not be obtained from the standard deviation in the mean value of each acquisition and bootstrapping was used to

determine the standard error of the mean. Furthermore, only molecules that underwent single-step photobleaching and were therefore deemed to be monomers were analysed.

Photophysical analysis of *in vitro* SM TIRF data of PA-JF$_{549}$ and FRET-enhanced PA-JF$_{549}$ was performed (Figure 7.23) and the properties of FRET-enhanced PA-JF$_{549}$ were compared relative to PA-JF$_{549}$ alone.

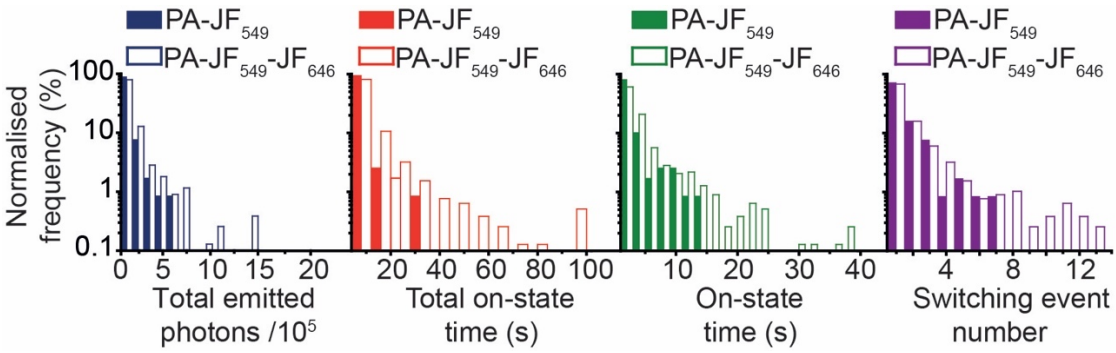

Figure 7.23. Histograms comparing the SM photophysical properties of PA-JF$_{549}$ and FRET-enhanced PA-JF$_{549}$ in PBS and 2 mM Trolox. The data was normalised to 100 % for mEos3.2 and FRET-enhanced mEos3.2 independently. There were n ≥ 150 molecules for each experiment.

A reduction in the intensity of FRET-enhanced PA-JF$_{549}$ of 19 ± 10 % was observed, close to the value expected from the bulk FRET efficiency calculation. Similar to FRET-enhanced mEos3.2 no significant change in the number of switching events was observed. Increases of 2.3-fold for on-state time and 2.0- and 1.7-fold increases, respectively, for the total on-state time and photon emission of FRET-enhanced PA-JF$_{549}$ were measured. As with FRET-enhanced mEos3.2, FRET-enhanced PA-JF$_{549}$ showed a relationship between intensity and total on-state time, with the lowest intensity molecules showing the greatest total on-state times (Figure 7.24).

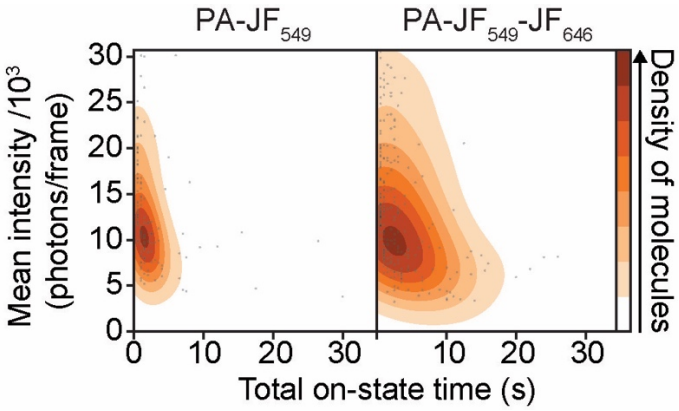

Figure 7.24. Density plots of the mean number of photons emitted per frame versus total on-state time for PA-JF_{549} and FRET-enhanced PA-JF_{549} in PBS with 2 mM Trolox.

Although the relative increases were lower compared to FRET-enhanced mEos3.2, these data suggest the potential generality of the approach. Moreover, these data provide support for the hypothetical model described in section 7.1.6. In this case, both the donor and acceptor, PA-JF_{549} and JF_{646}, were solvent exposed and therefore were able to interact with Trolox. Hence, a minor increase in the photon budget was expected due to the addition of another pathway for ground-state return, which alleviated photobleaching. Under the assumption that Trolox behaved in the same way with both PA-JF_{549} and JF_{646}, the non-linear photostabilising effect, experienced by FRET-enhanced mEos3.2, would not have occurred in this circumstance. This situation is unlikely; however, the data suggested that PA-JF_{549} experienced the effect of Trolox.

7.2 Conclusions and Future Work

Single-molecule research has reached a stage at which the next key challenge is the development of better fluorophores that underlie the technique. This includes not only the synthesis of new organic fluorophores but also alternative novel strategies to augment existing technologies, including ways to modify the photophysics of FPs to improve properties such as photostability. The work in

this chapter has addressed this with the development and application of a novel concept designed to modify the photophysical properties of PMFPs. In addition, preliminary work has been shown with the eventual aim of quantitatively characterising this concept.

A new FRET construct comprised of PCFP mEos3.2 as a donor and silicon rhodamine derived organic fluorophore JF_{646} as the acceptor was developed. FRET was exploited to modify the photophysical properties of mEos3.2 in the construct, termed FRET-enhanced mEos3.2, by providing an additional excited-state pathway to compete with photobleaching. Moderate improvements in mEos3.2 fluorescence properties such as on-state time, total on-state time and total photon emission resulted from ET to JF_{646}, however photobleaching of the acceptor was a limiter of the FRET. Employing a triplet state quencher, Trolox, to stabilise the solvent exposed JF_{646} imparted an indirect photostabilising effect on FRET-enhanced mEos3.2 and significantly improved enhancements in photophysical properties. This method was shown to be successful in a live-cell single-molecule tracking application when the dynamics of single CHD4 protein molecules were observed for longer times in the nuclei of ES cells. The concept of PM donor FRET-enhancement was shown to have some dependence on the concentration of Trolox and extended to another acceptor, AF647, a red-emitting cyanine dye, and an alternative donor, organic fluorophore, PA-JF_{549}. This was demonstrated by *in vitro* SM TIRF measurements.

This work represents the beginnings of a potentially universal method for improving existing fluorophores for a multitude of SM and SR fluorescence applications. There are several possibilities for further research based on the ground-work of this project. I believe the primary objectives involve detailed characterisation of the mEos3.2 FRET in the SM regime and the dynamics and relative populations of excited states at the bulk level.

Initially SM experiments would involve evaluation of the effect of excitation intensity to explore the saturation of the singlet excited state and assess whether emissive behaviour differs from expected hyperbolic dependence on pump power. Secondly, the investigation of alternative buffer conditions, including alternative redox additives such as cyclooctatetraene and 4-nitrobenzyl alcohol and D_2O based buffers will be explored. As FRET-enhancement of donor fluorophores has shown to be applicable with both rhodamine and cyanine acceptors in this work, it would be interesting to evaluate the effect with an oxazine acceptor in the absence and presence of blinking inducing buffers. Should a difference be observed, this may provide a method to create a novel environment sensitive PMFP. The preliminary characterisation suggests this may be applied to alternative PM acceptors, illustrated FRET-enhance PA-JF_{549}, therefore it may be possible to extend the functionality to other PM fluorophores including reversible photoswitchable and photoactivatable FPs. By systematic modification of properties, the potential for selective control of FP photophysics will be investigated.

Finally, bulk time-resolved transient absorption spectroscopy may be used to explore the formation of both singlet and triplet electronic excited states as well as excited state rate-constants. This would enable the complete quantification of the electronic state diagram and proof of the validity of the hypothetical model proposed in this work. Should the theory be correct, it is anticipated that the photon budget of the FRET-enhanced donor is linked to the photostability and photon budget of the acceptor.

A complete characterisation of this method will facilitate the possibility of simple, selective tuning of fluorophore photophysical properties for specific experiments. As opposed to the necessary use of multiple dyes individually incapable of fulfilling the requirements of the experiment, I envision individual fluorophores being selectively modified to perform optimally for the research task.

Concluding Remarks

The work reported in this thesis provides a detailed account of the development of novel fluorophores for single-molecule (SM) and super-resolution (SR) bioimaging. Moreover, this research has provided new approaches toward understanding the complex nature of the fluorophores that form the foundation of these techniques. The scope of this body of work spans two separate areas of biological interest and are therefore discussed in two respective parts (Project One and Project Two). Despite this, the fundamental objective remained constant; *to develop better fluorophores and new ways of understanding and augmenting existing technologies in single-molecule and super-resolution fluorescence microscopy.*

The main experimental technique used for this research was SM fluorescence microscopy, a method that, despite significant advances, could be considered in its infancy. However, SM fluorescence is underpinned by well-established physical principles, which are detailed in Chapters 1 and 2. As illustrated in Chapter 2, understanding these principles enabled the design and construction of a bespoke SM fluorescence microscope, which was optimised for the experiments described in Project One, Chapters 5,6 and Project Two, Chapter 7.

Project One is focussed on fluorescent probes for the study of neurodegenerative disease. Chapter 4 provides an introductory narrative to the key principles discussed in the proceeding results chapters. Chapter 5 details the characterisation of a novel library of fluorescent dyes derived from amyloid dye, Thioflavin-T (ThT) and a discussion of their unique bulk and single-aggregate level properties. Many of the dyes had **optical properties competitive with ThT** and one dye, **mE10, showed superior properties**. This work has allowed for **greater understanding of the relationships between**

structure and photophysical function. Moreover, it has laid the foundation for further development of probes with multi-functional properties. Chapter 6 shows the development of four new probes based on the ThT scaffold and combined with a boronate ester moiety for bifunctional sensing of both amyloid aggregates and reactive oxygen species. This hypothesis was applied at the bulk and single-aggregate level and **two probes, BE01 and BE02, were shown to be capable of simultaneously detecting both species *in vitro***. This work yielded one first author publication in the journal Royal Society Open Science (publication 1 in the Publications section).

Project Two re-directs the investigation toward photomodulatable probes used for SR and single-molecule tracking (SMT) based bioimaging applications. The focus of Chapter 7 is the development of new ways to improve the photophysics of photomodulatable fluorophores through Förster resonance energy transfer (FRET). This was implemented through the development, initial characterisation and application of novel FRET construct **mEos3.2-JF$_{646}$**. By combining FRET and existing technologies to improve organic dye photostability the **photophysical properties of mEos3.2 were enhanced significantly, in some cases by greater than 10-fold**. The chapter then detailed the early stages of a comprehensive characterisation of the photophysics through modification of multiple parameters. This work represents the beginnings of a novel way to modulate the properties of fluorophores and optimise them for specific experiments. This research yielded one first author publication in the journal Nature Communications (publication 2 in the Publications section).

It is through the understanding of the complex nature of fluorophores that research in the field will progress and new frontiers reached.

Appendices

A.1 Appendix to Chapter 5

A.1.1 Single-aggregate fluorescence image analysis

This code was written as a macro in ImageJ and was used to extract the mean fluorescence intensity of single aggregates in TIRF images.

```
run("Clear Results");
requires("1.33s");
  dir = getDirectory("Choose a Directory ");
  count = 0;
  countFiles(dir);
  n = 0;
 setBatchMode(true);
  processFiles(dir);
  function countFiles(dir) {
     list = getFileList(dir);
     for (i=0; i<list.length; i++) {
 if (!startsWith(list[i],"Log")){
       if (endsWith(list[i], "/"))
           countFiles(""+dir+list[i]);
         else
           count++;
     }
```

```
  }
}
   function processFiles(dir) {
      list = getFileList(dir);
      for (i=0; i<list.length; i++) {
if (!startsWith(list[i],"Log")){
         if (endsWith(list[i], "/"))
             processFiles(""+dir+list[i]);
         else {
            showProgress(n++, count);
            path = dir+list[i];
            processFile(path);
         }
}
      }
  }

  function processFile(path) {
       if (endsWith(path, ".tif") || endsWith(path, ".tiff"))
       {
                    open(path);
                    file= getTitle();
                    root = substring(file,0,indexOf(file, ".tif"));
                    setBatchMode(false);
                    title=getTitle();
                    selectWindow(title);
```

```
            makeRectangle(130, 85, 360, 360);

            run("Crop");

            run("Z Project...", "start=20 stop=200 projection=[Sum Slices]");

            run("Set Measurements...", "area mean standard min integrated
            redirect=None decimal=2");

            run("Measure");

            meanPix=getResult("Mean");

            maxPix=getResult("Max");

            stdPix=getResult("Standard");

            Threshold=((meanPix*2+stdPix));

            setThreshold(Threshold, maxPix);;

            run("Set Measurements...", "area mean min redirect=None
            decimal=2");

            run("Analyze Particles...", "size=0.7-Infinity show=Masks display
            clear include in_situ");

            if (isOpen("Results"))

            {

                selectWindow("Results");

                saveAs("Text", ""+dir+"\\"+title+"_AnalyzedParticles.txt");

            }

            else

            {

                setResult("AnalyzedParticles",0,0);

            }

            run("Close All");

    }

}
```

A.1.2 Fluorescence standards

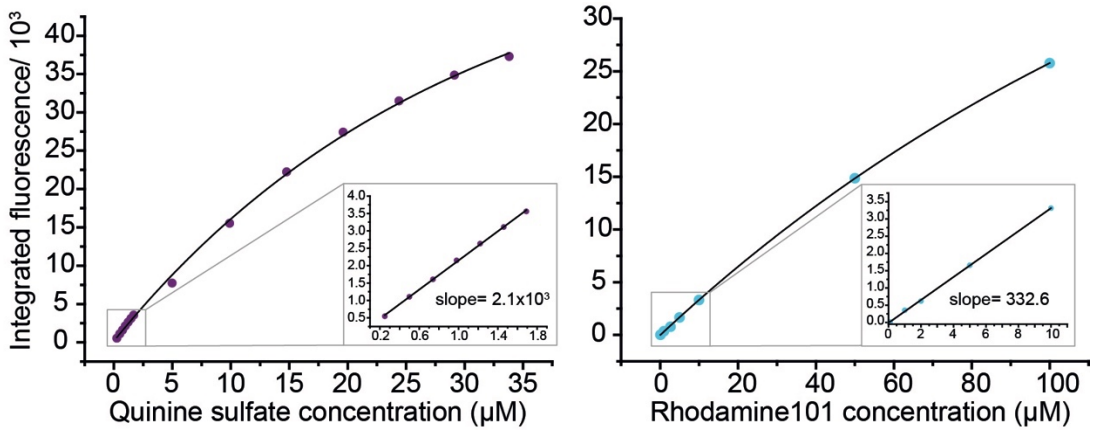

Figure A.1.2. Calibration curves of fluorescence standards quinine sulfate and Rhodamine 101. The linear parts of the curves were fitted with a straight-line equation (y=mx + c).

A.2 Appendix to Chapter 6

A.2.1 Boronate ester NMR spectra

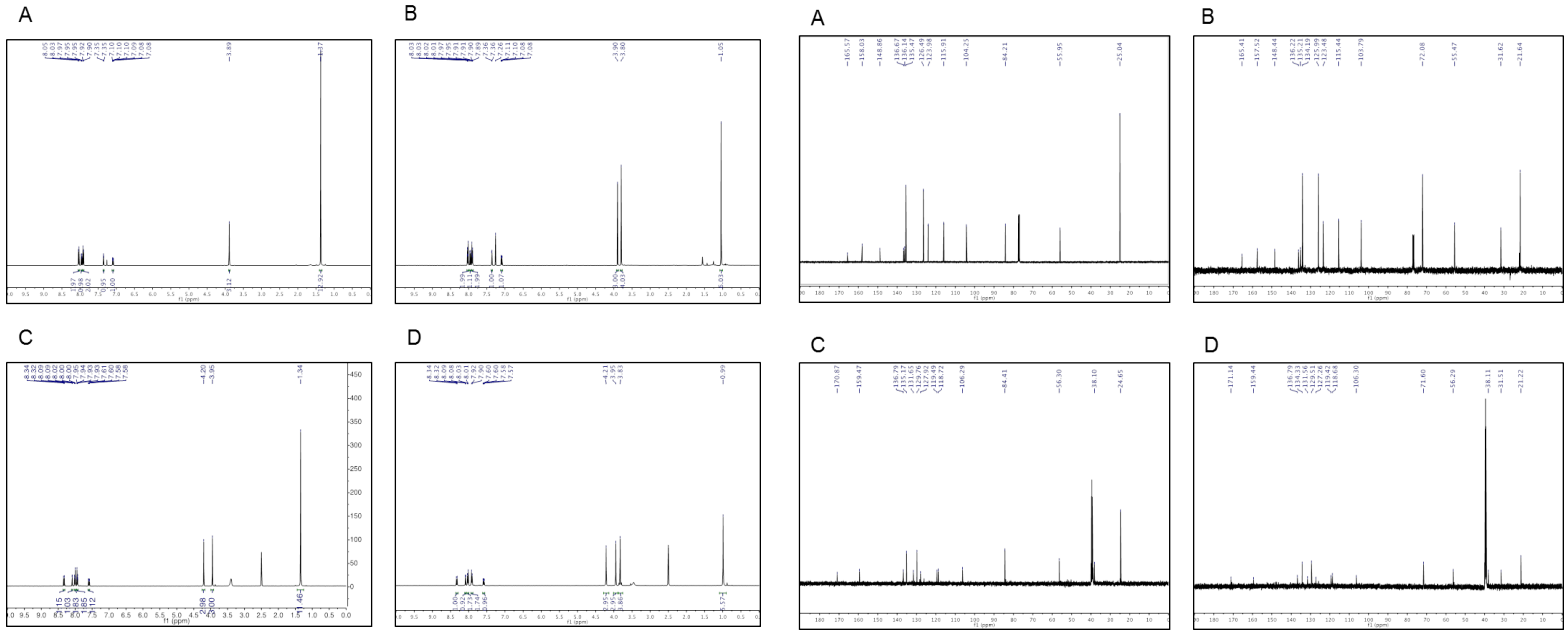

Figure A.2.1. ^{1}H NMR (left) and ^{13}C NMR (right) spectra of **A)** BE01 **B)** BE02 **C)** mBE01 and **D)** mBE02.

A.2.2 LCMS and fluorescence analysis of boronate ester reactions

Table A.2.1 Assessment of reaction of BE and mBE probes with H_2O_2 via LCMS.

		Hydrolyzed			Boronate ester			Oxidized		
	Time point (minutes)	Mass ($gmol^{-1}$)	Retention Time (minutes)	Rel. Area (%)	Mass ($gmol^{-1}$)	Retention Time (minutes)	Rel. Area (%)	Mass ($gmol^{-1}$)	Retention Time (minutes)	Rel. Area (%)
BE01	0	286.26	1.88	65	368.24	3.34	35			
BE01	60	286.18	1.88	47	368.40	3.34	53			
BE01 and 100 μM H_2O_2	60							258.14	2.04	100
BE02	0	286.26	1.88	100						
BE02	60	286.26	1.88	100						
BE02 and 100 μM H_2O_2	60	286.34	1.88	10				258.22	2.04	90
mBE01	0	300.28	0.49	100						
mBE01	60	300.28	0.49	100						
mBE01 and 100 μM H_2O_2	60	300.12	0.49	27				272.24	0.58	64
mBE02	0	300.20	0.49	100						
mBE02	60	300.28	0.49	100						
mBE02 and 100 μM H_2O_2	60	300.28	0.49	12				272.32	0.58	70

	Oxidized, de-methylated			
	Time point (minutes)	Mass (gmol-1)	Retention Time (minutes)	Rel. Area (%)
mBE01 and 100 μM H_2O_2	60	258.22	2.04	9.47
mBE02 and 100 μM H_2O_2	60	258.22	2.04	18.63

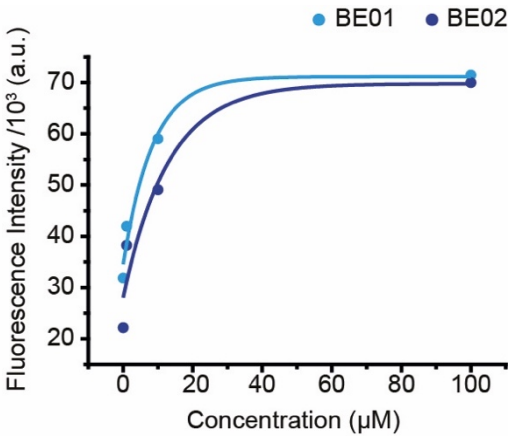

Figure A.2.2. Plot of total integrated emission of BE01 and BE02 against H_2O_2 concentration.

A.2.3 Analysis of boronate ester interactions with αSyn aggregates

Table A.2.3. Total integrated emission intensities of the BE, mBE dyes and ThT in the presence of 10 μM αSyn aggregates from three different aggregation mixtures

	Total Integrated emission /10^3			
Dye	**Aggregation 1**	**Aggregation 2**	**Aggregation 3**	**S.D.**
BE01	64.291	58.893	53.290	4.491
BE02	59.103	51.374	60.188	3.924
mBE01	6.842	8.321	7.017	0.659
mBE02	10.068	8.673	11.232	1.046
BE-Ox	60.963	34.842	26.312	14.741
mBE-Ox	0.885	0.458	1.923	0.615

A.3 Appendix to Chapter 7

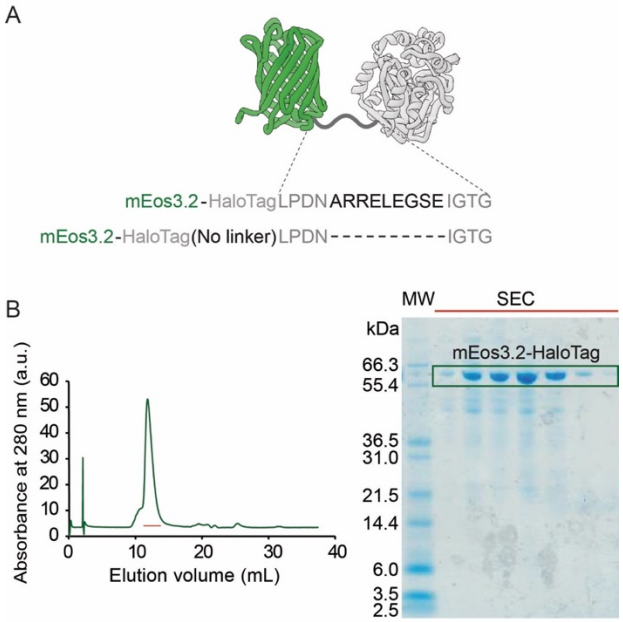

Figure A.3.1. **A)** Sequences of the linker region of the two constructs. **B)** Purification of the mEos3.2-HaloTag fusion protein.

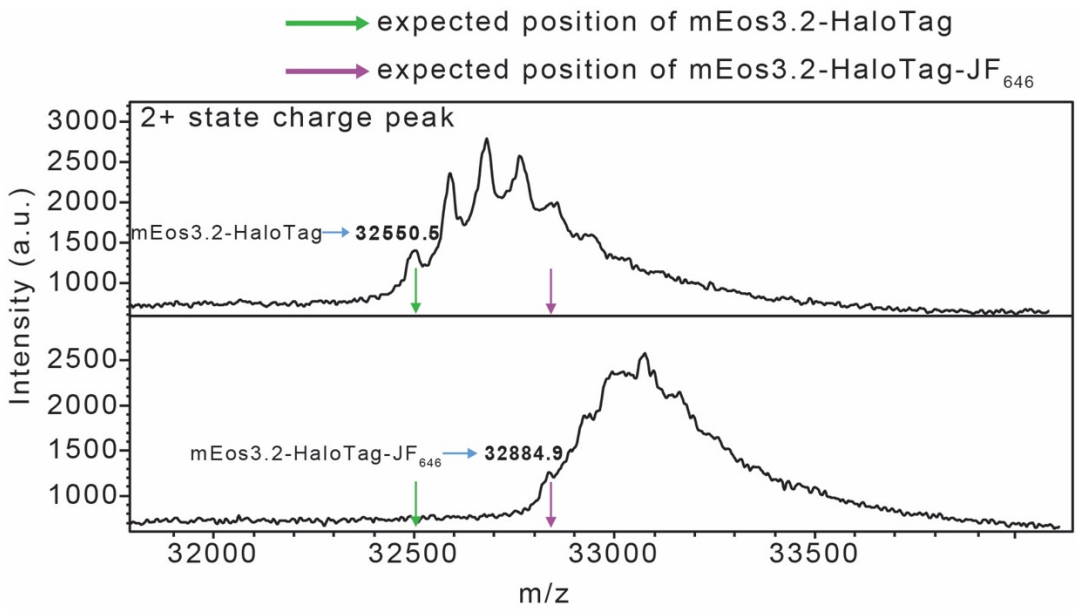

Figure A.3.2. Mass spectrum of JF_{646} labelled and unlabelled mEos3.2.

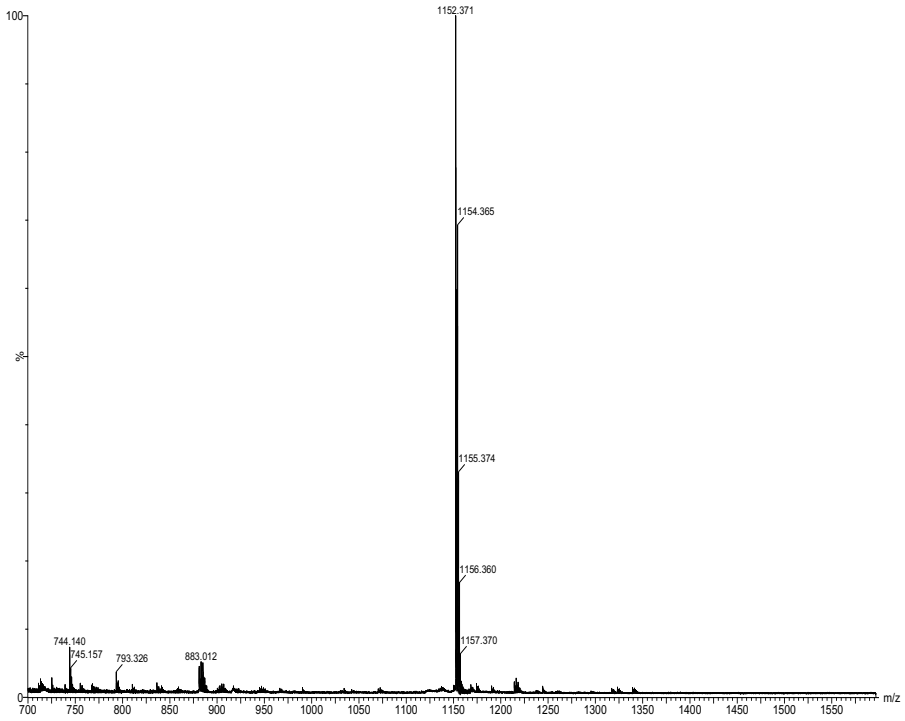

Figure A.3.3. MALDI mass spectrum of AF647-HaloTag ligand.

References

1. Atkins, P., and J. De Paula. 2014. Physical Chemistry. In: Atkins Physical Chemistry. . pp. 946–951.

2. Sauer, M., J. Hofkens, and J. Enderlein. 2011. Handbook of Fluorescence Spectroscopy and Imaging. .

3. Lakowicz, J.R. 2006. Principles of Fluorescence Spectroscopy Principles of Fluorescence Spectroscopy. .

4. Grimm, J.B., A.K. Muthusamy, Y. Liang, T.A. Brown, W.C. Lemon, R. Patel, R. Lu, J.J. Macklin, P.J. Keller, N. Ji, and L.D. Lavis. 2017. A general method to fine-tune fluorophores for live-cell and in vivo imaging. Nat. Methods. 14: 987–994.

5. Lord, S.J., N.R. Conley, H.L.D. Lee, S.Y. Nishimura, A.K. Pomerantz, K.A. Willets, Z. Lu, H. Wang, N. Liu, R. Samuel, R. Weber, A. Semyonov, M. He, R.J. Twieg, and W.E. Moerner. 2009. DCDHF fluorophores for single-molecule imaging in cells. ChemPhysChem. 10: 55–65.

6. Wang, Z., Y. Xie, K. Xu, J. Zhao, and K.D. Glusac. 2015. Diiodobodipy-styrylbodipy Dyads: Preparation and Study of the Intersystem Crossing and Fluorescence Resonance Energy Transfer. J. Phys. Chem. A. 119: 6791–6806.

7. Veerman, J.A., M.F. Garcia-Parajo, L. Kuipers, and N.F. Van Hulst. 1999. Time-varying triplet state lifetimes of single molecules. Phys. Rev. Lett. 83: 2155–2158.

8. Willets, K.A., O. Ostroverkhova, M. He, R.J. Twieg, and W.E. Moerner. 2003. Novel fluorophores for single-molecule imaging. J. Am. Chem. Soc.

125: 1174–1175.

9. Haidekker, M.A., and E.A. Theodorakis. 2007. Molecular rotors—fluorescent biosensors for viscosity and flow. Org. Biomol. Chem. 5: 1669–1678.

10. Drexhage, K.H. 1976. Fluorescence efficiency of laser dyes. J. Res. Natl. Bur. Stand. Sect. A Phys. Chem. 80A: 421.

11. Grabowski, Z.R., K. Rotkiewicz, and W. Rettig. 2003. Structural Changes Accompanying Intramolecular Electron Transfer: Focus on Twisted Intramolecular Charge-Transfer States and Structures. Chem. Rev. 103: 3899–4031.

12. Fu, M., Y. Xiao, X. Qian, D. Zhao, and Y. Xu. 2008. A design concept of long-wavelength fluorescent analogs of rhodamine dyes: replacement of oxygen with silicon atom. Chem. Commun. : 1780.

13. Sauer, M., J. Hofkens, and J. Enderlein. 2011. Fluorophores and Fluorescent Labels. Handb. Fluoresc. Spectrosc. Imaging from Ensemble to Single Mol. : 31–60.

14. Lippert, E. 1957. Spektroskopische Bestimmung des Dipolmomentes aromatischer Verbindungen im ersten angeregten Singulettzustand. Zeitschrift für Elektrochemie, Berichte der Bunsengesellschaft für Phys. Chemie. 61: 962–975.

15. Mataga, N., Y. Kaifu, and M. Koizumi. 1956. Solvent Effects Upon Fluorescence Spectra and the Dipole Moments of Excited Molecules. Bull. Chem. Soc. Jpn. 29: 465–470.

16. Bongiovanni, M.N., J. Godet, M.H. Horrocks, L. Tosatto, A.R. Carr, D.C. Wirthensohn, R.T. Ranasinghe, J.E. Lee, A. Ponjavic, J. V. Fritz, C.M. Dobson, D. Klenerman, and S.F. Lee. 2016. Multi-dimensional super-

resolution imaging enables surface hydrophobicity mapping. Nat. Commun. 7: 13544.

17. Klymchenko, A.S. 2017. Solvatochromic and Fluorogenic Dyes as Environment-Sensitive Probes: Design and Biological Applications. Acc. Chem. Res. 50: 366–375.

18. Stryer, L. 1966. Excited-State Proton-Transfer Reactions. A Deuterium Isotope Effect on Fluorescence. J. Am. Chem. Soc. 88: 5708–5712.

19. Lee, S.F., Q. Vérolet, and A. Fürstenberg. 2013. Improved super-resolution microscopy with oxazine fluorophores in heavy water. Angew. Chemie - Int. Ed. 52: 8948–8951.

20. Ong, W.Q., Y.R. Citron, J. Schnitzbauer, D. Kamiyama, and B. Huang. 2015. Heavy water: a simple solution to increasing the brightness of fluorescent proteins in super-resolution imaging. Chem. Commun. 51: 13451–13453.

21. Gayrard, C., and N. Borghi. 2016. FRET-based Molecular Tension Microscopy. Methods. 94: 33–42.

22. Shi, J., F. Tian, J. Lyu, and M. Yang. 2015. Nanoparticle based fluorescence resonance energy transfer (FRET) for biosensing applications. J. Mater. Chem. B. 3: 6989–7005.

23. Sekar, R.B., and A. Periasamy. 2003. Fluorescence resonance energy transfer (FRET) microscopy imaging of live cell protein localizations. J. Cell Biol. 160: 629–633.

24. Yasuda, R. 2006. Imaging spatiotemporal dynamics of neuronal signaling using fluorescence resonance energy transfer and fluorescence lifetime imaging microscopy. Curr. Opin. Neurobiol. 16: 551–561.

25. Holzmeister, P., B. Wünsch, A. Gietl, and P. Tinnefeld. 2014. Single-

molecule photophysics of dark quenchers as non-fluorescent FRET acceptors. Photochem. Photobiol. Sci. 13: 853–858.

26. Schuler, B., and W.A. Eaton. 2008. Protein folding studied by single-molecule FRET. Curr. Opin. Struct. Biol. 18: 16–26.

27. Deniz, A.A., T.A. Laurence, G.S. Beligere, M. Dahan, A.B. Martin, D.S. Chemla, P.E. Dawson, P.G. Schultz, and S. Weiss. 2000. Single-molecule protein folding: Diffusion fluorescence resonance energy transfer studies of the denaturation of chymotrypsin inhibitor 2. Proc. Natl. Acad. Sci. 97: 5179–5184.

28. Gambin, Y., and A.A. Deniz. 2010. Multicolor single-molecule FRET to explore protein folding and binding. Mol. Biosyst. 6: 1540.

29. Chung, H.S., and W.A. Eaton. 2018. Protein folding transition path times from single molecule FRET. Curr. Opin. Struct. Biol. 48: 30–39.

30. Lakowicz, J.R. 2006. Principles of fluorescence spectroscopy. Princ. Fluoresc. Spectrosc. : 1–954.

31. Kasha, M. 1950. Characterization of electronic transitions in complex molecules. Discuss. Faraday Soc. 9: 14–19.

32. Eggeling, C., J. Widengren, R. Rigler, and C.A.M. Seidel. 1998. Photobleaching of Fluorescent Dyes under Conditions Used for Single-Molecule Detection: Evidence of Two-Step Photolysis. Anal. Chem. 70: 2651–2659.

33. Dickson, R.M., A.B. Cubitt, R.Y. Tsien, and W.E. Moerner. 1997. On/off blinking and switching behaviour of single molecules of green fluorescent protein. Nature. 388: 355–358.

34. Moerner, W.E., Y. Shechtman, and Q. Wang. 2015. Single-molecule spectroscopy and imaging over the decades. Faraday Discuss. 184: 9–

36.

35. Zondervan, R., F. Kulzer, S.B. Orlinskii, and M. Orrit. 2003. Photoblinking of rhodamine 6G in poly(vinyl alcohol): Radical dark state formed through the triplet. J. Phys. Chem. A. 107: 6770–6776.

36. Cordes, T., M. Strackharn, S.W. Stahl, W. Summerer, C. Steinhauer, C. Forthmann, E.M. Puchner, J. Vogelsang, H.E. Gaub, and P. Tinnefeld. 2010. Resolving single-molecule assembled patterns with superresolution blink-microscopy. Nano Lett. 10: 645–651.

37. Gao, J., J. Chen, and H. Wang. 2017. Super-resolution imaging of membrane heterogeneity. In: Membrane Biophysics: New Insights and Methods. . pp. 117–145.

38. Heilemann, M., S. Van De Linde, A. Mukherjee, and M. Sauer. 2009. Super-resolution imaging with small organic fluorophores. Angew. Chemie - Int. Ed. 48: 6903–6908.

39. van de Linde, S., I. Krstić, T. Prisner, S. Doose, M. Heilemann, and M. Sauer. 2011. Photoinduced formation of reversible dye radicals and their impact on super-resolution imaging. Photochem. Photobiol. Sci. 10: 499–506.

40. Eggeling, C., J. Widengren, R. Rigler, and C.A.M. Seidel. 1999. Photostability of Fluorescent Dyes for Single-Molecule Spectroscopy: Mechanisms and Experimental Methods for Estimating Photobleaching in Aqueous Solution. In: Applied Fluorescence in Chemistry, Biology and Medicine. . pp. 193–240.

41. Kubitscheck, U., O. Kückmann, T. Kues, and R. Peters. 2000. Imaging and tracking of single GFP molecules in solution. Biophys. J. 78: 2170–2179.

42. Ha, T., and P. Tinnefeld. 2012. Photophysics of Fluorescence Probes for Single Molecule Biophysics and Super-Resolution Imaging. Annu Rev Phys Chem. 63: 595–617.

43. Jiménez-Banzo, A., X. Ragàs, S. Abbruzzetti, C. Viappiani, B. Campanini, C. Flors, and S. Nonell. 2010. Singlet oxygen photosensitisation by GFP mutants: oxygen accessibility to the chromophore. Photochem. Photobiol. Sci. 9: 1336.

44. Jiménez-Banzo, A., S. Nonell, J. Hofkens, and C. Flors. 2008. Singlet oxygen photosensitization by EGFP and its chromophore HBDI. Biophys. J. 94: 168–172.

45. Greenbaum, L., C. Rothmann, R. Lavie, and Z. Malik. 2000. Green fluorescent protein photobleaching: A model for protein damage by endogenous and exogenous singlet oxygen. Biol. Chem. 381: 1251–1258.

46. Dedecker, P., F.C. De Schryver, and J. Hofkens. 2013. Fluorescent proteins: Shine on, you crazy diamond. J. Am. Chem. Soc. 135: 2387–2402.

47. Starck, M., R. Pal, and D. Parker. 2016. Structural Control of Cell Permeability with Highly Emissive Europium(III) Complexes Permits Different Microscopy Applications. Chem. - A Eur. J. 22: 570–580.

48. To, A.G., F. Probes, and L. Technologies. 2010. The Molecular Probes® Handbook. Mol. Probes® Handb. : 99–121.

49. Taneja, L., A.K. Sharma, and R.D. Singh. 1995. Study of photophysical properties of Coumarins: substituent and concentration dependence. J. Lumin. 63: 203–214.

50. Kubin, R.F., and A.N. Fletcher. 1982. Fluorescence quantum yields of

some rhodamine dyes. J. Lumin. 27: 455–462.

51. Grimm, J.B., B.P. English, J. Chen, J.P. Slaughter, Z. Zhang, A. Revyakin, R. Patel, J.J. Macklin, D. Normanno, R.H. Singer, T. Lionnet, and L.D. Lavis. 2015. A general method to improve fluorophores for live-cell and single-molecule microscopy. Nat. Methods. 12: 244–250.

52. Grimm, J.B., B.P. English, H. Choi, A.K. Muthusamy, B.P. Mehl, P. Dong, T.A. Brown, J. Lippincott-Schwartz, Z. Liu, T. Lionnet, and L.D. Lavis. 2016. Bright photoactivatable fluorophores for single-molecule imaging. Nat. Methods. 13: 985–988.

53. Beija, M., C.A.M. Afonso, and J.M.G. Martinho. 2009. Synthesis and applications of Rhodamine derivatives as fluorescent probes. Chem. Soc. Rev. 38: 2410.

54. Lukinavičius, G., K. Umezawa, N. Olivier, A. Honigmann, G. Yang, T. Plass, V. Mueller, L. Reymond, I.R. Corrêa Jr, Z.-G. Luo, C. Schultz, E.A. Lemke, P. Heppenstall, C. Eggeling, S. Manley, and K. Johnsson. 2013. A near-infrared fluorophore for live-cell super-resolution microscopy of cellular proteins. Nat. Chem. 5: 132–139.

55. Wiederschain, G.Y. 2011. The Molecular Probes handbook. A guide to fluorescent probes and labeling technologies. Biochem. 76: 1276–1276.

56. Levitus, M., and S. Ranjit. 2011. Cyanine dyes in biophysical research: The photophysics of polymethine fluorescent dyes in biomolecular environments. Q. Rev. Biophys. 44: 123–151.

57. White, S.S., H. Li, R.J. Marsh, J.D. Piper, N.D. Leonczek, N. Nicolaou, A.J. Bain, L. Ying, and D. Klenerman. 2006. Characterization of a single molecule DNA switch in free solution. J. Am. Chem. Soc. 128: 11423–11432.

58. Cooper, M., A. Ebner, M. Briggs, M. Burrows, N. Gardner, R. Richardson, and R. West. 2004. Cy3B™: Improving the performance of cyanine dyes. In: Journal of Fluorescence. . pp. 145–150.

59. Shimomura, O., F.H. Johnson, and Y. Saiga. 1962. Extraction, Purification and Properties of Aequorin, a Bioluminescent Protein from the Luminous Hydromedusan,Aequorea. J. Cell. Comp. Physiol. 59: 223–239.

60. Chalfie, M., Y. Tu, G. Euskirchen, W. Ward, and D. Prasher. 1994. Green fluorescent protein as a marker for gene expression. Science (80-.). 263: 802–805.

61. Orm , M., A.B. Cubitt, K. Kallio, L.A. Gross, R.Y. Tsien, and S.J. Remington. 1996. Crystal Structure of the Aequorea victoria Green Fluorescent Protein. Science (80-.). 273: 1392–1395.

62. Strack, R.L., D.E. Strongin, L. Mets, B.S. Glick, and R.J. Keenan. 2010. Chromophore formation in DsRed occurs by a branched pathway. J. Am. Chem. Soc. 132: 8496–8505.

63. Reid, B.G., and G.C. Flynn. 1997. Chromophore formation in green fluorescent protein. Biochemistry. 36: 6786–6791.

64. Cranfill, P.J., B.R. Sell, M.A. Baird, J.R. Allen, Z. Lavagnino, H.M. De Gruiter, G.J. Kremers, M.W. Davidson, A. Ustione, and D.W. Piston. 2016. Quantitative assessment of fluorescent proteins. Nat. Methods. 13: 557–562.

65. Dean, K.M., J.L. Lubbeck, J.K. Binder, L.R. Schwall, R. Jimenez, and A.E. Palmer. 2011. Analysis of red-fluorescent proteins provides insight into dark-state conversion and photodegradation. Biophys. J. 101: 961–969.

66. Newman, R.H., M.D. Fosbrink, and J. Zhang. 2011. Genetically encodable fluorescent biosensors for tracking signaling dynamics in living cells. Chem. Rev. 111: 3614–3666.

67. Wang, L., W.C. Jackson, P.A. Steinbach, and R.Y. Tsien. 2004. Evolution of new nonantibody proteins via iterative somatic hypermutation. Proc. Natl. Acad. Sci. 101: 16745–16749.

68. Shaner, N.C., R.E. Campbell, P.A. Steinbach, B.N.G. Giepmans, A.E. Palmer, and R.Y. Tsien. 2004. Improved monomeric red, orange and yellow fluorescent proteins derived from Discosoma sp. red fluorescent protein. Nat. Biotechnol. 22: 1567–1572.

69. Cranfill, P.J., B.R. Sell, M.A. Baird, J.R. Allen, Z. Lavagnino, H.M. De Gruiter, G.J. Kremers, M.W. Davidson, A. Ustione, and D.W. Piston. 2016. Quantitative assessment of fluorescent proteins. Nat. Methods. 13: 557–562.

70. Shaner, N.C., P.A. Steinbach, and R.Y. Tsien. 2005. A guide to choosing fluorescent proteins. Nat. Methods. 2: 905–909.

71. Remington, S.J. 2006. Fluorescent proteins: maturation, photochemistry and photophysics. Curr. Opin. Struct. Biol. 16: 714–721.

72. Zhou, X.X., and M.Z. Lin. 2013. Photoswitchable fluorescent proteins: Ten years of colorful chemistry and exciting applications. Curr. Opin. Chem. Biol. 17: 682–690.

73. Patterson, G.H. 2002. A Photoactivatable GFP for Selective Photolabeling of Proteins and Cells. Science (80-.). 297: 1873–1877.

74. Subach, F. V., G.H. Patterson, S. Manley, J.M. Gillette, J. Lippincott-Schwartz, and V. V. Verkhusha. 2009. Photoactivatable mCherry for high-resolution two-color fluorescence microscopy. Nat. Methods. 6: 153–159.

75. Ando, R., H. Hama, M. Yamamoto-Hino, H. Mizuno, and A. Miyawaki. 2002. An optical marker based on the UV-induced green-to-red photoconversion of a fluorescent protein. Proc. Natl. Acad. Sci. 99: 12651–12656.

76. McKinney, S.A., C.S. Murphy, K.L. Hazelwood, M.W. Davidson, and L.L. Looger. 2009. A bright and photostable photoconvertible fluorescent protein. Nat. Methods. 6: 131–133.

77. Wiedenmann, J., S. Ivanchenko, F. Oswald, F. Schmitt, C. Rocker, A. Salih, K.-D. Spindler, and G.U. Nienhaus. 2004. EosFP, a fluorescent marker protein with UV-inducible green-to-red fluorescence conversion. Proc. Natl. Acad. Sci. 101: 15905–15910.

78. Zhang, M., H. Chang, Y. Zhang, J. Yu, L. Wu, W. Ji, J. Chen, B. Liu, J. Lu, Y. Liu, J. Zhang, P. Xu, and T. Xu. 2012. Rational design of true monomeric and bright photoactivatable fluorescent proteins. Nat. Methods. 9: 727–729.

79. Dittrich, P.S., S.P. Schäfer, and P. Schwille. 2005. Characterization of the photoconversion on reaction of the fluorescent protein Kaede on the single-molecule level. Biophys. J. 89: 3446–3455.

80. Nienhaus, K., and G. Ulrich Nienhaus. 2014. Fluorescent proteins for live-cell imaging with super-resolution. Chem. Soc. Rev. 43: 1088–1106.

81. Durisic, N., L. Laparra-Cuervo, Á. Sandoval-Álvarez, J.S. Borbely, and M. Lakadamyali. 2014. Single-molecule evaluation of fluorescent protein photoactivation efficiency using an in vivo nanotemplate. Nat. Methods. 11: 156–162.

82. Wang, S., J.R. Moffitt, G.T. Dempsey, X.S. Xie, and X. Zhuang. 2014. Characterization and development of photoactivatable fluorescent proteins for single-molecule-based superresolution imaging. Proc. Natl.

Acad. Sci. 111: 8452–8457.

83. Liu, Z., D. Xing, Q.P. Su, Y. Zhu, J. Zhang, X. Kong, B. Xue, S. Wang, H. Sun, Y. Tao, and Y. Sun. 2014. Super-resolution imaging and tracking of protein-protein interactions in sub-diffraction cellular space. Nat. Commun. 5: 1–8.

84. Etheridge, T.J., R.L. Boulineau, A. Herbert, A.T. Watson, Y. Daigaku, J. Tucker, S. George, P. Jönsson, M. Palayret, D. Lando, E. Laue, M.A. Osborne, D. Klenerman, S.F. Lee, and A.M. Carr. 2014. Quantification of DNA-associated proteins inside eukaryotic cells using single-molecule localization microscopy. Nucleic Acids Res. 42: e146.

85. Zhang, Y., H. Chang, L. Gu, Y. Zhao, T. Xu, and W. Ji. 2013. Super-resolution microscopy of live cells using single molecule localization. Chinese Sci. Bull. 58: 4519–4527.

86. Das, S., T. Yin, Q. Yang, J. Zhang, Y.I. Wu, and J. Yu. 2015. Single-molecule tracking of small GTPase Rac1 uncovers spatial regulation of membrane translocation and mechanism for polarized signaling. Proc. Natl. Acad. Sci. 112: E267–E276.

87. Schmidt, J.C., A.J. Zaug, and T.R. Cech. 2016. Live Cell Imaging Reveals the Dynamics of Telomerase Recruitment to Telomeres. Cell. 166: 1188–1197.e9.

88. Jares-Erijman, E.A., and T.M. Jovin. 2003. FRET imaging. Nat. Biotechnol. 21: 1387–1395.

89. Roy, R., S. Hohng, and T. Ha. 2008. A practical guide to single-molecule FRET. Nat. Methods. 5: 507–516.

90. Mujumdar, R.B., L.A. Ernst, S.R. Mujumdar, and C.J. Lewis. 1993. Cyanine Dye Labeling Reagents: Sulfoindocyanine Succinimidyl Esters.

Bioconjug. Chem. 4: 105–111.

91. ATTO Gmbh. 2013. Fluorescent Labels and Dyes. Fluoresc. Labels Dye. Cat. 49: 1–45.

92. Zheng, Q., and L.D. Lavis. 2017. Development of photostable fluorophores for molecular imaging. Curr. Opin. Chem. Biol. 39: 32–38.

93. Ha, T., and P. Tinnefeld. 2012. Photophysics of Fluorescent Probes for Single-Molecule Biophysics and Super-Resolution Imaging. Annu Rev Phys Chem. 63: 595–617.

94. Morgan, M.A., K. Okamoto, J.D. Kahn, and D.S. English. 2005. Single-molecule spectroscopic determination of Lac repressor-DNA loop conformation. Biophys. J. 89: 2588–2596.

95. Benítez, J.J., A.M. Keller, P. Ochieng, L.A. Yatsunyk, D.L. Huffman, A.C. Rosenzweig, and P. Chen. 2008. Probing transient copper Chaperone-Wilson disease protein interactions at the single-molecule level with nanovesicle trapping. J. Am. Chem. Soc. 130: 2446–2447.

96. Heilemann, M., E. Margeat, R. Kasper, M. Sauer, and P. Tinnefeld. 2005. Carbocyanine dyes as efficient reversible single-molecule optical switch. J. Am. Chem. Soc. 127: 3801–3806.

97. Kundel, F., L. Hong, B. Falcon, W.A. McEwan, T.C.T. Michaels, G. Meisl, N. Esteras, A.Y. Abramov, T.J.P. Knowles, M. Goedert, and D. Klenerman. 2018. Measurement of Tau Filament Fragmentation Provides Insights into Prion-like Spreading. ACS Chem. Neurosci. : acschemneuro.8b00094.

98. Meng, F., M.M.J. Bellaiche, J.Y. Kim, G.H. Zerze, R.B. Best, and H.S. Chung. 2018. Highly Disordered Amyloid-β Monomer Probed by Single-Molecule FRET and MD Simulation. Biophys. J. 114: 870–884.

99. Iljina, M., L. Tosatto, M.L. Choi, J.C. Sang, Y. Ye, C.D. Hughes, C.E. Bryant, S. Gandhi, and D. Klenerman. 2016. Arachidonic acid mediates the formation of abundant alpha-helical multimers of alpha-synuclein. Sci. Rep. 6: 33928.

100. Anderson, V.L., and W.W. Webb. 2011. Transmission electron microscopy characterization of fluorescently labelled amyloid β 1-40 and α-synuclein aggregates. BMC Biotechnol. 11.

101. Bajar, B.T., E.S. Wang, S. Zhang, M.Z. Lin, and J. Chu. 2016. A guide to fluorescent protein FRET pairs. Sensors (Switzerland). 16: 1–24.

102. Bajar, B.T., E.S. Wang, A.J. Lam, B.B. Kim, C.L. Jacobs, E.S. Howe, M.W. Davidson, M.Z. Lin, and J. Chu. 2016. Improving brightness and photostability of green and red fluorescent proteins for live cell imaging and FRET reporting. Sci. Rep. 6.

103. Yokota, H., Y. Ishii, and T. Yanagida. 2001. Blinking and its Effect on Single Molecule FRET Measurements. Single Mol. 2: 151–151.

104. Juillerat, A., T. Gronemeyer, A. Keppler, S. Gendreizig, H. Pick, H. Vogel, and K. Johnsson. 2003. Directed Evolution of O6-Alkylguanine-DNA Alkyltransferase for Efficient Labeling of Fusion Proteins with Small Molecules In Vivo. Chem. Biol. 10: 313–317.

105. Los, G. V, and K. Wood. 2007. The HaloTag: a novel technology for cell imaging and protein analysis. Methods Mol. Biol. 356: 195–208.

106. Keppler, A., M. Kindermann, S. Gendreizig, H. Pick, H. Vogel, and K. Johnsson. 2004. Labeling of fusion proteins of O6-alkylguanine-DNA alkyltransferase with small molecules in vivo and in vitro. Methods. 32: 437–444.

107. Klein, T., A. Löschberger, S. Proppert, S. Wolter, S. Van De Linde, and

M. Sauer. 2011. Live-cell dSTORM with SNAP-tag fusion proteins. Nat. Methods. 8: 7–9.

108. Keppler, A., S. Gendreizig, T. Gronemeyer, H. Pick, H. Vogel, and K. Johnsson. 2003. A general method for the covalent labeling of fusion proteins with small molecules in vivo. Nat. Biotechnol. 21: 86–89.

109. Crivat, G., and J.W. Taraska. 2012. Imaging proteins inside cells with fluorescent tags. Trends Biotechnol. 30: 8–16.

110. Urh, M. 2013. HaloTag, a Platform Technology for Protein Analysis. Curr. Chem. Genomics. 6: 72–78.

111. Englander, S.W., D.B. Calhoun, and J.J. Englander. 1987. Biochemistry without oxygen. Anal. Biochem. 161: 300–306.

112. Rasnik, I., S.A. McKinney, and T. Ha. 2006. Nonblinking and long-lasting single-molecule fluorescence imaging. Nat. Methods. 3: 891–893.

113. Zheng, Q., S. Jockusch, G.G. Rodríguez-Calero, Z. Zhou, H. Zhao, R.B. Altman, H.D. Abruña, and S.C. Blanchard. 2016. Intra-molecular triplet energy transfer is a general approach to improve organic fluorophore photostability. Photochem. Photobiol. Sci. 15: 196–203.

114. Vogelsang, J., T. Cordes, C. Forthmann, C. Steinhauer, and P. Tinnefeld. 2009. Controlling the fluorescence of ordinary oxazine dyes for single-molecule switching and superresolution microscopy. Proc. Natl. Acad. Sci. 106: 8107–8112.

115. Dai, M., R. Jungmann, and P. Yin. 2016. Optical imaging of individual biomolecules in densely packed clusters. Nat. Nanotechnol. 11: 798–807.

116. Lee, S., J. Lee, and S. Hohng. 2010. Single-molecule three-color FRET with both negligible spectral overlap and long observation time. PLoS One. 5.

117. Tyagi, S., V. Vandelinder, N. Banterle, G. Fuertes, S. Milles, M. Agez, and E.A. Lemke. 2014. Continuous throughput and long-term observation of single-molecule FRET without immobilization. Nat. Methods. 11: 297–300.

118. Tsunoyama, T.A., Y. Watanabe, J. Goto, K. Naito, R.S. Kasai, K.G.N. Suzuki, T.K. Fujiwara, and A. Kusumi. 2018. Super-long single-molecule tracking reveals dynamic-anchorage-induced integrin function. Nat. Chem. Biol. 14: 497–506.

119. Park, H.Y., A.R. Buxbaum, and R.H. Singer. 2010. Single mRNA Tracking in Live Cells. 1st ed. Elsevier Inc.

120. Gell, C., V. Bormuth, G.J. Brouhard, D.N. Cohen, S. Diez, C.T. Friel, J. Helenius, B. Nitzsche, H. Petzold, J. Ribbe, E. Schäffer, J.H. Stear, A. Trushko, V. Varga, P.O. Widlund, M. Zanic, and J. Howard. 2010. Microtubule dynamics reconstituted in vitro and imaged by single-molecule fluorescence microscopy. .

121. Abbe, E. 1873. Beiträge zur Theorie des Mikroskops und der mikroskopischen Wahrnehmung: I. Die Construction von Mikroskopen auf Grund der Theorie. Arch. für mikroskopische Anat. 9: 413–418.

122. Huang, B., M. Bates, and X. Zhuang. 2009. Super-Resolution Fluorescence Microscopy. Annu. Rev. Biochem. 78: 993–1016.

123. Yildiz, A., J.N. Forkey, S.A. McKinney, T. Ha, Y.E. Goldman, and P.R. Selvin. 2003. Myosin V walks hand-over-hand: Single fluorophore imaging with 1.5-nm localization. Science (80-.). 300: 2061–2065.

124. Rieger, B., and S. Stallinga. 2014. The lateral and axial localization uncertainty in super-resolution light microscopy. ChemPhysChem. 15: 664–670.

125. Thompson, R.E., D.R. Larson, and W.W. Webb. 2002. Precise nanometer localization analysis for individual fluorescent probes. Biophys. J. 82: 2775–2783.

126. T, W., and Tan J.B. 1993. Three dimensional image reconstruction in conventional and confocal microscopy. Bioimaging. 1: 176–184.

127. Yildiz, A., and P.R. Selvin. 2005. Fluorescence imaging with one nanometer accuracy: Application to molecular motors. Acc. Chem. Res. 38: 574–582.

128. Betzig, E., G.H. Patterson, R. Sougrat, O.W. Lindwasser, S. Olenych, J.S. Bonifacino, M.W. Davidson, J. Lippincott-Schwartz, and H.F. Hess. 2006. Imaging intracellular fluorescent proteins at nanometer resolution. Science (80-.). 313: 1642–1645.

129. Rust, M.J., M. Bates, and X.W. Zhuang. 2006. Sub-diffraction-limit imaging by stochastic optical reconstruction microscopy (STORM). Nat. Methods. 3: 793–796.

130. Dempsey, G.T., M. Bates, W.E. Kowtoniuk, D.R. Liu, R.Y. Tsien, and X. Zhuang. 2009. Photoswitching mechanism of cyanine dyes. J. Am. Chem. Soc. 131: 18192–18193.

131. Steinhauer, C., C. Forthmann, J. Vogelsang, and P. Tinnefeld. 2008. Superresolution microscopy on the basis of engineered dark states. J. Am. Chem. Soc. 130: 16840–16841.

132. Huang, B., W. Wang, M. Bates, and X. Zhuang. 2008. Three-Dimensional Super-Resolution Imaging by Stochastic Optical Reconstruction Microscopy. Science (80-.). 319: 810–813.

133. Glebov, O.O., R.E. Jackson, C.M. Winterflood, D.M. Owen, E.A. Barker, P. Doherty, H. Ewers, and J. Burrone. 2017. Nanoscale Structural

Plasticity of the Active Zone Matrix Modulates Presynaptic Function. Cell Rep. 18: 2715–2728.

134. Dudok, B., L. Barna, M. Ledri, S.I. Szabó, E. Szabadits, B. Pintér, S.G. Woodhams, C.M. Henstridge, G.Y. Balla, R. Nyilas, C. Varga, S.H. Lee, M. Matolcsi, J. Cervenak, I. Kacskovics, M. Watanabe, C. Sagheddu, M. Melis, M. Pistis, I. Soltesz, and I. Katona. 2015. Cell-specific STORM super-resolution imaging reveals nanoscale organization of cannabinoid signaling. Nat. Neurosci. 18: 75–86.

135. Heilemann, M., S. Van De Linde, M. Schüttpelz, R. Kasper, B. Seefeldt, A. Mukherjee, P. Tinnefeld, and M. Sauer. 2008. Subdiffraction-resolution fluorescence imaging with conventional fluorescent probes. Angew. Chemie - Int. Ed. 47: 6172–6176.

136. Dempsey, G.T., J.C. Vaughan, K.H. Chen, M. Bates, and X. Zhuang. 2011. Evaluation of fluorophores for optimal performance in localization-based super-resolution imaging. Nat. Methods. 8: 1027–1040.

137. Sharonov, A., and R.M. Hochstrasser. 2006. Wide-field subdiffraction imaging by accumulated binding of diffusing probes. Proc. Natl. Acad. Sci. 103: 18911–18916.

138. Reits, E.A.J., and J.J. Neefjes. 2001. From fixed to FRAP: Measuring protein mobility and activity in living cells. Nat. Cell Biol. 3.

139. Haustein, E., and P. Schwille. 2007. Fluorescence Correlation Spectroscopy: Novel Variations of an Established Technique. Annu. Rev. Biophys. Biomol. Struct. 36: 151–169.

140. Gebhardt, J.C.M., D.M. Suter, R. Roy, Z.W. Zhao, A.R. Chapman, S. Basu, T. Maniatis, and X.S. Xie. 2013. Single-molecule imaging of transcription factor binding to DNA in live mammalian cells. Nat. Methods. 10: 421–426.

141. Izeddin, I., V. Récamier, L. Bosanac, I.I. Cissé, L. Boudarene, C. Dugast-Darzacq, F. Proux, O. Bénichou, R. Voituriez, O. Bensaude, M. Dahan, and X. Darzacq. 2014. Single-molecule tracking in live cells reveals distinct target-search strategies of transcription factors in the nucleus. Elife. 2014.

142. Lippincott-Schwartz, J., and G.H. Patterson. 2009. Photoactivatable fluorescent proteins for diffraction-limited and super-resolution imaging. Trends Cell Biol. 19: 555–565.

143. Chen, J., Z. Zhang, L. Li, B.C. Chen, A. Revyakin, B. Hajj, W. Legant, M. Dahan, T. Lionnet, E. Betzig, R. Tjian, and Z. Liu. 2014. Single-molecule dynamics of enhanceosome assembly in embryonic stem cells. Cell. 156: 1274–1285.

144. Mazza, D., A. Abernathy, N. Golob, T. Morisaki, and J.G. McNally. 2012. A benchmark for chromatin binding measurements in live cells. Nucleic Acids Res. 40.

145. Geerts, H., M. De Brabander, R. Nuydens, S. Geuens, M. Moeremans, J. De Mey, and P. Hollenbeck. 1987. Nanovid tracking: a new automatic method for the study of mobility in living cells based on colloidal gold and video microscopy. Biophys. J. 52: 775–782.

146. Saxton, M.J. 2008. Single-particle tracking: Connecting the dots. Nat. Methods. 5: 671–672.

147. Chenouard, N., I. Smal, F. De Chaumont, M. Maška, I.F. Sbalzarini, Y. Gong, J. Cardinale, C. Carthel, S. Coraluppi, M. Winter, A.R. Cohen, W.J. Godinez, K. Rohr, Y. Kalaidzidis, L. Liang, J. Duncan, H. Shen, Y. Xu, K.E.G. Magnusson, J. Jaldén, H.M. Blau, P. Paul-Gilloteaux, P. Roudot, C. Kervrann, F. Waharte, J.Y. Tinevez, S.L. Shorte, J. Willemse, K. Celler, G.P. Van Wezel, H.W. Dan, Y.S. Tsai, C.O. De Solórzano, J.C.

Olivo-Marin, and E. Meijering. 2014. Objective comparison of particle tracking methods. Nat. Methods. 11: 281–289.

148. Saxton, M.J. 2014. A particle tracking meet. Nat. Methods. 11: 247–248.

149. Axelrod, D. 2001. Total internal reflection fluorescence microscopy in cell biology. Traffic. 2: 764–774.

150. Tokunaga, M., K. Kitamura, K. Saito, A.H. Iwane, and T. Yanagida. 1997. Single molecule imaging of fluorophores and enzymatic reactions achieved by objective-type total internal reflection fluorescence microscopy. Biochem. Biophys. Res. Commun. 235: 47–53.

151. Yildiz, A., and R.D. Vale. 2015. Total internal reflection fluorescence microscopy. Cold Spring Harb. Protoc. 2015: 801–810.

152. Axelrod, D., E.H. Hellen, and R.M. Fulbright. 2002. Topics in Fluorescence Spectroscopy. Boston, MA: Springer US.

153. Gahlmann, A., J.L. Ptacin, G. Grover, S. Quirin, A.R.S. Von Diezmann, M.K. Lee, M.P. Backlund, L. Shapiro, R. Piestun, and W.E. Moerner. 2013. Quantitative multicolor subdiffraction imaging of bacterial protein ultrastructures in three dimensions. Nano Lett. 13: 987–993.

154. Carr, A.R., A. Ponjavic, S. Basu, J. McColl, A.M. Santos, S. Davis, E.D. Laue, D. Klenerman, and S.F. Lee. 2017. Three-Dimensional Super-Resolution in Eukaryotic Cells Using the Double-Helix Point Spread Function. Biophys. J. 112: 1444–1454.

155. Wolfe, J.P., and S.L. Buchwald. 1997. Improved FunctionalGroup Compatibilityin the Palladium- Catalyzed Amination of Aryl Bromides. Tetrahedron Lett. 38: 6359–6362.

156. Yang, P., R. Wang, H. Wu, Z. Du, and Y. Fu. 2017. Pd-Catalyzed C−H Arylation of Benzothiazoles with Diaryliodonium Salt: One-Pot Synthesis

of 2-Arylbenzothiazoles. Asian J. Org. Chem. 6: 184–188.

157. Hoyer, W., T. Antony, D. Cherny, G. Heim, T.M. Jovin, and V. Subramaniam. 2002. Dependence of α-synuclein aggregate morphology on solution conditions. J. Mol. Biol. 322: 383–393.

158. Miller, E.W., A.E. Albers, A. Pralle, E.Y. Isacoff, and C.J. Chang. 2005. Boronate-based fluorescent probes for imaging cellular hydrogen peroxide. J. Am. Chem. Soc. 127: 16652–16659.

159. Horrocks, M.H., S.F. Lee, S. Gandhi, N.K. Magdalinou, S.W. Chen, M.J. Devine, L. Tosatto, M. Kjaergaard, J.S. Beckwith, H. Zetterberg, M. Iljina, N. Cremades, C.M. Dobson, N.W. Wood, and D. Klenerman. 2016. Single-Molecule Imaging of Individual Amyloid Protein Aggregates in Human Biofluids. ACS Chem. Neurosci. 7: 399–406.

160. Edelstein, A.D., M.A. Tsuchida, N. Amodaj, H. Pinkard, R.D. Vale, and N. Stuurman. 2014. Advanced methods of microscope control using μManager software. J. Biol. Methods. 1: 10.

161. Schindelin, J., I. Arganda-Carreras, E. Frise, V. Kaynig, M. Longair, T. Pietzsch, S. Preibisch, C. Rueden, S. Saalfeld, B. Schmid, J.Y. Tinevez, D.J. White, V. Hartenstein, K. Eliceiri, P. Tomancak, and A. Cardona. 2012. Fiji: An open-source platform for biological-image analysis. Nat. Methods. 9: 676–682.

162. Lord, S.J., Z. Lu, H. Wang, K.A. Willets, P.J. Schuck, H.L.D. Lee, S.Y. Nishimura, R.J. Twieg, and W.E. Moerner. 2007. Photophysical properties of acene DCDHF fluorophores: Long-wavelength single-molecule emitters designed for cellular imaging. J. Phys. Chem. A. 111: 8934–8941.

163. Magde, D., G.E. Rojas, and P.G. Seybold. 1999. Solvent dependence of the fluorescence lifetimes of xanthene dyes. Photochem. Photobiol. 70:

737–744.

164. Tian, Y., J. Halle, M. Wojdyr, D. Sahoo, and I.G. Scheblykin. 2014. Quantitative measurement of fluorescence brightness of single molecules. Methods Appl. Fluoresc. 2: 035003.

165. Wolter, S., A. Löschberger, T. Holm, S. Aufmkolk, M.C. Dabauvalle, S. Van De Linde, and M. Sauer. 2012. RapidSTORM: Accurate, fast open-source software for localization microscopy. Nat. Methods. 9: 1040–1041.

166. Ueda, K., H. Fukushima, E. Masliah, Y. Xia, A. Iwai, M. Yoshimoto, D.A. Otero, J. Kondo, Y. Ihara, and T. Saitoh. 1993. Molecular cloning of cDNA encoding an unrecognized component of amyloid in Alzheimer disease. Proc. Natl. Acad. Sci. 90: 11282–11286.

167. Spillantini, M.G., M.L. Schmidt, V.M.Y. Lee, J.Q. Trojanowski, R. Jakes, and M. Goedert. 1997. α-synuclein in Lewy bodies. Nature. 388: 839–840.

168. Soto, C. 2003. Unfolding the role of protein misfolding in neurodegenerative diseases. Nat. Rev. Neurosci. 4: 49–60.

169. Serrano-Cinca, C., Y. Fuertes-Callén, and C. Mar-Molinero. 2005. Measuring DEA efficiency in Internet companies. Decis. Support Syst. 38: 557–573.

170. Vidal, R., and B. Ghetti. 2011. Characterization of amyloid deposits in neurodegenerative diseases. Methods Mol. Biol. 793: 241–258.

171. Knowles, T.P.J., C.A. Waudby, G.L. Devlin, S.I.A. Cohen, A. Aguzzi, M. Vendruscolo, E.M. Terentjev, M.E. Welland, and C.M. Dobson. 2009. An analytical solution to the kinetics of breakable filament assembly. Science (80-.). 326: 1533–1537.

172. Serio, T.R., A.G. Cashikar, A.S. Kowal, G.J. Sawicki, J.J. Moslehi, L.

Serpell, M.F. Arnsdorf, and S.L. Lindquist. 2000. Nucleated conformational conversion and the replication of conformational information by a prion determinant. Science (80-.). 289: 1317–1321.

173. Rivers, R.C., J.R. Kumita, G.G. Tartaglia, M.M. Dedmon, A. Pawar, M. Vendruscolo, C.M. Dobson, and J. Christodoulou. 2008. Molecular determinants of the aggregation behavior of alpha- and beta-synuclein. Protein Sci. 17: 887–98.

174. Pedersen, J.S., G. Christensen, and D.E. Otzen. 2004. Modulation of S6 fibrillation by unfolding rates and gatekeeper residues. J. Mol. Biol. 341: 575–588.

175. Cremades, N., S.I.A. Cohen, E. Deas, A.Y. Abramov, A.Y. Chen, A. Orte, M. Sandal, R.W. Clarke, P. Dunne, F.A. Aprile, C.W. Bertoncini, N.W. Wood, T.P.J. Knowles, C.M. Dobson, and D. Klenerman. 2012. Direct observation of the interconversion of normal and toxic forms of α-synuclein. Cell. 149: 1048–1059.

176. Billings, L.M., S. Oddo, K.N. Green, J.L. McGaugh, and F.M. LaFerla. 2005. Intraneuronal Aβ causes the onset of early Alzheimer's disease-related cognitive deficits in transgenic mice. Neuron. 45: 675–688.

177. Kirschner, D.A., C. Abraham, and D.J. Selkoe. 1986. X-ray diffraction from intraneuronal paired helical filaments and extraneuronal amyloid fibers in Alzheimer disease indicates cross-beta conformation. Proc. Natl. Acad. Sci. U. S. A. 83: 503–7.

178. Stefani, M. 2010. Structural polymorphism of amyloid oligomers and fibrils underlies different fibrillization pathways: immunogenicity and cytotoxicity. Curr. Protein Pept. Sci. 11: 343–54.

179. Spillantini, M.G., R.A. Crowther, R. Jakes, M. Hasegawa, and M. Goedert. 1998. α-Synuclein in filamentous inclusions of Lewy bodies from

Parkinson’s disease and dementia with Lewy bodies. Proc. Natl. Acad. Sci. 95: 6469–6473.

180. El-Agnaf, O.M.A., and G.B. Irvine. 2002. Aggregation and neurotoxicity of α-synuclein and related peptides. Biochem. Soc. Trans. 30: 559–565.

181. Gibb, W.R.G., and A.J. Lees. 1988. The relevance of the Lewy body to the pathogenesis of idiopathic Parkinson’s disease. J. Neurol. Neurosurg. Psychiatry. 51: 745–752.

182. Koppenhöfer, D., F. Kettenbaum, A. Susloparova, J.K.Y. Law, X.T. Vu, T. Schwab, K.H. Schäfer, and S. Ingebrandt. 2015. Neurodegeneration through oxidative stress: Monitoring hydrogen peroxide induced apoptosis in primary cells from the subventricular zone of BALB/c mice using field-effect transistors. Biosens. Bioelectron. 67: 490–496.

183. Gandhi, S., and A.Y. Abramov. 2012. Mechanism of oxidative stress in neurodegeneration. Oxid. Med. Cell. Longev. 2012.

184. Coyle, J.T., and P. Puttfarcken. 1993. Oxidative stress, glutamate, and neurodegenerative disorders. Science (80-.). 262: 689–95.

185. Czarny, P., P. Wigner, P. Galecki, and T. Sliwinski. 2018. The interplay between inflammation, oxidative stress, DNA damage, DNA repair and mitochondrial dysfunction in depression. Prog. Neuro-Psychopharmacology Biol. Psychiatry. 80: 309–321.

186. Howie, A.J., and D.B. Brewer. 2009. Optical properties of amyloid stained by Congo red: History and mechanisms. Micron. 40: 285–301.

187. Howie, A.J., D.B. Brewer, D. Howell, and A.P. Jones. 2008. Physical basis of colors seen in Congo red-stained amyloid in polarized light. Lab. Investig. 88: 232–242.

188. Klingstedt, T., A. Åslund, R.A. Simon, L.B.G. Johansson, J.J. Mason, S.

Nyström, P. Hammarström, and K.P.R. Nilsson. 2011. Synthesis of a library of oligothiophenes and their utilization as fluorescent ligands for spectral assignment of protein aggregates. Org. Biomol. Chem. 9: 8356.

189. Åslund, A., C.J. Sigurdson, T. Klingstedt, S. Grathwohl, T. Bolmont, D.L. Dickstein, E. Glimsdal, S. Prokop, M. Lindgren, P. Konradsson, D.M. Holtzman, P.R. Hof, F.L. Heppner, S. Gandy, M. Jucker, A. Aguzzi, P. Hammarström, and K.P.R. Nilsson. 2009. Novel pentameric thiophene derivatives for in vitro and in vivo optical imaging of a plethora of protein aggregates in cerebral amyloidoses. ACS Chem. Biol. 4: 673–684.

190. Klunk, W.E., H. Engler, A. Nordberg, Y. Wang, G. Blomqvist, D.P. Holt, M. Bergström, I. Savitcheva, G.F. Huang, S. Estrada, B. Ausén, M.L. Debnath, J. Barletta, J.C. Price, J. Sandell, B.J. Lopresti, A. Wall, P. Koivisto, G. Antoni, C.A. Mathis, and B. Långström. 2004. Imaging Brain Amyloid in Alzheimer's Disease with Pittsburgh Compound-B. Ann. Neurol. 55: 306–319.

191. Kitts, C.C., and D.A. Vanden Bout. 2010. A spectroscopic study of 2-[4′-(Dimethylamino)phenyl]-benzothiazole Binding to Insulin Amyloid Fibrils. J. Fluoresc. 20: 881–889.

192. Groenning, M. 2010. Binding mode of Thioflavin T and other molecular probes in the context of amyloid fibrils-current status. J. Chem. Biol. 3: 1–18.

193. Varela, J.A., M. Rodrigues, S. De, P. Flagmeier, S. Gandhi, C.M. Dobson, D. Klenerman, and S. Lee. 2018. Optical structural analysis of individual α-synuclein oligomers. Angew. Chemie Int. Ed. : 1–6.

194. Deas, E., N. Cremades, P.R. Angelova, M.H.R. Ludtmann, Z. Yao, S. Chen, M.H. Horrocks, B. Banushi, D. Little, M.J. Devine, P. Gissen, D. Klenerman, C.M. Dobson, N.W. Wood, S. Gandhi, and A.Y. Abramov.

2016. Alpha-Synuclein Oligomers Interact with Metal Ions to Induce Oxidative Stress and Neuronal Death in Parkinson's Disease. Antioxid. Redox Signal. 24: 376–391.

195. Winner, B., R. Jappelli, S.K. Maji, P.A. Desplats, L. Boyer, S. Aigner, C. Hetzer, T. Loher, M. Vilar, S. Campioni, C. Tzitzilonis, A. Soragni, S. Jessberger, H. Mira, A. Consiglio, E. Pham, E. Masliah, F.H. Gage, and R. Riek. 2011. In vivo demonstration that α-synuclein oligomers are toxic. Proc. Natl. Acad. Sci. 108: 4194–4199.

196. Outeiro, T.F., P. Putcha, J.E. Tetzlaff, R. Spoelgen, M. Koker, F. Carvalho, B.T. Hyman, and P.J. McLean. 2008. Formation of toxic oligomeric α-synuclein species in living cells. PLoS One. 3.

197. Flagmeier, P., S. De, D.C. Wirthensohn, S.F. Lee, C. Vincke, S. Muyldermans, T.P.J. Knowles, S. Gandhi, C.M. Dobson, and D. Klenerman. 2017. Ultrasensitive Measurement of Ca2+ Influx into Lipid Vesicles Induced by Protein Aggregates. Angew. Chemie - Int. Ed. 56: 7750–7754.

198. Kaminski Schierle, G.S., M. Sauer, and C.F. Kaminski. 2013. Probing Amyloid Aggregation and Morphology In Situ by Multiparameter Imaging and Super-Resolution Fluorescence Microscopy. Bio-nanoimaging Protein Misfolding Aggreg. : 105–120.

199. Young, L.M., A.E. Ashcroft, and S.E. Radford. 2017. Small molecule probes of protein aggregation. Curr. Opin. Chem. Biol. 39: 90–99.

200. Ban, T., D. Hamada, K. Hasegawall, H. Naiki, and Y. Goto. 2003. Direct observation of amyloid fibril growth monitored by thioflavin T fluorescence. J. Biol. Chem. 278: 16462–16465.

201. Ban, T., M. Hoshino, S. Takahashi, D. Hamada, K. Hasegawa, H. Naiki, and Y. Goto. 2004. Direct observation of Aβ amyloid fibril growth and

inhibition. J. Mol. Biol. 344: 757–767.

202. Kalyanaraman, B., V. Darley-Usmar, K.J.A. Davies, P.A. Dennery, H.J. Forman, M.B. Grisham, G.E. Mann, K. Moore, L.J. Roberts, and H. Ischiropoulos. 2012. Measuring reactive oxygen and nitrogen species with fluorescent probes: Challenges and limitations. Free Radic. Biol. Med. 52: 1–6.

203. Ishikawa, K., K. Takenaga, M. Akimoto, N. Koshikawa, A. Yamaguchi, H. Imanishi, K. Nakada, Y. Honma, and J.I. Hayashi. 2008. ROS-generating mitochondrial DNA mutations can regulate tumor cell metastasis. Science (80-.). 320: 661–664.

204. Singh, P.K., M. Kumbhakar, H. Pal, and S. Nath. 2010. Viscosity effect on the ultrafast bond twisting dynamics in an amyloid fibril sensor: Thioflavin-T. J. Phys. Chem. B. 114: 5920–5927.

205. Freire, S., M.H. De Araujo, W. Al-Soufi, and M. Novo. 2014. Photophysical study of Thioflavin T as fluorescence marker of amyloid fibrils. Dye. Pigment. 110: 97–105.

206. Stsiapura, V.I., A.A. Maskevich, V.A. Kuzmitsky, V.N. Uversky, I.M. Kuznetsova, and K.K. Turoverov. 2008. Thioflavin T as a molecular rotor: Fluorescent properties of thioflavin T in solvents with different viscosity. J. Phys. Chem. B. 112: 15893–15902.

207. Naik, L.R., A.B. Naik, and H. Pal. 2009. Steady-state and time-resolved emission studies of Thioflavin-T. J. Photochem. Photobiol. A Chem. 204: 161–167.

208. Voropai, E.S., M.P. Samtsov, K.N. Kaplevskii, A.A. Maskevich, V.I. Stepuro, O.I. Povarova, I.M. Kuznetsova, K.K. Turoverov, A.L. Fink, and V.N. Uverskii. 2003. Spectral properties of thioflavin T and its complexes with amyloid fibrils. J. Appl. Spectrosc. 70: 868–874.

209. Stsiapura, V.I., A.A. Maskevich, V.A. Kuzmitsky, K.K. Turoverov, and I.M. Kuznetsova. 2007. Computational study of thioflavin T torsional relaxation in the excited state. J. Phys. Chem. A. 111: 4829–4835.

210. Erez, Y., Y.H. Liu, N. Amdursky, and D. Huppert. 2011. Modeling the nonradiative decay rate of electronically excited thioflavin T. J. Phys. Chem. A. 115: 8479–8487.

211. Sulatskaya, A.I., A.A. Maskevich, I.M. Kuznetsova, V.N. Uversky, and K.K. Turoverov. 2010. Fluorescence quantum yield of thioflavin T in rigid isotropic solution and incorporated into the amyloid fibrils. PLoS One. 5: e15385.

212. Van Der Meer, M.J., H. Zhang, and M. Glasbeek. 2000. Femtosecond fluorescence upconversion studies of barrierless bond twisting of auramine in solution. J. Chem. Phys. 112: 2878–2887.

213. Stsiapura, V.I., A.A. Maskevich, S.A. Tikhomirov, and O. V. Buganov. 2010. Charge transfer process determines ultrafast excited state deactivation of thioflavin T in low-viscosity solvents. J. Phys. Chem. A. 114: 8345–8350.

214. Stsiapura, V.I., S.A. Kurhuzenkau, V.A. Kuzmitsky, O. V. Bouganov, and S.A. Tikhomirov. 2016. Solvent Polarity Effect on Nonradiative Decay Rate of Thioflavin T. J. Phys. Chem. A. 120: 5481–5496.

215. Biancalana, M., and S. Koide. 2010. Molecular mechanism of Thioflavin-T binding to amyloid fibrils. Biochim. Biophys. Acta - Proteins Proteomics. 1804: 1405–1412.

216. Krebs, M.R.H., E.H.C. Bromley, and A.M. Donald. 2005. The binding of thioflavin-T to amyloid fibrils: Localisation and implications. J. Struct. Biol. 149: 30–37.

217. Maskevich, A.A., V.I. Stsiapura, V.A. Kuzmitsky, I.M. Kuznetsova, O.I. Povarova, V.N. Uversky, and K.K. Turoverov. 2007. Spectral properties of thioflavin T in solvents with different dielectric properties and in a fibril-incorporated form. J. Proteome Res. 6: 1392–1401.

218. Haberhauer, G., R. Gleiter, and C. Burkhart. 2016. Planarized Intramolecular Charge Transfer: A Concept for Fluorophores with both Large Stokes Shifts and High Fluorescence Quantum Yields. Chem. - A Eur. J. 22: 971–978.

219. Hsu, J.C.C., E.H.L. Chen, R.C. Snoeberger, F.Y. Luh, T.S. Lim, C.P. Hsu, and R.P.Y. Chen. 2013. Thioflavin T and its photoirradiative derivatives: Exploring their spectroscopic properties in the absence and presence of amyloid fibrils. J. Phys. Chem. B. 117: 3459–3468.

220. Hung, J., W. Liang, J. Luo, Z. Shi, A.K.Y. Jen, and X. Li. 2010. Rational design using Dewar's rules for enhancing the first hyperpolarizability of nonlinear optical chromophores. J. Phys. Chem. C. 114: 22284–22288.

221. Gogoleva, S.D., E. V. Kalganova, A.A. Maskevich, A.A. Lugovski, V.A. Kuzmitsky, M. Goswami, O. V. Buganov, S.A. Tikhomirov, and V.I. Stsiapura. 2018. Neutral derivatives of Thioflavin T do not exhibit viscosity-dependent fluorescence. J. Photochem. Photobiol. A Chem. 358: 76–91.

222. Zhang, Z., G. Zhang, J. Wang, S. Sun, and Z. Zhang. 2016. The mechanisms of Large Stokes Shift and Fluorescence Quantum Yields in anilino substituted Rhodamine analogue: TICT and PICT. Comput. Theor. Chem. 1095: 44–53.

223. Bahaidarah, E., A. Harriman, P. Stachelek, S. Rihn, E. Heyer, and R. Ziessel. 2014. Fluorescent molecular rotors based on the BODIPY motif: effect of remote substituents. Photochem. Photobiol. Sci. 13: 1397–1401.

224. Lee, Y., A. Jo, and S.B. Park. 2015. Rational Improvement of Molar Absorptivity Guided by Oscillator Strength: A Case Study with Furoindolizine-Based Core Skeleton. Angew. Chemie - Int. Ed. 54: 15689–15693.

225. Safir Filho, M., S. Fiorucci, A.R. Martin, and R. Benhida. 2017. Design, synthesis and photophysical studies of styryl-based push–pull fluorophores with remarkable solvatofluorochromism. New J. Chem. 41: 13760–13772.

226. Reichardt, C. 1994. Solvatochromic Dyes as Solvent Polarity Indicators. Chem. Rev. 94: 2319–2358.

227. Haidekker, M.A., and E.A. Theodorakis. 2010. Environment-sensitive behavior of fluorescent molecular rotors. J. Biol. Eng. 4: 1–14.

228. Ghosh, R., and D.K. Palit. 2015. Effect of Donor-Acceptor Coupling on TICT Dynamics in the Excited States of Two Dimethylamine Substituted Chalcones. J. Phys. Chem. A. 119: 11128–11137.

229. Rettig, W. 1994. Photoinduced charge separation via twisted intramolecular charge transfer states. In: Top. Curr. Chem. . p. 253.

230. Smallwood, I.M. 1996. Handbook of Organic Solvent Properties. .

231. Biancalana, M., K. Makabe, A. Koide, and S. Koide. 2009. Molecular Mechanism of Thioflavin-T Binding to the Surface of β-Rich Peptide Self-Assemblies. J. Mol. Biol. 385: 1052–1063.

232. Wu, C., M.T. Bowers, and J.E. Shea. 2011. On the origin of the stronger binding of PIB over Thioflavin T to protofibrils of the Alzheimer Amyloid-β peptide: A molecular dynamics study. Biophys. J. 100: 1316–1324.

233. Ali, J., A. Rimola, C. Rodr, L. Rodr, and M. Sodupe. 2013. Insights on the Binding of Thio fl avin Derivative Markers to Amyloid- Like Fibril Models

from Quantum Chemical Calculations. J. Phys. Chem. B. 117: 6674–6680.

234. Cazeau-Dubroca, C., A. Peirigua, M. Ben Brahim, G. Nouchi, and P. Cazeau. 1992. Hydrogen bonding and TICT molecules in ground state. Proc. Indian Acad. Sci. - Chem. Sci. 104: 209–217.

235. C. Cazeau-Dubroca, G. Nouchi, M. Ben Brahim, M. Pesquerb. 1994. Dual fluorescence of 4-NJ-dimethylaminopyridine. Role of hydrogen-bonded complex in the ground state. 80: 125–133.

236. Knowles, T.P.J., M. Vendruscolo, and C.M. Dobson. 2014. The amyloid state and its association with protein misfolding diseases. Nat. Rev. Mol. Cell Biol. 15: 384–396.

237. Ingelsson, M., H. Fukumoto, K.L. Newell, J.H. Growdon, E.T. Hedley-Whyte, M.P. Frosch, M.S. Albert, B.T. Hyman, and M.C. Irizarry. 2004. Early A accumulation and progressive synaptic loss, gliosis, and tangle formation in AD brain. Neurology. 62: 925–931.

238. Fearnley, J.M., and A.J. Lees. 1991. Ageing and Parkinson'S Disease: Substantia Nigra Regional Selectivity. Brain. 114: 2283–2301.

239. Lin, M.T., and M.F. Beal. 2006. Mitochondrial dysfunction and oxidative stress in neurodegenerative diseases. Nature. 443: 787–795.

240. Andersen, J.K. 2004. Oxidative stress in neurodegeneration: Cause or consequence? Nat. Rev. Neurosci. 10: S18.

241. Y, B.H., M. Veronique, L. Hua, B. Halliwell, M. V Clement, and L.H. Long. 2000. Hydrogen peroxide in the human body. FEBS Lett. 486: 14–17.

242. Schweitzer, C., Z. Mehrdad, A. Noll, E.W. Grabner, and R. Schmidt. 2003. Mechanism of photosensitized generation of singlet oxygen during oxygen quenching of triplet states and the general dependence of the

rate constants and efficiencies. J. Phys. Chem. A. 107: 2192–2198.

243. Rodina, N.P., M.I. Sulatsky, A.I. Sulatskaya, I.M. Kuznetsova, V.N. Uversky, and K.K. Turoverov. 2017. Photophysical Properties of Fluorescent Probe Thioflavin T in Crowded Milieu. J. Spectrosc. 2017.

244. Yildiz, A., J.N. Forkey, S.A. McKinney, H. Taekjip, Y.E. Goldman, and P.R. Selvin. 2003. Single fluorophore imaging with 1.5 nm accuracy shows myosin V walks hand-over-hand. Science (80-.). XXX: XXX–XXX.

245. Subach, O.M., G.H. Patterson, L.M. Ting, Y. Wang, J.S. Condeelis, and V. V. Verkhusha. 2011. A photoswitchable orange-to-far-red fluorescent protein, PSmOrange. Nat. Methods. 8: 771–780.

246. Chudakov, D.M., V. V. Verkhusha, D.B. Staroverov, E.A. Souslova, S. Lukyanov, and K.A. Lukyanov. 2004. Photoswitchable cyan fluorescent protein for protein tracking. Nat. Biotechnol. 22: 1435–1439.

247. Merzlyak, E.M., J. Goedhart, D. Shcherbo, M.E. Bulina, A.S. Shcheglov, A.F. Fradkov, A. Gaintzeva, K.A. Lukyanov, S. Lukyanov, T.W.J. Gadella, and D.M. Chudakov. 2007. Bright monomeric red fluorescent protein with an extended fluorescence lifetime. Nat. Methods. 4: 555–557.

248. Young, R.M., J.K. Arnette, D.A. Roess, and B.G. Barisas. 1994. Quantitation of fluorescence energy transfer between cell surface proteins via fluorescence donor photobleaching kinetics. Biophys. J. 67: 881–888.

249. Eggeling, C., A. Volkmer, and C.A.M. Seidel. 2005. Molecular photobleaching kinetics of Rhodamine 6G by one- and two-photon induced confocal fluorescence microscopy. ChemPhysChem. 6: 791–804.

250. Cordes, T., J. Vogelsang, and P. Tinnefeld. 2009. On the Mechanism of

Trolox as Antiblinking and Antibleaching Reagent. J. Am. Chem. Soc. 131: 5018–5019.

251. Wu, T.W., N. Hashimoto, J. Wu, D. Carey, R.K. Li, D. a Mickle, and R.D. Weisel. 1990. The cytoprotective effect of Trolox demonstrated with three types of human cells. Biochem. Cell Biol. 68: 1189–1194.

252. Saxton, M.J. 1997. Single-particle tracking: The distribution of diffusion coefficients. Biophys. J. 72: 1744–1753.

253. Roy, A., M.J. Field, V. Adam, and D. Bourgeois. 2011. The nature of transient dark states in a photoactivatable fluorescent protein. J. Am. Chem. Soc. 133: 18586–18589.

254. Berardozzi, R., V. Adam, A. Martins, and D. Bourgeois. 2016. Arginine 66 Controls Dark-State Formation in Green-to-Red Photoconvertible Fluorescent Proteins. J. Am. Chem. Soc. 138: 558–565.

255. O'Shaughnessy, A., and B. Hendrich. 2013. CHD4 in the DNA-damage response and cell cycle progression: not so NuRDy now. Biochem. Soc. Trans. 41: 777–782.

256. Elf, J., G.W. Li, and X.S. Xie. 2007. Probing transcription factor dynamics at the single-molecule level in a living cell. Science (80-.). 316: 1191–1194.

257. Vogelsang, J., R. Kasper, C. Steinhauer, B. Person, M. Heilemann, M. Sauer, and P. Tinnefeld. 2008. A reducing and oxidizing system minimizes photobleaching and blinking of fluorescent dyes. Angew. Chemie - Int. Ed. 47: 5465–5469.

258. Dave, R., D.S. Terry, J.B. Munro, and S.C. Blanchard. 2009. Mitigating unwanted photophysical processes for improved single-molecule fluorescence imaging. Biophys. J. 96: 2371–2381.

259. Watanabe, R., N. Soga, M. Hara, and H. Noji. 2016. Arrayed water-in-oil droplet bilayers for membrane transport analysis. Lab Chip. 16: 3043–3048.

260. Belov, V.N., G.Y. Mitronova, M.L. Bossi, V.P. Boyarskiy, E. Hebisch, C. Geisler, K. Kolmakov, C.A. Wurm, K.I. Willig, and S.W. Hell. 2014. Masked Rhodamine Dyes of Five Principal Colors Revealed by Photolysis of a 2-Diazo-1-Indanone Caging Group: Synthesis, Photophysics, and Light Microscopy Applications. Chem. - A Eur. J. 20: 13162–13173.